Development of a 3D cancer model for MRI and radiobiology studies

Thesis submitted for the title of Doctor of Philosophy

Tong Long

Student number: 110071889

Supervisors: Kate Ricketts, Gary Royle and Marilena Loizidou

Department of surgery and interventional science

University College London

October 2019

Declaration:

I, Tong Long, confirm that the work presented in this thesis is my own. Where information has been derived from other sources, I confirm that this has been indicated in the thesis.

Signature: Tong Long

Abstract:

The biological experiments are often carried out in two-dimensional (2D) monolayer cultures. However, two-dimensional cell models are reported could not accurately reflect the three-dimensional *in vivo* tumour microenvironment such as oxygen gradient, nutrient supply. Then there is a further development of a three-dimensional collagen based *in vitro* cancer model from our group research. The novelty includes the three-dimensional (3D) cancer spheroid model developments and development of high collagen density 3D cancer models. Types of colorectal cancer cell lines are used to build the 3D cancer models and the biological properties including metabolism and cell invasion were characterized. The development of 3D cancer model was also applied on MRI session to explore the relationship between MR imaging contrast, collagen density and cell density. This included sample design, the T_1 and T_2 imaging sequence parameter optimization and data analysis. There was image signal at dense boundaries of artificial cancer mass. The 3D cancer model was also applied in radiobiology studies. The cancer models were either proton or photon irradiated, followed by immunofluorescent staining and imaging. Cell apoptosis marker, DNA double strand break marker and hypoxia marker were used to analyze the biological changes after irradiation. The effect of radiation on hypoxia cell was analyzed. There were problems in imaging DNA double strand break of 3D models because the magnification power and blurring caused by thick samples means spatial resolution was worsened. The conclusion was that the project developed a MRI imageable and radiobiology analyzable 3D collagen tumor model. Cancer cells were cultured in 3D tumoroid or spheroid form and 3D tumoroid model expanded the collagen density range. There was a methodology of measuring collagen and cell density under MRI condition. The 3D tumoroid model after proton or photon irradiation could correlate the dose profile versus sample depth and length if specimen were vibratome sliced

properly. Fluorescent radiobiology study showed that higher irradiation dose leads to overexpression of apoptosis markers in proton and photon irradiated collagen cancer cell models. DNA double strand break in 3D radiobiology was difficult to measure due to image resolution and sample washing.

Impact Statement:

The 3D collagen cancer model has its inside academia benefic in wide range of physical, biological and biomedical research applications. It is a customable and controllable platform of cancer cell biology. The advantage of 3D tumor culture could be the reason to use in cancer biology laboratory internationally. For example in this project, there are applications in magnetic resonance imaging and fluorescent radiobiology study. The relevant researches based on 3D cancer model could have clinical applications.

Content:

Chapter 3: Developing a methodology using the 3D collagen cancer model for magnetic resonance imaging applications

Chapter 4: The implementation of 3D collagen cancer models for photon and proton irradiation

List of Figures:

Abbreviation:

2D: two dimensional; 3D: three dimensional; 53BP1: p53-binding protein 1; ACM: artificial cancer mass; BSA: bovine serum albumin; CAIX: carbonic anhydrase IX; CIMP: CpG island methylator phenotype; DMEM: Dulbecco's modified Eagle's medium; ECM: extracellular matrix; FBS: fetal bovine serum; FLASH: fast low angle shot; GE: gradient echo; IR: inversion recovery; MCTS: multicellular tumour spheroids; MSI: microsatellite instability; MEM: Dulbecco's modified minimal essential Eagle's medium; MRI: magnetic resonance imaging; PBS: phosphate-buffered saline; RARE: rapid acquisition refocused echoes; RF: Radiofrequent pulses; ROI: region of interest; ROS: reactive oxygen species; SE: spin echo; SEM: scanning electron microscopy; SOBP: spread-out Bragg peak; TACS: tumour-associated collagen signatures; TE: echo time; TEM: transmission electron microscopy; TI: inversion time;

Chapter 1:
Introduction and literature reviews

The aim of Chapter 1 is to give basic information of cancer cell biology especially for colorectal cancers which is the main cancer type of the project. There are reasons to use 3D models and reviews of the technics and materials of current 3D cancer models. The literature reviews also introduce current models of irradiation and magnetic resonance imaging. These are the backgrounds of the project.

1.1. Cancer crisis in statistics numbers

Cancer is one of the most lethal diseases that threaten human life. In 2015, 15.7% of human death was due to cancer [1]. There are numbers of statistical indexes concerning cancer, such as cancer incidence rate, cancer mortality rate, cancer survival rate, cancer awareness, early diagnosis, outcome improvement of cancer, and quality of life. The statistical data can be age-specific, tumour type-specific, time trends, time trends by age and trends by birth cohort. The two key factors in cancer statistics are the incident rate of cancer and the survival rate of cancer. There were 166,444 deaths from cancer in the UK in 2016, which accounted for 28% of total deaths in the UK that year. Most of the time, patients of the most commonly diagnosed cancers have a ten-year survival rate of 50% or more in England and Wales from 2010 to 2011. In 2012, worldwide, 8.2 million people died from cancer. Lung cancer is the most common cancer type worldwide and it accounts for the largest number of deaths from cancer [2].

The statistics of cancer is age-relevant. The age-standardized rate (ASR) is the measure of the incidence of cancer rises sharply with age. People of different age have different cancer incidence rates. The elderly population has a higher cancer crude rate than young populations. The crude rate is the number of patients who live

in a given area divided by the population of that area. The crude rate and age-standardized rate (ASR) are the two measurements of cancer incidence based on the sum of new cases of diagnosed cancer [3]. The age-standardized rate has an advantage in data comparison between different areas or different time periods, which displays the differences in age distribution. According to the report by the Office of National Statistics (ONS), in 2016, among all the malignant cancer registrations at all age groups in the UK, 228,569 cases were male and 204,962 were female. The direct age-standardized rate per 100,000 population of newly diagnosed cases of all malignant cancer registrations was 986.8 for male and 746.4 for female in 2016. There were more male patients diagnosed with cancer than females across the majority of cancer sites. The number of cancer registered cases grew by 3212 from 2015 to 2016. The data were collected by the National Cancer Registration and Analysis Service (NCRAS) within Public Health England (PHE) [4].

Cancer mortality is defined as the number of patients who died from cancer. The statistics show the number and the rate of cancer deaths per year. As mentioned above, 166,444 people died from cancer, accounting for 28% of the total deaths in the UK in 2016. The crude rate and age-standardized rate are two measures of cancer mortality as well as cancer incidence. The gage-standardized rate is used in data comparison. The net survival index for adults was 69.6 in the UK in 2013. The data was collected from the Clinical Commissioning Group (CCG). The net survival index is an estimate of the probability of survival from cancer alone. It is the ratio of the observed and expected survival if cancer patients have experienced the same background mortality by age and sex as the general population [5].

Breast cancer, prostate cancer, lung cancer, and colorectal cancer are the most frequent cancer types in the UK and worldwide. They account for over half of the cancer registration for all age groups in the UK and around 40% worldwide [2]. Colorectal cancer is the fourth most frequent cancer type in the UK. Colorectal cancer

accounted for 11.5% of the total cancer registration in 2016. The malignant neoplasm of colon and rectum was responsible for 19581 cases for male patients and 15371 cases for female patients in the UK in 2016. The direct age-standardized rate per 100,000 population of newly diagnosed malignant neoplasm of colon and rectum were 84.4 for male and 55.4 for female in 2016 [4]. Classified by stage, according to the statistics from the National Cancer Institute's SEER database between 2007 and 2013, the five-year relative survival rate for people with stage I colorectal cancer was about 88.1% and the proportion decrease at later stages. The five-year relative survival rate for people with stage IV colorectal cancer was about 12.6% [6].

1.2. Hallmarks of cancer

The research by Douglas and Robert (2000) specified six key hallmarks of cancer, which were the self-sufficiency in growth signals, evading apoptosis, insensitivity to anti-growth signals, sustained angiogenesis, limitless replicative potential, and tissue invasion and metastasis [7]. In the past decade, the studies on tumour microenvironment gave further mechanistic underpinnings, broadening the scope of the conceptualization to each hallmark of cancer and finally contributing to a more accurate foundation to study the biology of cancer. The research by Douglas and Robert (2014) changed the subtitles of the hallmarks to sustaining proliferative signaling, resisting cell death, evading growth suppressors, inducing angiogenesis, enabling replicative immortality, and activating invasion and metastasis, as shown in Figure 1.
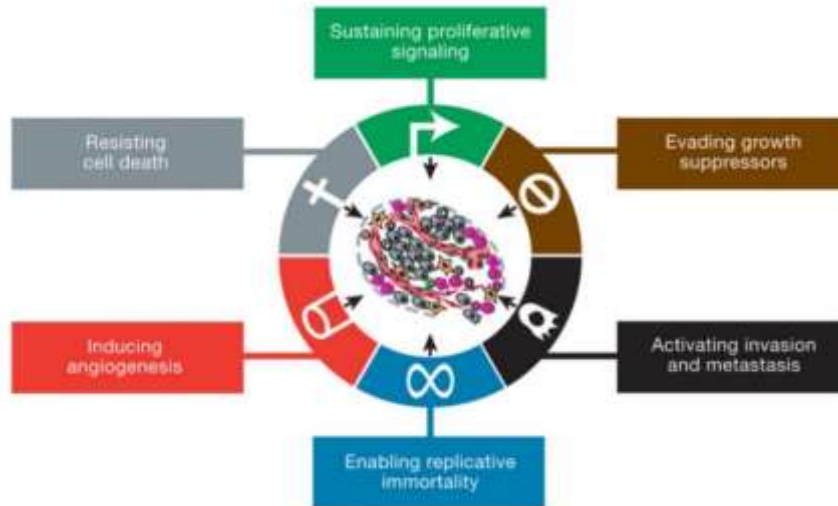
Figure 1: The six key hallmarks of cancer [8]

The first hallmark of cancer is the sustaining proliferative signaling. Normal cells have programmed cell growth, cell division and cell apoptosis with regulated proliferative signaling. Cancer cells fail to regulate types of pathways and sustain the proliferative signaling by alternative methods. For example, the cell survival and energy metabolism of cancer cells are different from normal cells due to deregulation of growth factors that bind to cell-surface receptors and influence the cell cycle as well as cell growth [8]. The study of mitogenic signaling of cancer cells suggests that the sustaining proliferative signaling of cancer cells could produce growth factor ligands themselves by autocrine proliferative stimulation or by sending signals to activate normal cells in the tumour-associated stroma to supply several types of growth factors to cancer cells [8]. The constitutive activation of certain elements of signaling pathways affects the downstream pathway of these ligand-mediated receptors. For example, somatic mutations can activate additional downstream pathways of growth factors [9, 10]. The disruption of negative-feedback loops could attenuate proliferative signaling of cancer cells. The negative-feedback loops dampen the regular signal flux and ensure homeostatic regulation of intracellular circuitry [11]. The defect of the negative-feedback mechanism may affect the development of adaptive resistance toward drugs targeting mitogenic signaling [8]. Moreover, excessive proliferative signaling could trigger cell senescence. Senescence means that cells go into a viable but no longer proliferative state irreversibly.

The second hallmark of cancer is the evasion of growth suppressor. There are lots of tumour suppressor genes limiting cell growth and proliferation. The canceration process normally accompanies with the inactivation of such suppressor genes that encode RB (retinoblastoma-associated) and TP53 proteins [8]. The RB protein integrates cellular signals and acts as a gatekeeper for cell growth and cell division cycle regulation [12]. TP53 protein that receives feedback from stress and abnormality sensors can then terminate further cell-cycle progression until such stress and abnormality are normalized [8]. The regulation of RB and TP53 forms networks to control cell functional redundancy. Two research results reflected the operations of redundantly acting mechanisms that serve to constrain inappropriate replication of cells lacking these key proliferation suppressors [8].

The third hallmark of cancer is resisting cell apoptosis of cancer cells. The programmed cell apoptosis mechanism balances the overall cell numbers. The upstream regulators of cell apoptosis receive and process extracellular death-inducing signals and the downstream regulators of cell apoptosis sense and integrate intracellular signals [13]. The Bcl-2 regulatory protein family is responsible for apoptosis. Bcl-2, together with the relatives (Bcl-xL, Bcl-w, Mcl-1, A1), is inhibitors of apoptosis. They suppress Bax and Bak proapoptotic triggering proteins. Those two proapoptotic triggering proteins disrupt the integrity of the mitochondrial membrane and release proapoptotic signaling protein such as cytochrome c, which actives a cascade of caspase family to induce cellular changes under the apoptotic program [13, 14]. Autophagy can mediate cancer cell survival and apoptosis. For example, the down-regulation of the PI3K signaling pathway and the deregulation of stress transducing BH3 protein can induce autophagy and cell apoptosis. Furthermore, the necrosis of cancer mass has proinflammatory potential and could promote tumour growth [8].

The fourth hallmark of cancer is the enabling replicative immortality of cancer cells. Cancer cells break the barrier of limited proliferation, senescence, and crisis. Senescence means that cells go into a viable but no longer proliferative state irreversibly, and crisis involves functions of cell death and loss proliferation. Researches have concluded that telomers can protect the ends of chromosomes and are keys to cell immortality [15, 16]. Cancer cells enable replicative immortality because they can upregulate expression of telomerase or enter a recombination-based telomere maintenance mechanism to maintain telomeric DNA at sufficient lengths so that the senescence or crisis will not be triggered [8].

The fifth hallmark of cancer is angiogenesis. The tumour-associated neovasculature provides a new vascular circulatory system to supply oxygen, nutrition and evacuate metabolic waste, carbon dioxide to tumour cells. The angiogenesis starts with the growth of new endothelial cells and those cells assemble into a tube shape and form new blood vessels. The angiogenesis is always active in tumour area because of the need for nutrition and oxygen due to an unlimited proliferation of cancer cells. Besides the formation of new blood vessels, the normal quiescent vasculature also sprouts out new blood vessels to help neoplastic growth [17]. The angiogenesis is controlled by two countervailing factors, vascular endothelial growth factor-A (VEGF-A) and thrombospondin-1 (TSP-1) [18]. The tumour-associated neovasculature produces aberrant blood vessels because of chronically activated angiogenesis and unbalanced mix of proangiogenic factors. In morphology, such blood vessels have convoluted and excessive vessel branching, precocious capillary sprouting, distorted vessel shape, and erratic blood flow [19]. Recent researches have discovered that pericytes are important components for tumour neovasculature, while endogenous angiogenesis inhibitors can present natural barriers to tumour angiogenesis and a variety of bone marrow-derived cells can contribute to tumour angiogenesis [20, 21].

The sixth hallmark of cancer is the activation of metastasis and invasion. There is

characterized alteration in cancer cells during invasion and metastasis. One typical alteration is the reduction of E-cadherin expression in cancer cells as well as the extracellular matrix around cancer cells. This protein governs cell adhesion. It aids the epithelial cells to assemble into cells sheet and maintain the quiescence of cells in those cell sheets. The observed downregulation and mutation inactivation of E-Cadherin in tumour area is the suppressor of hallmarks of cancer [22]. The sequence of discrete steps of cell behavior from invasion to metastasis is called invasion-metastasis cascade. It begins with the local invasion and followed by intravasation of cancer cells into blood or lymphatic vessels. The cancer cells are transited to other organs or tissues and form highly invasive micrometastases after extravasation. Finally, the growth of micrometastases into bulk tumours is called colonization [23]. The epithelial-mesenchymal transition (EMT) program broadly regulates invasion and metastasis. In this process, epithelial cells gain the ability to invade, resist apoptosis, and disseminate [23]. Within cancer cell invasion and metastasis process, the EMT program can be activated either transiently or stably at various levels [8].

1.3. Cancer induction and morphology

For cancer induction, three main extrinsic reasons are responsible: 1) physical reasons such as X-ray, 2) chemical reasons such as benzene and 3) the oncogene such as Rous sarcoma virus. Varmus and Bishop started the discovery of oncogene in their researches in the 1970s. They found that the cellular-src (c-src) gene in healthy cells could be induced to canceration when the gene was transfected with a retrovirus. The c-src gene is called proto-oncogene because it has the potential to be activated to cause cancer. Hence, it is an intrinsic reason to trigger cancer. Besides of c-src gene, there are plenty of proto-oncogenes in healthy cellular genomes such as the H-ras gene and myc gene. In summary, several proto-oncogenes in cellular genomes can be activated by retroviruses (mainly in animal models), or by point mutation (in human models) to initiate canceration. This activation of oncogene could be base

substitution, gene copy amplification or chromosomal translocation [24]. Normal cells undergo cellular proliferation to multiply the cell amount in control. However, some cells are affected by oncogenes, and then those cells undergo uncontrolled, continuous cell division, evading apoptosis and forming malignant proliferative cells (cancer cell). As mentioned in the preceding subtitle, there are tumour-suppressor genes such as P53. Those genes code for protein and operate as a specific inhibitory pathway. The mutation of tumour-suppressor genes will inactivate critical tumour-suppressor proteins, depriving cells of this restraint on cell division [25].
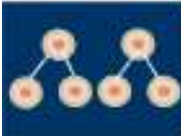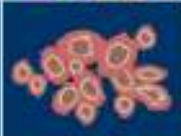
Figure 2: The differences between cancer and normal cells in morphology [26]

The morphology and cell biology of cancer cells are different from normal cells. Figure 2 illustrates the differences between cancer and normal cells. Cancer cells have one to five times larger nuclei than normal cells, and nuclei in cancer cells display various

shapes. Cancer cells lose specialized cell features and they are arranged disorderly with poorly defined cell boundary. The cytoplasmic volume is reduced in cancer cells. Moreover, cancer cells have nuclear hyperchromatism because of a large volume of chromatin. There are many dissociative ribosomes exposed in the cytoplasm of cancer cells. A key change in the cell biology of cancer cells is that the amount of glycosidoprotein on the cell membrane has been reduced. This leads to the decreasing of tackiness between cancer cells prone to cell translocation and invasion [27].

The formation of cancer is due to environmental factors (such as the three main extrinsic reasons and other factors like lifestyle), and inherited factor to a certain degree. The process is complicated and multistage. Cancer cells undergo gene alteration and get survival advantages at each stage and finally achieve malignant proliferation. Traditionally, radiotherapy and chemotherapy are used for cancer treatment. The challenge of cancer treatment is closely related to the understanding of cancer. There are many unknown areas about its biological mechanism, targeting, drug delivery, early-stage diagnosis and final-stage survival. Traditional chemotherapy has great side effects. There are many investigations about drug delivery using nanotechnology to increase efficiency and decrease the side effect. Traditional radiotherapy has low efficiency to the hypoxic tumour mass. The detailed mechanisms are described in other subtitles of this chapter. The difficulty of treatment is specific targeting of cancer cells without affecting healthy cells.
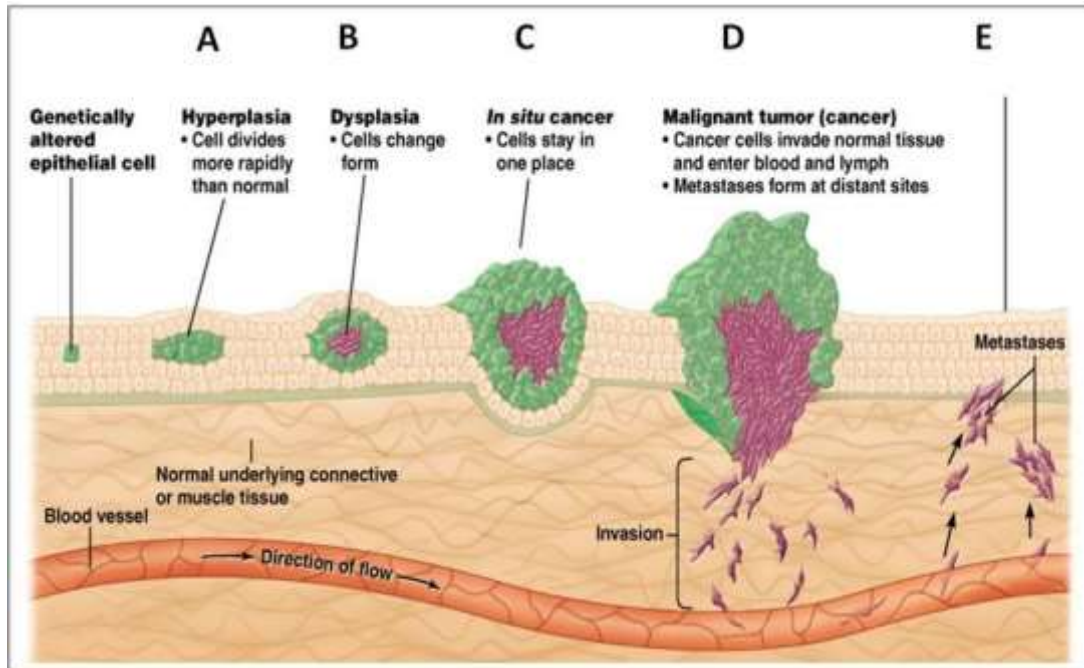
Figure 2A: Stages of tumor development and metastases [27+]

Figure 2A shows the example of tumor development. Normal cells undergo aforementioned environmental and inherited factors are genetically altered and become hyperplasia and dysplasia. Normal cells changed their morphology and characterization as shown in Figure 2. The *in-situ* cancer grows to be malignant tumor and then invade to periphery blood and/or lymph vessels. The malignant cancer cells metastasize to another site of body and form another *in-situ* cancer. Detailed microenvironment will be introduced in 1.4 of Chapter 1.

1.4. Colorectal cancers

There are a number of types of colorectal cancer. About 90% of colorectal cancers are adenomatous polyp type whose growth rate is comparatively slow. About 5% of colorectal cancer cases are villous adenoma whose growth rate is dangerously accelerated. There are other rare types such as Juvenile polyposis syndrome and Peutz-Jeghers syndrome [28]. The malignancy rate of mild adenomatous polyp types increases by 30% if the tumour size is larger than 2cm. The environmental and genetic

factors are important in colorectal carcinogenesis. Environmental factors can account for over 70% of all sporadic colorectal cancers [29]. The environmental factors include living conditions, diet, insulin resistant and fiber intake. Other factors include inflammatory bowel disease, ureterosigmoidostomy, smoking and genetic factors [30].

The microenvironment of colorectal cancer is similar to that of other tumours. Tumour cells and stromal cells, especially cancer-associated fibroblasts and immune cells, take part in each step of tumour progression. The conflicting signals can re-educate or corrupt signal components and lead to a different outcome. The microenvironment of colorectal cancer is illustrated in Figure 3 below:
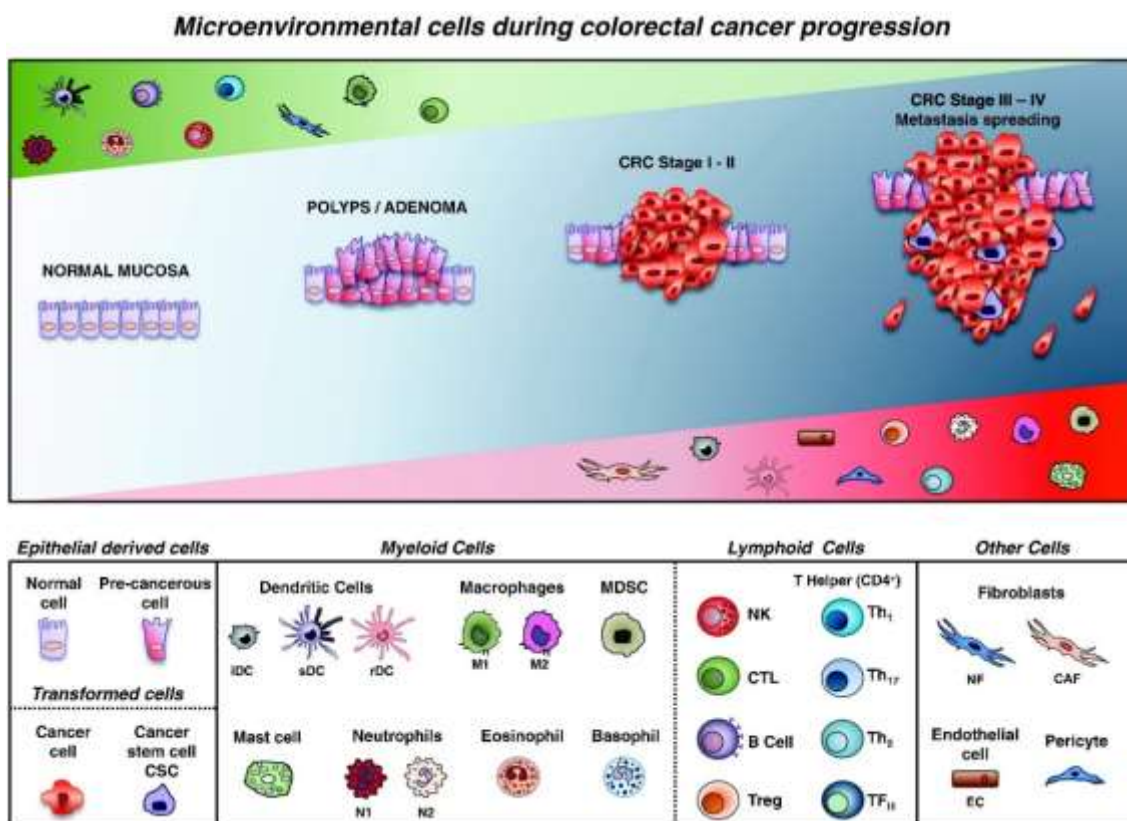
Figure 3: The microenvironment of colorectal cancers during cancer progression [31]

The microenvironment of colorectal cancer cells can be used to classify cancer subtypes. There are four subtypes: CMS-1, CMS-2, CMS-3, CMS-4 plus their mixed or indeterminate phases. The pathway, molecular feature, microenvironment composition, potential target therapy, and clinical associations differ depending on the

subtype. Figure 4 below shows the classification and their compassion.

A novel TME-based CRC classification

Omics Analysis (18 Colorectal Cancer data sets n= 4,151)	%	CRC subtypes	Clinical and prognostic associations	Molecular features	Pathways involved
DNAs / RNAs / Proteins (Whole tumour samples profiling)	14	CMS1 (MSI-Immune)	• Good prognosis • Poor survival after relapse • Frequently diagnosed in females • Higher histopathological grade • Right-sided lesions (77%)	• MSI (76%) • Hypermutation (94%) • SCNA LOW • CIMP HIGH • Enriched *BRAF-mut* (42%)	• RTK and MAPK pathways activation
	37	CMS2 (Canonical)	• Better survival rates after relapse • Left-sided lesions (59%)	• MSS (99%) • SCNA HIGH (*HNF4a-amp*) • CIMP LOW	• Wnt and MYC hyper-activation • Low Mesenchymal, EMT, TGFβ activation • High miR-17–92 cluster
	13	CMS3 (Metabolic)	• Right-sided lesions (51%)	• MSI (16%) • Hypermutation (28%) • SCNA LOW • CIMP LOW • Enriched *KRAS-mut* (68%)	• Metabolic burst • RTK and MAPK-activation • Low VEGF/VEGFR • Low Mesenchymal, EMT, TGFβ activation • Low let-7 miR family
	23	CMS4 (Mesenchymal)	• Worse relapse free and overall survival • Diagnosed at more advanced stages (III and IV)	• MSS (92%) • SCNA HIGH • CIMP LOW	• Angiogenic signature (High VEGF/VEGFR) • Inflammatory signature • Immunosuppressive signature • Mesenchymal, EMT, TGFβ activation • Low miR-200 family
	6	Mixed			
	7	Indeterminate			

Figure 4: A novel tumor microenvironment based colorectal cancer classification [32]

The underlying pathological mechanism of colorectal cancers is largely unknown. Recently, there are more pieces of evidence showing that inflammatory mediators such as cytokines and their receptors are the key components in regulating cancer growth, angiogenesis and metastasis [33,34]. Cytokines secreted by colorectal cancer and stromal cells can influence the behavior of cancer cells and regulate tumour growth microenvironment. A proinflammatory cytokine called Interleukin-6 (IL-6) secreted by stromal cells can associate with colorectal cancer cell progression by inducing complex signaling cascades and triggering mitogenic, pro-proliferative and

pro-angiogenic effect in tumour cells [35,36,37]. Interleukin-1β (IL-1β) is one of the key stimulating signals to regulate IL-6. Researches show that increased expression of IL-1β/IL-6 network is relevant to the upregulation of potential proangiogenic factor cyclooxygenase-2 (COX-2) in human colorectal cancers [36,39].

There are typically three molecular signaling pathway alterations in colorectal cancers. The first one is chromosomal instability which is the culprit in 80% of colorectal cancers [40]. Some tumour suppressor genes such as APC, P53 and SMAD4 are mutated because of external damaging factors. APC involves in the regulation of the intracellular level of β-catenin in the Wnt pathway [41]. The mutation of APC is followed by the mutations of the K-RAS and P53 genes and finally leads to the transformation of carcinomatous cells from epithelial cells. The second one is the inactivation of mismatch repair genes (MMR). Patients with HNPCC or Lynch syndrome are subject to this type of mutation [42]. Sporadic colorectal cancer also has defects in the inactivation of MMR. The mutation of base excision repair gene MUTYH and NTHL1 is common in colorectal cancers. MUTYH protects DNA from reactive oxygen species damage of irradiation especially at the cell division stage [43]. NTHL1 mutation shows a tendency for canceration in several anatomical locations. Without the function of MMR, DNA can accumulate mutation in downstream tumour suppressor and proto-oncogene genes [44]. BRAF mutation of colorectal cancer is another reference in clinical implication because patients increase the risk of poorly differentiated tumour [45]. There are mutations in Bax receptors and transforming growth factor (TGF) β receptor genes as well. Bax genes mutation is responsible for wide invasion and metastasis. TGF-β receptor is associated with limiting cellular proliferation linked to relapse after treatment [46]. The third one is CpG island hypermethylation phenotype (CIMP) pathway alteration. This is unique because it is epigenetic-based. This alteration leads to accumulation of defects in genes such as KRAS, BRAF and P53 [47].

The growth and invasion of colorectal cancer cells are related to the epithelial-mesenchymal transition (EMT) program. This is the process that epithelial cells decrease their cell polarity and cell-cell adhesion ability, and then turn to be mesenchymal stem cells hence able to migrate and invade [48]. Mesenchymal stem cells can differentiate into types of cells and it is related in the initiation of metastasis in cancer progression. Elevated levels of E-cadherin and loss of E-cadherin of epithelial cells are the key features expressed during the EMT process [49]. Hypoxia and several cells signaling pathways such as TGF-β, fibroblast growth factor (FGF), epidermal growth factor (EGF) and WnT/beta-catenin can induce EMT [50]. The p63 factor van inhibits EMT and reduction of some p63 isoforms are relevant to the development of epithelial cancers [51]. Extracellular stimuli from tumour microenvironment regulate EMT abnormally including growth factors, inflammatory cytokines. Hence, tumour cells adapt to the changes in tumour microenvironment and become metastasized through EMT programming. For colorectal cancers, there are three major groups of EMT-activating transcription factors: the SNAIL family of zinc-finger transcription factors SNAIL/SLUG, the zinc finger E-box binding homeobox (ZEB) family of transcription factors ZEB1/ZEB2, and the TWIST family of basic helix-loop-helix (bHLH) transcription factors TWIST1/TWIST2 [52]. The positive expression of SNAIL family is associated with distant metastasis and correlated in lower survival of cancer patients [53,54]. The high expression of the ZEB family is correlated with liver metastasis and poor prognosis in CRC [55]. The upregulation of TWIST family is associated with shorter overall survival and poor prognosis [56,57].

Typically, colorectal cancers start from a benign tumour in polyp form which turns to be cancer over time. Then colorectal can be diagnosed by obtaining a living specimen of colon through sigmoidoscopy or colonoscopy. Surgical resection is the mainstay treatment plan for colorectal cancers. Tiny polyp could be removed through colonoscopy. After screening and biopsy of large polyp specimen, treatment plans such as a combination of surgery, radiation therapy, chemotherapy and targeted

therapy, can be made for patients[58]. The key prognosis determinant of colorectal cancers is the pathologic stage at presentation. The presentation includes stage I, IIA, IIB, IIC, IIIA, IIIB, IIIC and IV according to the 2010 American Joint Committee on Cancer (AJCC) staging criteria [59]. The five-year survival stratified data by tumour stage at diagnosis is the ideal presentation of the pathologic stage. Besides that, there are other prognostic determinants such as extramural tumour deposits, lymphovascular and perineural invasion, microsatellite instability (MSI), RAS and BRAF mutation [60].

1.5. Tumor microenvironment and metastasis

As mentioned in the previous section, tumour microenvironment includes cancer cells, angiogenesis, stroma, immune cells and the overall immune system. In an ideal 3D microenvironment model, cancer cells are the main body. Around cancer cells, there are extracellular matrix (ECM), cancer-associated fibroblast (CAF), macrophage, lipocyte, and mastocyte to form the stroma. Angiogenesis includes the blood vessels and angiogenesis-related proteins such as the epithelial growth factor (EGF). The immune system and immune cells are killer T cells and regulatory T cells [61]. A balanced stroma can prevent tumourigeneses, while an abnormal stroma results in tumour formation. In tumour stroma, the disorganized structure can develop mutations to soluble products released tumour altering genes. Figure 5 below shows the tumour microenvironment.
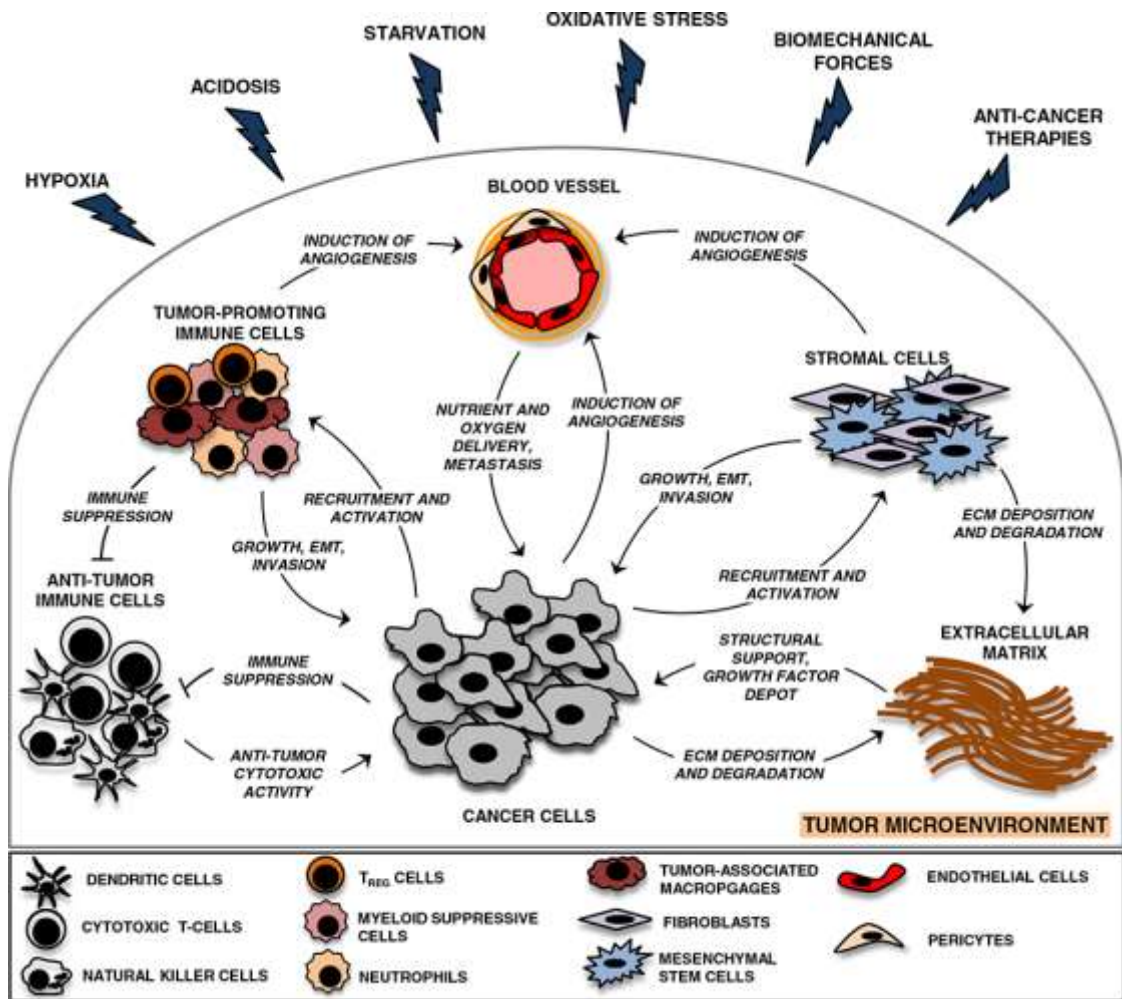
Figure 5: Tumour microenvironment includes the cells and external factor [61]

Within the tumour growth process, the typical 3D tumour model/tumour microenvironment shows that there is necrosis in the center, surrounded by hypoxia tumour mass and active tumour cells in the outermost layers [61]. There are three reasons that cause hypoxia. 1) Firstly, the abnormal neoangiogenesis of tumour microvessels resulted in acute perfusion-related hypoxia that is transient and affects cells up to the vessel wall. 2) Secondly, the distance between a blood vessel and expanding tumour mass increases, so the competition for oxygen supply results in chronic diffusion-related hypoxia which affects cells greater than 70-100 micrometer from nearest capillaries. Moreover, the critical thickness for oxygen diffusion of tumouroid or spheroid in the hydrogel is 600 micrometers [62]. 3) Thirdly, anemic hypoxia is because of the reduced oxygen-carrying capacity of hemoglobin because

of disease or treatment-related anemia [63]. In hypoxia condition, the cellular metabolism is changed such as accelerated glucose uptake, glycolysis and synthesis of lactic acid. Those changes are regulated by hypoxia-inducible factor 1 (HIF-1). HIF-1 promotes hypoxia cells to upregulate more than 100 proteins that promote survival and raise aggressiveness of hypoxia tumour mass. HIF-1 can also enhance the expression of vascular endothelial growth factor (VEGF) and promote angiogenesis and reconstruction of tumour oxygen supply pathway indirectly [24].

The final stage of tumour growth, after tumour neoangiogenesis (because without angiogenesis, the size of tumour will be no larger than 1mm), is the invasion of tumour cells. Cancer metastasis is a complicated and multistep process described as invasion-metastasis cascade. Primary tumour invades the surrounding tissues and enters the lymphatic system, and then the circulatory system via intravasation. After that, the tumour cells are transported or spread to another location. After extravasation, the tumour locates at new tissues and form micrometastases. The micrometastases are highly proliferative and cause colonization soon to complete the cancer metastasis.

1.6. The benefit of 3D cancer models

In 2D monolayer cell culture of cancer cell lines, the culture process and nutrition supply are quite fundamental. The cells in a 2D coordinate system poorly mimic *in vivo* biological functions compared with those in 3D models. 2D models lack the ability to correctly mimic stromal heterogeneity and tumour-stromal components. The nutrient, oxygen supply and pH gradients are not recapitulated. 2D models can not represent *in vivo* tumour realistically and 3D models are designed to overcome those shortcomings of conventional 2D cultures [64]. 3D models can simulate tumour microenvironment with cell-cell interaction, cell-ECM interaction, spatial architecture and cellular heterogeneity. The 3D structure establishes nutrient, oxygen, signaling factor gradients and could establish unique gene expression patterns which are similar

to *in vivo* solid tumour [65].

A study showed that when the 2D and 3D models of the MCF-10-DCIS breast cancer cell lines with human mammary fibroblasts, known as the ductal carcinoma in situ (DCIS) to invasive ductal carcinoma (IDC) transition, were compared, the 3D model increased paracrine signaling, and enhanced the rate of invasive behavior than 2D models [66]. This research validates that the 3D microenvironment has better paracrine interactions. 3D cell culture models have improved cell migration, differentiation, survival and growth than 2D cell culture models. Another important advantage of 3D cell model is that this model has greater stability and longer lifespan of cells because the gene expressions are more closely resembled than *in vivo*. For protein expression between 2D and 3D models, the cancer cells normally will not express different molecules, but the degree of expression may be varying. The 3D scaffold fabrication has advantages in complex geometry creation, porosity control, growth factor control and multiple cells co-culture [67]. In summary, 3D modeling has numerous advantages compared with 2D modeling and it is a step forward in realistic tumour simulation.

1.7. Choice of biomaterial for 3D models

Biomaterials interact with the biological system. The choice of biomaterial is depending on the design criteria of 3D models. Normally, biomaterials are classified by chemical and physical composition, biodegradability, type of origin, and generations of modifications [68,69]. The biomaterials could be ceramic, polymers or composites. Ceramic biomaterials are mainly used in orthodontal applications. Polymers are mainly used in soft tissue bioengineering and composites are the blends of those two types. Composites are mainly used in orthopedic and dental tissue engineering. For 3D model design, the most suitable biomaterial is polymers because of their similarity with connective tissues. There are natural and synthetic polymers. Natural biomaterials

include collagen, chitosan, hyaluronic acid, and agarose. The merits of natural biomaterials are its biocompatibility, biodegradability and abundant availability. Synthetic biomaterials can be degradable and non-degradable polymers. Non-degradable polymers such as poly(methyl)acrylates and polysiloxanes are used in sutures, orthopedic implants because of reproducible quality, tailored mechanical property and shapes. Degradable polymers such as polylactones and polycarbonates are used in scaffold and drug delivery systems because of the degradation rate control and growth factor release rate [70]. We don't choose synthetic biomaterials because we don't need rigid mechanical shape and degradation controls.

Collagen is abundant in human bodies and it is the main structural protein in the extracellular matrix in types of connective tissues in animal bodies [71]. Collagen family has a 25% to 35% proportion of whole-body protein content in human bodies. The chemical structure of collagen consists of different amino acids binding together to form triple-helices and then form elongated fibrils. The collagens are mostly found in fibrous tissues in human bodies such as tendons, ligaments and skin [72]. Currently, 28 types of collagen have been identified, among which collagen type I, type II, type III, type IV and type V are the most common ones. Moreover, among these five types, over 90% collagen in the human body belongs to collagen type I. Collagen type I is the key component of the organic parts of bones and it is also important in skin, tendon, vasculature and organs. Collagen type II is the main collagenous component of cartilage. Collagen type III is the main component of reticular fiber. Collagen type IV forms basal lamina and collagen type V are found in cell surfaces and hair [73]. In our 3D model design, we choose the most widely used collagen type I for modeling because of its availability and it is suitable for organ and soft tissue modeling. Furthermore, collagen has a great tensile strength to maintain the structure and it has pore, permeable and stable structure *in vitro* and *in vivo*. It has good compatibility, growth response and there are no immunogenic reactions. Those made it the most suitable choice for 3D model design.

Chitosan has a similar chemical structure as hyaluronic acid. The degree of acetylation is a controlling factor to meet the designed criteria of the degradation rate. Research groups use chitosan to construct a 3D scaffold for MCF-7 breast tumour cell culture and determine the cytotoxicity of tamoxifen [74]. Chitosan has natural antimicrobial, hemostatic and hypoallergenic properties [70]. We don't choose chitosan because we need gel-based biomaterial to simulate extracellular matrix and tumour microenvironment.

There are Matrigel and hydrogel as well, which are popular choices in 3D modeling. Matrigel is a trading name of Corning company. It is a gelatinous protein mixture secreted by Engelbreth-Holm-Swarm (EHS) mouse sarcoma cells. It resembles the complex extracellular environment found in many tissues and it is ideal for cell culture [75, 76]. We don't choose Matrigel because the cost is high, and we don't need such cultural advantages at our research stage. Matrigel does not contain proper ratios of collagen type I or hyaluronan as those found in the stromal area of *in vivo* tumour [77]. Moreover, the heterogeneous composition of structural proteins could affect the quality of specific fluorescent antibody staining. Hydrogel is a highly hydrated hydrophilic polymer network which has a structure similar to the natural extracellular matrix. It can be obtained either naturally or through synthesis [78]. Hydrogels are biocompatible and processable from amorphous gels to semi-stiff sheets. It can be an alternative biomaterial for my project, but our research group prefers research on collagen and has experience in this area.

1.8. Current 3D model tissue engineering techniques in colorectal cancer and the innovation in our 3D model design

3D culturing modeling can be scaffold-free or scaffold-based. Scaffold-free 3D culturing models are best exemplified by tumour spheroids, and scaffold-based 3D

culturing model can be classified by biomaterial and process method [79]. The synthetic or natural biomaterials mentioned before are chosen and tailored to the specific 3D structure by different techniques. Among the most techniques, the 3D printing biomaterial platform is developing rapidly in recent years. 3D printing can permit multi-level spatial control of cell organization and placement of materials and biomolecules, so the extracellular matrix properties of tumour microenvironment can be precisely recapitulated [80]. For example, computer-aided 3D printing can be used to create large 3D models for dentistry and orthopedic applications. 3D printing can also create micro 3D models. There are 3D hydrogel bio-printing samples to deposit biomaterials in a layer-by-layer fashion to simulate 3D tissue construction [78]. Figure 6 below shows the common schematics of scaffold-free technologies used for 3D *in vitro* tumour spheroids assembly.
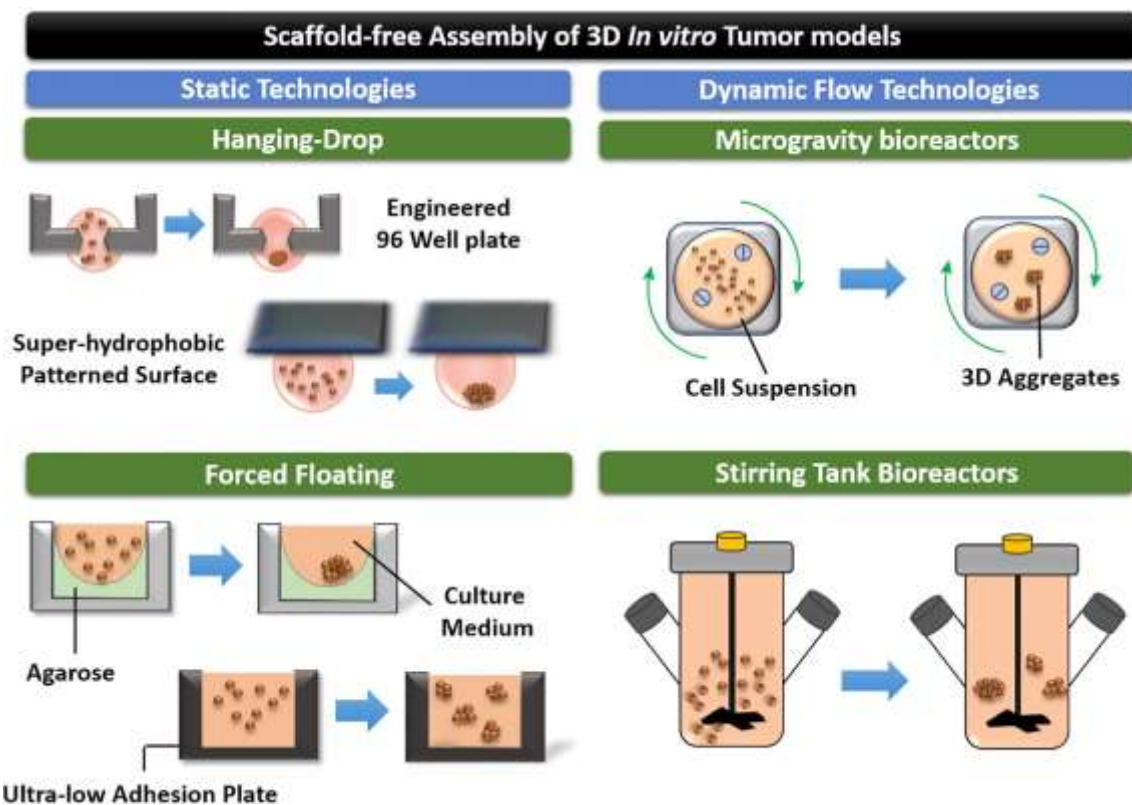
Figure 6: Common schematics of scaffold-free technologies used for 3D *in vitro* tumour spheroids assembly [81].

One research group has harvested HCT-116 colorectal cancer cell lines from tissue culture plates and then seeded the cells on bio-fabricated alginate beads as the 3D *in vitro* model. This 3D model controls alginate concentration, calcium chloride concentration, gelling time and fabrication parameters such as voltage, flow rate and frequency to achieve microsphere with maximal diameter up to 600 micrometers [82]. In comparison to our 3D spheroid model in a collagen matrix, there is a scaffold-free technology based on Corning™ ultra-low attachment multiple well plates. The spheroids are harvested and then transferred into 3D collagen "sandwich" with maximal diameter up to 400 micrometers. As mentioned in Figure 6, there are four typical scaffold-free 3D spheroid models. There are scaffold-free 3D cultures optimized for specific design criteria. For instance, Synthecon® rotary cell culture systems are based on microgravity bioreactors, which is ideal for 3D spheroids culture under low-shear stress conditions [83].

There are various scaffold-based 3D model developments and designs. One research group used hybrid collagen alginate hydrogel as a platform for 3D tumour spheroid invasion. That hybrid hydrogel has well-organized, homogenous microenvironment with adjustable mechanical stiffness and excellent permeability. The mechanical stiffness is subject to collagen and alginate concentration and ratio [84]. There are also well-established commercial scaffold-based 3D culture solutions such as AlgiMatrix®, Alvetex® and Cytodex™. AlgiMatrix® is alginate-based scaffold with a highly porous matrix which is suitable for 3D cell culture and microtissue formation [85]. Alvetex® is another type of highly porous polystyrene scaffold suitable for 3D cell culture and microtissues formation [86]. Cytodex™ is a crosslinked dextran matrix-based particles used for 3D cells expansion [87].

For colorectal cancer, some research groups have used 3D organoid models. The common method is an enzymatic digestion of tumour tissue to obtain tumour organoids. The mouse- and human-originated tumouroid collected by such method

are plated in Matrigel for further studies [88]. It is difficult to get organoid and our tumouroid model design is aimed to simulate the essential microenvironment of tumour. The tumouroid will be plated on a 3D matrix. Our research group used collagen instead of Matrigel. The reason will be explained in the last subtitle.

We focus on natural collagens because of its closer physiological relevance. Even though the technology is attractive and the choice of ink for 3D bioprinting can be collagen or hydrogel to create tumour microenvironment, our 3D tumour model does not need specific scaffold shape and sophisticated biological functions. Our 3D tumour model design is a cost-saving and flexible model that can simulate essential tumour microenvironment for research purposes. The 3D structure can be scaffold-free for 3D spheroid culture. It can be uncompressed 3D collagen gel for proton irradiation or compressed artificial cancer mass surrounded by stroma or uncompressed collagen for MRI session and photon irradiations. It is a very flexible and simplified design.

1.9. Key studies and techniques of models in radiation biology

Genetically engineered mouse models (GEMMs) are generated approximately 40 years ago. They are popular research tools in cancer researches. GEMMs are used in radiobiology studies of (1) *in vivo* short hairpin RNA (shRNA) to investigate normal tissue radiation injuries and carcinogenesis, (2) the Cre-loxP technology to study normal tissue radiation injuries, (3) the Cre-loxP and FLP-FRT technology to dissect mechanisms of tumour response to radiation and (4) the RCAS-TVA system to model primary cancers [89].

There are amorphous track models in radiobiology study. This model uses the response of a system to gamma-rays and the radial distribution of dose about an ion's path to describe survival and other cellular endpoints from irradiations [90]

The most attractive models for my project are the human 3D tissue models in radiation biology. It is developed from the well-established 2D monolayer targeted and non-targeted cell culture model of ionizing radiation. The advantages of 3D over 2D is illustrated in previous subtitles. There are 3D skin models, lung models, breast models, and endothelium models. Skin models use EpiDerm MatTek^{TM} as 3D matrix. Lung models use EpiAirway MatTek^{TM} 3D system. Endothelium models use Matrigel or collagen gel and breast models use acini or Matrigel [91].

1.10. Key models in MRI imaging

The detailed working theory of MRI will be introduced in Chapter 3. MRI imaging techniques increase the resolution of images and the ability of imaging tissue functions in recent years. The strength of the magnetic field also has been improved from 3-T to 7-T technology [92]. For colorectal cancer diagnosis, pelvic MRI is frequently used. Pelvic MRI is expensive and time-consuming. It has similar sensitivity and specificity to economic endorectal ultrasonography in early-stage studies. Thanks to advances in relevant technologies and imaging resolution, MRI in nowadays is more common for routine diagnosis [93]. Moreover, diffusion-weighted MRI (DW-MRI) is a functional imaging tool as a standard MRI protocol for the investigation of patients with colorectal cancer. DW-MRI can be used to identify micro-displacement of water molecules in colorectal tissues and provides exceptional accuracy to discriminate the benign stage from malignant tumour stage. DW-MRI can also detect colorectal neoplasms and peritoneal implants to confirm the metastases of colorectal cancer. It can also track local tumour relapse within fibrotic changes [94]. This technique detects the differences in the mobility of water molecules in the extracellular matrix of colorectal tissues and the signal intensity is related to the impeded diffusion of water molecules.

1.11. The impact of irradiations on cell behaviors

Irradiation creates reactive oxygen species (ROS) that damage cells especially in the nuclei area. The incident radiation will cause radiation absorption of local areas. The excitation and ionization occurred in about 10^{-15} seconds. It is followed by free radical formation in the order of 10^{-10} to 10^{-9} seconds. The breakage of chemical bonds will finally lead to biological effects [95]. DNA is the prime target of radiation. There are single-strand breaks (SSB) and double-strand breaks (DSB) of DNA after irradiation. SSBs can be repaired readily using the opposite strand as a template so it has little biological changes. On the contrary, DSBs are the key lesion produced in chromosomes by radiation, and they will result in apoptosis, carcinogenesis or mutation [95]. Figure 7 below shows how DNA is damaged and the activation of DNA damage response (DDR) pathway.
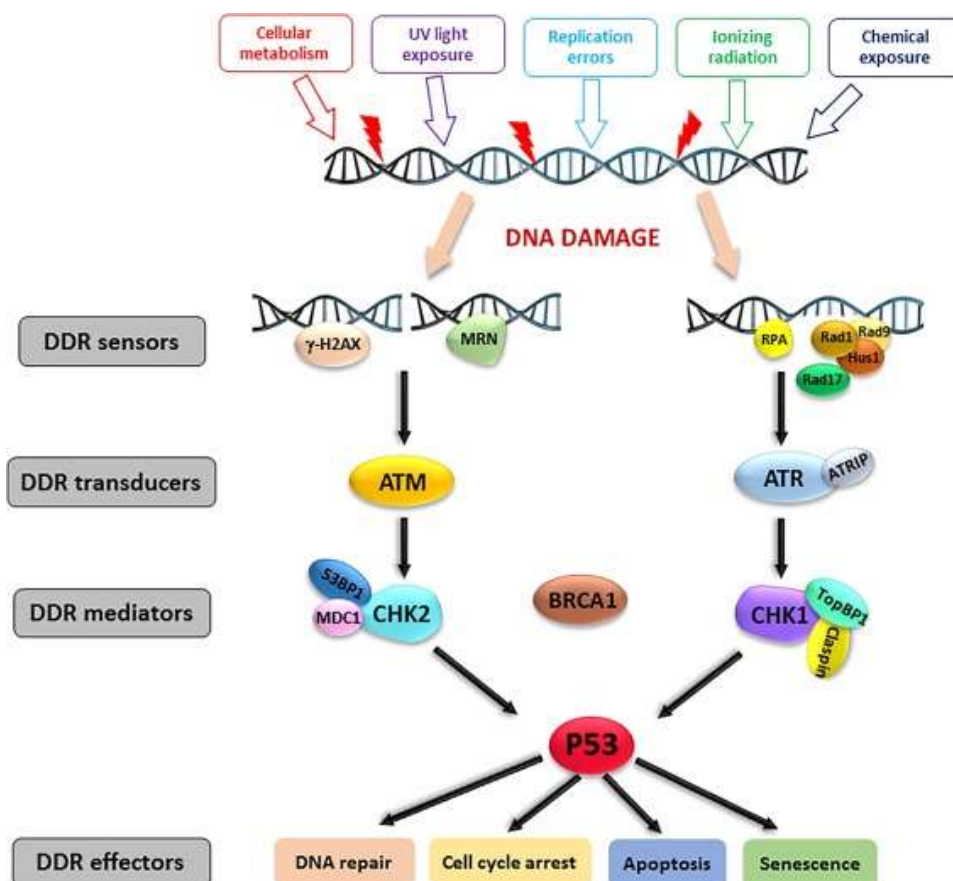
Figure 7: DNA damage response network [96]

Chapter 2:
Characterizing 3D collagen cancer model for spheroid and tumouroid cell culture

2.1. Aim

The 3D collagen cancer model is designed as a multifunctional platform for different applications. The cultured cell types can be spheroid or tumouroid and the applications range from clinical tests to biological researches. This kind of model enables cancer cells to grow and show biological activities during the cultural period. The aim of this chapter is to characterize the 3D collagen cancer model for spheroid and tumouroid cell culture so that the model can be used as an imageable biophantom for biological researches.

2.2. Design criteria

An ideal 3D collagen cancer model should provide proper collagen density and high reproducibility for cells. The 3D structure is stable and the collagen geometry, collagen density, and cell seeding density are controllable. In the model, cancer cells live and grow in the 3D structure and display biological properties such as cell growth, cell invasion, and hypoxia. The size of MRI and irradiation is in mm scale.

2.2.1. 3D collagen model as a multifunctional platform

2.2.1.1. Controllable 3D collagen model

2.2.1.1.1. Reproducibility

The reproducibility of the 3D collagen model can be controlled by standardized working procedures and precise degrees of pH neutralization. The design criteria of the 3D collagen model should provide a high reproducibility so that the collagen gel can always be optimized, and the collagen dimension can be controlled. The ratio of the collagen mixture is fixed, and two concentrations of alkali are used for

accurate pH control. With chemicals and instruments, the collagen matrix is reproducible.

2.2.1.1.2. Collagen density

The collagen density can be controlled by applying physical compression when the collagen mixture is placed in the metal mould. The weight of metal plunger is fixed. Hence, the control of compression time or set the compression level can change the collagen density. The design criteria are to control and reproduce the collagen density within the 3D collagen model. The relationship between compression time and collagen density will be described in this chapter. The collagen density range needs to fit actual *in vivo* tissue collagen density. Soft tissues have less than 10% collagen weight density and dense tissues such as bones can have a collagen density of up to 30% [97]. The design criteria of traditional 3D collagen model can have collagen density to fit soft tissues and with the help of extra plastic blocker, the collagen density can further increase to around 20% to mimic dense tissues. The detailed comparison of experimental data is shown in discussion session 2.5.1.2.2.

2.2.1.1.3. Cell seeding density

As an artificial cancer mass, the cell seeding density can be controlled as well as the collagen density. Our research group mainly adopted a low cell seeding density from $1\text{-}10\text{x}10^6$ cells/mL collagen mixture and I am also interested in high cell seeding density application from $1\text{-}10\text{x}10^7$ cells/mL collagen mixture. The reason to explore the high cell seeding density is to extend the application range to simulate the *in vivo* tumour microenvironment. As reported from previous studies by our research group and after a personal talk with Mr. Tarig Magdeldin about his experiment test, the maximal cell seeding density is $4\text{x}10^6$ cells/mL in collagen mixture, because the collagen will not set when seeding with higher cell seeding numbers.

2.2.1.2. 3D collagen model for imaging application

In my project, the 3D collagen models are used in the light microscopy, confocal microscopy, fluorescent microscopy, and MRI applications. The gel collagen matrix is tailored to the design criteria of the 3D collagen model to fit the image instruments so that good image contrast can be displayed. For example, the confocal microscopy requires a thin sample thickness to get high resolution, and the MRI needs a methodology to reduce the air bubble artifacts.

2.2.1.2.1. Cell metabolism

As a design criterion, the cells in the 3D collagen model should maintain healthy metabolism during the cultural period. AlamarBlue^{TM} assay was used to measure, quantitatively, the proliferation of cancer cell lines. AlamarBlue^{TM} assay uses non-fluorescent indicator resazurin in oxidized form to measure cellular proliferation spectrophotometrically. The indicator resazurin reacts with multiple enzymes in cytoplasm and mitochondria such as flavin reductase, diaphorases and quinoneoxidoreductase and then reduce to highly fluorescent resorufin [97+]. The growth and innate metabolic activities of cells under the oxidation-reduction indicator were fluorometric and colorimetric in AlamarBlue^{TM} assay. The excitation wavelength is 540nm and the emission wavelength is 595nm of the fluorescent assay. The measure of the chemical reduction response for the growth medium can indicate cell growth or cell metabolism [98].

2.2.1.2.2. Cell distribution uniformity

In the real situation, the cancer mass is not uniform due to the necrotic core and active surrounding tissues [98]. After a collagen mixture has been made, if there is no compression, the cancer cells are evenly distributed in the 3D collagen environment. However, if any extra load is applied to compress the collagen, the cell distribution in the peripheral area would be denser than that in the core of

collagen mass. The phenomenon is obvious in a high-collagen-density model, but not in a high-cell-seeding-density model. The detailed relationship between the compression level and collagen uniformity is difficult to measure because of the irregularity of samples.

2.2.1.2.3. Collagen uniformity and distribution

The collagen uniformity is depending on the compression. Without any compression, the collagen distribution is uniform. With extra compression to minimize the size and increase the collagen density, the collagen distribution in the peripheral area would be denser than that in the core of collagen mass. This phenomenon was the same as the cell distribution uniformity. The design criteria are to design a uniform 3D collagen model for both cell and collagen distribution because relevant experiments can be standardized. The metal plunger compression introduces heterogeneous uniformity to the collagen model design. However, the RAFT^{TM} 3D collagen model perform has a much better performance when facing this problem and have a higher sample uniformity. The morphologies of the collagen matrix are shown in Chapter 3. In a proton irradiation experiment, the collagen matrix is uncompressed. In a photon irradiation experiment, the collagen matrix is normally compressed with the aid of the metal stopper, so the sample uniformity is controlled within a tolerate degree. The extra high collagen density models are only used in MRI experiments. The collagen boundaries shown with imaging contrast and a detailed discussion will be described in Chapter 3.

2.2.1.2.4. Collagen model size control

The 3D collagen model is flexible, and the collagen mass can be tailored to fit different applications. We have well-established RAFT^{TM} 3D culture systems which use a standardized 96-well plate and 48-well plate solution (TAP Biosystems, Royston, UK). The 96-well plate has a 6.4mm bottom diameter and approximately 0.32cm^2 cell growth area. The 48-well plate has an 11mm bottom

diameter and approximately 0.95cm^2 cell growth area [99]. Our research team has also developed a technique to compress the collagen mixture in a metal mould by a metal plunger with a weight of 177g. Followed by the manufacturer's instructions for the RAFT^{TM} system, the size of collagen is like a thin lamella, whose diameter is the same as that in the multi-well plate and whose height ranges between 0.2cm and 0.4cm. The mould/plunger technique enables researchers to control the collagen size. The standard size could be around 0.5-1.5 cm^3.

2.2.1.2.5. Imageability for various applications

The 3D Collagen model can be imageable by various imaging systems from the basic light microscope to the confocal microscope. As the collagen density and size can be controlled, the 3D model can be made to fit different penetration depths of microscopes. The thickness of a collagen sample required for a precise and detailed confocal microscope is 100-400 µm. A standard fluorescent microscope can image the 3D model with higher tolerance range in millimeters.

2.2.1.2.6. Degradation of extracellular matrix (ECM)

The stromal component of the 3D collagen model plays a similar role in the extracellular matrix. The ECM is defined as a collection of extracellular molecules secreted by cells in the collagen matrix that provides structural and biochemical support for surrounding cells [100, 101]. The difference is that the stromal component mainly provides structural support. Even though the stromal cells can secrete molecules to provide biochemical microenvironment, the biochemical microenvironment is mainly determined by an external supplement of protein and nutrition. As a design criterion, the degradation of the extracellular matrix shows the average duration for cells to be cultured in a stable and healthy 3D collagen microenvironment. In the 3D collagen model, the acellular collagen can also be used to surround the artificial cancer mass. The degradation of the extracellular matrix is determined by the cell seeding number. For spheroid cell

culture with a low seeding number in 3D, the extracellular matrix can maintain cell behavior longer than 3 weeks after an experiment. For tumouroid cell culture with a high seeding number in 3D, the extracellular matrix can also maintain cell behavior in 5 days if the seeding number is 40 million. Metabolism and cell growth images can show cell behavior over time.

2.2.1.2.7. Penetration and response of antibodies and chemicals

Normal fluorescent markers are applicable to the tumouroid 3D collagen cancer model for staining to obtain fluorescent images. However, there was a dim background fluorescence in the collagen area. The fluorescence highlight of stained objects has sufficient contrast to distinguish the background fluorescence of collagen from antibody-marked proteins. For example, in the fluorescence microscopy, the imaging contrast is determined by the number of photons collected from the specimen, the dynamic range of the signal, optical aberrations of the imaging instrument, and the number of pixels per unit area in the final image [102]. The type of imaging instrument determines the limit of spatial resolution and image quality. The specimen themselves need to meet the sample thickness requirements and try to avoid extremely faint or bright display, and nonspecific autofluorescence of tumour tissues by choosing suitable fluorophores [103].

2.2.1.3. 3D collagen model for irradiation studies

2.2.1.3.1. 3D model configuration for irradiation experiment/geometry

I used the 96-well plate to culture 3D spheroid and used the fluoro dish or 48-well plate to culture 3D tumouroid from Corning®. Spheroids are less than 1000 μm, so the 96-well plate is the most suitable culture plate. On the contrary, tumouroids require a larger space, so the 48-well plate was the best choice. The design criteria of 3D collagen model for irradiation studies are defined by the following parameters. These parameters measure the practical value as a multifunction platform.

2.2.1.3.2. Spheroid/tumouroid volume and shape

The volume of tumouroids is important to the sample thickness control of microscopy. The homogenous spherical shape of spheroids means the preferred regular nutrition distribution and biochemical gradient. The volume of tumouroids was controlled to 0.5-1.5 cm^3 after physical compression. The shape of tumouroids was cuboid. The perfect shape of spheroids should be spherical because of the homogeneous dividing and growing of a single tumour cell. This is valid when the seeding number is appropriately low. When the seeding number is too high, the shape of spheroid will be elongated cuboid. The detailed volume of spheroids will show in this chapter later.

2.2.1.3.3. Irradiation resistance

The 3D cancer model can be adapted to ionizing radiation studies. Intercellular contact, intercellular communication, oxygen, damage repair and apoptosis induction of tumour could control ionizing radiation sensitivity [104]. The irradiation resistance studies started from the early seventies and the main object is on multicellular tumour spheroids (MCTS) [105]. The irradiation resistance of MCTS was explained by hypoxia [106] and cell-cell contacts [105]. Especially for the HT29 colorectal cancer cell line, one research found that enhanced compaction level can lead to a higher irradiation resistance [106]. The well-compacted late-stage spheroids appear to be more resistant than loose early-stage spheroids, in either morphology change or cell cycle delay/arrest. The loose spheroids are prior to plasma membrane blebbing compared with well-compacted spheroids after irradiation. The absence of cell cycle delay and the onset of necrosis were observed in loose spheroids, while an evident G2/M cell cycle arrest and the onset of apoptosis were present in well-compacted spheroids after irradiation [106]. Early-stage spheroids will growth to late-stage well-compact spheroids after cell culture. The mechanism is proposed to be the DNA

repair-related alterations such as cell shape–mediated gene expression, and chromatin packaging [107]. I used both the standard 3D collagen model protocol and high collagen and cell seeding density procedure. The compaction level is not always uniform due to the morphology and cell number irregularity of initial spheroids. The track of individual spheroids in later experiments preferred late-stage high-compact level spheroids.

2.2.1.3.4. Hypoxia

Molecular oxygen is an electron-affinitive molecule that can absorb energy from irradiation, and then causes DNA damage [108]. An ultra-low level of molecular oxygen is required for radiosensitization within cells and working as a potent chemical radiosensitizer. Anoxic cells are about three times more resistant to irradiation than normoxic cells [109]. In the last century, the hypoxia effect is measured indirectly as "radiobiological hypoxia fraction" due to the limitation of experimental methods. Later, oxygen probes and fluorescent markers were used to measure hypoxia in cancer cells. Studies from a solid tumour found that around 10-20% of the viable tumour cells were radio-resistant due to hypoxia. Furthermore, hypoxia hugely influences the response of tumours to high doses. Hypoxic cells or tumours have a higher surviving fraction, as shown in Figure 8. The slope of normally-aerated tumour changes due to the kill of aerobic cells and remaining of radio-resistant hypoxic cells [110]. In 3D collagen culture, tumouroids with a thickness of more than 200µm will show hypoxia, and the relevant results are demonstrated in the last chapter.
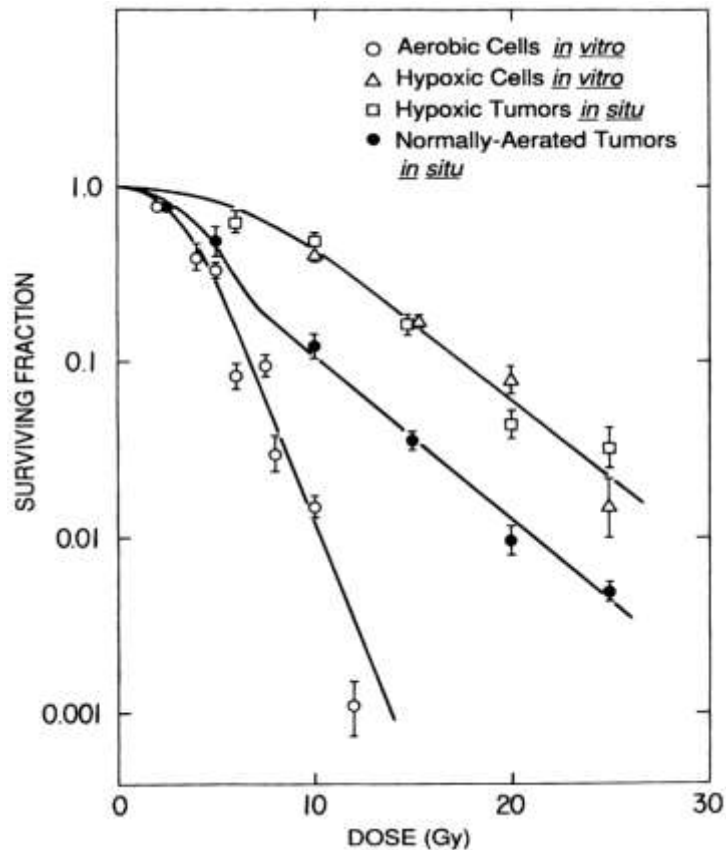
Figure 8: Radiobiological Hypoxic Fraction curve of EMT6 mouse mammary tumour in the experiment. The hypoxic tumour in situ was made fully anoxic and normally the aerated tumour in situ was irradiated in air-breathing mice. The figure shows not only the higher surviving fraction of hypoxic cells or tumour but also the importance of hypoxic cells in normally-aerated tumours. In low doses, the normally-aerated tumour has a similar surviving fraction with aerobic cells. However, high irradiation doses kill aerobic cells, and then the surviving fraction of normally aerated tumour changes to go parallel with hypoxic cells. [110]

2.3. Experiment Method

2.3.1. Cell types and relevant experiment

Human dermal fibroblast is responsible to generate connective tissues on the human dermis layer. Human dermal fibroblast also secretes important protein molecules including laminin and fibronectin, which comprise the extracellular matrix. This cell type is ideal for 3D collagen model stromal construction [111]. The molecular

phenotypes, microsatellite instability (MSI), CpG island methylator phenotype (CIMP), and gene mutation vary depending on the type of cancer cell lines. The HT29 human colorectal adenocarcinoma cell line is a widespread type, while the HCT116 human colorectal carcinoma cell line is a fast-growing metastasis type. Both HT29 (Sigma-Aldrich, 85061109) and HCT116 (Sigma-Aldrich, 91091005) are originated from human primary tumours. The SW620 (Sigma-Aldrich, 87051203) human colorectal adenocarcinoma cell line is originated from human colon lymph nodes [112]. The HT29 human colorectal adenocarcinoma cell line is the main cell line used in most of my experiment because of its availability.

Cell type	Experiment	Aim
HT29 (Human colorectal adenocarcinoma cell line)	1. 2D and 3D cell morphology 2. 3D metabolism (AlamarBlue^{TM} assay and use collagenase to dissolve the matrix) 3. Cell invasion in the 3D collagen model 4. Spheroid culture in the 3D collagen model	1. Show sample uniformity. Compare 3D morphology with *in vivo* condition. 2. Determine viable lifetime of cells in a 3D condition and find the optimal seeding density in 3D condition. 3. Show mean invading distance and develop a 3D invasion assay in response to an irradiation dose. 4. Find the best seeding number for spheroid culture and culture

		spheroid to find out the cell growth and invasion in a 3D collagen condition.
HCT116 (Human colorectal carcinoma cell line)	1. 2D and 3D cell morphology 2. 2D metabolism (AlamarBlue™ assay) 3. 3D metabolism (AlamarBlue™ assay and use collagenase to dissolve the matrix)	1. Show sample uniformity. Compare 3D morphology with *in vivo* condition and with 2D cells. 2. Determine viable lifetime of cells in 2D condition and use for reference of 3D seeding. 3. Determine viable lifetime of cells in 3D condition and find the optimal seeding density.
SW620 (Human colorectal adenocarcinoma cell line)	1. 2D and 3D cell morphology 2. 2D metabolism (AlamarBlue™ assay) 3. Cell invasion in the 3D collagen model	1. Show sample uniformity. Compare 3D morphology with *in vivo* condition. 2. Determine viable lifetime of cells in 2D condition and use it as reference for 3D seeding.

		3. Find out the mean invading distance and develop a 3D invasion assay in response to an irradiation dose.
HDF (Human dermal fibroblast)	1. 2D and 3D cell morphology 2. 3D cell invasion (HT29 to HDF) for the spheroid model	1. Show cell invasion of the 3D model and HDF in 3D collagen is used as the stroma. The result will be the guideline for irradiation experiments.

2.3.2. Cell maintenance

The HT29 and SW620 human colorectal adenocarcinoma cell line and HCT116 human colorectal carcinoma cell lines were used. My main work focused on the HT29 cell line, and also used human dermal fibroblast as stromal cells in the collagen model. Those cells were the stocks at the department of Surgery and Interventional Science of UCL and originated from Sigma Aldrich. The cell lines were routinely cultured in 2D monolayer in Dulbecco's modified Eagle's medium (DMEM, Sigma-Aldrich, UK) supplemented with 1g/L glucose, 10% v/v fetal bovine serum (FBS, Sigma-Aldrich, UK), 100 units/mL penicillin and 100 μg/mL streptomycin at 37°C cell culture incubator (5% CO_2/air and 95% humidity). The cells were passaged when the flask was confluent, and the medium was replenished every 3 days.

2.3.3. Making 3D collagen tumouroid model

(1) The metal mould, metal plunger, nylon mesh, metal mesh, forceps, round paper and glass slide were autoclaved before experiments for sterilization.

(2) The buffer containing 250µl of HEPES (Sigma-Aldrich, UK) was added to the 10ml of DMEM medium in 25ml universal tube via pipettes.

(3) The cancer cells on each confluent tissue culture flask were detached by adding 3ml of 1x trypsin and were cultured in the incubator for about 2min. The flasks were shaken, and the cells were detached from the tissue culture plastic surface. Then, 7ml of DMEM medium was added to the flasks to get the cell suspension. All the cell suspension was transferred to a 25ml universal tube via pipettes. The 3D collagen experiments needed a sufficient number of cells, so the concentration of cell suspension varied. The cell suspension was centrifuged for 5min and 1200 rpm to get the cell pellet. The 2ml of HEPES buffed with DMEM medium was added to the cell pellet and the solution was mixed through pipettes to get the dense cell suspension.

(4) 10µl of dense cell suspension was added to a 1ml vial. Another 10µl of trypan blue was added to the vial as well. After 3min, the dyed cell suspension in the bijou vial was transferred to a cytometer via pipettes to count the cell density.

(5) 0.4ml of 10x MEM medium (Sigma-Aldrich, UK) and 3.2ml of rat tail collagen type I (First Link, UK) was added to a 25ml universal tube. The color of the solution was light yellow. A small volume of 5M NaOH was aspirated by syringe and about 6 drops of 5M NaOH was added to the collagen solution. The universal tube was shaken for a full mixture when each drop of 5M NaOH was added. The solution was in light yellow or dark yellow.

(6) A small volume of 1M NaOH was aspirated by syringe and several drops of 1M NaOH were added to the collagen solution carefully to change the color from dark yellow to light pink. The universal tube was shaken for a full mixture when each drop of 1M NaOH was added. The neutralization process was very sensitive, so the accuracy may change to half drop. If the color of the solution was changed to deep pink, the collagen is not set up and the experiments would fail.

(7) When the collagen solution was neutralized, 0.4ml of dense cell suspension was added to the collagen solution (the total volume was about 4ml).

(8) A piece of round paper was placed underneath. A glass slide was placed in the middle and the metal mould was placed on the top.   All the cell-collagen solution (step 7) was transferred to the hole of the mould carefully to avoid air bubbles.

(9) After 45min for collagen to set up, the nylon mesh was placed on the top of the mould. The metal mesh was placed above the nylon mesh, and the glass slide was placed above the metal mesh. The top of the glass slide was covered with a round piece of paper and then the whole unit was reversed upside down.

(10) The glass slide and paper placed under the mould in step 8 was removed and the metal plunger was inserted to the hole of the mould. The plunger was pushed down naturally for 10 seconds for collagen compression.

(11) If the collagen has been set up, there would be a stripe of white solid gel. The gel was transferred to a petri dish and the gel was cut into 4 even pieces (by eye) by a surgery knife. The small pieces of gel were covered by HEPES medium in a petri dish and then the petri dish was put into the incubator.

(12) 0.4ml of HEPES buffed DMEM medium, 0.4ml of 10x MEM medium and 3.2ml of rat tail collagen type I were added to a 25ml universal tube. The neutralization process in step 5 and step 6 were repeated to get the neutralized collagen solution (the total volume was about 4ml).

(13) The petri dish was taken out from the incubator and each of the small collagen pieces was transferred to the center of each well in a 12-well tissue culture plastic. 1ml of the collagen solution in step 12 was aspirated to each well of the 12-well plate with collagen pieces inside.

(14) The 12-well plate was incubated for a while and then each well with collagen gel was covered by 500µl of HEPES buffed DMEM medium on the top.

(15) The 3D collagen model was stored in the incubator and the medium was replenished every two days.
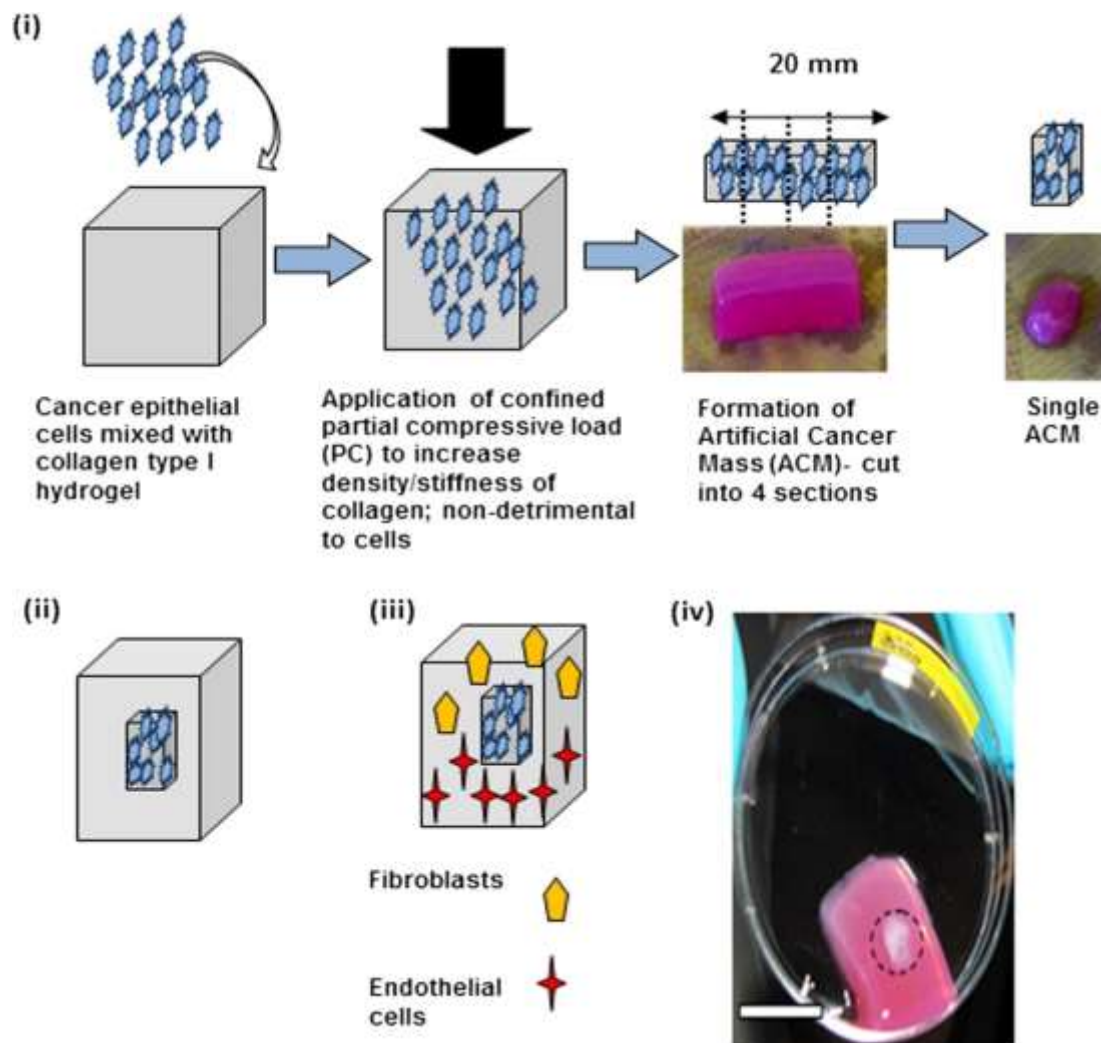
Figure 9: Schematic demonstrating the construction of the 3D *in vitro* cancer model. (i) Method to produce an ACM. (ii) Insertion of the ACM into the acellular collagen gel. (iii) The ACM in acellular collagen gel is populated with fibroblasts and/or endothelial cells to form stroma. (iv) The real image of ACM [113].

2.3.4. Making the 3D collagen spheroid model

(1) Ultra-Low attachment 96-well tissue culture plates (Corning® Costar®, Sigma-Aldrich, UK) were used to culture a 3D collagen tumour spheroid. Cancer cells cultured in this kind of plate would not attach to the bottom surface due to its surface tension coating. Therefore, a single cell could be divided to form a spheroid. Adjacent cells would bind together to form a spheroid as well.

(2) Cancer cells were harvested from confluent tissue culture flasks. After cell counting, 1,000 cancer cells were aspirated to each well of the ultra-low attachment 96-well plate. Then, 200µl of DMEM was added to each well.

(3) The DMEM was to be refreshed every three days. After nine days, there were tumour spheroids on each ultra-low attachment plate, ready for further use.

(4) The 3D spheroid model would build on a normal 96-well plate. Firstly, 0.4ml of 10x MEM medium, 0.4ml of HEPES buffered DMEM and 3.2ml of rat tail collagen type I were added to a 25ml universal tube. The color of the solution was light yellow. A small volume of 5M NaOH was aspirated by syringe and about 6 drops of 5M NaOH was added to the collagen solution. The universal tube was shaken for a full mixture when each drop of 5M NaOH was added. The solution was in light yellow or dark yellow. A small volume of 1M NaOH was aspirated by syringe and several drops of 1M NaOH were added to the collagen solution carefully to change the color from dark yellow to light pink. The universal tube was shaken for a full mixture when each drop of 1M NaOH was added. The neutralization process was very sensitive, so the accuracy may change to half drop. If the color of the solution changed to deep pink, the collagen would not be set up and the experiment would fail. When the collagen solution was neutralized, 30µl of collagen mixture was added to each well of 96-well plate as the base. The collagen mixture needed to be placed in an icy box to avoid aggregate.

(5) The 10µl pipette tips with pipette gun could be used to pick up spheroids from wells of the ultra-low attachment plate. Ideally, one perfect spheroid from each well of the ultra-low attachment plate could be transferred to the collagen base of the normal 96-well plate. The residual medium needed to be removed and only spheroids were transferred to the center of the collagen base.

(6) Step (4) was repeated to create another collagen mixture of a different portion. 30µl of collagen mixture was added to each well of the 96-well plate above the previous 30µl collagen base and spheroids were used as covers to ensure that the depth of spheroids was reproducible to assist imaging. The final 3D geometry was

displayed in a "sandwich" shape.

(7) The 3D spheroid model was toppled with 140μl of DMEM and the medium was replenished every three days.

2.3.5. Dissolved collagen matrix by collagenase

In the original plan, I analyzed 10 stacks of collagen sections from 3D to 2D using collagenase type I (Life Technology, 17018-029). Hence, I developed an AlamarBlue[TM] assay to analyze the impact of collagenase on cell viability. 25,000 HT29 cells were seeded on the 48-well plate and 25,000 HT29 cells per cm^2 per ml were dissolved and harvested from 3D tumouroid to seed on the 48-well plate as well. On day two, I measured the fluorescent reduction of AlamarBlue[TM] in 2D culture and 3D-to-2D culture. The absorbance of AlamarBlue[TM] was measured and the percentage difference was calculated.
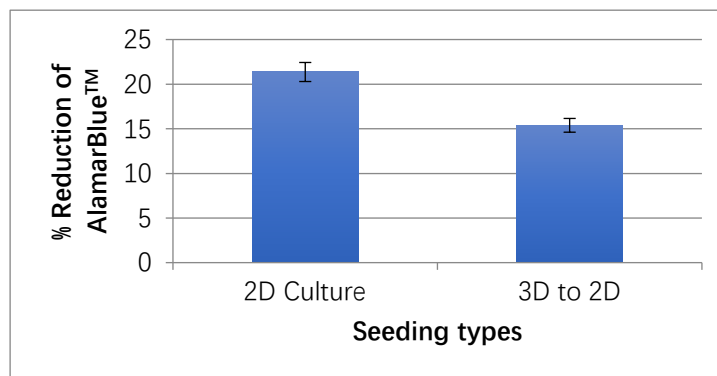
Figure 10: The AlamarBlue[TM] reduction percentage difference of 2D culture HT29 and collagenase dissolved 3D culture HT29 (3 repeats, n=3 per dish)

The calculated percentage difference between 2D culture and 3D to 2D culture was 28%. The difference in the percentage of AlamarBlue[TM] reduction is 6%. This means the application of collagenase to dissolve collagen from 3D to 2D culture condition has a measurable impact on cell viability, then this type of comparison is not valid. The comparison between 3D and 3D/2D and 2D is suggested.

2.3.6. AlamarBlue™ assay for cell metabolism

(1) The cells were harvested from tissue culture flasks by using trypsin to detach cells from the surface. The cell suspension was centrifuged at 1200 rpm for 5min.

(2) The AlamarBlue™ agent was dissolved in PBS buffer in 1: 10 ratio. The cell pellet from step 1 was dissolved by adding 5ml AlamarBlue™ solution. After the solution was completed, the cell suspension was mixed gently.

(3) 500µl of cell suspension was transferred to each well of the 96-well black tissue culture plate. The position of cell suspension was labeled.

(4) 500µl of DMEM medium was added to a well of the 96-well black tissue culture plate for reference. If the DMEM medium did not display phenol red, this step is not necessary.

(5) The 96-well black tissue culture plate was incubated at 37°C for 5 h.

(6) After incubation, the 96-well black tissue culture plate was read under fluorescent ranging from 560nm to 600nm. The data was recorded, and the cell proliferation curve could be plotted.

2.3.7. Freeze-drying to measure collagen density

A freeze-drying machine utilizes air pressure and wind flow to dry out ice and water content in biological samples. The compressed acellular collagen mass was transferred to an empty 25ml universal tube. The residual water should be removed to increase the accuracy of the calculation. The wet weight of the compressed acellular collagen mass in an empty universal tube and the net weight of the empty universal tube were measured by balance. The ice dryer was used to dry the compressed acellular collagen mass for around 12h. In the next day, the weight of the solid collagen dry pellet in the universal tube was measured by balance. The collagen density of the acellular collagen mass could be calculated by the following formula: %Collagen density = (Dry weight of collagen in universal – Weight of empty universal) / (Wet weight of collagen in universal – Weight of empty universal). This method can be used to measure the collagen density of the uncompressed collagen

as well.

2.3.8. Sample preparation for the confocal and light microscopy

2.3.8.1. Standard sample preparation

For imaging application, the light microscope and fluorescent microscope can image thin layers of the specimen. 3D tumour spheroid models using 96-well plates were easily imaged and can get superior results. Fully compressed tumouroids could also get reasonable results on a standard tissue culture plate.

2.3.8.2. Sample design for confocal imaging – fluoro dish

A fluoro dish (World Precision Instruments, US) was used to get better image quality for the invented confocal fluorescent microscope because the glass bottom could minimize backscattering and increase the image resolution. The bottom glass diameter was 23.5mm, internal diameter 33mm, and height 7.8mm. The collagen mixture could flatten the fluoro dish to create a thin uncompressed collagen model for DNA double-strand breaking irradiation study because imaging nuclei foci requires high magnification power, and the image depth was very narrow.

2.3.8.3. Vibratome sample processing

I developed this technique to get longitudinal information about the bulk tumouroid. This means a bulk tumouroid was sliced to continuous get several thin specimens. By imaging those specimens and combining the information, I could plot the change in the bulk tumouroid with length. This was useful for the proton irradiation experiment because the dose slope was very sharp at same areas of the bulk 3D collagen cancer model. Then, I can measure the response on such a sharp slope.

(1) This method was optimized for a slideflask (Lunc^{TM} Lab-Tek^{TM}, Thermo Fisher). The cancer cells in uncompressed collagen were filled into slide flasks to fit proton irradiation resources.

(2) The back of slide flasks could be peeled off and the uncompressed collagen was

transferred to a square-shaped tissue culture plate. The collagen model was fixed at first.

(3) I used the agarose gel to surround the soft uncompressed collagen to increase the physical rigidness before vibratome sample slicing. After several experiments, the optimal agarose solution concentration was confirmed to be 2.5% w/v. When the concentration of agarose was as low as 0.5% w/v, the agarose was soft. However, when the concentration was as high as 5% w/v, the agarose was too solid to cut. The agarose with a concentration as warm as 2.5% w/v was filled in the square-shaped tissue culture plate and enclose the uncompressed collagen cancer model. When the agarose gel cools down, the structure will be a solid cube.

(4) Superglue was used to stick the solid cubic agarose gel on the stand of vibratome. Notes the direction to glue was important for getting longitudinal information. PBS was added to fill in the sink of vibratome and razor blade was attached on the vibratome. The amplitude was set to maximal and the speed was set to medium.

(5) The razor blade cut the solid agarose gel and the 3D collagen model enclosed was processed simultaneously. The thin slice floating on the PBS was transferred to a tissue culture plate and topped with fresh PBS.

(6) The height of the vibratome was adjusted to control the thickness of the sample. Depending on the sample condition, the thickness could range from 100µm to 400µm. It was easier to cut thick samples than thin samples. Step (5) was repeated, and the vibratome processed the rest of the agarose gel until there was no collagen model enclosed in the agarose structure. The slices were labeled in order.

2.3.9. Spheroid transfer

In my experiment, spheroids were transferred to a 3D collagen base by aspirating spheroids from the 2D ultra-low attachment plate via the pipette gun and tips. Without total aseptic condition in the lab, the working process was in a biological safety cabinet. Otherwise, with the help of a microscope, one could precisely transfer each spheroid at a specific position from the cell culture plate. The spheroid transfer

process by the pipette gun and tips was time-consuming. Therefore, I usually confirmed the position of each spheroid using a light microscope at first. On an ultra-low attachment plate, if the plate was leaned at a 45º angle, spheroids would move to the lower bottom of each well. This facilitated the pick-up process of spheroids.

2.4. Experimental Results

2.4.1. Cell morphology - 2D vs 3D culture cell morphology HDF / HT29 / HCT116 / SW620.

In order to establish any differences in cell morphology in the 2D and 3D setting, a number of light microscope images were taken in both settings, and relevant qualitative comparison was made. There were some marked differences in cell size and shape between the two settings, as shown in Figure 11 and 20. For example, HT29 in the 2D and 3D culture environment, the diameter of a single cell was around 45µm in 2D culture (20 cells average) and that of a single cell was around 7µm in the 3D culture (20 cells average).
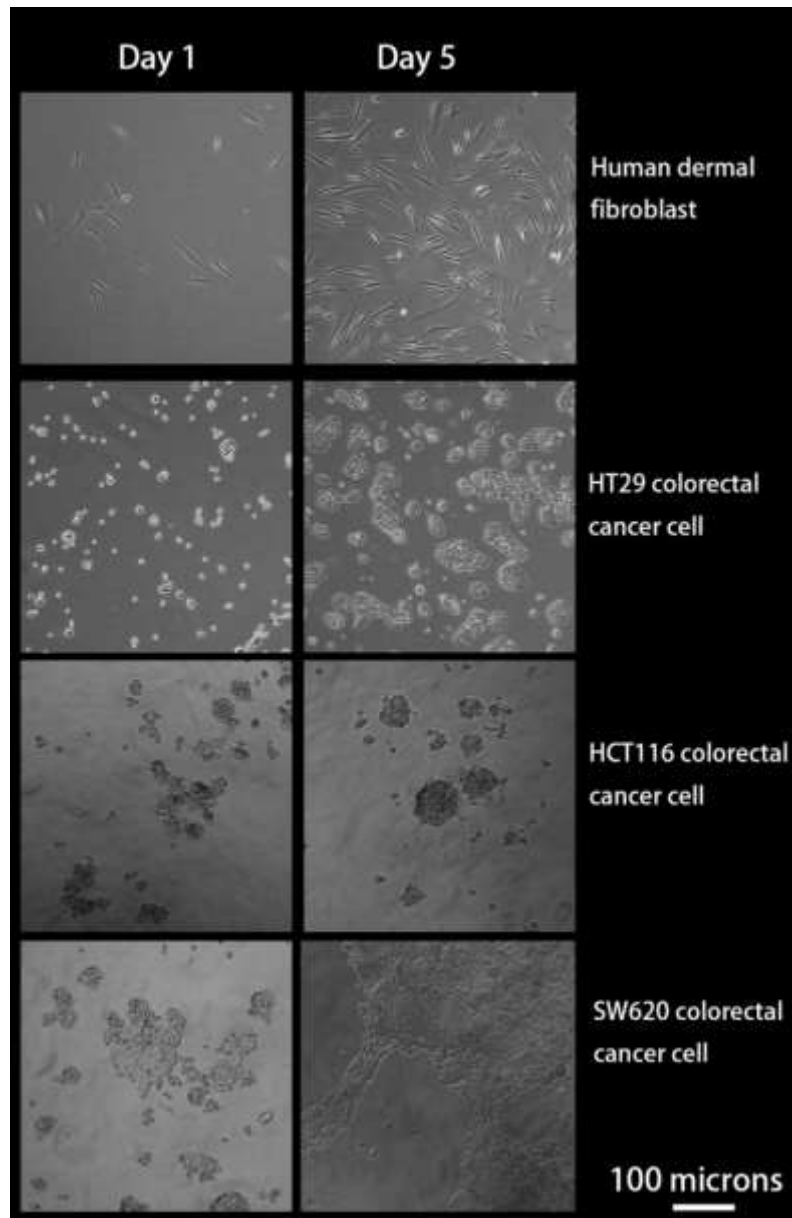
Figure 11: 2D cell morphology of HDF, HT29, HCT116 and SW620 cell lines on day 1 and day 5 cultured in low glucose DMEM

In 2D culture condition, the morphology of fibroblast was in fusiform per single cell, HT29 colorectal cancer cell was in round single cells and HCT116 and SW620 colorectal cancer cell lines were in small colonies. In the first row of Figure 11, on day 5, elongated fusiform fibroblasts formed a cell network and the flask became confluent. In the second and third rows of Figure 11, on day 5, single or small groups of HT29 and HCT116 colorectal cancer cells divided into colonies, and large colonies bound

together to further increase the scale. In the fourth row of Figure 11, SW620 the colorectal cancer cell line was divided, and colonies were connected to form a cancer cell area.

Figure 17 shows the morphology of HT29 spheroid 3D culture in the collagen model in section 2.4.4.1. Comparing culture cells in 2D with that in 3D shown in Figure 11 and Figure 17, the morphology expression of cancer cells was totally different. It was not a flatbed culture, and cells were attached to the tissue culture plastic. The 3D geometry of cancer cells provided a different cell microenvironment and cell signaling [114]. I only compared the HT29 colorectal cancer cell line in 2D with that in 3D culture because this cell line was the main cell line used in my experiments.

2.4.2. Cell metabolism in the 3D collagen model

The aim of AlamarBlue^{TM} assay of 3D culture was to confirm that the cell viability of such seeding number was in an acceptable range for a short experimental period. Then people can use the viability data to guide the experiment design. For low seeding numbers, the cells in the 2D and 3D condition could increase the viability with culture time. In order to compare the cell viability difference between 2D and 3D culture settings, cell metabolism via AlamarBlue^{TM} assay was measured and quantitatively compared. Figure 12 and Figure 13 demonstrate the 2D and 3D cell metabolism results, respectively. The cell metabolism of HT29 colorectal cancer cell line in 2D and 3D were difficult to compare directly because the cell seeding number was significantly different. For example, the 2D culture had a cell seeding number of 50,000 per well while the 3D culture had a cell seeding number of 30 million. The cell growing microenvironment and nutrition supply were also different. In Figure 10, I measured the degree of how collagenase impact cell metabolism measurements of the AlamarBlue^{TM} assay.

2.4.2.1. 2D cell metabolism SW620/ HCT116/ HT29 colorectal cancer cell line
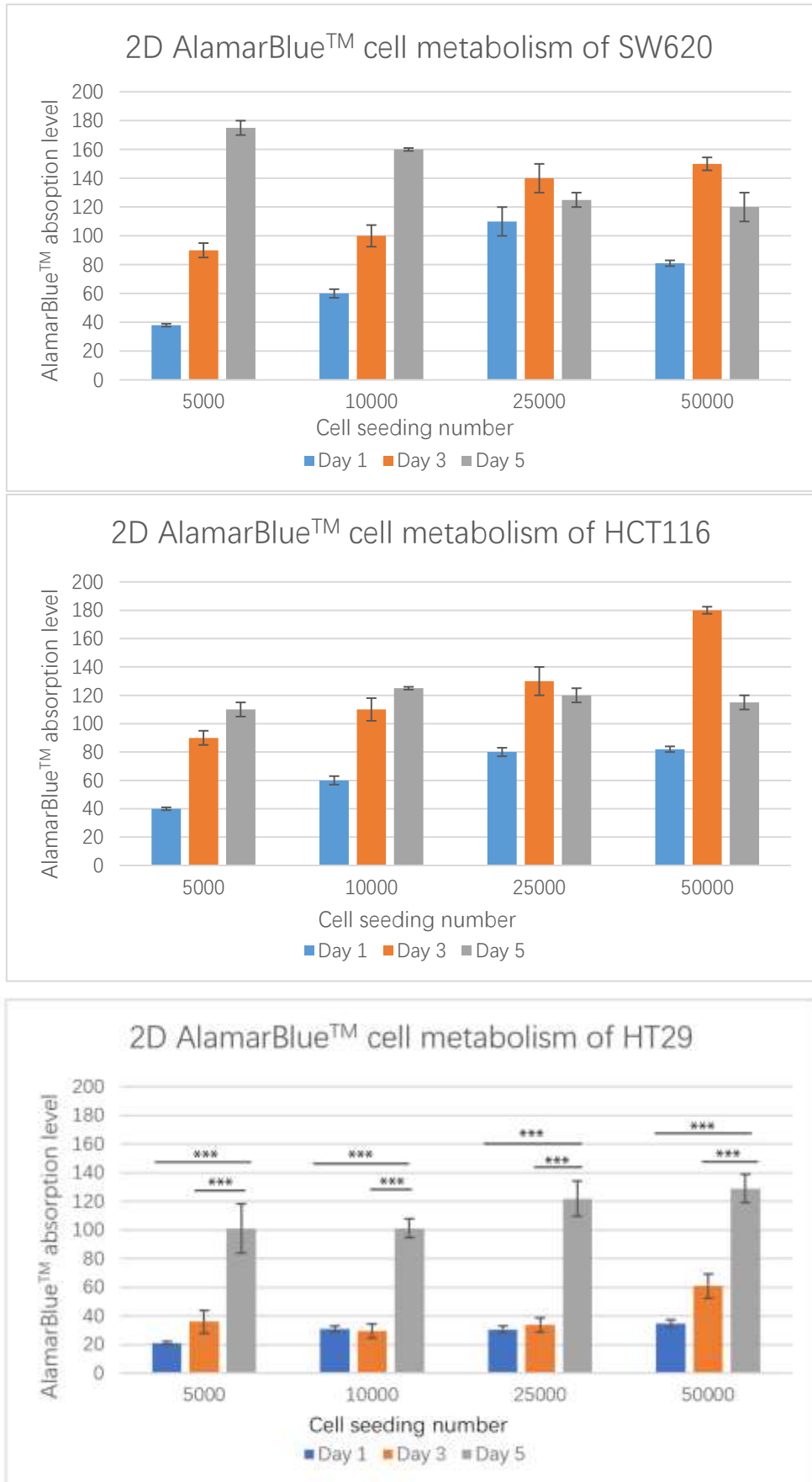
Figure 12: AlamarBlue^{TM} cell metabolism of SW620, HCT116 and HT29 in 2D culture

condition (3 repeats). The sign *** indicates P<0.001.

There are missing data for the statistical analysis of 2D Alamar blue assay because of the data storage breakdown in my second academic year. As a result, the data was managed to be collected a texted essay, but the raw data was missing. However, the comparison between 2D and 3D Alamar blue assay was indirect. The high AlamarBlue™ absorption level represented a higher cell metabolism rate. From plots of the 2D AlamarBlue™ absorption of SW620 colorectal cancer cell line shown in Figure 12, 5,000 and 10,000 lower seeding cell numbers cancer cells in a 96-well tissue culture plate showed increasing cell metabolism from day 1 to day 5. 25,000 and 50,000 higher seeding numbers cancer cells had the highest cell metabolism in day 3 before starting to decrease. The plot of 2D AlamarBlue™ absorption trend of HCT116 was similar to that of SW620. 5,000 and 10,000 lower seeding numbers showed increasing cell metabolism from day 1 to day 5, but 25,000 and 50,000 cell seeding numbers the cell metabolism start to decrease from day 3. Especially for 50,000 cell seeding numbers, the cell metabolism of day 5 was significantly lower than that on day 3. HT29 colon cancer cell line is the main cell line used in the project. Sidak's multiple comparison test of HT29 was processed based on the two-way ANOVA analysis. For all seeding numbers from 5,000 to 50,000, day 5 has significant higher cell metabolism than day 1 and day 3

According to the plots, the best seeding number of 2D AlamarBlue™ was 5,000 and 1,000 because the cells could continuously grow and showed increasing metabolism within 5 days. For short cultures, 25,000 and 50,000 seeding numbers were also usable, but the cell metabolism started to decrease from day 3. The 2D AlamarBlue™ assay was used to establish the methodology to specify the differences in the metabolism rate between 2D and 3D models. It could also be used to characterize the metabolism rate of a cancer cell line. Due to technical problems in the comparison of the metabolism rate between 2D and 3D culture models, the 2D AlamarBlue™ assay

result did not provide any help for my experiments because the cell seeding number in 3D culture is much more than that in 2D culture, and the cell culture microenvironment is different as well.

2.4.2.2. 3D cell metabolism of HCT116 and HT29 colorectal cancer cell line (use collagenase to dissolve the matrix)

HT29 was the main cell line that I used in most of my experiments. The 3D cell metabolism of HCT116 just selected two cell seeding numbers due to consumable limitation.
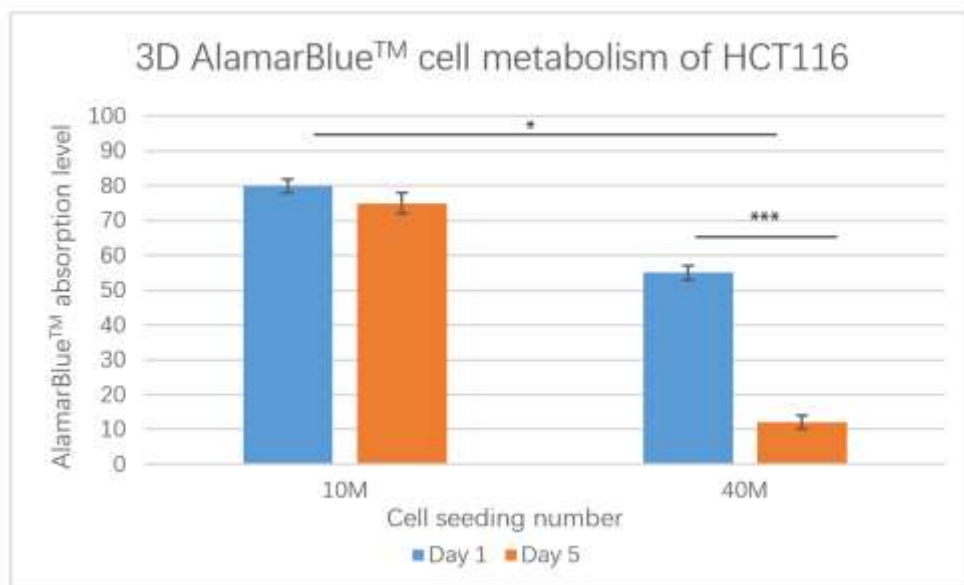
Figure 13: AlamarBlue^{TM} assay result plot of 3D tumouroid with different seeding numbers (10M and 40M, HCT116 on Day 1 and Day 5) (3 repeats). The sign * indicates P<0.05 and *** indicates P<0.001.
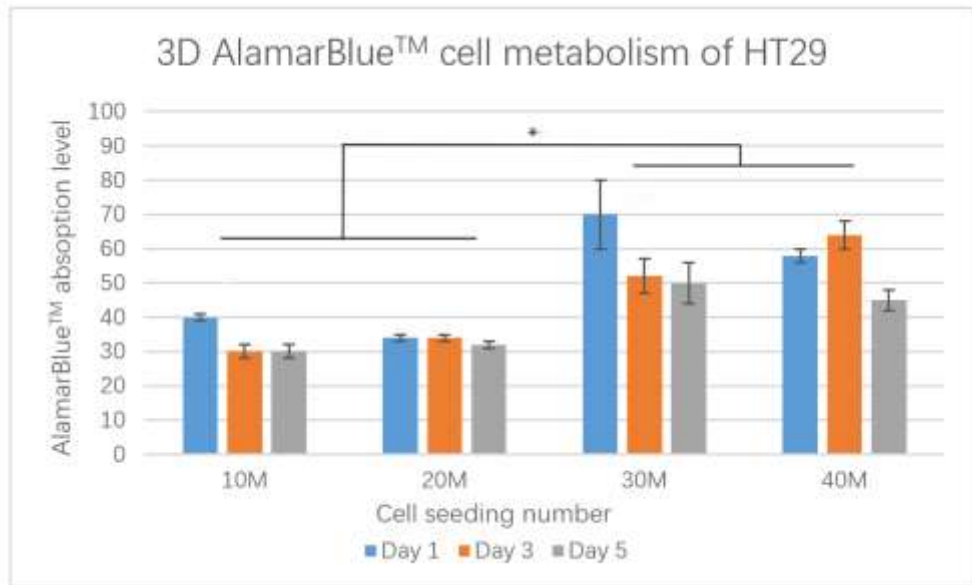
Figure 14: AlamarBlue™ assay for HT29 colon cancer cell 3D metabolism on day 1, day 3 and day 5. 10 million, 20 million, 30 million and 40 million cell seeding numbers in 4ml-collagen mixtures, respectively (3 repeats). The sign * indicates P<0.05.

The 3D tumouroid culture using AlamarBlue™ assay is compressed by metal mould and the 3D structure was dissolved to 2D by applying collagenase. The 3D geometry enabled a higher seeding capacity of up to 40 million. For the highly invasive HCT116 cancer cell line, Sidak's multiple comparison test of Figure 14 was processed based on the two-way ANOVA analysis for HT29 colon cancer cell, which is the main cell line of the project. The 3D AlamarBlue™ absorption suggested that the 10 million seeding number of tumouroids had a healthy and stable cell metabolism from day 1 to day 5. The viability just slightly decreased but not significant. For the higher seeding number of 40 million, the tumouroids even had a lower AlamarBlue™ absorption value than that of tumouroids with 10 million seeding number on day 1 but not significant. Moreover, high seeding number of HCT116 tumouroids dramatically decreased the viability from day 1 to day 5. A 40 million seeding number of HCT116 tumouroids had a very low metabolism rate on day 5, so it was not usable for experiments. The 10 million seeding number of HCT116 could ideally cover experiments within 5 days. For the less invasive HT29 cancer cell line, higher seeding number did not play a key role

in cell viability. The cell viability of HCT116 3D culture decreased as the number of culture days increased. The decrease rate graduated for all seeding numbers. Especially for the seeding number from 10 million to 30 million, the viability changed in a small degree from day 3 to day 5. The seeding number range was suitable for experiments. For 40 million seeding number, the viability difference between day 3 and day 5 was higher than that of 10 million to 30 million, but it was also usable for experiments within 5 days.

Again, the AlamarBlue[TM] absorption rate difference between 2D and 3D was difficult to be directly compared. The seeding number and cell culture microenvironment were different. The trend of high seeding number was similar, for both 2D culture and 3D culture, the viability decreases according to the number of culture days.

2.4.3. Collagen density study
2.4.3.1. Rationale to control collagen density
The aim of measuring collagen density was to control the reproducibility and uniformity of collagen. The collagen density measurements were references to other design criteria.

2.4.3.2. Measurement of low and high collagen density in the 3D model
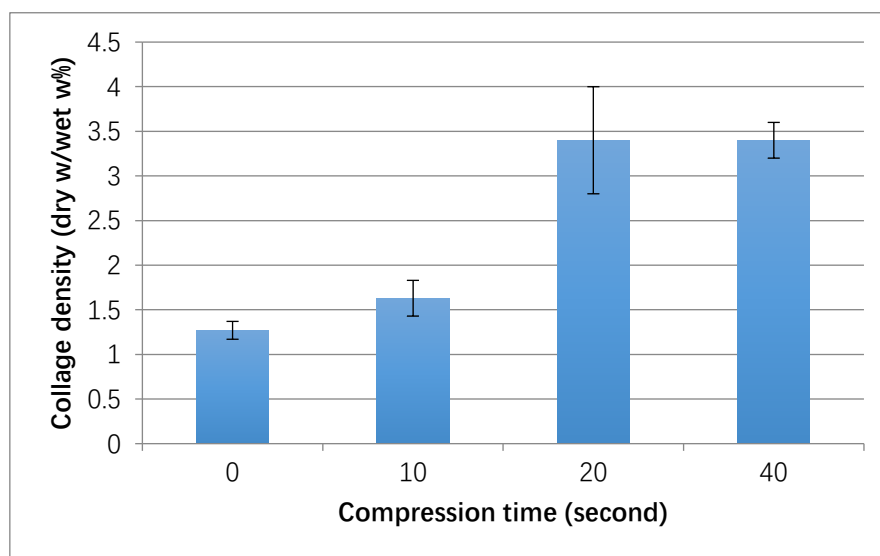
Figure 15: Compression time (Zero compression, 10s, 20s and 40s) VS collagen density (old protocol, as described in method session 3.3) (3 repeats)
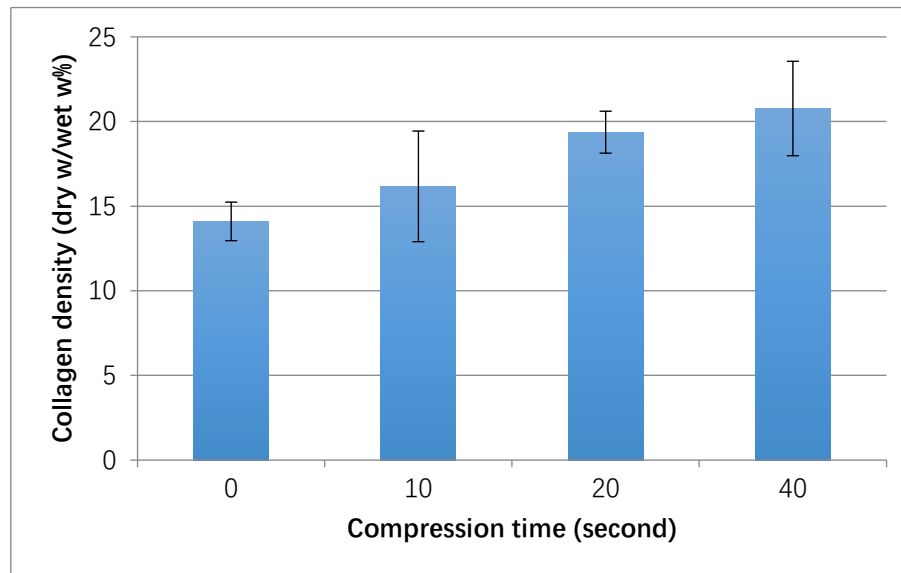
Figure 16: Compression time (After plastic block zero compression, 10s, 20s and 40s) and collagen density (new protocol, as described in method session 3.3, with a 4mm height plastic block to stop the compression) (3 repeats)

If a plastic blocker 4mm in height is applied to stop the compression and then natural compression using a metal mould is adopted, the 3D model can increase the collagen density and the value can be controlled by compression time. For natural compression using the metal mould, the uncompressed collagen gel has a dry/wet collagen density of 1.25%. The collagen density can increase to around 3.5% when compressing a longer time on both sides. The application of a plastic blocker physically limits the collagen density to a certain value. A plastic blocker 4mm in height can increase the collagen density to a very high level of around 14%, and with additional natural compression, the collagen density can increase to around 20%. For most of my experiments, I used the old protocol to make tumouroids with collagen density around 3.5% (40 seconds of compression for both sides). The collagen density can be controlled by design criteria.

2.4.4. Cell invasion in 3D collagen model

2.4.4.1. Boundary effect
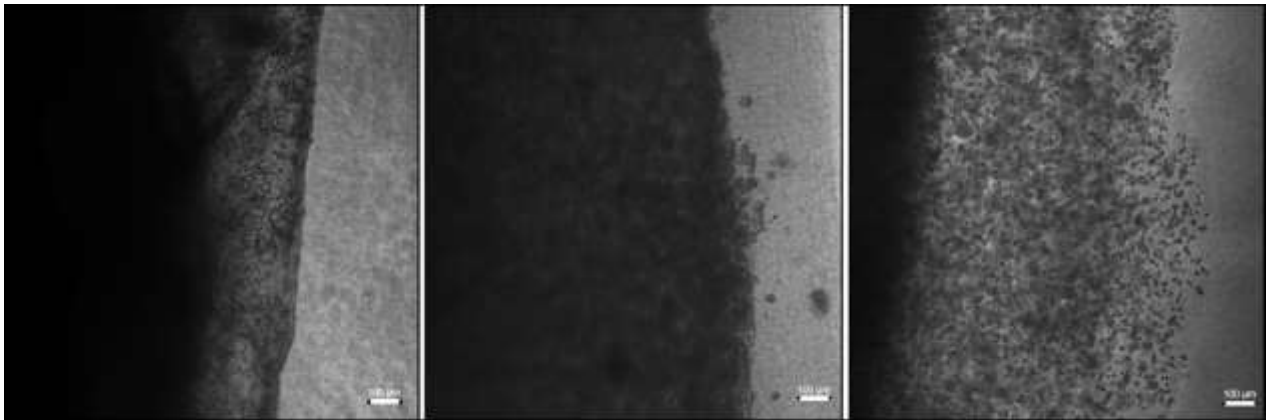
Figure 17: Boundary effect of cutting which affects cancer cell invasion in 3D collagen model. Various positions of a 20 million seeding number of SW620 tumouroids on day 6. The scale bar refers to 100µm and the magnification power is 40x

I found that the razor blade cutting boundary promoted cell invasion. The compressed 3D collagen gel had a tight and rigid boundary. Physical damages to those boundaries not only broke the structure but also carved out a way for cell invasion. There was less resistance for cancer cells to invade from cutting boundaries.

2.4.4.2. Invasion of SW620 - 40M cut to 3 ACM [about 15M cell number per ACM] - Day 1/6/12/18
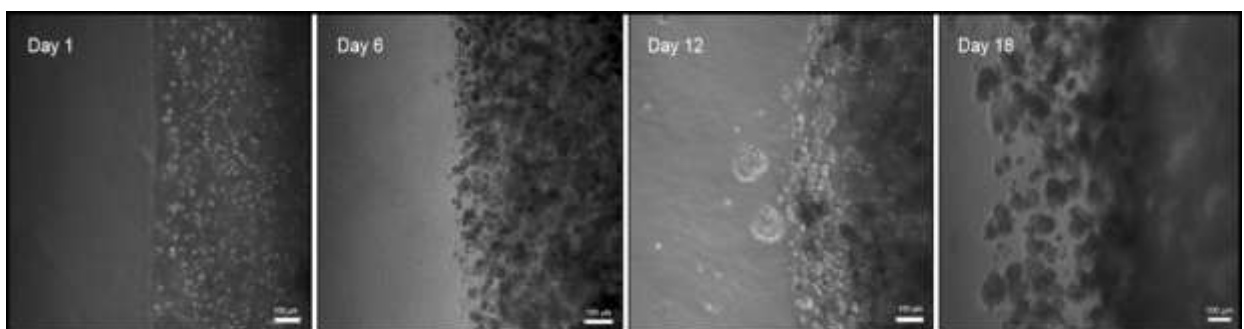
Figure 18: The invasion of 3D SW620 colorectal cancer cells in dense artificial cancer mass to acellular collagen gel on day 1, day 6, day 12 and day 18 (2 repeats) 40 Million SW620 colon cancer cell for each ACM, and each ACM was cut into 3 pieces [about 15M cell number per ACM]. The scale bar refers to 100µm and the magnification

power is 40x.

The SW620 colorectal cancer cell line started to invade from day 6 to day 12, during which there were spheroid colony formation and invasion to uncompressed collagen area. There were morphological changes at the boundaries of collagen cancer mass. On day 18, the spheroid colony grew further and the distance between colonies also increase. On day 1, the average size of a single SW620 cancer cell in the 3D collagen model is around 10μm (measured 20 cells to get the average). I measured 10 farthest invading bodies from the collagen boundary and measured the average invasion distance, as shown in Figure 19 below. The actual invasion distance of each cancer cell is less than the farthest invasion distance. On day 6, SW620 cancer cells invaded from ACM to acellular collagen and had an invasion distance around 100μm. On day 12, the invasion distance dramatically increased to around 395μm, but on day 18, the invasion distance did not change too much to 416μm. Instead of cell invasion, the invading body changed the morphology from single cells to a cluster of cells, and finally, there was the formation of spheroids. This phenomenon was obvious on day 18.
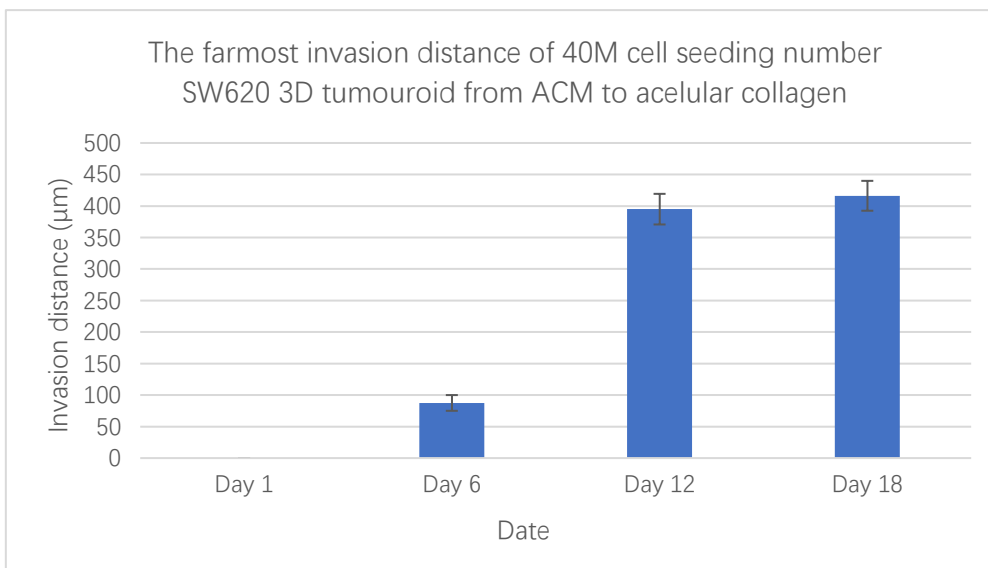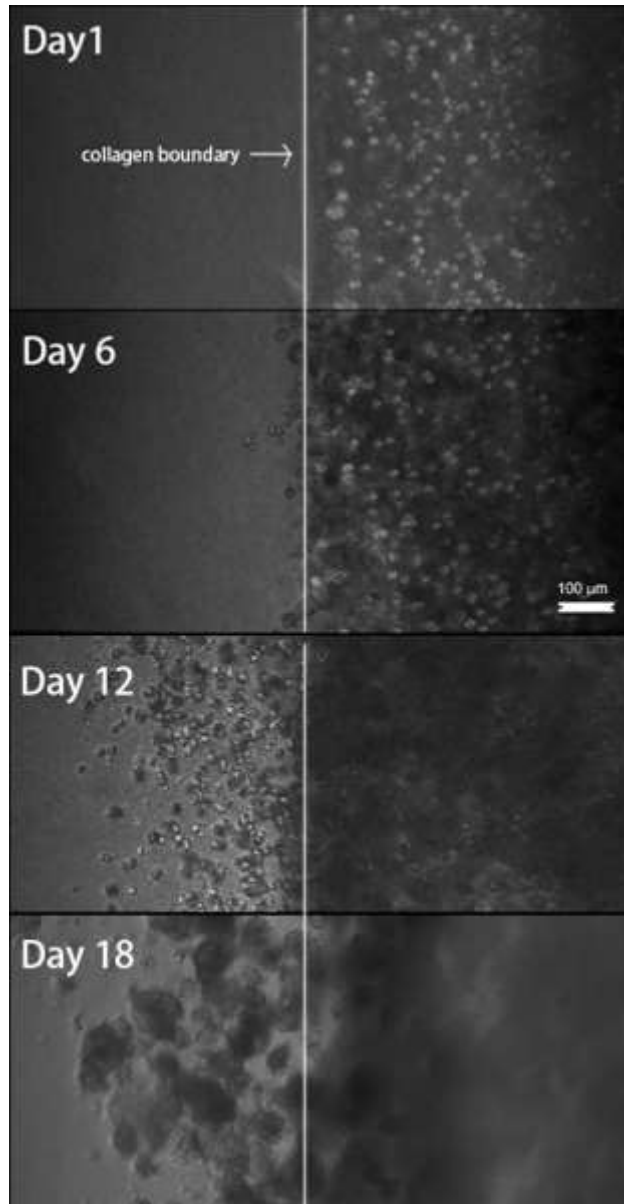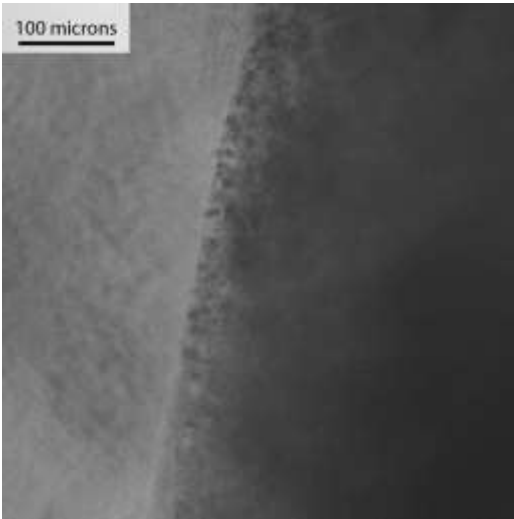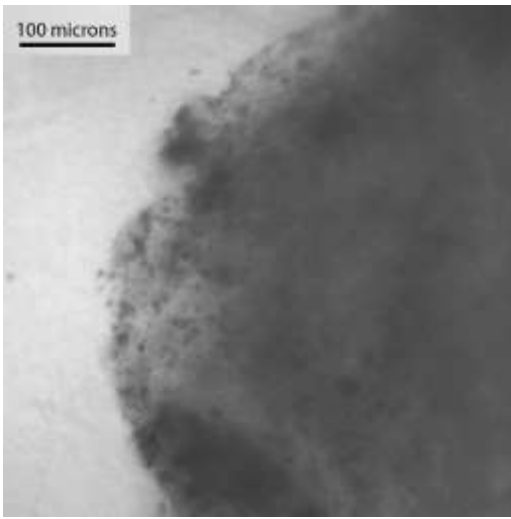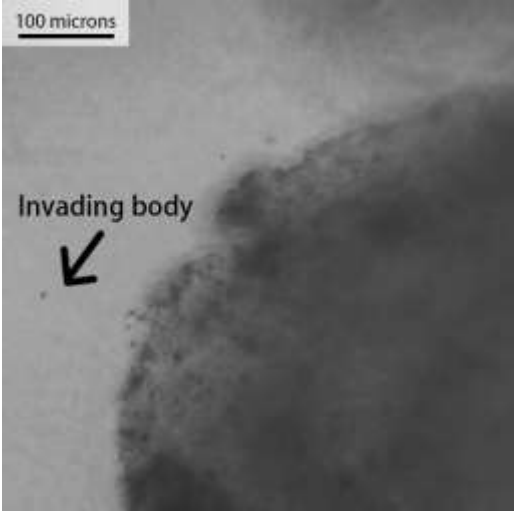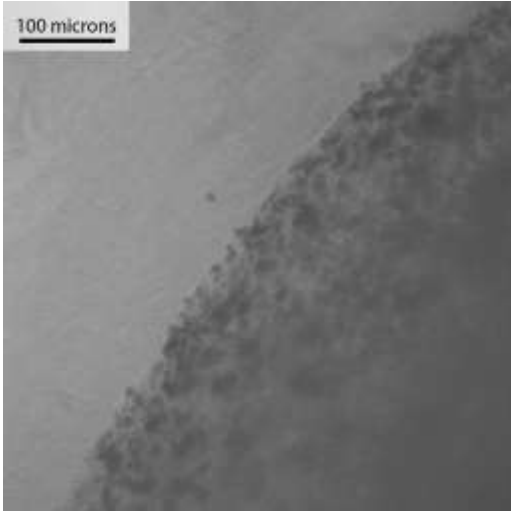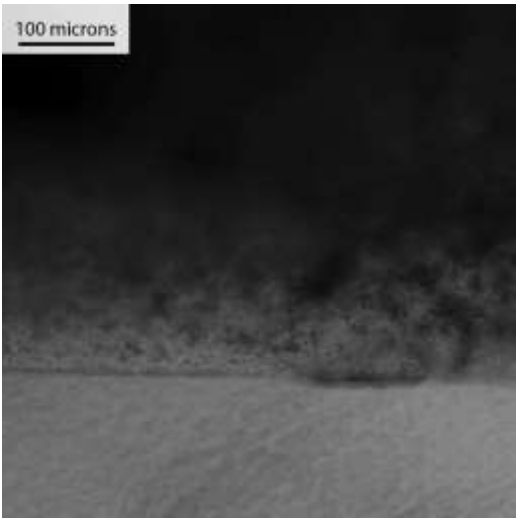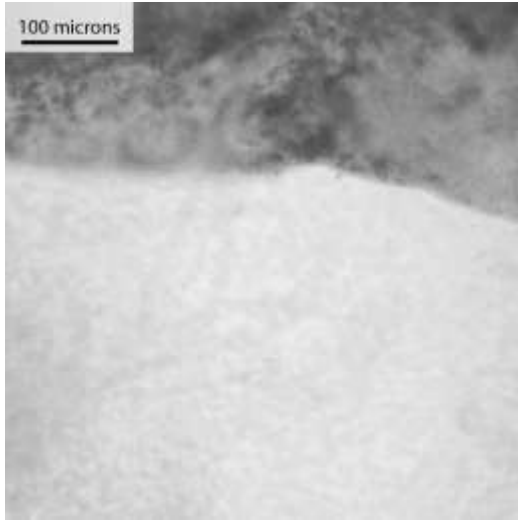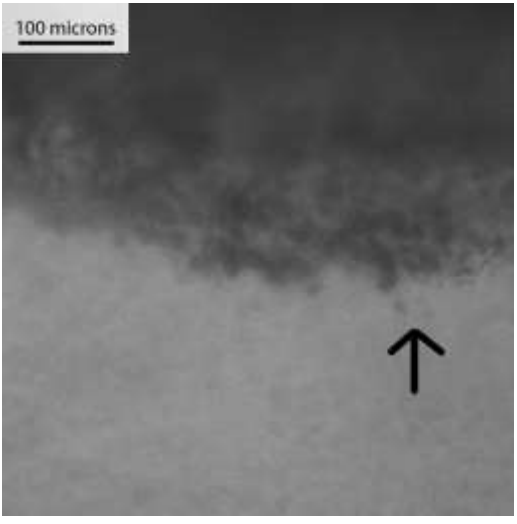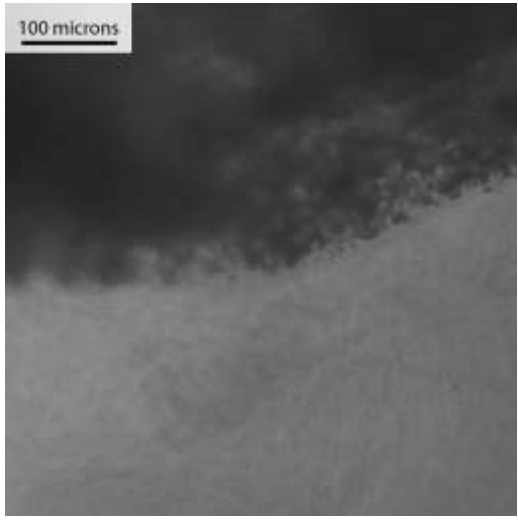
Figure 19: (Top) Examples of invasion distances on day 1, day 6, day 12 and day 18
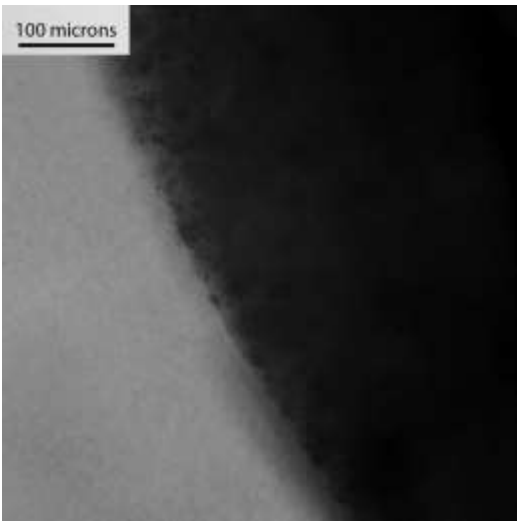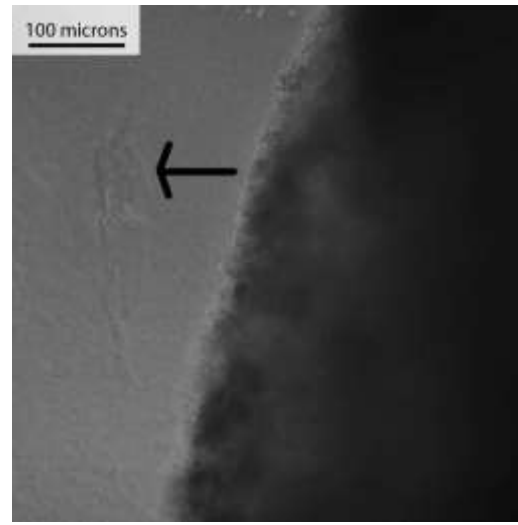
for a 40M seeding number of 3D SW620 colorectal cancer cells in dense artificial cancer mass to acellular collagen for each ACM, and each ACM was cut into 3 pieces [about 15M cell number per ACM]. The magnification power is 40x. (Bottom) The farthest invasion distance of the 40M seeding number of 3D SW620 colorectal cancer cells from ACM to acellular collagen VS time.

2.4.4.3. Invasion of HT29 – 10M/20M/30M cut to 3 ACM – Day 1/6/12/18

Seeding density	Day 1	Day 6
2.5×10^6 cells/mL		
	Day 12	Day 18

	Day 1	Day 6

5x10⁶ cells/mL	 Day 12	 Day 18

	Day 1	Day 6

7.5x10^6 cells/mL	Day 12	Day 18

Figure 20: 10 million, 20 million and 30 million seeding number 3D cell morphology of the HT29 cancer cell line in low glucose DMEM on day 1, day 6, day 12 and day 18. The arrows show the invading bodies and the magnification power is 10x.
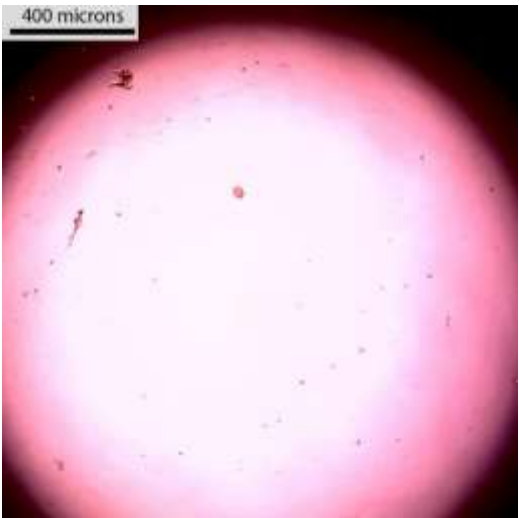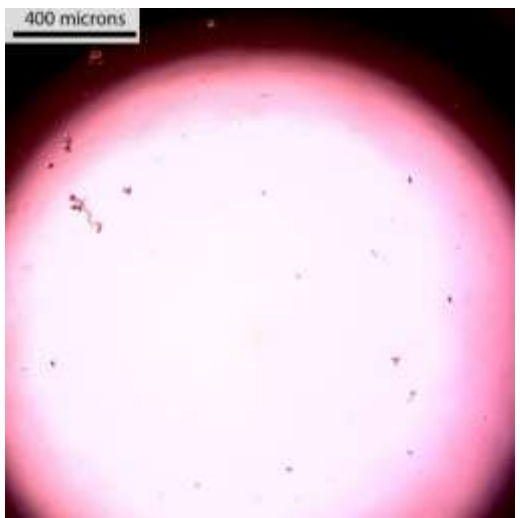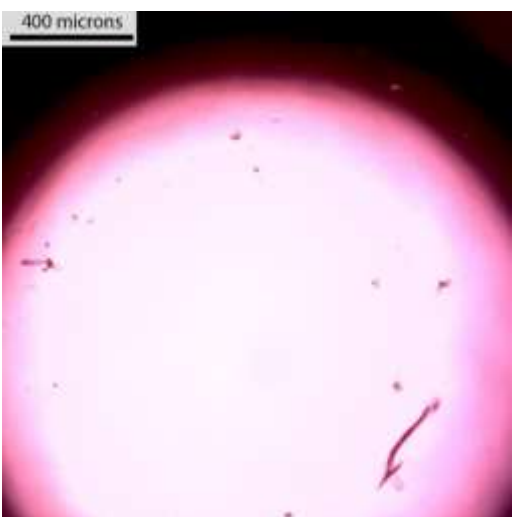
As the HT29 colorectal cancer cell line was the main cell line that used in most of my experiments, I collected 3D collagen HT29 tumouroid morphology, cell growth and invasion in different seeding density environments, as shown in Figure 20. The tumouroid was compressed by metal mould followed by the method mentioned in the previous section. Due to the nature of the HT29 cancer cell line, it was less invasive, and the cells were stable in tumouroid. Therefore, the invasion phenomenon was not obvious, and the invasion distance was short. As shown in Figure 20, 10 million and 20 million low seeding number of HT29 tumouroids showed cell invasions at some edges from day marked using the arrow-guided points. When the seeding number increased to 30 million, the invasion of each HT29 3D tumouroid was much more obvious. The arrow points out the collagen fiber on day 6, and this collagen fiber can guide the cancer cell invasion on day 12 and day 18, as shown in Figure 20.
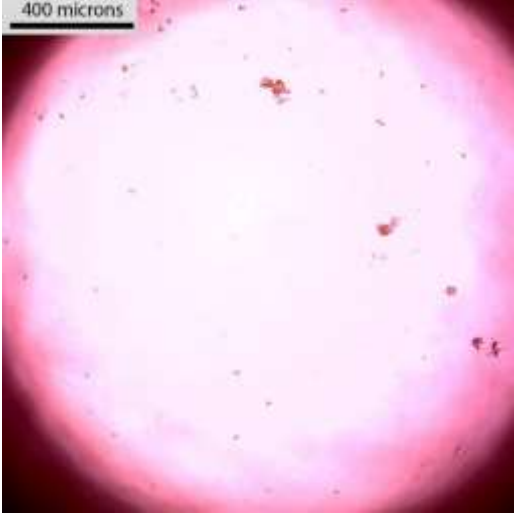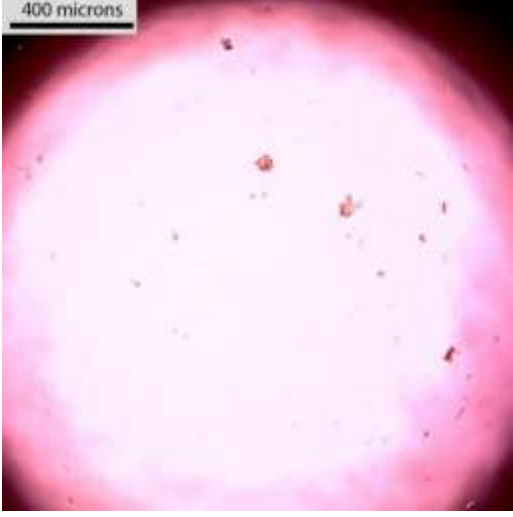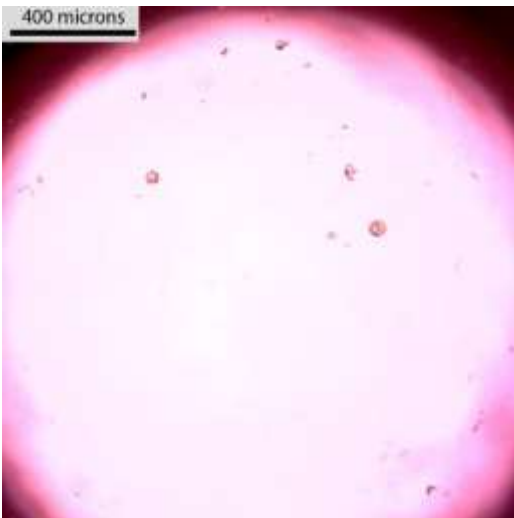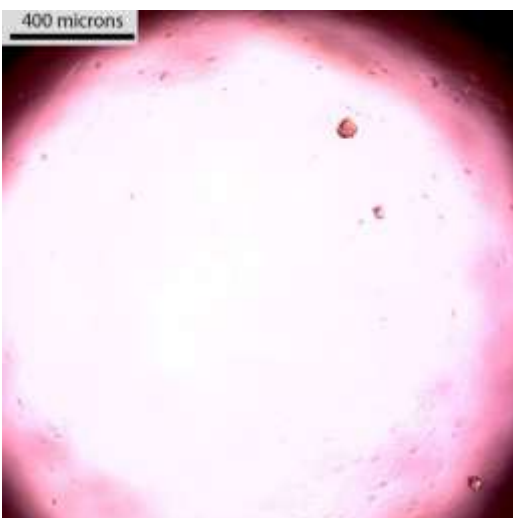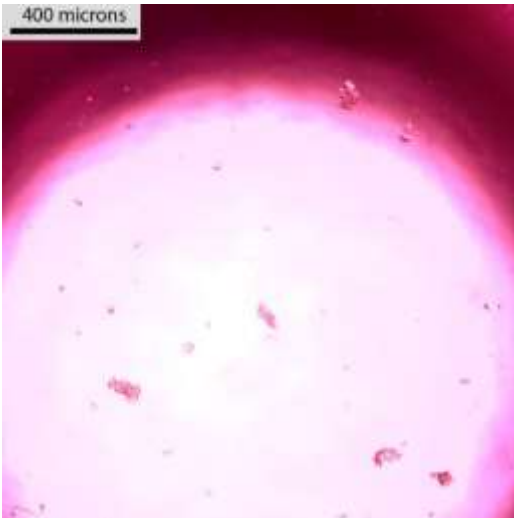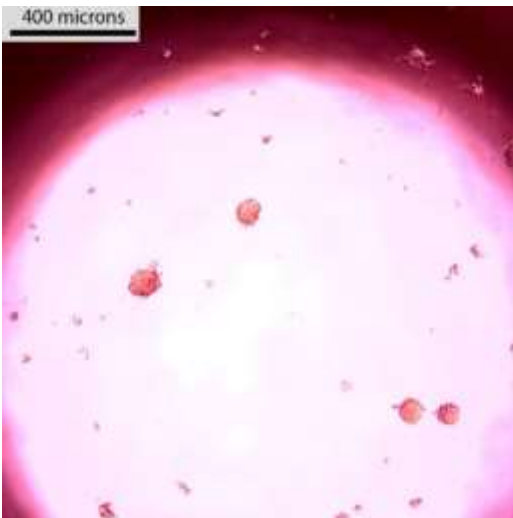
2.4.5. Spheroid culture

2.4.5.1. Spheroid culture morphology on the 2D Ultra-low attachment plate

This section deals with the methodology developed to set spheroids in 3D collagen

surround. Quantification of all results is displayed in Chapter 4.

Cell seeding number	Time of image	
100	Day 0	Day 4
	Day 6	Day 8
500	Day 0	Day 4

	400 microns Day 6	400 microns Day 8
1000	400 microns Day 0	400 microns Day 4
	400 microns Day 6	400 microns Day 8

Figure 21: The 2D morphology and growth of 100, 500 and 1,000 initial HT29 cancer cell line cell seeding number on an ultra-low attachment plate on day 0, day 4, day 6 and day 8.

To harvest enough spheroids to be cultured in the 3D model, the suggested cell seeding number is 1000 on the initial stage of the culture process using the ultra-low attachment plate. Due to the surface tension of an ultra-low attachment plate, the morphology of the HT29 cancer cell line is not flatbed attachment and the geometry is similar to that of 3D spheroids. For the 1000 cell seeding number, there was spheroid formation on day 4. On day 6, the spheroid increased the scale and on day 8, the spheroid increased the density and some adjacent spheroid could be bound together.

2.4.5.2. How the initial cell seeding number affect the spheroid shape

Figure 22: Spheroid morphology of 50,000 initial cell seeding number of the HT29 cancer cell line on an ultra-low attachment plate on day 8

Figure 22 shows a failure example of cell culture on an ultra-low attachment plate. If the initial cell seeding number is high, they will not form any spheroid. The cells on the ultra-low attachment plate will form a randomly-twisted long cell chain. This cell chain is not desirable in experiments.

2.4.5.3. Collagen fiber guide the spheroid movement

Figure 23: Example of collagen fiber-guided spheroid movement. The cell seeding number is 1000 and the sample is on day 6

There is a hypothesis that the physical structure can guide the movement of cells. The figure shows that the metastatic spheroids on an ultra-low attachment plate were guided by collagen fibers. The cells invaded along the collagen fiber. The middle position of the collagen fiber was clean, but there were cells on two sides of the fiber that connects two spheroids. This means that the cells migrated along the fiber, and the movement started from a spheroid to the other end of the fiber.

2.4.5.4. Spheroid moving to the edge of well

Figure 24: Example of a spheroid moving to the edge of a well. The cell seeding number was 1000 and the sample was on day 6.

For all cell seeding numbers on the ultra-low attachment plate, as those spheroids grew, they would move to the edge of the plate. This was preferred for a 3D cell culture. The cells moved to somewhere to support the cell growth, just like the attachment to the plate surface in a 2D culture.

2.4.5.5. Spheroids starting to invade on the ultra-low attachment plate
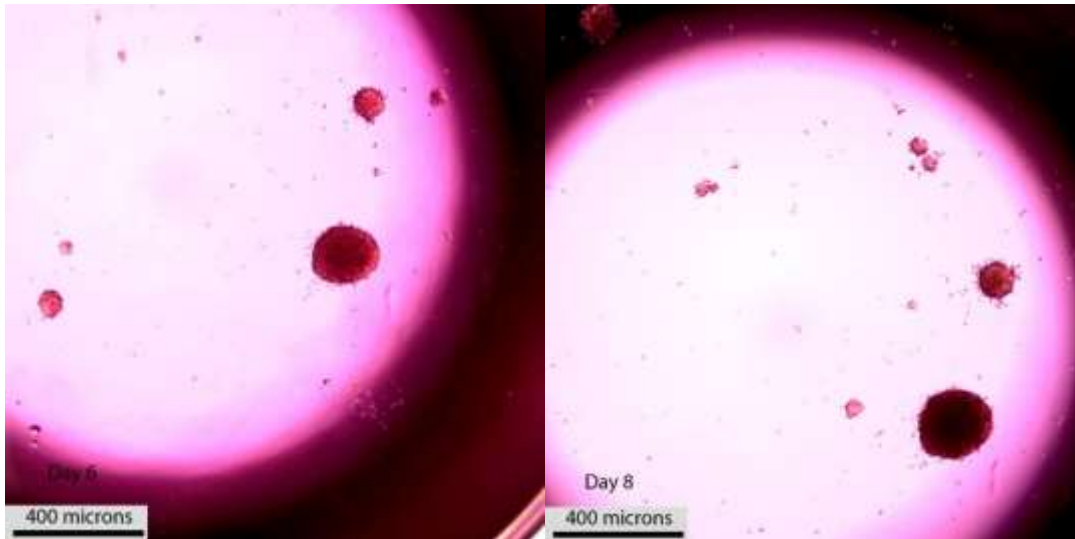
Figure 25: Example of a spheroid starting to invade on ultra-low attachment plate The cell seeding number was 1000 and the sample was on day 6 and day 8.

As mentioned previously, the spheroid formation was on day 4. Starting from day 6, the cells on the edge of large spheroids migrated to the culture medium.

2.4.5.6. Spheroids binding together during the culture process on the ultra-low attachment plate
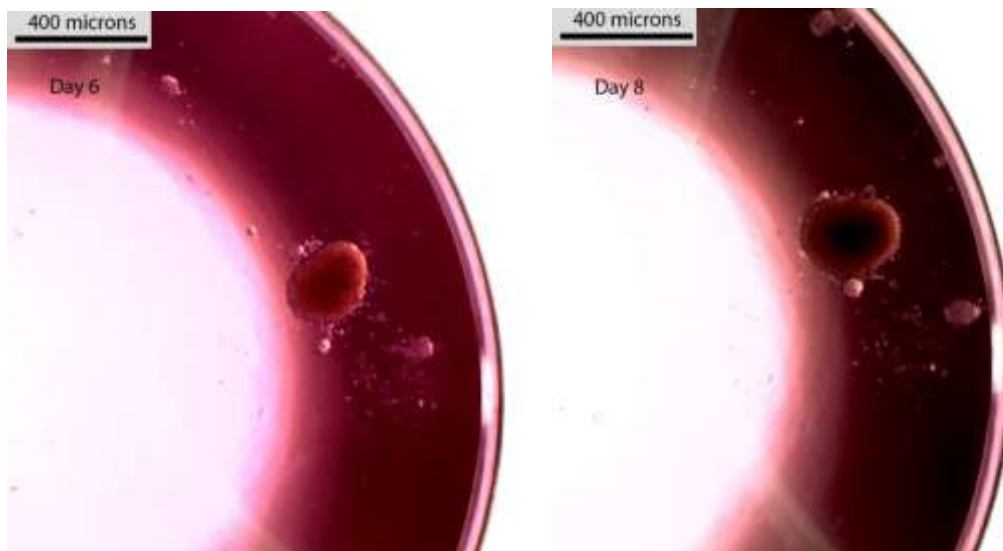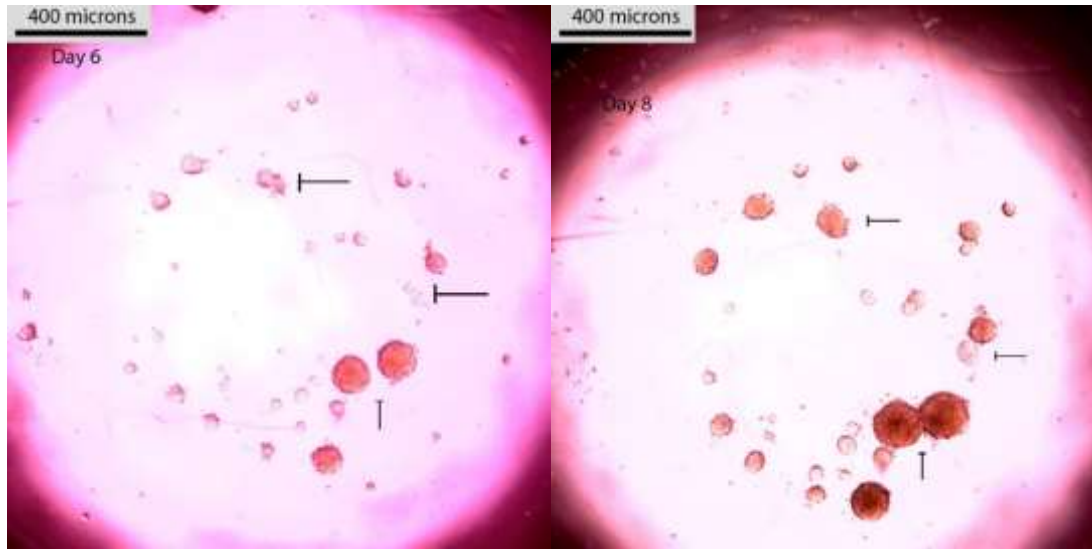
Figure 26: Example of spheroids binding together during the culture process on the ultra-low attachment plate. The cell seeding number was 1000 and the sample was on day 6 and day 8.

In the experiment, adjacent small spheroids bound together to form a large spheroid when HT29 cancer cells were cultured on an ultra-low attachment plate. Cell colonies in irregular shape would expand themselves and turned to be a round spheroid. This process added heterogeneity to the combined spheroid body because the origins of initial spheroids and their microenvironments were different.

2.4.5.7. Spheroid size growth during the culture process on the ultra-low attachment plate

Figure 27 below shows the spheroid size measurement of 1000 initial seeding number of HT29 on the ultra-low attachment plate on day 2, day 4, day 6 and day 8.
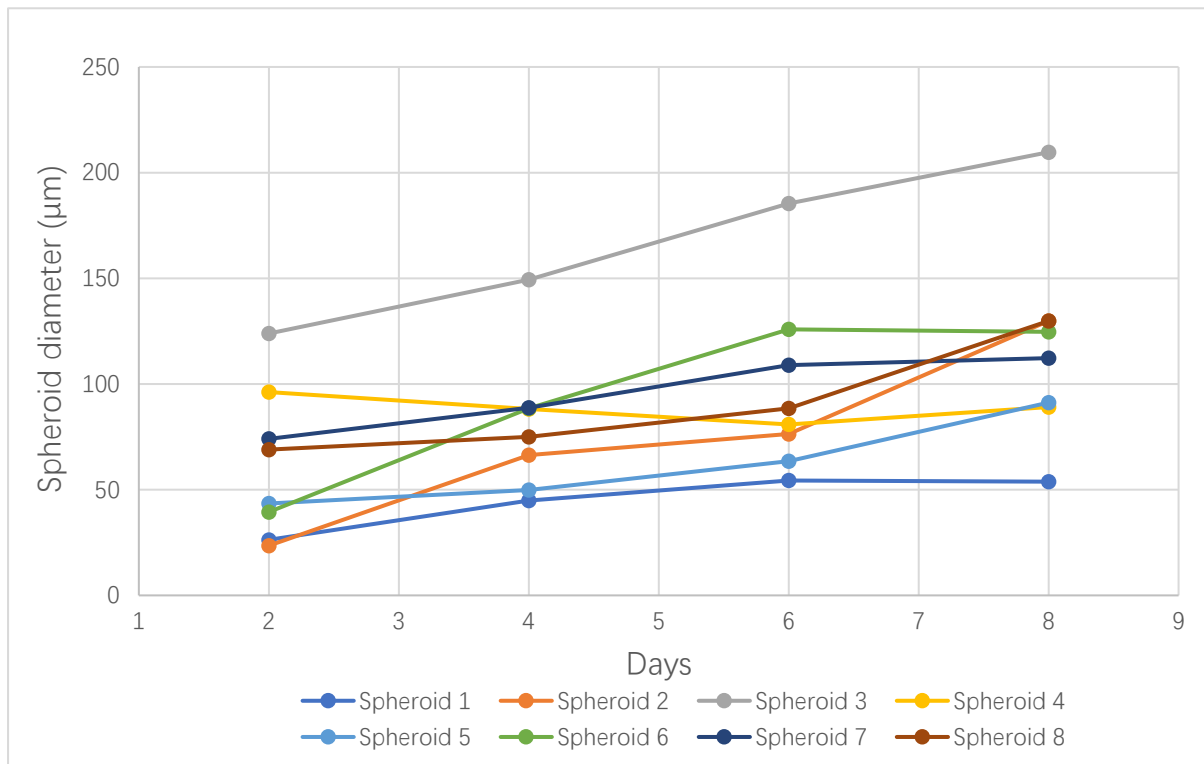
Figure 27: Spheroid size measurement on day 2, day 4, day 6 and day 8. Eight individual spheroids in different culture wells were tracked. The initial seeding number was 1000 but all the spheroids grew to have various cell numbers before seeding in the 3D collagen matrix.

2.5. Discussion

2.5.1. Several types of 3D collagen models and their potential applications

2.5.1.1. Traditional 3D collagen model

2.5.1.1.1. Basic design concept

The 3D collagen model developed by our group shows biological behavior similar to the *in vivo* cancer mass. The published thesis proved that the 3D collagen cancer model showed migration, hypoxia, and release of pro-angiogenetic factors [115]. The collagen type I is highly recommended and most frequently used because it is the most abundant collagen type in the human body. Collagen type I is biocompatible and it can mimic the extracellular composition of a natural tumour microenvironment [116,117]. The method to make the 3D collagen model is based on the metal mould compression of the collagen and cell suspension mixture. The cancer mass after

physical compression is dense and stable. Other cell lines can add to the uncompressed collagen to form the stroma that surrounds with the cancer mass as the extracellular matrix. This is the basic concept of traditional 3D collagen model of our research group.

2.5.1.1.2. In different containers

The traditional 3D collagen model can be applied to a different container to fit the experiment design. For example, in the proton irradiation experiment, I used slideflask to load cancer cells to the 3D collagen because the slideflask fit the chamber of irradiation instrument. Optimal fluorescent imaging of 3D collagen culture requires a glass-bottom fluoro dish. For most of the biological property assays, normal light microscopy and some confocal microscopy, the 3D collagen models can be contained in a 24-well or 48-well tissue culture plate. MRI imaging of the 3D collagen model requires the model to fit in a 7ml bijou, and AlamarBlue^{TM} assay requires the model to be seeded on a 96-well tissue culture plate. Various containers can be adopted because the jelly uncompressed collagen or collagen stroma can fit the shape of different containers.

2.5.1.1.3. Potential applications

Up to the date research in our group, there are projects forwarding on the 3D collagen model. The 3D collagen model can be used in pharmacological testing [118]. The cytotoxicity and viability of cancer cells in 3D are measured when drugs are applied to the 3D platform. It is an open platform and kinds of cellular behavior analysis can be performed on it.

2.5.1.2. High collagen density 3D collagen model
2.5.1.2.1. Basic design concept

According to previously demonstrated figures, although natural compression using a metal mould of the traditional 3D collagen model can provide collagen density control

from 1.25% to 3.5% by changing the compression time. It can mimic the collagen density in most of the soft connective tissues. A plastic blocker 4mm in height to physically stop the compression can dramatically increase the collagen density from 14% to 20% as shown in Figure 15. By changing the height of plastic blocker and changing the compression time, the final collagen densities of the 3D model can be controlled, and it can mimic more types of tissue microenvironments.

2.5.1.2.2. Collagen density of *in vivo* tissues

The amount of collagen content, collagen density and the extent of collagen cross-linking will directly impact the tissue mechanical properties such as ultimate stress and strain. Measurements from low collagen density tissues such as the anterior cruciate ligament of knees to high collagen density tissues such as the lumbar anterior longitudinal ligament of spine, a higher collagen fibril density, mean a higher modulus of elasticity of tissues [118]. Soft tissues have low collagen density and dense tissues like bones can have a collagen density of up to 30% [119]. It is common that human tissues have different collagen densities. According to other literature reviews, for the collagen density of 0.2% which is the value of hydrogel, the complex modulus of cell-encapsulated collagen gel is less than 20Pa, which is much lower than living tissues [120]. My 3D collagen model can be applied to higher collagen density from 1.25% to 20% by different methodology and this is a step toward better biomimicry.

2.5.1.2.3. Collagen density affect tumour biological properties

According to research reports, the collagen density can affect tumour malignancy, invasion, and metastasis [121]. Even the collagen fiber orientation can significantly enhance and facilitate cell intravasation during metastasis [122]. As shown in Figure 21, the metastatic of spheroids on an ultra-low attachment plate could be guided by collagen fiber if there is a fiber to connect spheroids to somewhere. Collagen density and collagen fiber orientation together with tumour cells are defined as tumour-associated collagen signatures (TACS). However, the influences of the reorganized

collagen tissue on tumour cells are difficult to have a quantitative analyze *in vivo* due to the limitation of the existing method. 3D *in vitro* model is the new way to explore the relationship between TACS and tumour cell behavior.

2.5.1.2.4. Potential applications

The control of collagen density can alter the physical property and mechanical strength of a 3D collagen model. The 3D collagen model with appropriate collagen density can mimic the microenvironment of specific tumour growing condition *in vivo*. The methodology of creating a high collagen density collagen model extends the application range of 3D collagen cancer models.

2.5.1.3. 3D Spheroid model
2.5.1.3.1. Basic design concept

Making a 3D spheroid model requires the culture of spheroids and the transfer of spheroid into a 3D collagen matrix. The spheroid culture is on an ultra-low attachment plate with predesigned seeding number and culture time. The spheroids are transferred to a 3D collagen gel base and then covered by another portion of 3D collagen gel. Then the spheroids are in the 3D structure and ready for experiments.

2.5.1.3.2. Potential applications

3D spheroid models are reported to be used *in vitro* for anti-cancer drug therapeutic screening and drug testing [123, 124, 125]. Spheroids are usually cultured on a 96-well plate. The large sample numbers are suitable for drug screening and even gene screening. The 3D spheroid model is also a type of 3D collagen model that can be used for analyzing biological property assays.

2.5.2. How to increase 3D collagen model reproducibility in practical terms
2.5.2.1. Temperature control

The gelation process of the collagen mixture process is temperature-sensitive. The rat

tail collagen type I is always stored in cold condition before experiments. The HEPES buffer DMEM and MEM are mixed in cold condition as well and usually placed into an icy box to maintain the low temperature. The thermo- and pH-responsive polymers are used to achieve physical crosslinking that responds to physiological conditions (a neutral pH and body temperature 37°C) without using cytotoxic chemical stimulation [125]. The physical crosslinking of collagen will pose little or no cytotoxicity to the cells in the hydrogel and hence increase the biocompatibility [126, 127, 128]

2.5.2.2. pH neutralization sensitivity

The gelation process of collagen mixture process is pH sensitive. The protein molecules are stable in acidic solution in cold temperature and able to form nanofibrils that respond to body temperature and neutral pH [129, 120]. The pH neutralization process can be controlled by carefully adding high and low Mole number sodium hydroxide alkali drop by drop. 6-7 drops of 5 Mole sodium hydroxide are added to a 4ml collagen mixture to change the color of acidic collagen mixture solution from yellow to dark yellow. After that, 1 Mole sodium hydroxide can be added drop by drop to further change the color of acidic collagen mixture solution from dark yellow to light pink. An over neutralization of collagen mixture has a deep pink color. The solution in light pink is preferred to make perfect neutralization, and the collagen will set then and used for metal mould compression. The collagen can be set in deep pink as an uncompressed collagen gel, but an over neutralized collagen gel will have problems in metal mould compression. The reason is that the pH imbalance breaks the physical stability of collagen nanofibrils whose structure is fragile for physical compressions.

2.5.3. The biological properties of the 3D collagen cancer model

2.5.3.1. Summary of main biological properties of 3D collagen model

Collagen is the first choice to form a gel system among other biocompatible polymers because of its biocompatibility, bioabsorbability, and cell adhesiveness [131]. In previous sections, I have pointed out the biological properties of our 3D collagen

cancer model, i.e. migration, hypoxia and release of pro-angiogenesis factors. My studies further confirm the metabolism and cell invasion in a 3D condition, especially at a high cell seeding condition.

2.5.3.2. Comparison with 2D models

In comparison with 2D models, a 3D microenvironment has increased paracrine interactions as discussed in Chapter 1. 3D cell culture models have improved cell migration, survival, and growth than 2D cell culture models. Another important advantage of a 3D cell model is that this model has greater stability and longer lifespan of cells because the gene expressions are more alike than those of *in vivo*. [132]. A 3D spheroid model can visualize the process of spheroid invasion and sphere formation in real time while keeping the spheroid active, alive and intact so that they can be transferred to *in vivo* assays [133].

2.5.3.3. Comparison with animal models

Any experiment taking an animal model requires ethic approval whose process is usually long. Experiments on animal models are the precursor toward *in vivo* trials. The main disadvantage of a xenograft cancer model is that the genetics and histology of the cells are normally not representative of respective human tumours, while xenograft cancer models have not been as predictive of therapeutic success as contemplated [134]. Animal models are less controllable than 3D culture. The numbers of animals needed for mechanistic studies can be reduced by using these 3D models. The 3D collagen model has successfully used for culture from primary tumour cells, and tumour cell line culture is well-established in my research group. The cells have no genetic or histology problems in the culture process but increase the difficulty to build extracellular matrix design. The components and design of stroma can determine the biological behavior of 3D cancer core.

2.5.4. Cancer cell invasion in 3D between different cell lines

2.5.4.1. Invasion type

When referring to Tarig's studies, HT29 cells formed irregularly-shaped cell aggregates, and HCT116 cell aggregates demonstrated a more 'grape-like' phenotype with the cells apparently forming loose clusters with poor cell-cell adhesion in comparison to HT29 cells [135]. However, his research was based on RAFT^{TM} 3D collagen system. My project used the traditional 3D collagen protocol to produce the collagen matrix. The collagen density is lower but the cell seeding number is much higher. Figure 20, displaying 10 million, 20 million and 30 million seeding numbers in 3D cell morphology of the HT29 cancer cell line on day 1, day 6, day 12 and day 18, shows that low seeding numbers. When the seeding number was as low as 10 million and 20 million of HT29 tumouroids, cell invasions occurred at some edges from day 12. However, when the seeding number was as high as 30 million, the invasion of HT29 3D tumouroids became much more obvious. The invasion of SW620 is displayed in Figure 20. There was cellular aggregate formation on day 6 and the morphology changed at the boundary of the collagen cancer mass. On day 18, the spheroid colony further grew and the distance between colonies also increased.

2.5.4.2. Invasion distance

The invasion distance is depending on the metastatic characteristics of cell lines. In Figure 19, the HT29 is less invasive and the invasion distance is difficult to be measured due to not enough invasion bodies to make statistical validation. Figure 18 also shows significant influence by cutting boundaries on the invasion distance of 3D tumouroids.

2.5.5. Spheroid 3D model design in practical applications

2.5.5.1. Seeding number

Figure 20 shows the morphology, sphere formation process and the influence of the initial cell seeding number in an ultra-low attachment plate for 2D culture. A higher initial cell seeding number can shorten the spheroid culture time. For example, in my

preliminary experiment, there are no well-compacted spheroids on day 9 if the cell seeding number is 100, but there will be sufficient well-compacted spheroid on day 9 if the cell seeding number is 1000. The disadvantage is that if the seeding number is too high, a randomly twisted long cell chain, which is not usable in experiments, may be formed, as shown in Figure 21. The cell microenvironment is different for single cells growing into a spheroid and for a small colony of cells growing into a large spheroid using the paracrine cell signaling. The choice of initial seeding number is important. According to my researches, the initial cell seeding number of 1000 with a culture period of nine days is highly recommended to get spheroid with perfect shape and varied sizes.

2.5.5.2. Spheroid harvest time

If a low seeding density is adopted to start spheroid culture, such as 100 cells, there will be spheroid formation as well if the culture period is longer. The harvest time is optimized by the experiment design. An urgent experiment may require a high seeding number and short spheroid harvest time. For a planned experiment, a low seeding density and longer spheroid culture time are preferred because the spheroid developed from a single cell has better homogeneity.

2.5.5.3. Spheroid size

I have not averaged the effect of the spheroids such as average size, because I track individual spheroid behavior averaging dilutes information about the heterogeneity of spheroid growth and response to radiotherapy. The detailed plot is displayed in Figure 27 in section 2.4.5.7. The spheroid size is growing with the culture time. Some spheroid on track show shrinkage but most of the spheroids increase their size. The spheroid diameter grows from 25 to 125 μm on day 2 and grows in a 50 to 210μm range on day 8. Most of the spheroids have a mean diameter of 100μm on day 8.

2.5.5.4. Volume and shape variability

There is spheroid-shape heterogeneity on the ultra-low attachment plate. The ideal spheroid should originate from single cells. The spheroid formation by adjacent cells changes the microenvironment and morphology regularity. The shape is depending on the initial seeding number. The example displayed in Figure 22 shows the irregularity of cell grow when seeding number is too high. If the seeding number is low, the volume and shape are variable as well.

2.5.5.5. Relationship between viability and shape

One research of 3D spheroid culture shows that the cells of the inner core of spheroid are dead and the outmost boundary surface the cells are active and proliferative. The variation in tumour shape will accompany the change in dimension of the proliferative area and necrosis area [136].
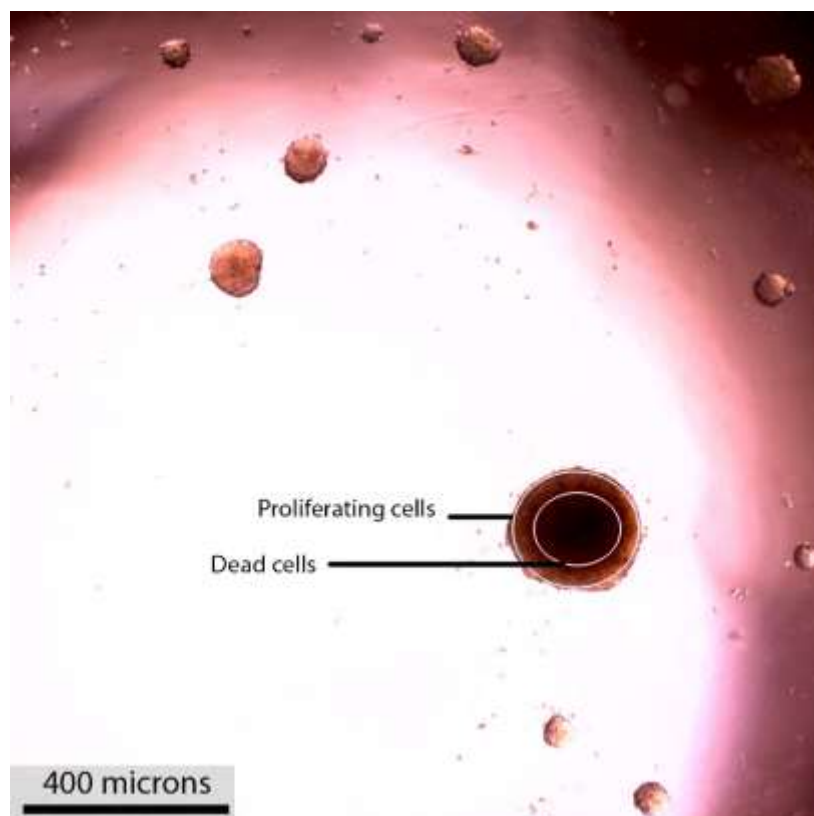
Figure 28: Relation between shape and viability of spheroids on an ultra-low attachment plate. The cell seeding number was 1000 and the sample was on day 8.

2.6. Conclusions:

The 3D collagen cancer model can be used as an imageable biophantom for biological researches after characterization. The metabolism of cancer cells in the 3D collagen model is depended on cell lines. The cell viability decreases as the number of culture days increases. The decrease rate is gradual for all seeding numbers. The collagen density of the 3D collagen tumouroid model can be controlled. Traditional metal mould compression can create collagen density range from 1.25% to 3.5%. With the aid of a 4mm-high plastic blocker to stop the compression, the collagen density can increase up to 20%. This increases the application range of the 3D tumouroid model because it can simulate a specific tumour microenvironment. The cutting of a 3D tumouroid affects the invasion of cancer cells. The cancer cells are not uniformly distributed in artificial cancer mass because the physical compression increases the local collagen density at boundaries. For the more invasive SW620 cancer cell line, cells start to invade on day 6, and on day 18 the mean invasion distance could be 416 μm in an uncompressed collagen gel. The invading body changes its morphology, from single cells to cluster of cells and finally spheroids. This phenomenon is obvious on day 18. For the less invasive HT29 cancer cell line, there is less invasion and the details are determined by the cell seeding number. The cell seeding number of 1000 is suggested to culture spheroid on an ultra-low attachment plate and the cells are ready to harvest on day 9. An extra high cell seeding number leads to random elongated morphology of spheroids. The fibers can guide the invasion of spheroids, and adjacent spheroids bind together after cell culture. However, current 3D collagen cancer models provide low reproducibility due to the pH level control inaccuracy and compression methodology. The uniformity of tumouroid is also low. These problems can be improved by changing the compression method such as the application of the RAFT™ 3D collagen system.

Chapter 3:

Developing a methodology using the 3D collagen cancer model for magnetic resonance imaging applications

3.1. Aim

The aim of this chapter is to design an MR-imageable 3D *in vitro* tumour model, to investigate what properties of the tumour model can contribute to image signals, and set up an MR environment that can image samples of interest. The model should be biocompatible and show the image contrast of the tumouroid. The contrast mechanism of 3D collagen tumouroid model will be the main topic to be discussed in this section.

3.2. Design criteria of the 3D collagen cancer model for MRI application

3.2.1. Need for an MR platform to image 3D samples

There are plenty of imaging modalities available in the laboratory for collagen model analysis such as the confocal microscopy, fluorescent microscopy, TEM, and SEM. The sample depth of a resolution varies depending on different the type of imaging modalities. Bio-samples have a thickness ranging from meters (whole animal) to nanometers (ultra-cut preparation for electron microscopy such as TEM) [137]. The confocal microscopy has a maximum penetration sample depth of about 100µm to 200µm in an ideal condition, which means a transparent specimen mounted on a correct thickness of the coverslip with a suitable mounting medium and a proper working distance of objective lens [138]. For opaque materials, the laser can only visualize the surface of materials. The resolution of the confocal microscopy is depending on the laser pathway, the equipment and the spherical aberrations limitation of the system [139]. If more bulk 3D changes in tumour size, shape and composition in response to therapies need to be measured, only limited imaging solutions can be adopted. My project focus on MR imaging using 3D collagen samples,

because it can measure much thicker samples (up to the size of patients), and is a common clinical modality, which allows my results to have the potential to be translated for patient benefit. Also, the non-ionizing measurement will not damage the samples.

3.2.2. Model design background

As an alternative to animal models and clinical trials, which require ethical approval and time to apply, this model is easy to–make with rapid reaction. Therefore, it is more applicable to experiments to form reproducible multifunctional 3D collagen tumour models on imaging platforms that can have controllable cell growth microenvironment and show biological properties mentioned in Chapter 2. The final goal is to measure changes in biological properties, for example, biological assays, drug testing, and irradiation response, as future work. The first step is to confirm the relationship between MR image signal and components of this 3D collagen tumour model.

3.2.3 Experiment design background

The 3D collagen model has features similar to real tumours summarized in Chapter 2. It is reproducible, controllable and can be used in multimodal image studies such as the confocal microscopy and fluorescent microscopy discussed in Chapter 2 and Chapter 4. By changing the compression time, the collagen density can be controlled, and by changing cell seeding number and compression time, the cell density can be controlled as well. An ideal artificial cancer mass should provide image contrast in different imaging modalities (anatomical and functional acquisitions) and viable during transporting. I had a cooperative project with Catarina Veiga, a 3rd year PhD student at the Department of Medical Physics of UCL. My duty was on 3D tumouroid design, 3D tumouroid manufacture, improvement of tumouroid development, and any other biological aspects described in the method and discussion sections in Chapter 2, while she was responsible for all the physical aspects such as MRI data acquisition and parameter improvement. The hypothesis was that collagen and cell components

contribute to the MR signal. The changes in components were imageable by MRI. Catarina did the preliminary image test in the low-density tumouroid model, which applied tumouroid into a hydrogel-based universal tube. The detailed experiment parameters were unknown, but her conclusion was that computer tomography image gets no contrast and magnetic resonance images show some boundaries on such models with visible contrast. Then we planned to develop a high seeding density tumouroid for magnetic resonance imaging applications [174].

3.2.4. Model design goals

The design of the original 3D collagen cancer model is identical to that of the 3D collagen tumouroid model in section 2.3 Method of Chapter 2. We further extended the application to multimodal and sequential MRI studies. The novelty of my project is to develop an MR methodology and MR-compatible 3D tumour model to enable future MR monitoring of samples in response to therapies. The first step is the confirmation of imaging contrast of the 3D collagen model under MR imaging. There are few studies on 3D model bioimaging. One research group used a simple 3D biophantom to verify nanoparticles as the MRI contrast agent [140]. The applications of 3D collagen tumouroid on MRI not only are the exploration of a novel method to analyze biological changes of 3D cell culture but also has potential to provide pre-clinical evidence for different treatment plan of patients. For instance, by establishing an optimized MR imaging platform for tumouroids, and monitoring their response to therapies, this can be translated for patient benefit *in vivo*.

3.3. Physics of MRI

3.3.1. Magnetic field under MRI

In comparison with X-ray, which is ideally suited for dense tissues such as bones, MRI is ideally suited for soft tissue imaging such as brain tumour and spinal infections [141]. The reason why MRI can specifically target soft tissues is that the human body has the sufficient number of hydrogen atoms in forms of water and other organic molecules. The protons of hydrogen are electrically charged as a magnet, which has poles and is

subject to magnetic fields. The standard speed of proton spin is defined as Larmor frequency. When hydrogen protons are exposed under magnetic fields such as that of an MRI scanner, the protons will align themselves parallel to the magnetic field (M_0) in the z-axis direction (B_0). Radio frequent pulses (RF) with a specific frequency can trigger the hydrogen protons to move from out-of-phase to in-phase state. The out-of-phase state is the natural state under the magnetic field that hydrogen protons are aligned but not spinning synchronously. When RF matches the Larmor frequency of hydrogen protons, the hydrogen protons spin simultaneously, and this is the in-phase state. Moreover, the RF rotate the magnetic field from the z-axis direction to the xy-axis direction by a flip angle (α). The net magnetization (M_0) will decrease in the z-axis and increase in the x-y plane [142].
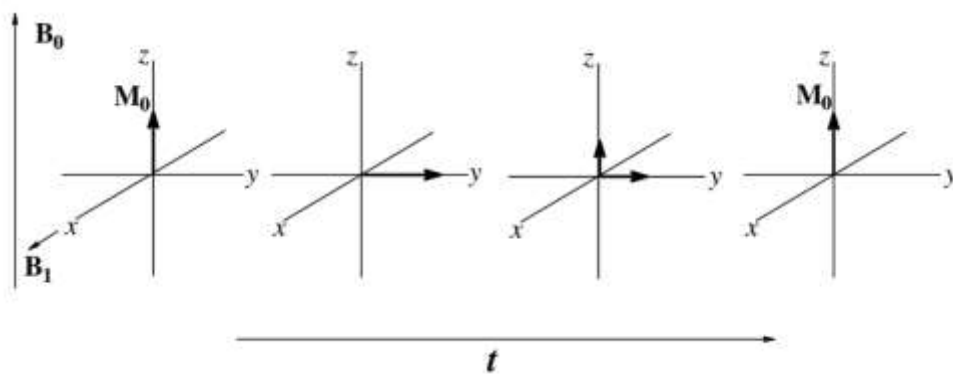
Figure 29: MR relaxation to equilibrium. The first image is the equilibrium state of magnetization (M_0), the net magnetization is aligned with z-axis (B_0). The second image shows that when a 90° pulse (B_1) is applied, the magnetization rotates to x-y plane. The third image shows the equilibrium state of the second image. The last image shows that the magnetization field returned to the equilibrium state when $t > T_1$ [143].

3.3.2. Relaxation process

The signal decays in the x-y axis and then the magnetic field in the z-axis is restored to the equilibrium stage. When the magnetic field is changed, or RF pulse is removed, the protons are no longer spin synchronously and dephase from in-phase to out-of-phase. The relaxation process is measured in T_1 (spin-lattice) and T_2 (spin-spin) types.

In T_1 relaxation, the magnetization realigns because of the external magnetic field (B_0) after a while. It is in this process that the magnetization of the x-y plane decreases, and that of the longitudinal z-axis increases. T_2 relaxation measures the decay of the resonance signal in the x-y plane at an exponential rate. T_2^* is another kind of T_2 measurement that combines inhomogeneity of the real system magnetic field. T_1 relaxation time is defined as the time of the longitudinal magnetization to reach 63% in the equilibrium magnetic field. T_2 relaxation dephases quicker than T_1 relaxation. So T_2 relaxation time is defined as the time of the transversal magnetization to reach 37% in the equilibrium magnetic field [144]. T_1 and T_2 relaxation times vary depending on the materials, but the exact value also depends on the strength of the external magnetic field and temperature [145].
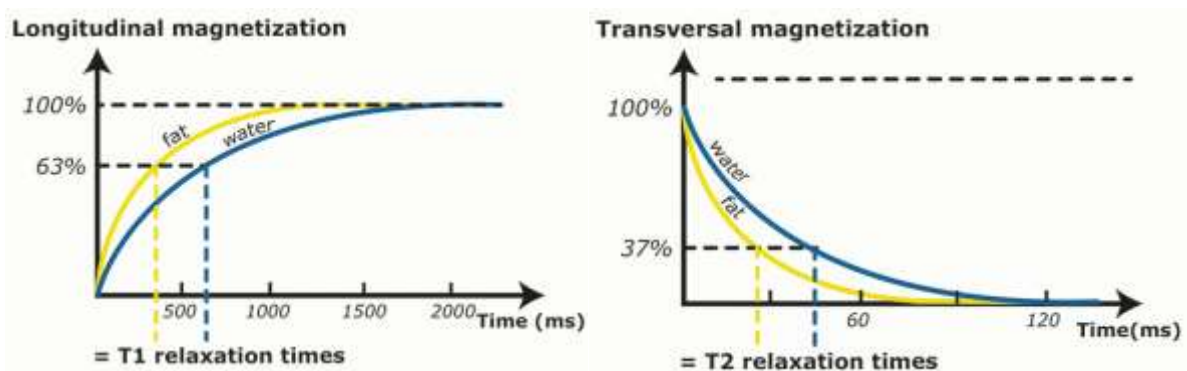
Figure 30: T_1 and T_2 relaxation times of fat and water [144]

Therefore, by imaging the magnetic resonance of hydrogen in water, which is the main content of the human body, people can get the map distinguishing the specific distribution of soft tissues with contrast from dense tissues like bones.

3.3.3. Pulse sequences and spatial resolution of MR

The information of MR images is expressed as a pulse sequence. The pulse sequence has both RF pulses and gradient pulses. They are measured as spin-echo (SE) and gradient-echo (GE). Key parameters to measure the pulse sequence include repetition time (TR), echo time (TE), inversion time (TI) and flip angle (α). Spin echo normally

applies a 90º or 180º pulse to generate echoes for signal intensity measurement. Spin echo model records a higher image quality, but longer acquisition time. The gradient echo only uses a single RF pulse plus a field gradient reversal to create an echo without a 180º pulse. The gradient echo model is sensitive to field inhomogeneities [146]. In this chapter, we used a fast gradient echo model with lower flip angle called FLASH (Fast Low Angle Shot) and a multi-echo fast spin-echo model called RARE (Rapid Acquisition Refocused Echoes).

As mentioned in subtitle 10 of Chapter 1, the spatial resolution of MR is related to the RF coil. An RF coil with higher signal-to-noise ratio can achieve better spatial resolution if the scan time and 3D scan area (voxel) are fixed. Moreover, the spatial resolution of a 3D voxel is depending on three structural parameters: field-of-view (FOV), matrix size, and slice thickness. The FOV is the dimension of the matrix of phase-frequency encoding directions. The matrix size is the number of frequency-phase encoding steps. The slice thickness determines the depth of the matrix. The maximal spatial resolution *in vivo* images of a human brain has a resolution of 0.13mm x 0.13mm x 0.8mm at 9.4T, which was recorded in the study by Daniel Stucht's group in 2015 [146]. The highest isotropic resolution is up to 10 microns at 9.4T as described in the book *Principle of Nuclear Magnetic Resonance Microscopy* by Paul T. Callaghan [146]. The MR equipment in my experiment was Bruker ICON^{TM} and the official brochure has an example of a flyer with 49 microns isotropic resolution. In my experiment, the spatial resolution range was between 0.125mm x 0.125mm x 1mm and 0.42mm x 0.42mm x 1mm.

3.3.4. T_1 and T_2 relaxation times

The measurement of T_1 needs continuous inversion recovery (IR) sequences with different inversion periods. Inversion recovery inverts M_0 by applying an 180º inversion pulse to initiate the recovery process. The inversion time (TI) is defined as the waiting time for the 180º pulse to invert before continuing with the SE imaging sequence. The

application of 90° pulse may not turn all the fields into a positive condition, so there will be a mixture of positive and negative echoes. TR should be 5 times greater than the longest T_1 for the invasion pulses to reach the relaxation state. In this case, the signal T_1 can be calculated by the following formula:

$$M_z = M_0(1-2e^{-TI/T1})$$

In the formula, M_z is the net magnetization in the z-axis, M_0 is the net magnetization in the equilibrium state, TI is the inversion time and T_1 is the T_1 relaxation time.

The train of SE sequences can be used to measure the signal intensity at different TEs. Therefore, T_2 can be calculated by the following formula:

$$M_{xy} = M_0e^{-TE/T2}$$

In this formula, M_{xy} is the net magnetization in the x-y axis, M_0 is the net magnetization in the equilibrium state, TE is the echo time, and T_2 is the T_2 relaxation time.

3.4. 3D collagen cancer model for MRI applications

3.4.1. Design specification

The 3D collagen cancer model is designed to be compatible with MRI (sample holder designed with no metal) and have imaging contrast under different imaging sequences of MRI. The artificial cancer mass and surrounded uncompressed collagen should have different imaging signals to provide a contrast between the two components. We will investigate whether changes in imaging contrast of the artificial cancer mass are relevant to biological property changes such as cell density, collagen density, and possibly sample treatments.

3.4.2. Experiment design

In cooperation with Caterina Veiga, there are three studies about the 3D collagen cancer model under MR imaging.

3.4.2.1. Study I – acellular collagen mass and 30M cancer mass

In order to investigate how colorectal cancer cells contribute to imaging signal, a dense

cancer mass with acellular and 30M cell seeding number (7.5×10^6 cells/ml seeding density) surrounded by uncompressed collagen were tested in the 7ml tissue culture universal (3 repeats).

3.4.2.2. Study II – two acellular collagen mass

To investigate the imaging signal variance of the same sample, two acellular dense cancer masses surrounded by uncompressed collagen were tested in one 7ml tissue culture universal (3 repeats)

3.4.2.3. Study III – a) two groups of acellular collagen mass and 40M cancer mass in opposite orders; b) two groups of acellular collagen mass and 20M cancer mass in opposite orders

Study III discriminated the differences between cellular and acellular ACM for 40M high cell seeding number (1×10^7 cells/ml cell seeding density), and 20M lower cell seeding number (5×10^6 cells/ml cell seeding density). There are four samples. There are two dense cancer masses surrounded with uncompressed collagen in one 7ml tissue culture universal for all these four samples. The first sample has acellular collagen mass on the top and 40M cancer mass at the bottom. The second sample has 40M cancer mass on the top and acellular collagen mass at the bottom. The third and the fourth ones have 20M cancer mass on the top and acellular collagen mass at the bottom. (2 repeats)

(a)　　　　　　　　　(b)　　　　(c)
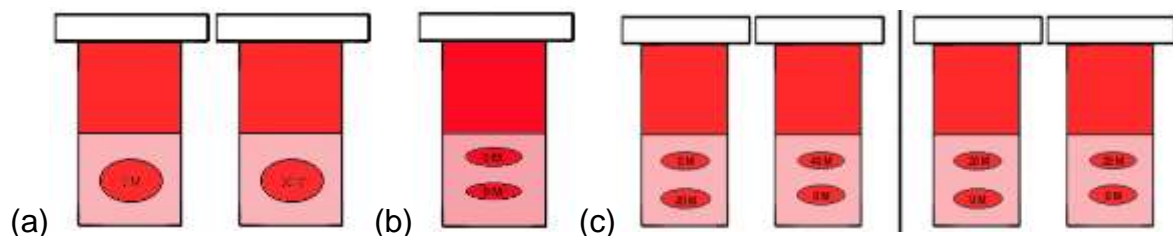
Figure 31: The schematic diagram of sample fabrication for MRI studies (A) Study 1, (B) Study 2 and (C) Study 3. The cell line is the HT29 colon cancer cell. Pink areas

represent uncompressed acellular collagen and dense tumouroids are seeded inside, topped with the medium. Note that some universal has a plastic marker or wooden toothpick as the signal calibration reference or coordinate indicator.

3.4.2.4. Study IV – four acellular collagen masses at different compression levels
I also cooperated with Pablo Ledesma Lopez, an MSc student at the Department of Medical Physics and Bioengineering of UCL, to explore the relationship between the collagen density and MR imaging contrast. There are three pieces of acellular compressed dense collagen mass made by the RAFT[TM] 3D collagen system. 10min, 15min, and 25min RAFT[TM] 3D collagen system compressed dense collagen (vary in collagen density) masses are placed in the uncompressed collagen gel in a "sandwich" structure. (3 repeats)

3.5. MRI system for imaging

3.5.1. MRI system specification
The Bruker ICON[TM] MRI machine at CABI (Centre for Advanced Biomedical Imaging) of UCL was used as the MR system in the experiment. The field strength of the machine was 1 Tesla and it was designed for MRI of mice models. Clinical equipment has a larger space to cover the whole body and it can control the field strength, field area, and field angles. The sample holder was horizontally placed and there was an RF coil embedded in the magnet bore. There was a warm water system in the magnet bore as well. A plastic vessel connected with the water bath controlled the temperature and there was another system to monitor the real-time temperature. All live 3D collagen tumouroid samples are imaged by T_1, T_2 and T_2^* sequences. Figure 32 shows the MRI machine used in my project and Figure 33 shows the structure of the coil folder of the MRI machine. In Figure 33, RF provider, RF tuning, and temperature probe are connected to the RF coil, and the biological sample is placed in the center of the RF coil cylinder.
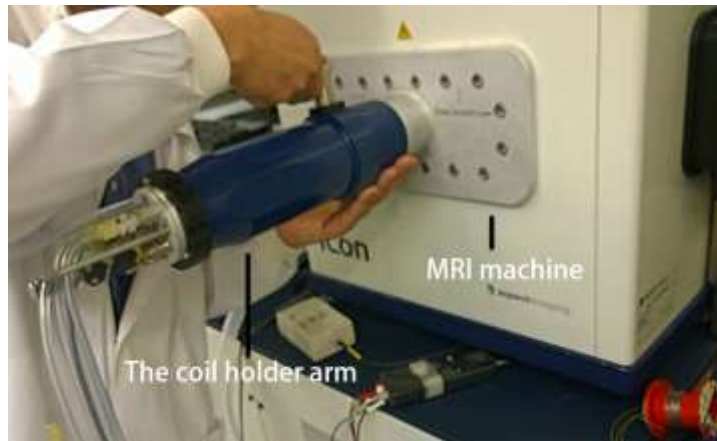
Figure 32: The Bruker ICON^{TM} MRI machine at the Centre for Advanced Biomedical Imaging of UCL
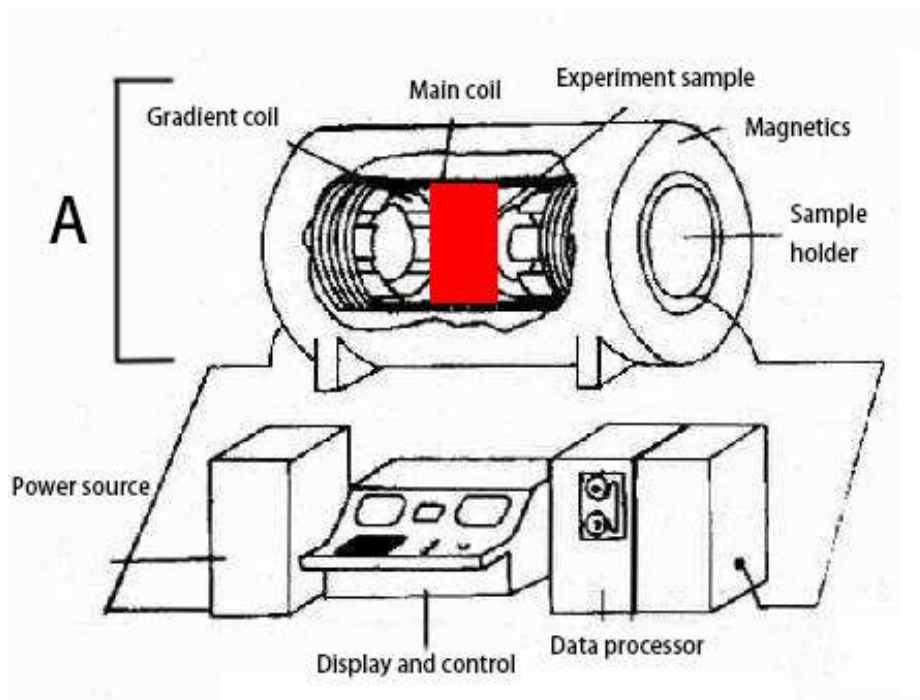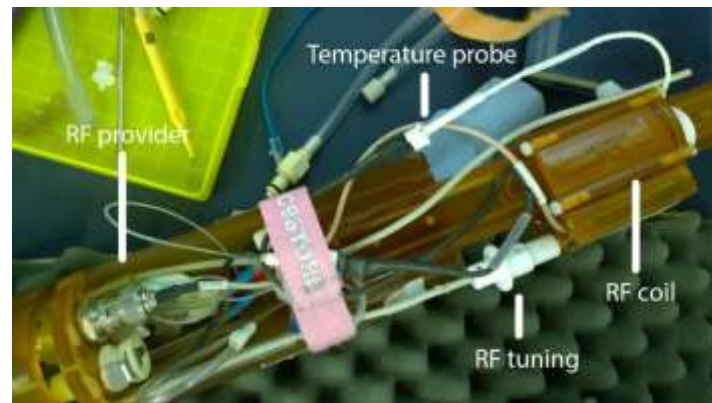
Figure 33: (Up) The coil holder of Bruker ICON^{TM} MRI machine. (Down) The diagram

of MRI. Area A is the same with the coil holder of Bruker ICON^{TM} MRI machine

3.5.2. MRI setup and sample holder design

The dimension of the RF coil holder is 40mm in length and 23mm in diameter. The RF coil holder dimension is larger than that of a 7ml plastic tube (length: 38 mm; diameter: 18mm). Thanks to the design of Caterina Veiga and workshop of Robert Moss, George Randall (Department of Medical Physics and Biomedical Engineering, UCL), a 3D-printed plastic sample holder is created to fill in the gap between the RF coil holder and 7ml plastic tube. Attributing to the slope designed for the sample holder, the unavoidable air bubbles inside the 7ml plastic tube were driven to areas that will not affect MR imaging.
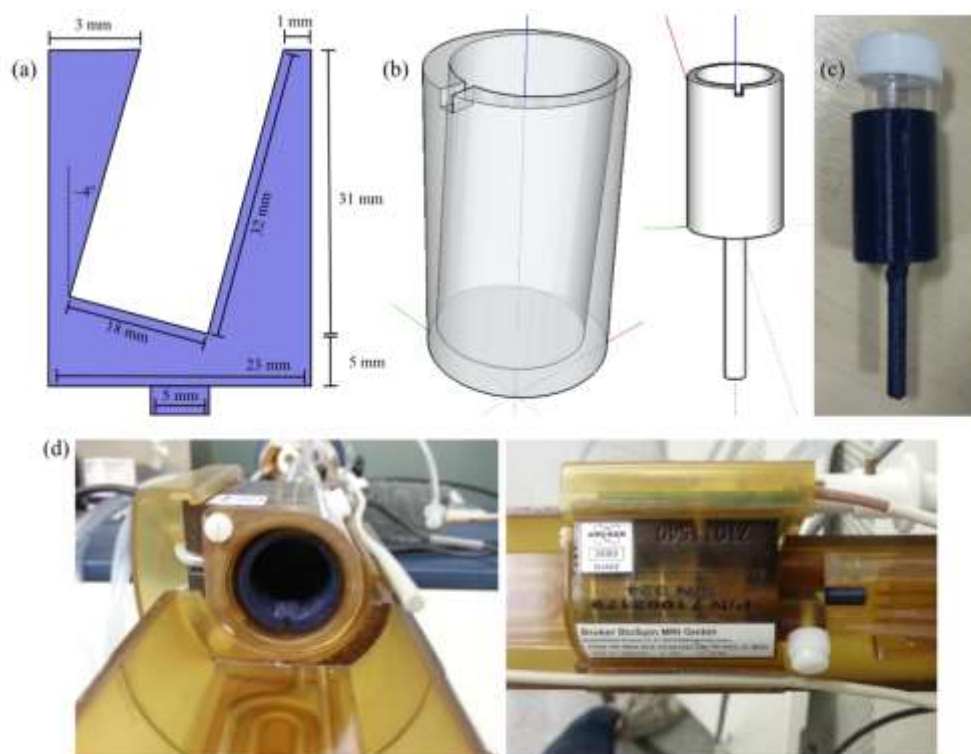
Figure 34: The design of the sample holder to fit the RF coil. (a) Schematic diagram, (b) 3D sketch, (c) plastic tube in the sample holder, and (d) the sample holder in the RF coil. Courtesy of Caterina Veiga [147].

3.5.3. Fiducial marker

Fiducial markers can coordinate the spatial information after MR imaging sessions.

The marker acts as a reference point to guide image acquisition. The fiducial marker which provides a clear contrast to the main object and whose material does not express MR signal can be selected. The material also needs to be magnetic field stable and biocompatible.

Four types of fiducial markers were used during the project. They were 1) a plastic marker, 2) a wood marker, 3) a PinPoint fiducial marker and 4) a Gold Anchor™ fiducial marker. The PinPoint fiducial marker was not usable due to the size limitation and Gold Anchor™ generate artifacts in images. In the end, we used the plastic marker and wood marker in the experiments. The plastic marker and wood marker are both manually made. The plastic marker included irregular pieces cut from a plastic tube using scissors. The wood maker is the shortcuts of a toothpick.

3.6. Method:

3.6.1. Sample preparation

The protocol of the artificial cancer mass fabrication was the same as that in the method for the high collagen density 3D collagen model, which used a metal plunger to increase the collagen density as mentioned in Method section 2.3.3 of Chapter 2. The artificial cancer mass was placed into a 7ml plastic tube (length: 38 mm; diameter: 18mm) and filled will an uncompressed collagen gel so that the artificial cancer mass was in the center of the uncompressed collagen. The volume of uncompressed collagen was 4ml and the volume of the artificial cancer mass was approximately $0.5cm^3$.
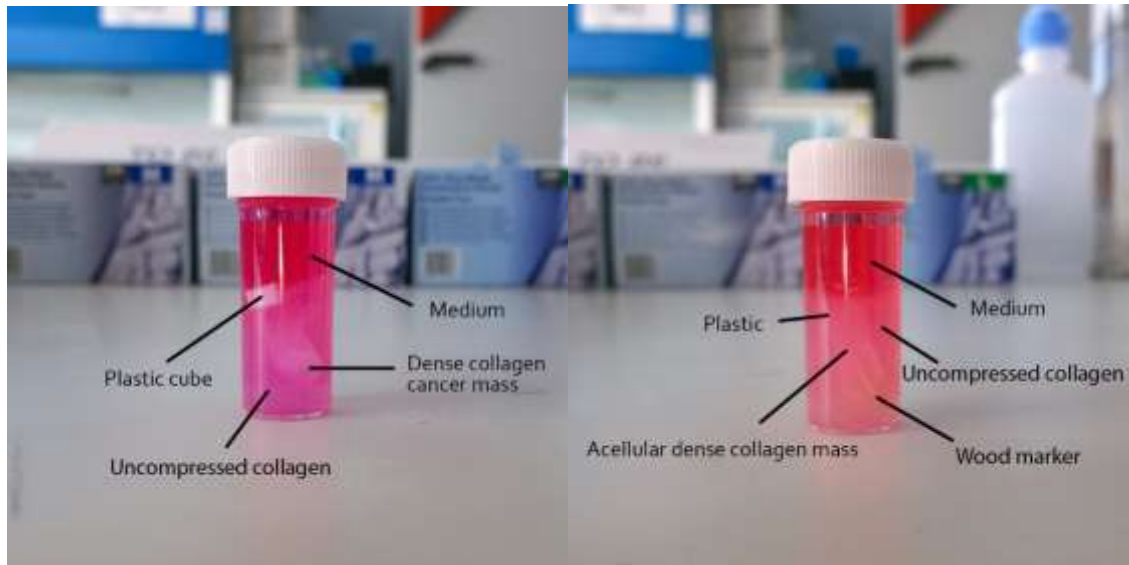
Figure 35: 3D collagen model in plastic tubes

3.6.2. Sample transportation

The samples were manufactured in the Division of Surgery and Interventional Sciences at Royal Free Hospital, and the samples were irradiated at CABI. Before transportation, the samples were incubated at 37°C in a CO_2 incubator. One polystyrene plastic box was used to transport the samples from Royal Free Hospital to CABI. The time of travelling was 40 min and the samples were kept in an oven when transferred to CABI. When imaging, there was a warm water bath set at 32°C.

During the transportation of some imaging sessions, some of the uncompressed collagen was detached from the wall of the plastic universal tube. This means that the collagen gel was sensitive to temperature change and vibration during transportation. It was important to prepare backup samples for this problem. Once this uncompressed collagen was detached from the wall, physical compression could be applied to adjust the gel to the original position because the floating 3D collagen model in a plastic universal tube could affect the positioning of MRI set up.

3.6.3. Imaging schedule

The 3D collagen tumouroid model was produced one day before the MR imaging

session. For a single 3D tumouroid sample, it takes 45min to complete the model construction. The transportation time was 40min. It took the MR imaging session around four to five hours to depend on the sample condition. After MR imaging, the samples were kept in an oven for 20 hours at CABI before transported back to the Royal Free Hospital.

3.6.4. Sample fixation

Chemicals were used to fix the biological sample and to terminate biochemical reactions prior to the microscopy image analysis. Hence, biological samples after fixation could prevent autolysis, putrefaction, and decay, and strengthen the biological samples for better storage [148]. The fixation technique was beneficial to bioimaging, especially the fluorescent microscopy. Two research results pointed out the influence of chemical fixation to MR signals; the T_2 signal strength decreased while the fixation time increased [149,150]. 10% of formaldehyde fixatives were added to all 3D collagen tumouroid models after MR imaging. These samples were left for fixation in room temperature overnight. Then, the samples were washed with PBS for three times and stored in fresh PBS.

3.6.5. Measurement of T_1 and T_2 relaxation time and their curve fitting

The mathematic formula to measure T_1 and T_2 relaxation times is listed in section 3.3.4 of Chapter 3. The data could be processed either by ROI-based approaches or pixel-by-pixel fitting. The ROI-based approach measured the average signal level of such region of interest, while the pixel-by-pixel approach used a histogram of relaxation time map to find how the peaks in T_1 or T_2 corresponding to different constituents of the samples. Firstly, the signal data was normalized to the background level to compare with different TI or TE settings. The pure noise area is the reference for the zero signal level. For more accurate measurement of T_1 relaxation time, the formula is changed to include the loss of efficiency during the inversion recovery process due to the existence of the base noise level. The formula is as follows:

$$M_z = M_0(1 - \ni \times e^{-TI/T1})$$

In the new formula, Mz is the net magnetization in the z-axis, M0 is the net magnetization in the equilibrium state, $\ni$ is the efficiency of the inversion recovery process, TI is the inversion time, and T_1 is the T_1 relaxation time.

For more accurate measurement of T_2 relaxation time, the formula is changed to include an offset (ΔM) during the inversion recovery process due to Rician properties of the MR noise, which state that M_{xy} is not measured as decaying to zero but rather to an offset value. The formula is as follows:

$$M_{xy} = M_0 e^{-TE/T2} + \Delta M$$

In the formula, M_{xy} is the net magnetization in the x-y axis, M_0 is the net magnetization in the equilibrium state, TE is the echo time, T_2 is the T_2 relaxation time, and ΔM is the offset value.

The code to estimate T_1 and T_2 relaxation times was implemented in MATLAB, using the curve-fitting tool (non-linear least squares method and the trust-region algorithm), provided by Caterina Veiga [147].

T_1 and T_2 fitting processes were measured by a region-of-interest approach. Catarina Veiga was responsible for its physical measurement part. For both T_1 and T_2 fitting, the noise of data was processed first. Each TI had an individual acquisition in T_1 mapping. The signal needed to be normalized according to the noise level. The range of TE is acquired in a train of SE sequences in T_2 mapping, so the normalization of signals to noises was impossible. The average noise of a non-signal region is used to correct each data set to reach the valid signal level. Then the relaxation time can be calculated by those signal levels.

3.7. Results:

3.7.1. Relationship between cell density and imaging contrast

3.7.1.1. Study I – acellular collagen mass and 30M cancer mass

The aim of Study I was to investigate how cells contribute to the imaging signal. The MR session images of the three studies were listed before collecting the results. Figure 8 and Figure 9 were the T_1, T_2, and T_2^* sequences of acellular dense collagen masses.
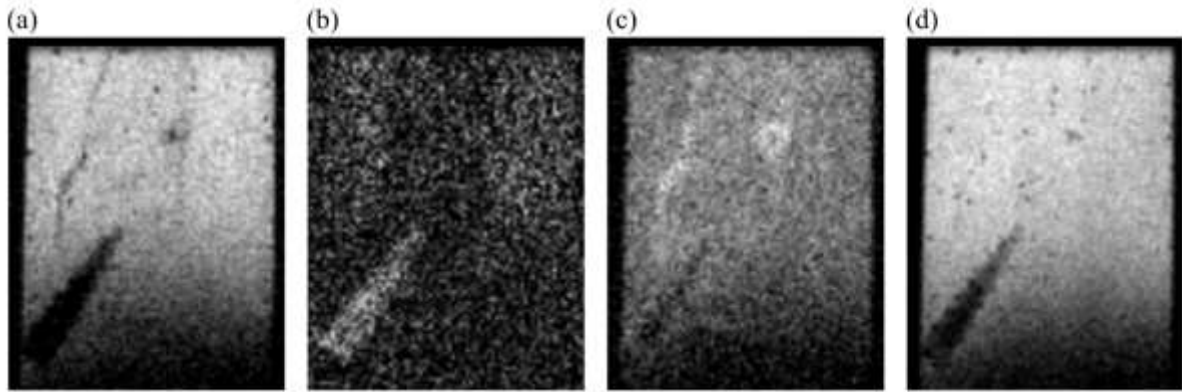
Figure 36: T_1 inversion recovery RARE sequence images of an acellular tumouroid with TI of (a) 500, (b) 1500, (c) 2000, and (d) 2500ms (TE=12ms; TR=10,000ms). The scale was 20mm in the vertical direction. The black arrow at the lower left corner is the wood marker [147]

The inversion recovery RARE was used to image the T_1 sequence images of the acellular dense collagen mass in Figure 35. The imaging parameters were: TE = 12ms, TR = 10000ms and TI were 500, 1500, 2000 and 2500ms in order. The field of the volume was 20 x 20 mm^2 and the imaging resolution was 0.208 x 0.208 x 1 mm^3. The toothpick on the left bottom corner was used as the coordinate indicator for sample alignment.

The T_1 sequence of the acellular dense collagen mass showed image contrast of dense collagen boundary (the shadows in Figure 36 (a) and (c) on the upper left corner), but the inside of the dense collagen mass had no apparent difference compared with the external uncompressed collagen in imaging contrast. The boundary effect was discussed in section 6.1 of Chapter 2. The boundary of the physical compressed collagen mass had a higher collagen density at boundaries. The MR signal showed boundaries of the acellular dense collagen, which indicated that the

higher collagen density had a higher imaging signal. The image with the best quality was that of the lowest TI setting, at 500ms. Due to the low quality of image, I have not done the greyscale threshold analysis of the inversion recovery RARE sequence images of the acellular tumouroid.
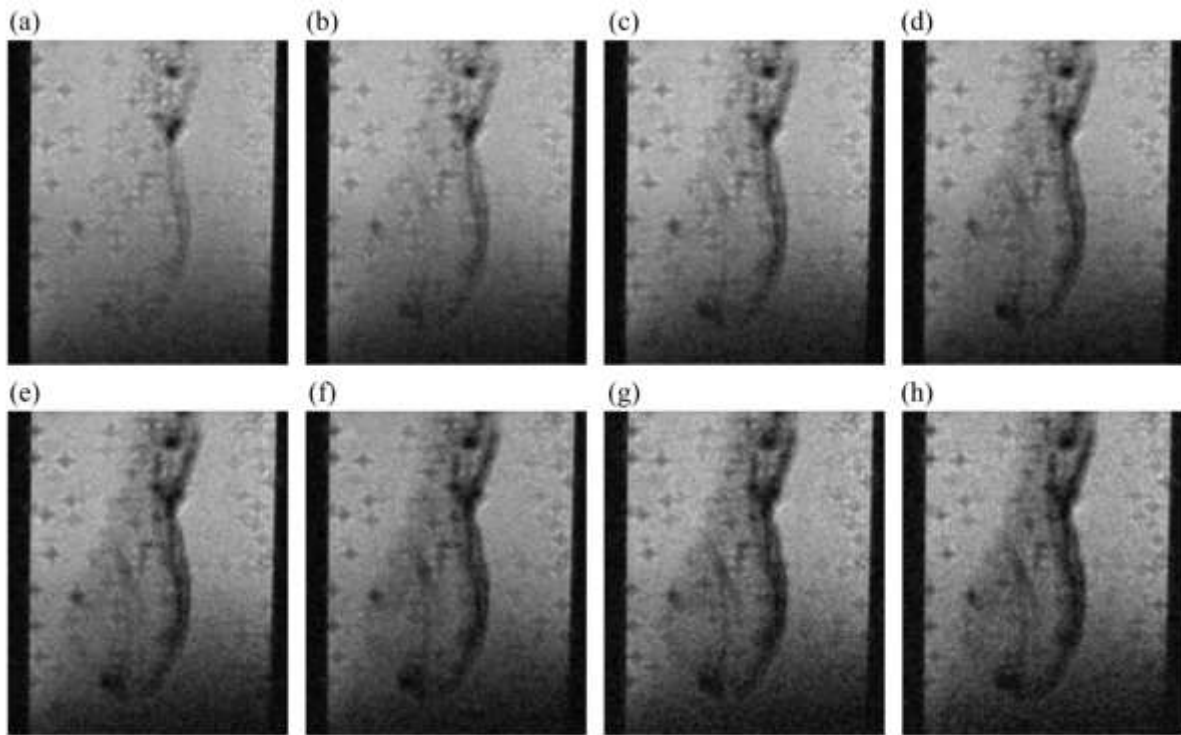
Figure 37: T_2 MSME images of an acellular tumouroid with a TE of (a) 50, (b) 100, (c) 150, (d) 200, (e) 250, (f) 300, (g) 350 and (h) 400ms (TR=6000ms). The scale was 20mm in vertical direction. The object in the center of the image is the tumoroid [147]

The multi-slice multi-echo (MSME) technique was used to image the T_2 sequence images of the acellular dense collagen mass in Figure 37. The imaging parameters were: TE = 25:25:400ms (a total of 16 echoes) and TR = 6000ms. The field of the volume was 20 x 20 x 14 mm^3, and the imaging resolution was 0.125 x 0.125 x 1 mm^3.

The T_2 sequence of the acellular dense collagen mass showed a better imaging contrast of dense collagen boundaries, even including the contrast between the inside area of dense collagen mass and the external uncompressed collagen. As the TE grew

from 50ms to 400ms, the imaging contrast between the inside area of dense collagen mass and external uncompressed collagen increased. The boundary of the physical compressed collagen mass had a higher collagen density at the boundaries. The MR signal showed boundaries of acellular dense collagen, which indicated that the higher collagen density will have a higher imaging signal. The image with the best quality was that of the highest TE setting, at 400ms. The collagen distribution of tumouroids was heterogeneous due to the boundary effect. There was enough imaging contrast to show the difference between the uncompressed collagen and the dense tumouroid at a longer TE.
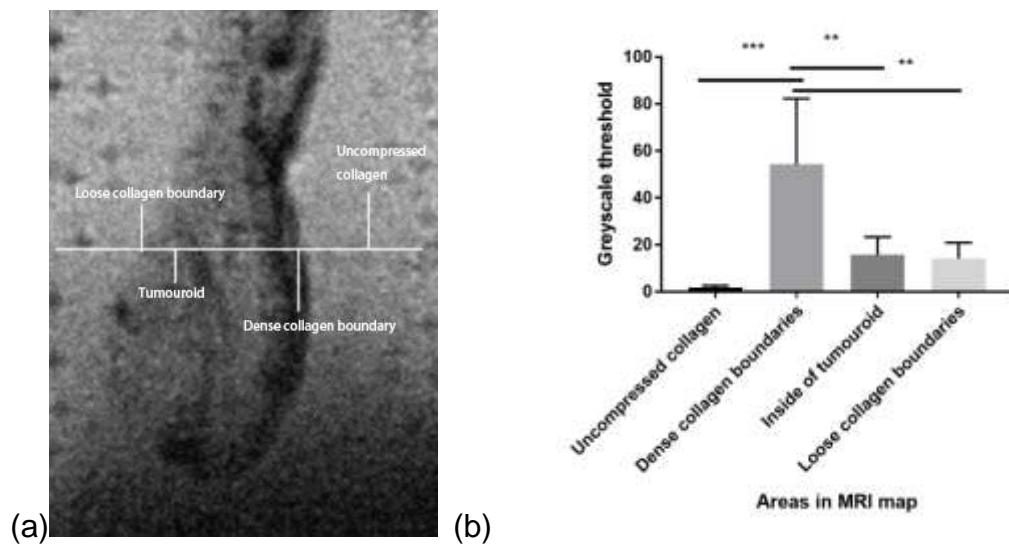
Figure 38: T_2 MSME image MR signal analysis of an acellular tumouroid with 400ms TE (TR=6000ms). The scale was 20mm in the vertical direction. (a) The MRI image and areas in MRI map. (b) The greyscale threshold of different areas in MRI map. The sign ** means $P<0.05$ and *** means $P<0.001$.

The greyscale thresholds of three ROIs of each area were measured. Tukey's multiple comparison test was processed based on the one-way ANOVA analysis. The result showed that great significant greyscale differences existed between uncompressed collagen areas and dense collagen boundaries, between dense collagen boundaries and loose collagen boundaries, and between dense collagen boundaries and inside

areas of tumouroids. However, there was no significant difference between inside areas of tumouroids and loose collagen boundaries. There were signal differences between uncompressed collagen and inside areas of tumouroids, but the differences were not significant.
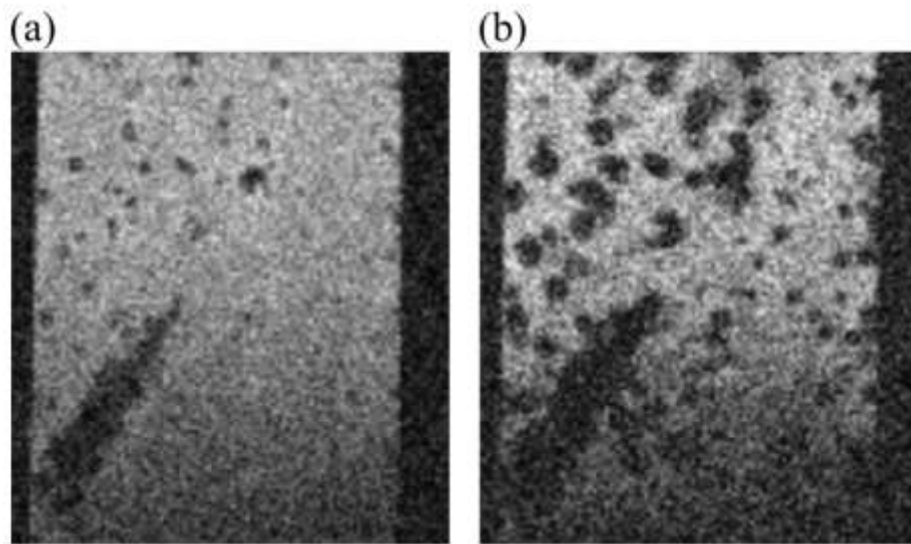
Figure 39: T_2* FLASH sequence images of an acellular tumouroid with (a) TE=5ms, TR=400ms, α=30∘ and (b) TE=40ms, TR=800ms, α=30∘. The scale was 20mm in the vertical direction. The black arrow at the lower left corner is the wood marker [147].

Two FLASH sequences were used to image the T_2* sequence images of the acellular dense collagen mass in Figure 39. The imaging parameters were: TE = 5ms, TR = 400ms, and α=30° for the first sequence and TE = 40ms, TR = 800ms, and α=30° for the second sequence. The field of the volume was 20 x 20 x 14 mm^3 and the imaging resolution was 0.156 x 0.156 x 1 mm^3. The toothpick on the left bottom corner was used as the coordinate indicator for sample alignment.

The T_2 imaging was sensitive to air bubbles. However, air bubbles generated artifacts in imaging for all TE settings. T_2* sequences containing acellular dense collagen masses had a very low image quality due to the severe artifacts of air bubbles, so this type of imaging sequence was not suitable for imaging contrast acquisition. Due to the

low quality of image, I have not done the greyscale threshold analysis of the T_2* FLASH sequences images of an acellular tumouroid.
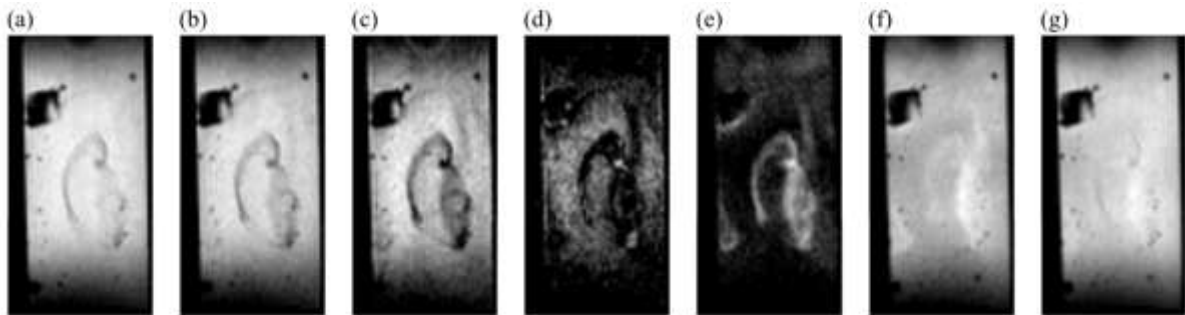
Figure 40: Inversion recovery RARE sequences images of a 30M seeding number (7.5×10^6 cells/ml seeding density) HT29 tumouroid with TI of (a) 205, (b) 500, (c) 1000, (d) 1500, (e) 2000, (f) 4000, and (g) 6000ms (TE=12ms, TR=10,000ms).The scale was 32mm in vertical direction. The black block at the upper left corner is the plastic marker and the object in the center of the image is the tumoroid [147]

The inversion recovery RARE was used to image the T_1 sequence images of 30 million seeding number (7.5×10^6 cells/ml seeding density) tumouroid in Figure 40. The imaging parameters were: TE = 12ms, TR = 10,000ms and TI were 205, 500, 1000, 1500, 2000, 4000 and 6000ms in order. The field of the volume was 32 x 32 mm^2 and the imaging resolution was 0.333 x 0.333 x 1 mm^3. The plastic tube on the top left corner was used as the coordinate indicator for sample alignment.
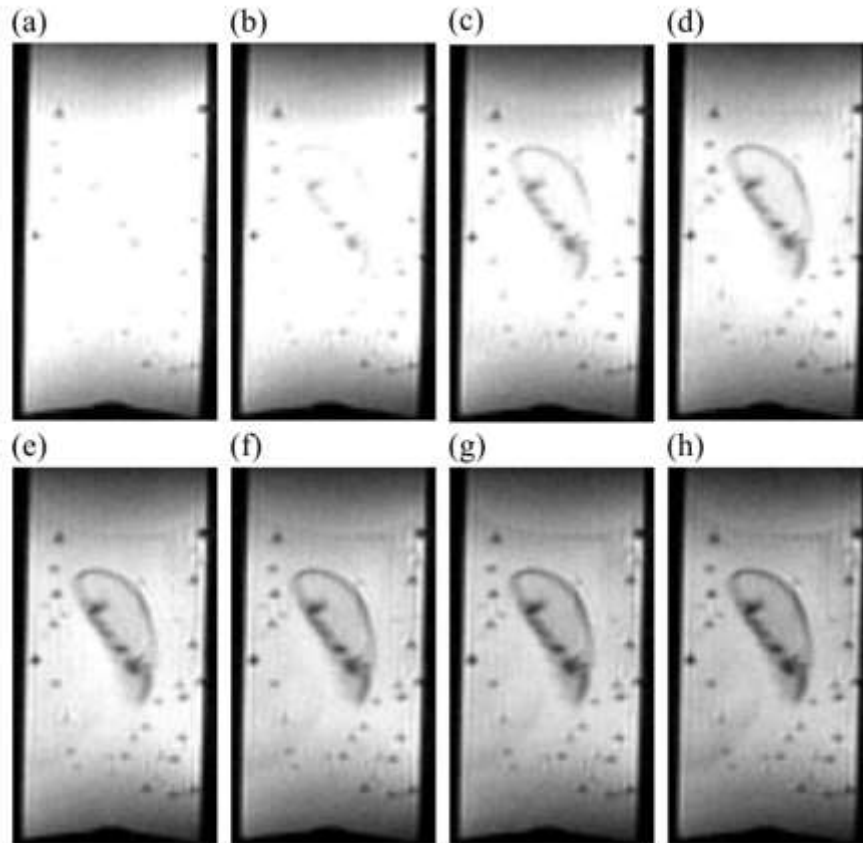
Figure 41: T_2 MSME images of a 30M seeding number (7.5×10^6 cells/ml seeding density) HT29 tumouroid with a TE of (a) 50, (b) 100, (c) 150, (d) 200, (e) 250, (f) 300, (g) 350 and (h) 400ms (TR=6000ms). The scale was 32mm in vertical direction. The object in the center of the image is the tumoroid [147]

The multi-slice multi-echo (MSME) technique was used to image the T_2 sequence images of the 30 million seeding number tumouroid in Figure 41. The imaging parameters were: TE = 25:25:400ms (a total of 16 echoes) and TR = 6000ms. The field of the volume was 32 x 32 x 14 mm^3 and the imaging resolution was 0.333 x 0.333 x 1 mm^3.

(a) (b)
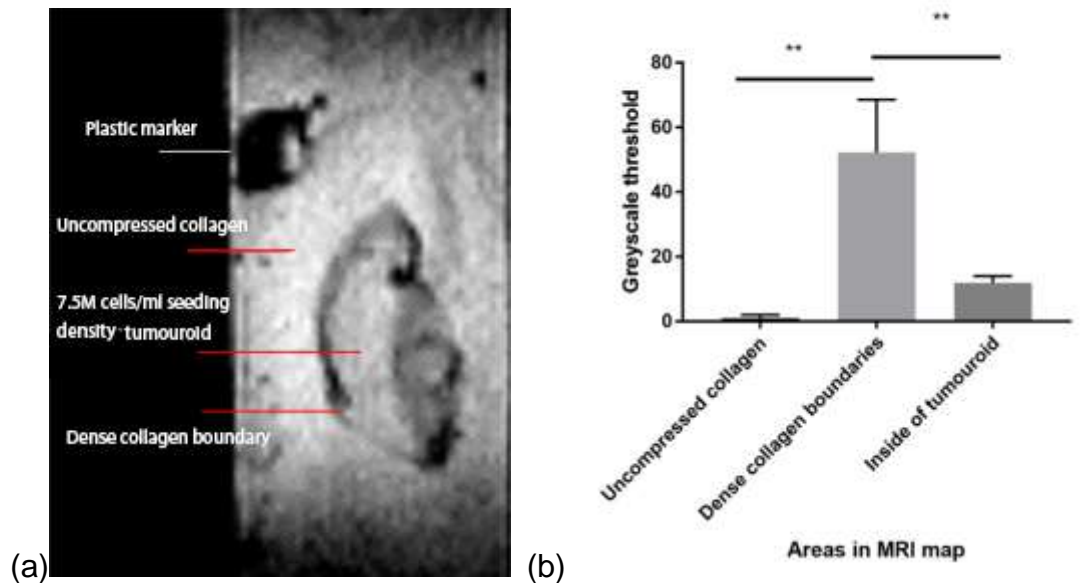
Figure 42: The inversion recovery RARE image MR signal analysis of a 30 million seeding number (7.5×10^6 cells/ml seeding density) HT29 tumouroid with 1500ms TI (TR=15000ms and TE=12ms). The scale was 32mm in the vertical direction (a) The MRI image and areas in MRI map. (b) The greyscale threshold of different areas in MRI map. The sign ** indicates $P < 0.05$.

The dark area represents a high greyscale intensity while light area low intensity. The plastic marker here was not only used as the coordination indicator and calibration tool but also used to reference the darkest part of the image to form a contrast. The greyscale thresholds of three ROIs of each area were measured. Tukey's multiple comparison test was processed based on the one-way ANOVA analysis. The result showed that there were significant greyscale differences between uncompressed collagen area and dense collagen boundaries and between dense collagen boundaries and inside areas of tumouroids. However, there were signal differences between uncompressed collagen areas and inside areas of tumouroids, but the differences were not significant.

(a) (b)
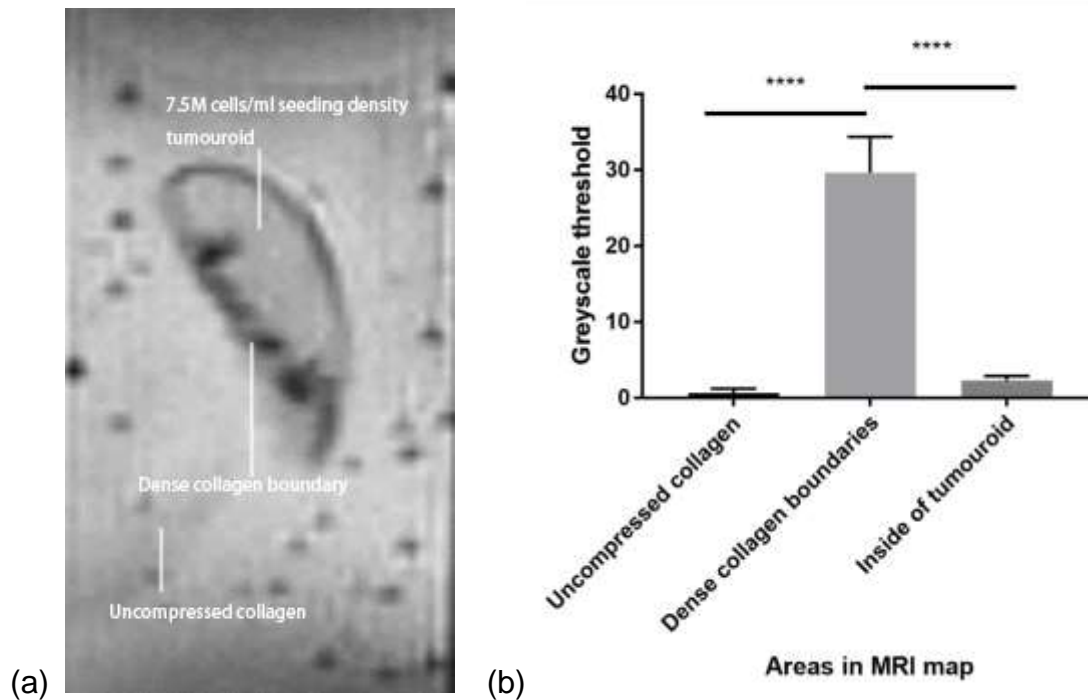
Figure 43: T$_2$ MSME images MR signal analysis of a 30 million seeding number (7.5x10^6 cells/ml seeding density) HT29 tumouroid with 400ms TE (TR=6000ms). The scale was 32mm in the vertical direction (a) The MRI image and areas in MRI map. (b) The greyscale threshold of different areas in MRI map. The sign **** indicates P<0.0001.

The greyscale thresholds of three ROIs of each area were measured. Tukey's multiple comparison test was processed based on the one-way ANOVA analysis. The result showed that there were great significant greyscale differences between uncompressed collagen areas and dense collagen boundaries and between dense collagen boundaries and inside areas of tumouroids. However, there was little signal difference between uncompressed collagen and inside of tumouroid, and the differences were not significant.
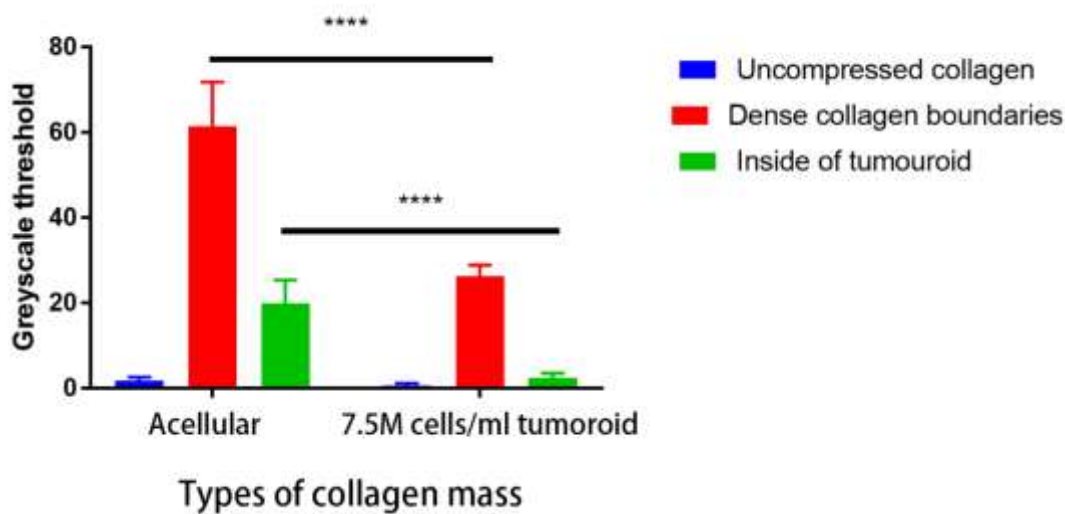
Figure 44: T_2 MSME images MR signal greyscale threshold differences analysis between acellular tumouroids and 30 million seeding number (7.5×10^6 cells/ml seeding density) HT29 tumouroids with 400ms TE (TR=6000ms). The sign **** indicates P<0.0001.

The greyscale thresholds of five ROIs of each area were measured. Sidak's multiple comparison test was processed based on the two-way ANOVA analysis. The result showed that the dense collagen boundaries had a great significant greyscale difference between acellular tumouroids and 7.5×10^6 cells/ml seeding density HT29 tumouroids. The inside areas of tumouroids also had a great significant greyscale difference between acellular tumouroids and 7.5×10^6 cells/ml seeding density HT29 tumouroids. However, there was no significant greyscale difference between acellular tumouroids and 7.5×10^6 cells/ml seeding density HT29 tumouroids for uncompressed collagen.

3.7.1.2. Study II – two acellular collagen mass

The aim of Study II was to investigate the mechanism of contrast generation and to investigate the imaging signal variance of the same samples. Study II used inversion recovery RARE and MSME to obtain MR imaging contrast of two acellular dense

collagen masses.
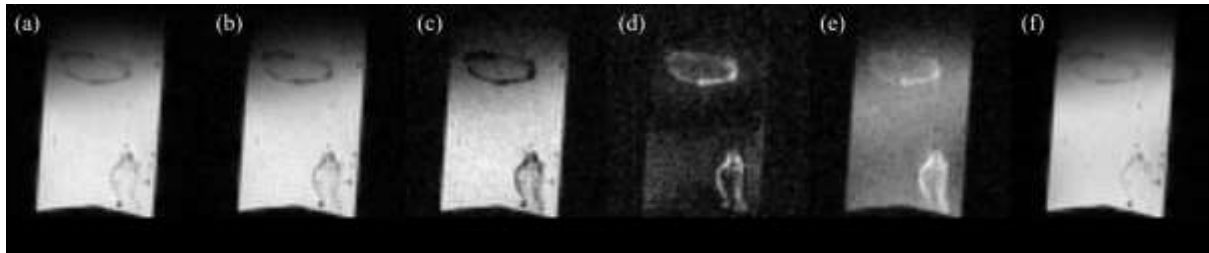
Figure 45: Inversion recovery RARE sequence images of two acellular tumouroids with TI of (a) 250, (b) 500, (c) 1000, and (d) 1500ms, (e) 2000ms, and (f) 8000ms (TE=12ms, TR=10,000ms). The scale was 40mm in vertical direction. The two objects shown in the image are two acellular tumoroids [73]

The inversion recovery RARE was used to image the T_1 sequence images of two acellular dense collagen masses in Figure 44. The imaging parameters were: TE = 12ms, TR = 10000ms and TI are 250, 500, 750, 1000, 1250, 1500, 1750, 2000, 4000, 6000 and 8000ms in order. The field of the volume was 40 x 40 mm^2 and the imaging resolution was 0.42 x 0.42 x 1 mm^3.
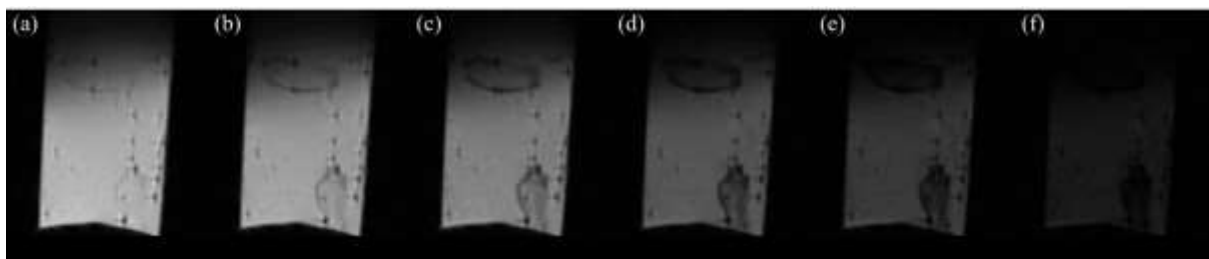
Figure 46: T_2 MSME images of two acellular tumouroids with a TE of (a) 100, (b) 200, (c) 400, (d) 800, (e) 1200, and (f) 2000ms (TR=5000ms). The scale is 40mm in vertical direction. The two objects shown in the image are two acellular tumoroids [73].

The multi-slice multi-echo (MSME) technique was used to image the T_2 sequence images of 30 million seeding number tumouroids in Figure 46. The imaging parameters were: TE = 25:25:3200ms (a total of 128 echoes) and TR = 5000ms. The field of the volume was 40 x 40 x 14 mm^3 and the imaging resolution was 0.25 x 0.25

x 1 mm^3.
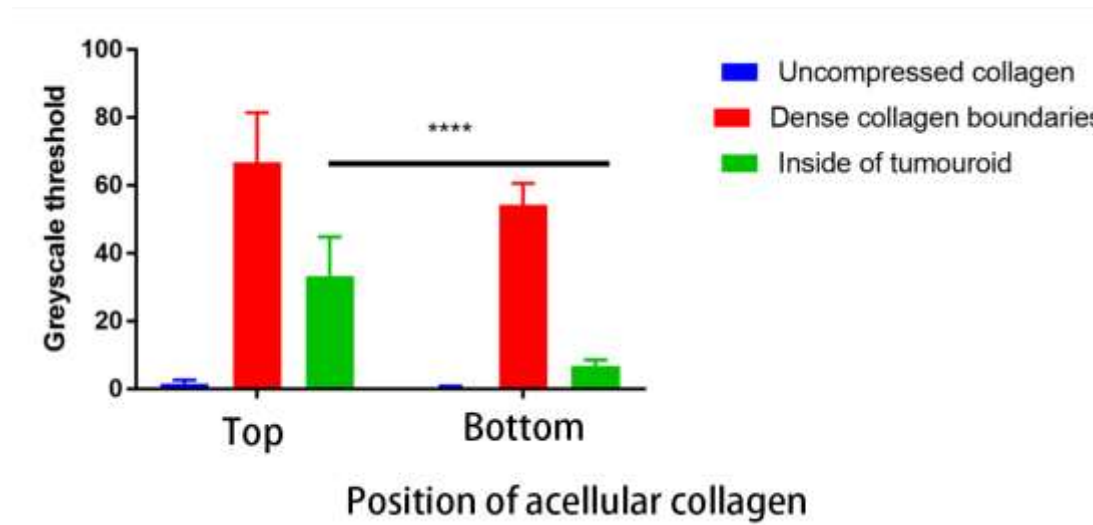
Figure 47: T$_1$ inversion recovery RARE image MR signal greyscale threshold analysis of two acellular tumouroids with 1000ms TI (TE=12ms, TR=10,000ms). The sign **** indicates P<0.0001.

The greyscale thresholds of five ROIs of each area were measured. Sidak's multiple comparison test was processed based on two-way ANOVA analysis. The result shows that the inside areas of tumouroids had a great significant greyscale difference between the acellular tumouroids on the top and that at the bottom. The acellular tumouroids on the top had a higher greyscale threshold than that at the bottom, but the difference was not significant. The uncompressed collagen had the lowest greyscale threshold. I measured the adjacent greyscale thresholds of uncompressed collagen around each tumouroid, so the value was not the same.
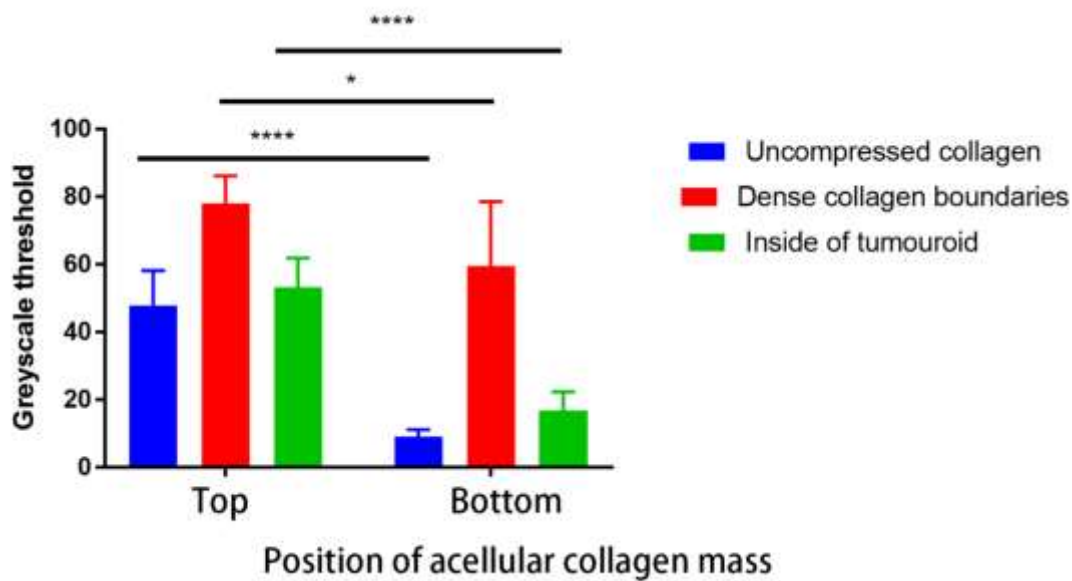
Figure 48: T_2 MSME image MR signal greyscale threshold analysis of two acellular tumouroids with 400ms TE (TR=5000ms). The sign **** indicates P<0.0001 and the sign * indicates P<0.05.

The greyscale thresholds of five ROIs of each area were measured. Sidak's multiple comparison test was processed based on the Two-way ANOVA analysis. The result showed that the uncompressed collagen and inside areas of tumouroids had a great significant greyscale difference between the acellular tumouroid on the top and that at the bottom. The dense collagen boundaries had a minor significant greyscale difference between the acellular tumouroid on the top and that at the bottom. I measured the adjacent greyscale thresholds of the uncompressed collagen around each tumouroid, so the value was not the same. The enormous differences in the uncompressed collagen were due to the threshold paraclade of low-quality images which will be discussed later.

Both T_1 and T_2 measurements show that there were significant signal differences between two acellular tumouroids for dense collagen boundaries and inside areas of tumouroid. This indicated a low reproducibility of tumouroids. The differences between dense collagen boundaries and inside areas of tumouroids indicate the low sample

uniformity of tumouroids.

3.7.1.3. Study III – a) two groups of acellular collagen masses and 40M cancer masses in opposite orders; b) two groups of acellular collagen masses and 20M cancer masses in opposite orders

The aim of Study III was to discriminate the difference between cellular and acellular ACM for 40M high cell seeding number (1×10^7 cells/ml seeding density) and 20M low cell seeding number (5×10^5 cells/ml seeding density). Study III used inversion recovery RARE and MSME to obtain MR imaging contrast of several combinations of acellular dense collagen masses and tumouroids with different cell seeding numbers.
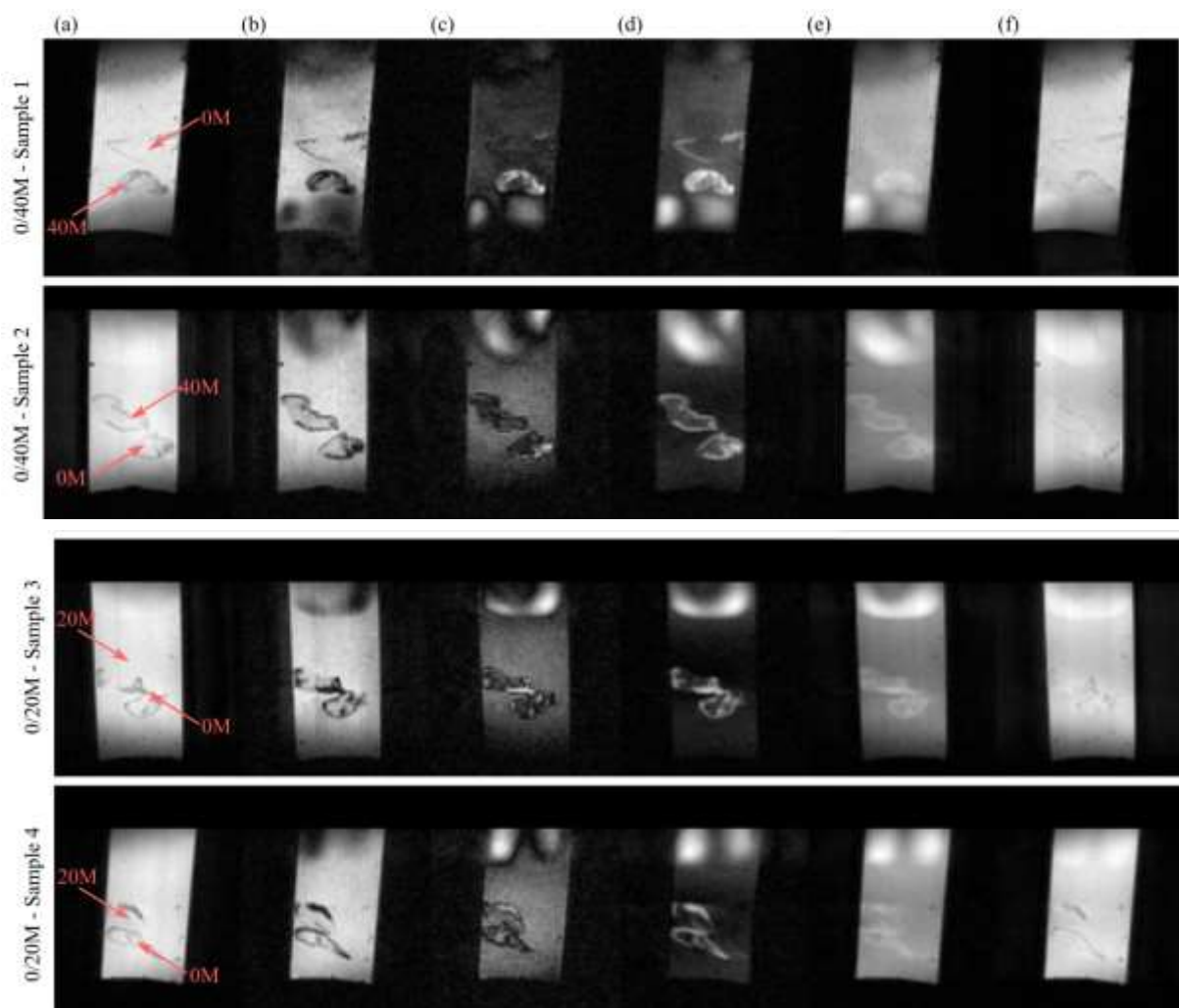
Figure 49: Inversion recovery RARE sequences images of the different samples imaged with TI of (a) 250, (b) 1000, (c) 1500, (d) 2000, (e) 4000, and (f) 8000ms (TE=12ms, TR=10000ms). Sample 1 in the first row included a dense acellular

collagen mass on the top and a 40 million tumouroid at the bottom. Sample 2 in the second row included a 40 million tumouroid on the top and a dense acellular collagen mass at the bottom. Sample 3 and sample 4 in the third and fourth row included a 20 million tumouroid on the top and a dense acellular collagen mass at the bottom. The scale was 40mm in the vertical direction [147]

The inversion recovery RARE was used to image the T_1 sequence images of these four samples in Figure 48. The imaging parameters were: TE = 12ms, TR = 10000ms and TI were 250, 500, 750, 1000, 1250, 1500, 1750, 2000, 4000, 6000 and 8000ms in order. The field of the volume was 40 x 40 mm^2 and the imaging resolution was 0.42 x 0.42 x 1 mm^3.
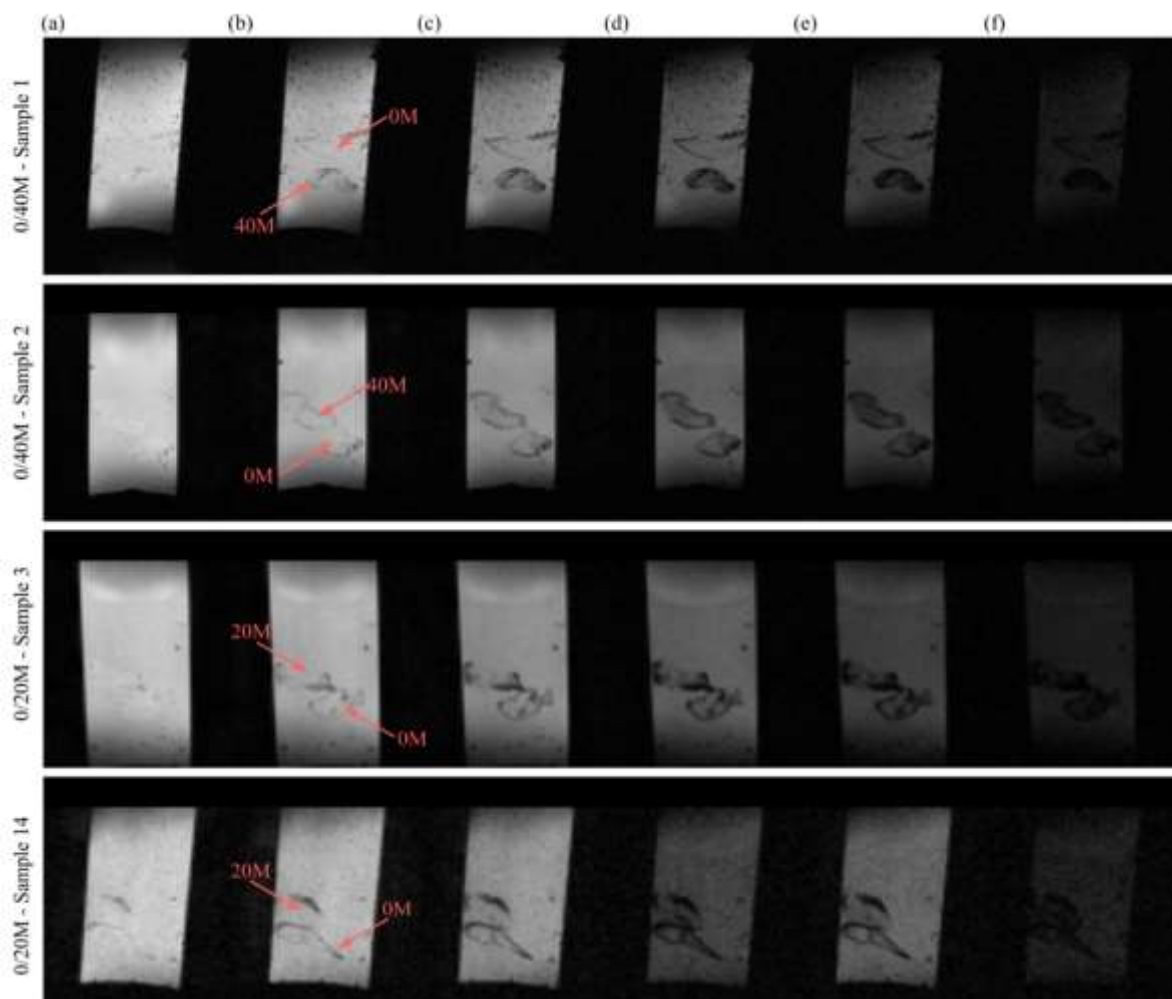
Figure 50: T_2 MSME sequence images of the different samples imaged with TE of (a)

100, (b) 200, (c) 400, (d) 800, (e) 1200, and (f) 2000ms (TR=5000ms). Sample 1 in the first row included a dense acellular collagen mass on the top and a 40 million tumouroid at the bottom. Sample 2 in the second row included a 40 million tumouroid on the top and a dense acellular collagen mass at the bottom. Sample 3 and sample 4 in the third and fourth row included a 20 million tumouroid on the top and a dense acellular collagen mass at the bottom. The scale was 40mm in the vertical direction [147]
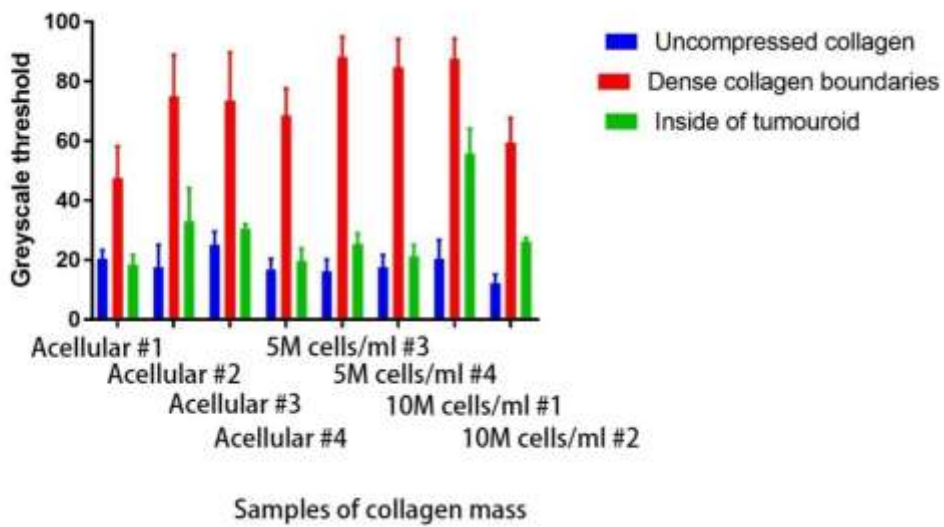
Figure 51: T_1 inversion recovery RARE image MR signal greyscale threshold analysis of all individual tumouroids in Study III with 1000ms TI (TE=12ms, TR=10,000ms)
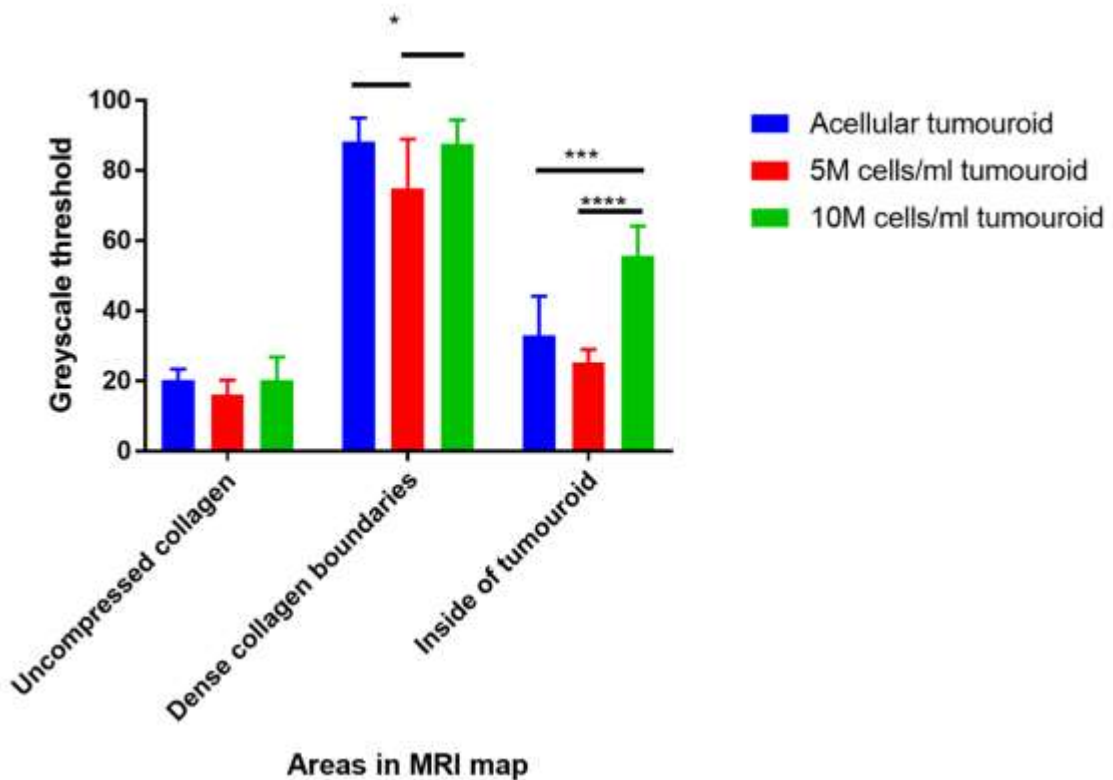
Figure 52: T_1 inversion recovery RARE image MR signal greyscale threshold analysis of tumouroid groups in different areas in the MRI map with 1000ms TI (TE=12ms, TR=10,000ms). The sign * indicates $P<0.05$, the sign *** indicates $P<0.001$, and the sign **** indicates $P<0.0001$.

The greyscale thresholds of five ROIs of each area were measured. Sidak's multiple comparison test was processed based on the two-way ANOVA analysis. For the uncompressed collagen, the acellular, 5M and 10M cells/ml seeding density tumouroids showed no significant difference in greyscale intensity. For dense collagen boundaries, the acellular, 5M and 10M cells/ml seeding density tumouroids had the highest level of greyscale threshold, but it did not increase with the ascending cell seeding densities. This situation was the same for inside areas of tumouroids. The 10M cells/ml seeding density tumouroid had the highest greyscale threshold. There was no evidence that the MR imaging contrast was enhanced with the increasing cell seeding density from the plot.
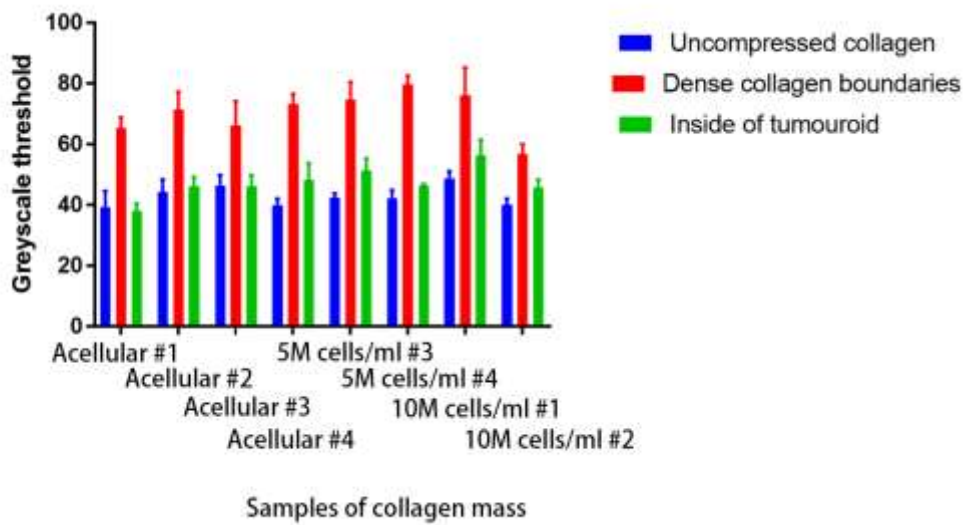
Figure 53: T_2 MSME sequence image MR signal greyscale threshold analysis of all individual tumouroid in Study III with 400ms TE (TR=5000ms)
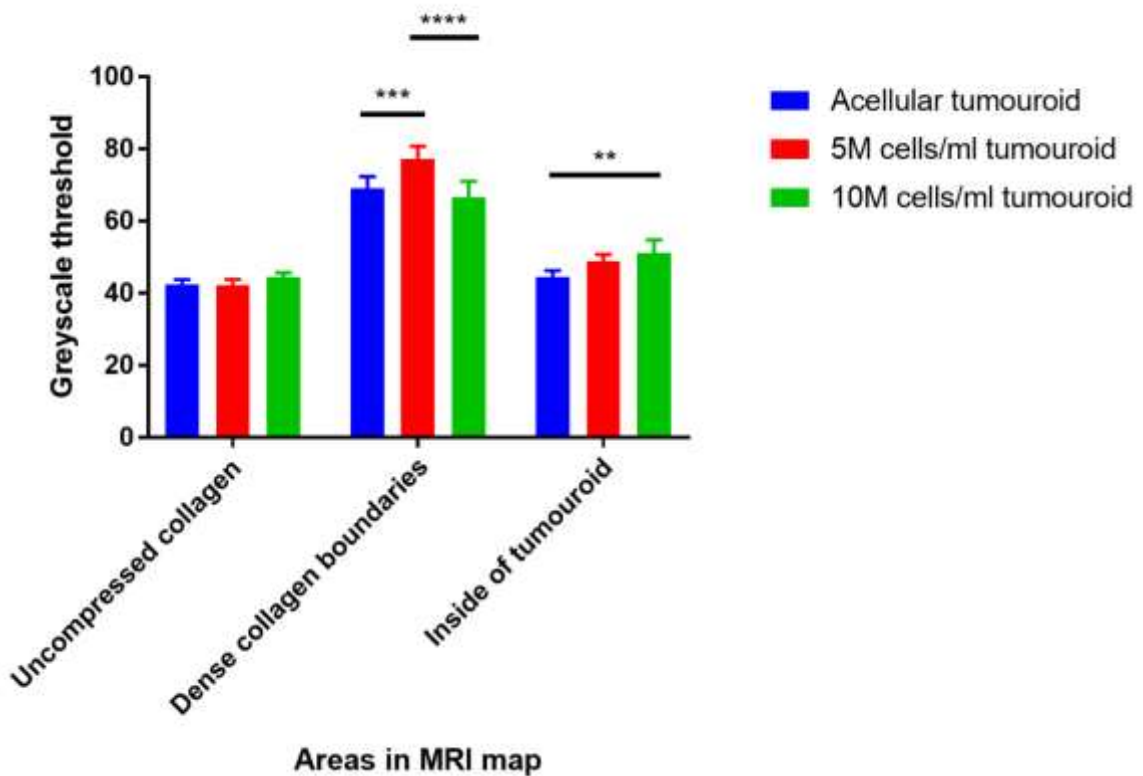
Figure 54: T_2 MSME sequence image MR signal greyscale threshold analysis of tumouroid groups in different areas in the MRI map with 400ms TE (TR=5000ms). The sign ** indicates $P<0.01$, the sign *** indicates $P<0.001$, and the sign **** indicates

P<0.0001.

The greyscale thresholds of five ROIs of each area were measured. Sidak's multiple comparison test was processed based on the two-way ANOVA analysis. For the uncompressed collagen, the acellular, 5M and 10M cells/ml seeding density tumouroids showed no significant differences in greyscale intensity. For dense collagen boundaries, the acellular, 5M and 10M cells/ml seeding density tumouroids had the highest level of greyscale threshold, but it did not increase with ascending cell seeding densities. For inside areas of the tumouroids, the greyscale thresholds of the acellular, 5M and 10M cells/ml seeding density tumouroids increased with ascending cell seeding densities. There was no evidence that the MR imaging contrast was enhanced with the increasing cell seeding density from the plot.
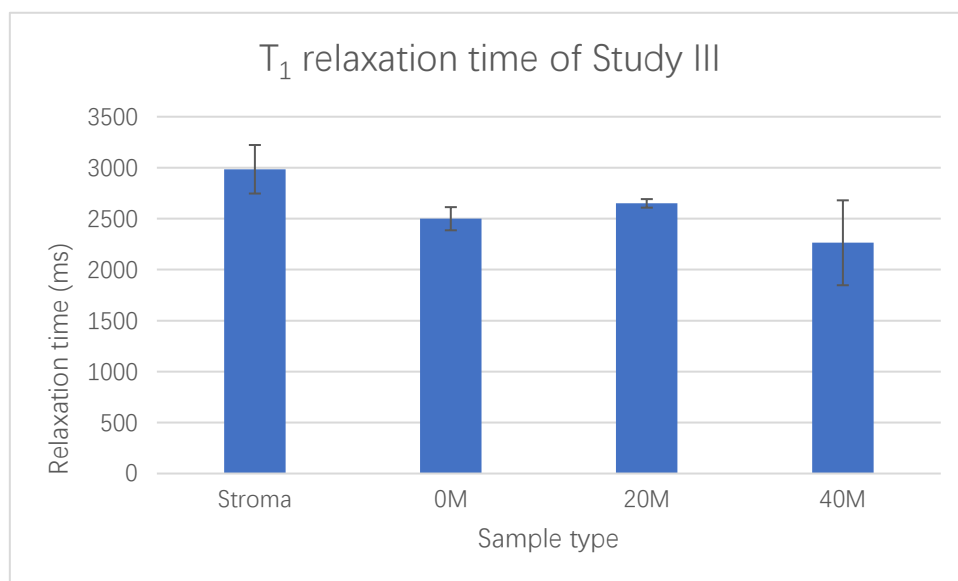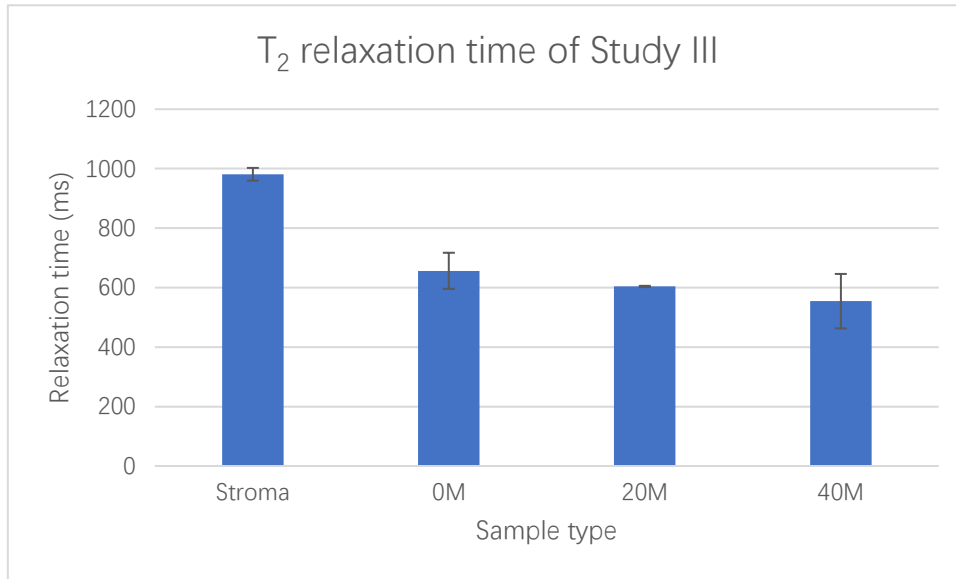
Figure 55: T₁ and T₂ relaxation time of Study III
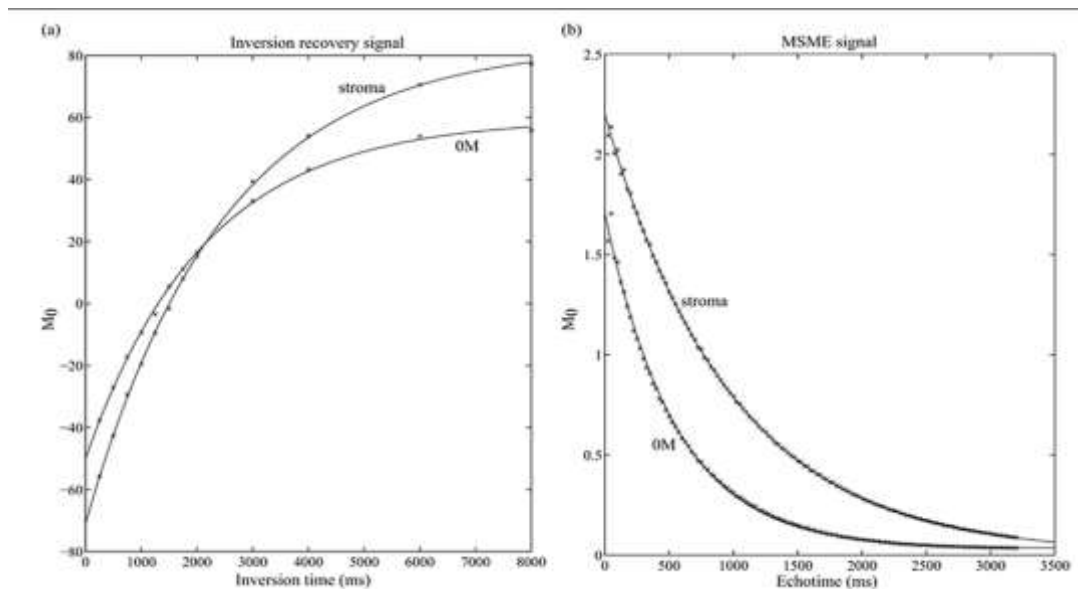
Figure 56: T₁ and T₂ curve fittings of Study II. The fitting was done on the average intensity adopting a region-of-interest approach. M0 in the vertical axis at 0 means the equilibrium state. a) The T1 inversion recovery of stroma and 0M acellular collagen mass with increasing inversion time. b) The T2 MSME signal of stroma and 0M acellular collagen mass with increasing echo time [147].

T₁ and T₂ relaxation times of Study III for the uncompressed collagen as stroma, dense acellular collagen mass, 20 million seeding number HT29 tumouroids and 40 million

seeding number HT29 tumouroids were plotted in Figure 58. The result showed that T_2 fitting of samples was more stable and reproducible than T_1 fitting. The uncompressed collagen as stroma always had different relaxation times from the dense acellular collagen. The problem was that the difference of relaxation times between the dense acellular collagen mass, 20M and 40M tumouroids were uncertain due to the low reproducibility of samples.

3.7.1.4. The collagen density and collagen morphology of the RAFT™ 3D collagen model under different compression time

The collagen morphology of the RAFT™ 3D collagen model after compression can directly compare with the collagen density measurement result. As shown in Figure 57, as the compression time increased, the collagen morphology became denser. These defined the physical properties of the RAFT™ 3D collagen model after compression.
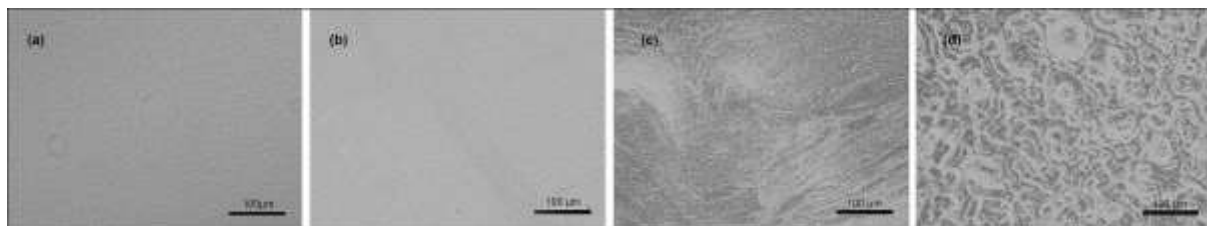
Figure 57: The collagen morphology of the RAFT 3D collagen system compression samples for MR scans. From (a) to (d), it represents zero compression, 10min, 15min, and 25min compression followed the production instructions. The scale was 100 microns.
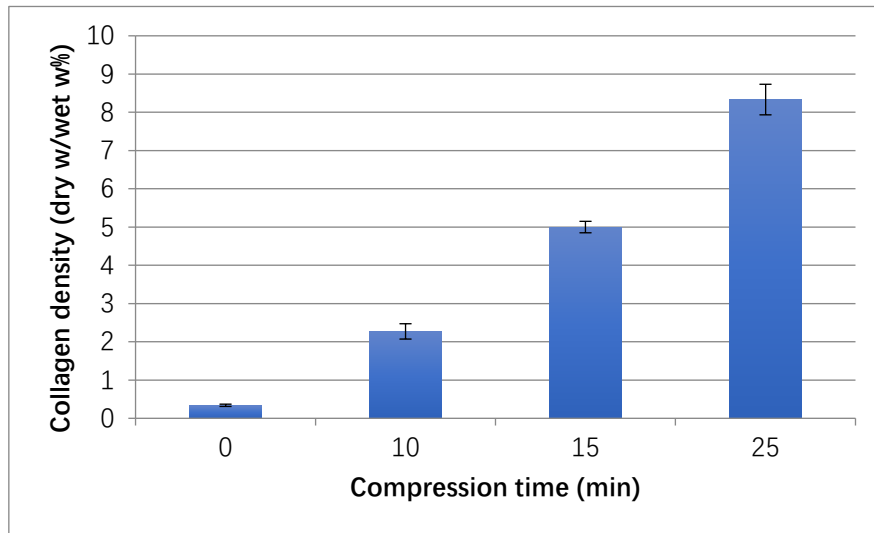
Figure 58: The collagen density data in the RAFT 3D collagen system compression samples for MR scans. The collagen volume was 4ml and the compression time ranges from 0, 10min, 15min to 25min (N=3).

As the compression time increased from 0min, 10min, 15min to 25min in the RAFT 3D collagen system, the morphology of collagen changes. There was no visible collagen fiber in the uncompressed collagen (collagen density 0.34%). At least 10min of compression were required for visible collagen fibers to appear (collagen density 2.2%). To see areas of aligned collagen fibers and the binding area of different collagen fiber orientation as long as 15min of compression was required (collagen density 5%). When the compression time reached 25min, the collagen fibers were in dense granule form (collagen density 8.3%). The collagen densities were measured by the freeze dryer and the method has been described in section 3.7 of Chapter 2.

3.7.1.5. Study IV – four acellular collagen masses at different compression levels

The aim of Study IV is to explore the relationship between the collagen density and MR imaging contrast. The physical properties of those collagen masses have been defined in section 1.4. Figure 59 shows the MR image of the RAFT 3D collagen tumouroid model. The right-hand side color scale from blue to yellow shows the relaxation time from 1000ms to 4000ms. The T_1 color map shows the distribution and strength of the three collagen slices with different collagen densities.
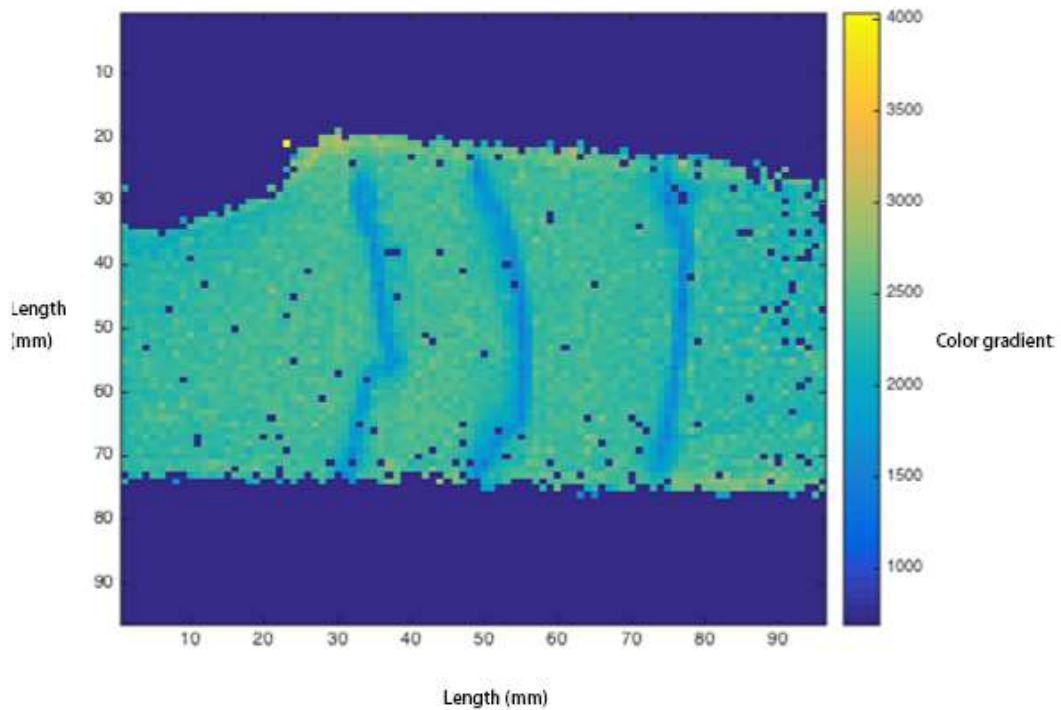
Figure 59: Example image, T_1 color gradient map of RAFT^{TM} 3D collagen slices with TE =11.7ms, TR = 16000ms and TI from 200ms to 15000ms / 0min uncompressed collagen gel, a 10min, 15min and 25min compressed dense collagen (vary in collagen densities).
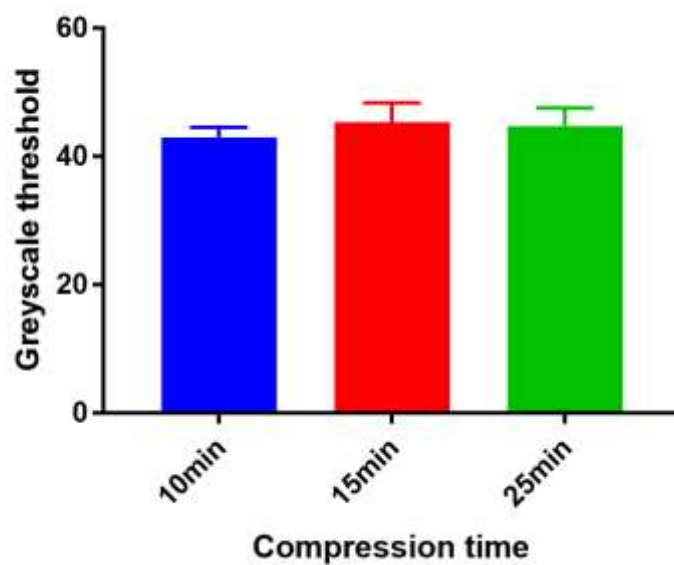
Figure 60: The greyscale threshold of RAFT^{TM} 3D collagen slices with TE =11.7ms,

TR = 16000ms and TI from 200ms to 15000ms after 10min, 15min and 25min compressed (vary in collagen densities)

The color maps of RAFT^{TM} 3D collagen slices were converted with TE =11.7ms, TR = 16000ms and TI from 200ms to 15000ms after 10min, 15min and 25min compressed (vary in collagen densities) into greyscale and then measure the greyscale threshold. The greyscale thresholds of five ROIs of each area were measured. Tukey's multiple comparison test was processed based on the one-way ANOVA analysis. The result showed that there was no significant greyscale difference between dense collagen slices with different compressed time (hence collagen densities).

3.8. Discussion

3.8.1. The relationship between cell density and imaging contrast

3.8.1.1. Study I – acellular collagen mass and 30M cancer mass

The aim of Study I was to evaluate the possibility of generating imaging contrast of tumouroid under MR acquisitions and to investigate how do cells contribute to the imaging signal. Firstly, the acellular dense collagen model was used as a reference to imaging calibration, and then the setup and tuning were optimized for the next experiments. The 30 million seeding number (7.5×10^6 cells/ml seeding density) tumouroid was then imaged to compare the image contrast with the acellular dense collagen mass.

In conclusion, Study I confirmed that the imaging contrast of tumouroids or dense collagen masses could be achieved under MR imaging sessions. The source of imaging contrast was collagen, cells, and air bubbles. How the source of contrast contributes to the final contrast is still unclear at present. The hypothesis is that a higher collagen density will contribute to the contrast because visual inspection of the tumouroids immediately after production shows regions of stronger white coloring and dense areas at the boundaries edge.

As shown in Figure 44 which was the T_2 MSME images MR signal greyscale threshold differences analysis between acellular tumouroids and 30 million seeding number (7.5×10^6 cells/ml seeding density) HT29 tumouroids with 400ms TE (TR=6000ms). At the boundaries of tumouroids or dense collagen masses, there was more imaging contrast than uncompressed collagen, and inside areas of

tumouroids. The inside areas of tumouroids had a higher imaging contrast than uncompressed collagen, but it was not significant and subject to imaging parameter settings. There was no evidence to show that MR imaging contrast increased with cell seeding densities from the plot.

3.8.1.2. Study II – two acellular collagen masses

The aim of Study II was to investigate the mechanism of contrast generation and to investigate the imaging signal variance of the same samples. The acellular dense collagen masses were similar to Study I but the morphology was different. This means the reproducibility of compressed collagen mass was low, especially in morphology. The collagen density was not measured for every individual collagen mass, but the low reproducibility can affect the collagen density. The results of Study II shown in Figure 47 and Figure 48 further confirmed that compressed collagen was one of the sources of imaging contrast. Dense boundaries have stronger signals. Both T_1 and T_2 measurements showed that significant signal differences existed between two acellular tumouroids for dense collagen boundaries, and inside areas of tumouroids. This indicated a lower reproducibility of tumouroids. The differences between dense collagen boundaries and inside areas of tumouroids indicated low sample uniformity of tumouroids.

3.8.1.3. Study III – a) two groups of acellular collagen masses and 40M cancer masses in opposite orders; b) two groups of acellular collagen masses and 20M cancer masses in opposite orders

The aim of Study III was to discriminate the difference between cellular and acellular ACM for 40M higher cell seeding number (1×10^7 cells/ml seeding density) and 20M lower cell seeding number (5×10^6 cells/ml cell seeding density). There were three different cell seeding numbers: (1) 0, (2) 20 million and (3) 40 million cells. The tumouroids with different cell seeding numbers were assembled into 4 plastic bijous. Sample 1 included a dense acellular collagen mass on the top and a 40 million tumouroid at the bottom. Sample 2 included a 40 million tumouroid on the top and a dense acellular collagen mass at the bottom. Sample 3 and sample 4 included a 20 million tumouroid on the top and a dense acellular collagen mass at the bottom.

Visual inspections of these samples observed that the morphology of the tumouroids with three different cell seeding numbers was similar as shown in Figure 49 and Figure 50. This indicates that there is low reproducibility and low uniformity within tumouroids. Each tumouroid had one portion of bulk tumouroid cut by a surgery blade. The morphology changed and each portion of tumouroids had different uniformity.

As shown in Figure 51 which is the T_1 inversion recovery RARE image MR signal greyscale threshold analysis of tumouroid groups at different areas in MRI map with 1000ms TI (TE=12ms, TR=10000ms), and shown in Figure 52 which is the T_2 MSME sequence image MR signal greyscale threshold analysis of tumouroid groups in different areas in the MRI map with 400ms TE (TR=5000ms). There was no evidence that MR imaging contrast increased with cell seeding densities from the plot.

3.8.2. T_1 and T_2 imaging sequences optimization towards better MRI signal
3.8.2.1. T_1 and T_2 imaging sequences parameter optimization

As shown in all T_1 and T_2 experiment images, in T_1 inversion recovery RARE image sequences, with increasing TI, the signal contrast increased and then convented to the opposite phase. For T_1 inversion recovery RARE image sequence, the images had the best signal contrast with 1000ms TI, 12ms TE, and 10000ms TR. In T_2 MSME

image sequences, with increasing TE, the imaging contrast of inside areas of tumouroids was visible, but the overall image luminosity decreased. For T_2 MSME image sequences, the images had the best signal contrast with 400ms TE and 5000-6000ms TR parameter settings.

3.8.2.2. T_1 and T_2 imaging sequence imaging quality

As shown in all T_1 and T_2 experiments images, T_2 MSME image sequences had better imaging contrast than T_1 inversion recovery RARE image sequences. The T_1 inversion recovery RARE image sequences needed an optimized TI to get the suitable imaging contrast and avoid the opposite phase. However, T_2 MSME image sequences could find the best imaging luminosity and contrast with increasing TE. As shown in all T_1 and T_2 experiment plots, for example, in Figure 51 shows the T_1 inversion recovery RARE image MR signal greyscale threshold analysis of tumouroid groups in different areas in the MRI map, and Figure 54 shows the T_2 MSME sequence image MR signal greyscale threshold analysis of tumouroid groups in different areas in the MRI map. T_2 MSME imaging sequences could get more signal contrasts for inside areas of tumouroids, and then get more accurate data than that of T_1 inversion recovery RARE imaging sequences. The T_2 MSME imaging sequences also had shorter error bar than T_1 inversion recovery RARE imaging sequences.

3.8.3. How MR image quality affects the measurement and analysis

Caterina Veiga was responsible for the data acquisition [147], and the files had been processed by MATLAB or other relevant software. The resolution of MRI equipment was not high because this was a mini MRI equipment optimized for mouse brain animal experiments. Furthermore, the imaging quality and imaging resolution of files were not at a high standard. For example, in Figure 59, the T_1 color map of RAFT[TM] 3D collagen slices of Study IV, the pixels were visible, and the resolution was low. The collagen slices were composed of several pixels so that the region-of-interest approach could have a higher inaccuracy. Again, the low resolution and low image quality of images

will cause histogram paraclade. This also affected the accuracy of the region-of-interest approach. These aspects could be improved by changing the imaging acquisition settings to the highest level, which requires a longer data acquisition time and changing of imaging equipment.

3.8.4. The design criteria of Study I, II and III

The design criteria of the model should be biocompatible and can show the imaging contrast of tumouroid. The tumouroid samples were imaged alive and the 3D metabolism results in Chapter 2 could prove that the metabolism rate was high for MR imaging if imaging on the second day of sample manufacture (Day 1). The tumouroids were imageable in T_1 and T_2 sequences and were able to get imaging contrast. The T_2^* sequence imaging was not suitable due to the severe air bubble artifacts. There were signal level differences between the uncompressed collagen as stroma and dense acellular collagen masses. The signal level difference between dense acellular collagen masses and tumouroids with different seeding numbers is uncertain. There was clear imaging contrast at boundaries of dense acellular collagen masses or tumouroids. There was no evidence that MR imaging contrast increased with cell seeding densities from the plots. The low reproducibility and uniformity were the main problem of the current model. To achieve the design criteria, the reason of low reproducibility and uniformity will be discussed.

3.8.5. Reasons for low reproducibility and uniformity

3.8.5.1. Sample neutralization

As mentioned in Chapter 2, the collagen neutralization is pH sensitive. The neutralization process is a drop-wise method. The pH error is difficult to control, and the neutralization requires a rapid process.

3.8.5.2. Metal mould compression

The 3D collagen mass is compressed by the metal mould using the traditional 3D

collagen model protocol. The results of collagen density measurements have been described in Chapter 2. The problem is that the collagen density can be controlled by changing the compression time, but the sample uniformity can't be improved. Visual inspection can find dense boundaries due to physical compression. The morphology of collagen masses is irregular. The experiment protocol itself needs to be optimized for better reproducibility and uniformity, for example, the RAFT^{TM} 3D collagen system has a better reproducibility control and sample uniformity than traditional 3D collagen model manufacture as mentioned in section 2.3 Experiment Method of Chapter 2.

3.8.6. Improving the reproducibility and uniformity of the experiment

The pH level control of the collagen neutralization process requires a real-time pH monitor to give precise quantitative control. The mould compression process has added lots of uncontrollable factors to sample manufacturing. The 3D collagen model can be produced by a more standard method, such as through the well-established RAFT^{TM} system. A 3D model has homogeneous uniformity and controllable cell, and collagen density is the ideal design criteria.

3.8.7. Relationship between the collagen density and imaging contrast

To validate the relationship between the collagen density and imaging contrast of MR, the RAFT^{TM} 3D collagen model is used to obtain different collagen densities with better uniformity and reproducible controls. Figure 55 shows the morphology of the RAFT 3D collagen system after zero compression and 10min, 15min and 25min of compression following the production instruction. Figure 56 shows the measurements of the collagen density of the RAFT 3D collagen system after zero compression and 10min, 15min and 25min of compression. The uncompressed collagen gel, and collagens after 10min, 15min and 25min of compression had collagen densities of 0.3%, 2.1%, 5%, and 8.2%, respectively. Figure 56 shows the T_1 color map of 3D collagens with these four different collagen densities. There is no visible difference in the signal levels between slices of 10min, 15min and 25min of compression. It indicates that the

uncompressed collagen has differences in imaging contrast from compressed collagens, but there is no significant imaging contrast between slices of different collagen densities as shown in Figure 58. This conclusion is in accordance with the results in Study I and II.

3.9. Conclusion:

The aim of this chapter was to design an MR-imageable 3D *in vitro* tumour model, investigating what properties of the tumour model contributed to image signal, and setting up an MR environment that can image tumouroid samples. The 3D collagen tumouroid model is biocompatible and can show imaging contrast under MRI session. T_1 inversion recovery RARE and T_2 MSME MR imaging sequences were processed to imaging four individual sample groups. Due to the low reproducibility of collagen compression, pH neutralization accuracy, and low sample uniformity after collagen compression, the inside areas of tumouroids had significantly lower signal intensity than that of the dense collagen boundaries (the boundary effect has been discussed in Chapter 2). T_2 MSME MR imaging sequences can get more signal contrast for inside areas of tumouroids and then get more accurate data than T_1 Inversion recovery RARE imaging sequences. The T_2 MSME imaging sequences also had a shorter error bar than T_1 inversion recovery RARE imaging sequences. The images of four studies suggest that 1000ms TI, 12ms TE, and 10000ms TR for T_1 inversion recovery RARE to get best signal contrast and suggest 400ms TE and 5000-6000ms TR for T_2 MSME MR imaging sequences to get the best signal contrast. The methodology of the RAFT[TM] 3D collagen cancer model system can increase the sample reproducibility and uniformity. Such a model was used in Study IV to test the relationship between the MR signal contrast and different collagen densities. The morphology has confirmed the sample uniformity and the technique is reproducible. The result suggests that there is no significant relation between the collagen density and MR imaging contrast. This conclusion is the same as the analysis of Study II, which tested the MRI sessions of two acellular tumouroids. According to the results of Study I and Study III, the

uncompressed collagen, the acellular tumouroid, 5M and 10M cells/ml seeding density tumouroids show no significant difference in greyscale intensity. For dense collagen boundaries, the acellular, 5M and 10M cells/ml seeding density tumouroids had the highest level of greyscale threshold, but it did not increase with ascending cell seeding densities. For inside areas of tumouroids, the acellular, 5M and 10M cells/ml seeding density tumouroids had higher greyscale thresholds than uncompressed collagen areas, but the differences were not significant. There is no evidence that MR imaging contrast increased with cell seeding densities from the plot. There is no significant greyscale difference between acellular tumouroids and 7.5M cells/ml seeding density HT29 tumouroids for uncompressed collagen in Study I. Therefore, currently, the plots suggest that the imaging contrast does not significantly depend on the cell seeding density or collagen density. However, the pixel resolution and imaging quality affect the accuracy of the region-of-interest approach. These aspects could be improved by changing the imaging acquisition settings to the highest level which requires a longer data acquisition time and changing the imaging equipment. Further work requires an MRI session of reproducible and high uniformity RAFT[TM] 3D collagen models with different cell seeding densities to explore the relationship between the cell seeding density and MRI contrast.

Chapter 4:
The implementation of 3D collagen cancer models for photon and proton irradiation

1. Aim

The aim of this chapter is to further explore the implementation 3D collagen cancer models to meet the photon and proton irradiation experiment requirements, and then to use immunofluorescent staining methods to measure biological behavioral changes after irradiation by confocal and fluorescent microscopy. Originally, the focus of my experiments was on proton irradiation. However, due to imaging resource limitation, most of experiments I could take were photon irradiation. I used p53-binding protein 1 (53BP1) antibodies to stain the DNA double strand break, carbonic anhydrase IX (CAIX) antibodies to stain the hypoxia and Caspase-3 antibodies to stain the cell apoptosis. The cancer cell behavior after irradiation is quantified by analyzing the stained fluorescent images.

2. Radiobiology theories

   2.1. How irradiation affects the cell behavior

When an electron passes through a cell, it releases energy to excite the cell or ionize it. The atoms accept donated energy and become unstable. For example, for water content in human body, there will be reactive oxygen species (ROS) formation after irradiation. Such reactive oxygen species are chemically reactive and exist for several microseconds. They react with surrounded molecules and result in breakage of chemical bonds or oxidation of the affected molecules. The most important damage to cells are DNA single or double strand breakage. DNA single strand breakage can be repaired by natural mechanism, but double strand breakage will lead to mismatch in repair and result in induction of point mutations, chromosome aberrations or cell death [151].

2.2. Cell apoptosis

The cells that undergo apoptosis will show nuclear chromatin compaction and segregation with the formation of sharply delineated, granular masses that are marginated against the nuclear at the earliest stage. The cell morphology will change and the cytoplasm will condense. At a later stage, the apoptotic bodies will bud from the cell and then digested by nearby cells via phagocytosis [152,153,154]. Cell apoptosis is one form of cell death. There are other forms such as necrosis, cornification, and autophagy [155].

2.3. Hypoxia

Hypoxia is one feature of the tumour microenvironment. For example, about 50% of locally advanced breast cancer cases exhibit hypoxic or anoxic tissue areas within the tumour mass. This is because abnormalities of the structure and function of tumour microvessels result in perfusion related to acute hypoxia which is transient and affect cells up to the vessel wall. Or, increased diffusion distance between a blood vessel and the growing tumour mass competing for oxygen results in diffusion-related chronic hypoxia, which affects cells greater than 70 to 100μm from the nearest capillary [156]. Hypoxia influences the outcome of treatment with radiotherapy and chemotherapy, because hypoxic tumour cells are resistant to radiation [157]. In this thesis, I tried to find the relationship between tumour hypoxia and the cell apoptosis after irradiation.

2.4. DNA double strand break

Ionizing radiation will damage DNA and finally lead to types of changes in the genome, including gene mutations. The ionizing damage is non-specific, so it will damage or kill both tumour and normal cells. Many repair and signaling proteins are recruited to the site of double-strand breaks to produce ionizing radiation-induced foci after ionization radiation [158, 159, 160]. The number of ionizing radiation-induced foci per nucleus reaches a peak value around 0.5-1h after irradiation. Those ionizing radiation-induced foci have a half-life of 0.5-1h during the first few hours [161]. The samples are fixed at

0.5h after radiation because this time point has the highest detectable foci numbers. The other fixation time can check the cell recovery response after irradiation.

3. Method

3.1. 2D cancer model experiment details

All the 2D HT29 colorectal cancer cell lines were cultured on 48-well tissue culture plates. The initial cell seeding number was 50,000 cells per well. The cells were seeded on the plate and kept 1d for them to adhere, proliferate, and show biological properties before photon irradiation.

3.2. 3D cancer model experiment details

3.2.1. Photon tumouroid irradiation (RFH)

The 3D HT29 colorectal cancer cell model was developed on a FluoroDish culture dish. The cell seeding number was 10 million cells per tumouroid, and the volume of the collagen mixture gel was 2ml before gelation. The cell-collagen mixture filled the glass bottom of the FluoroDish culture dish and the thickness of the 3D sample was suitable for fluorescent imaging.

3.2.2. Proton tumouroid irradiation (Sicily)

3.2.2.1. Proton irradiation facility

The 3D HT29 colorectal cancer cell line model was cultured in a slide flask. The cell seeding number was 1 million cells per tumouroid. The cancer cells were uniformly distributed in a 4ml 3D collagen matrix before gelation. The proton-irradiated 3D cancer model was fixed and seeded into an agar mould prior to vibratome sample processing (whose method has been described in Chapter 2). The final sample slice after vibratome processing had a thickness of 200µm. The sample slice was stained with fluorescent markers and then imaged by confocal microscope in the Department of Bioscience at UCL.

3.2.2.2. Dose profile
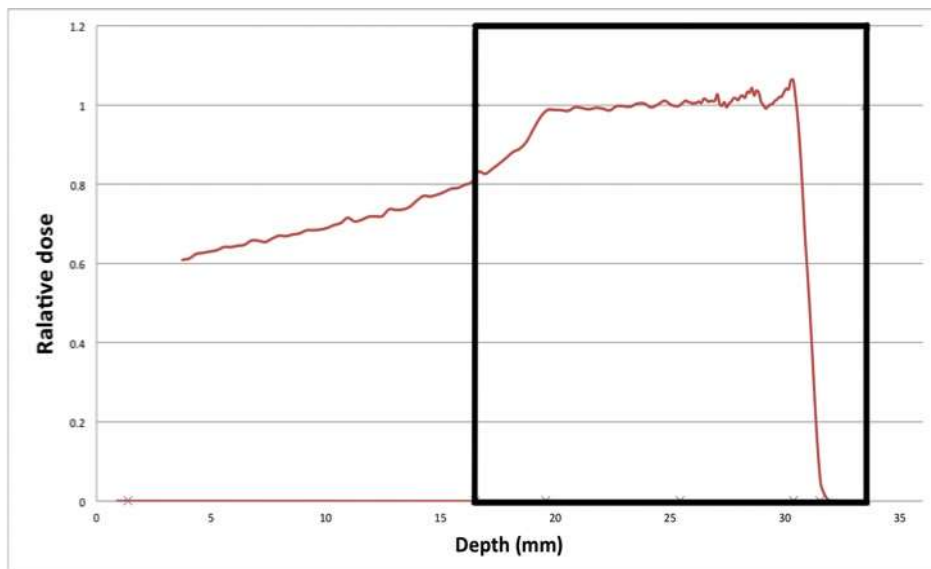
Figure 61: Dose profile of 1Gy proton irradiation. The black box area is the actual sample area covered by proton irradiation.

The black box in Figure 60 showed the actual area and dose profile of the slide flask. There was a flat spread-out Bragg peak (SOBP) of the 1Gy proton irradiation dose in the actual sample area, which was the slide flask. For photon irradiation, the relative dose increased to the peak at around 10mm and then gradually decreased. The SOBP of proton irradiation could maintain flat high relative dose between 20mm and 50mm depending on the parameter setting. The pristine proton irradiation gradually increased the relative dose as soon as the beam penetrated the sample and reached the peak value at a deeper depth than photon beams. Both SOBP and pristine proton irradiation had sharp slopes of relative dose decreasing after them reached the maximal relative dose. Their differences were shown in Figure 62 below:
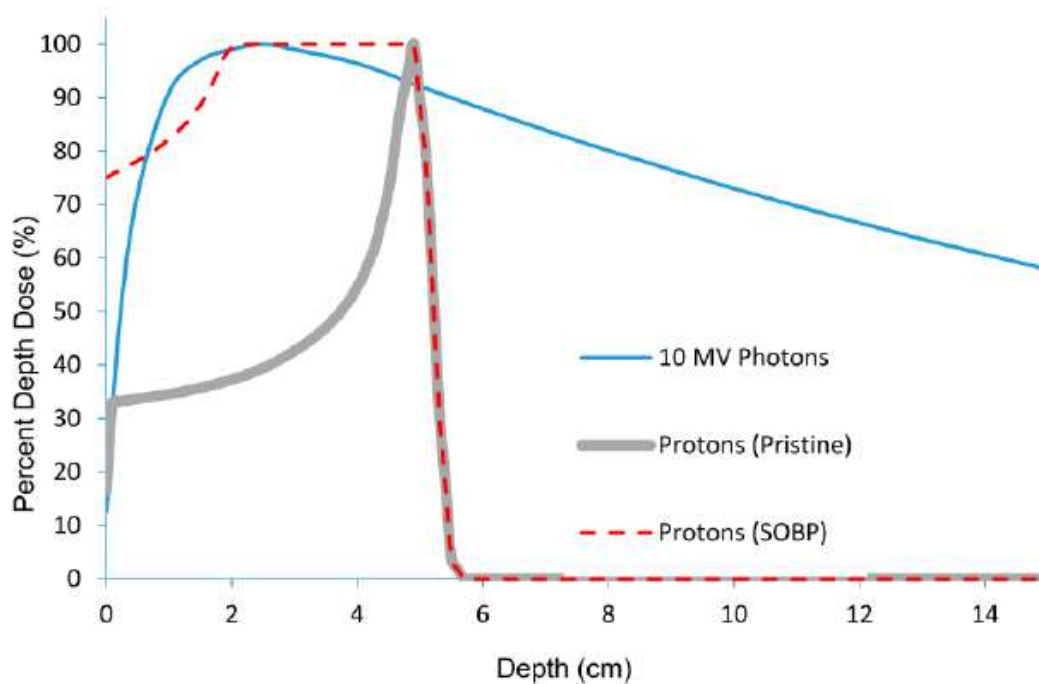
Figure 62: Relative irradiation dose of electron, photon and proton irradiations versus depth [162].

3.3. 3D spheroid model for photon irradiation experiment

The HT29 colorectal cancer cell spheroids were cultured on 96-well ultra-low attachment plate for 9 days with an initial seeding number of 5,000 cells per well. The spheroids were transferred to a 3D collagen matrix for 1d and then had linac photon irradiation. The irradiation dose was 0Gy, 4Gy, 8Gy and 12Gy. There were 30 wells per dose group, and each well contained at least one spheroid. However, the size and growth condition of spheroids were different. There were 15 individual spheroids on track with single round spheroid body and vary in sizes per dose group. Figure 83 shows the mean volume of spheroid cultured from Day 0 to Day 12 after irradiation and Figure 84 displays the mean diameter of spheroids. The images were taken every 2 days. Photoshop was used to measure the diameter of spheroid on the image and calculate the real diameter when correlated with the scale bar. The method to calculate the mean diameter was as follows: first, the longest diameter was measured, then another perpendicular line was drawn to measure the diameter at the center point of the longest diameter and finally the mean diameter was calculated as the average of

the longest diameter and perpendicular diameter. The mean volume (y-axis) was in logarithmic scale. The mean volume of spheroids was calculated using the following formula:

$$V = 4/3 * \pi * (\text{mean radius})^3$$

3.4. Sample storage and transportation of proton experiment (Sicily)

All the liquids including the DMEM medium, MEM medium, PBS, and collagen were stored in travel luggage by airway. The HT29 colorectal cancer cells were cultured in a T75 cm^2 tissue culture flask and are fully filled with DMEM medium before travelling. As soon as I arrived at the proton irradiation center in Sicily, all the liquid was stored in fridge. The medium in cancer cells in tissue culture flasks were refreshed and then the tissue culture flasks were stored in 37°C and placed in a CO$_2$ incubator.

3.5. Sample processing after proton experiment (Sicily)

As mentioned in section 3.2.1 of Chapter 3, the confocal microscopy requires a sample thickness of 100-200µm to get the optimal results. The method to process the sample after irradiation was mentioned in method section 3.8.3 of Chapter 3.
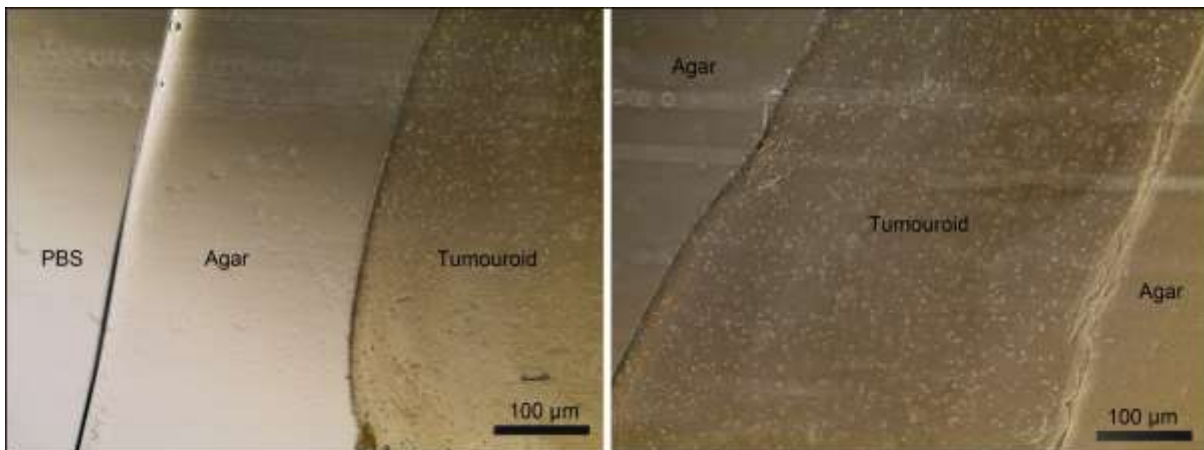
Figure 63: Thin slice of tumouroid in an agar mould after the vibratome process under a light microscope

3.6. Immunofluorescence staining
3.6.1. Antibody staining theory

Immunofluorescence staining consisted of a labeled antibody with a fluorescent marker, ensuring that the labeled antibody reacted with their specific antigen to observe the reaction products under the fluorescent microscope. There were direct and indirect antibody staining. The labeled antibody was the primary antibody, and the fluorescent dye was the secondary antibody. The primary antibody targeted the specific antigen of cells. Direct antibody staining could show fluorescence because the primary antibody also worked as a fluorophore. If not, there was another secondary antibody to bind on the receptor of primary antibody. The secondary antibody worked as a fluorophore, so that the specific antigen could also have the fluorescent signal with an uncertain wavelength of the secondary antibody.

3.6.2. Method to quantify fluorescence of antibody images

The dimension of position of interest was standardized (small area around 400μm and large area around 1000-2000μm), then the fluorescent light dots were counted or/and the average fluorescent background signal was detected.

3.6.3. Antibody staining protocol

(1) The samples were fixed first before antibody staining. 10% formaldehyde was used to fix the sample overnight and then washed using PBS solutions for 3 times. The samples were incubated with a 0.1% v/v Triton-X in a PBS solution to increase antibody surface penetration.

(2) The solution was decanted, and the samples were washed using PBS solutions for 3 times, and each time took 5min. Then the samples were incubated with a 1% BSA PBST solution (PBS solution + 0.1% Tween-20) for 30min to block unspecific binding of antibodies.

(3) The primary antibody was diluted in the 1% BSA PBST solution according to the guidance concentration. The 1% BSA PBST solution was removed from the samples and the primary antibody diluted using the 1% BSA PBST was added to the samples to stain overnight at room temperature.

(4) On the second day, the solution was decanted, and the samples were washed using PBS solutions for 3 times, and each time took 5min. The secondary antibody was diluted in a 1% BSA PBST solution according to the guidance concentration. The 1% BSA PBST solution was removed from the samples and the secondary antibody diluted using the 1% BSA PBST was added to the samples to stain for 2h at room temperature. The secondary antibody was light sensitive, so this step was processed in dark environment.

(5) The solution was decanted, and the samples were washed by PBS solutions for 3 times, and each time took 5min. The samples were incubated using DAPI solutions for 5min at room temperature to stain the nuclei. After that, the solution was decanted, and the samples were washed by PBS solutions for 3 times, and each time took 5min.

(6) Finally, the samples were stored in PBS solutions, keep in dark environment and ready for fluorescent imaging.

3.7. Statistics strategy

The data presented throughout were displayed as the mean value plus standard deviation and was calculated using GraphPad Prism 6 software (GraphPad, San Diego, CA). One-way or two-way ANOVA analysis was processed by such software to get the statistical significance. The p-value was less than 0.05 considering the statistical significance.

4. Results

4.1. The apoptosis expression of cancer cells with increasing radiation dose (result of the 2D culture experiment)

4.1.1. Sample set 1: Preliminary result of fluorescent staining of apoptosis marker Caspase-3 on the 2D culture HT29 colorectal cancer cell line after photon irradiation

Dose: 0Gy, 1Gy and 5Gy

Fixation time: 0.5h and 24h after irradiation

Repeats: 3
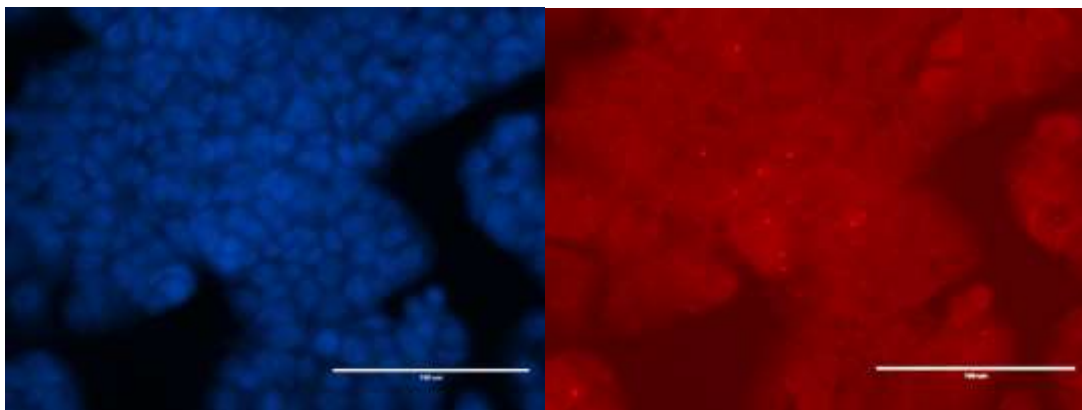
Figure 64: Sample images of 5Gy photon irradiated 2D HT29 colorectal cancer cell line culture and fixed at 8 hours after irradiation. The nuclei was stained by the DAPI (left) solution and the apoptosis marker was Caspase-3 (right). The magnification power was 20x. The length of scale bar was 100μm.

In Figure 64, the fluorescent intensity of Caspase-3 in the right image diffused the nuclei area, which was stained in blue in the left image. There was strong back fluorescence as well. The light dots in the right image was the actual fluorescent staining of Caspase-3 foci which located inside of the nuclei. There was no further analysis of this sample set. The aim of this experiment was to confirm the fluorescent signal expression, and then guided the experimental design. The experiment showed that there was strong back fluorescent staining. In the next step, a bleach may be used in the sample washing process and a specific buffer should be added in the dilutant to prevent non-specific binding.

4.1.2. Sample set 2: Fluorescent staining of apoptosis marker Caspase-3 on the 2D culture HT29 colorectal cancer cell line after photon irradiation
Dose: 0Gy, 1Gy and 5Gy
Fixation time: 0.5h, 2h, 24h and 48h after irradiation
Repeats: 3

151

Figure 65: Apoptosis fluorescence expression levels of 2D HT29 colorectal cells for 0Gy, 1Gy and 5Gy photon irradiation. Samples were fixed at 0.5h, 4h, 8h and 24h after irradiation of Sample set 2.
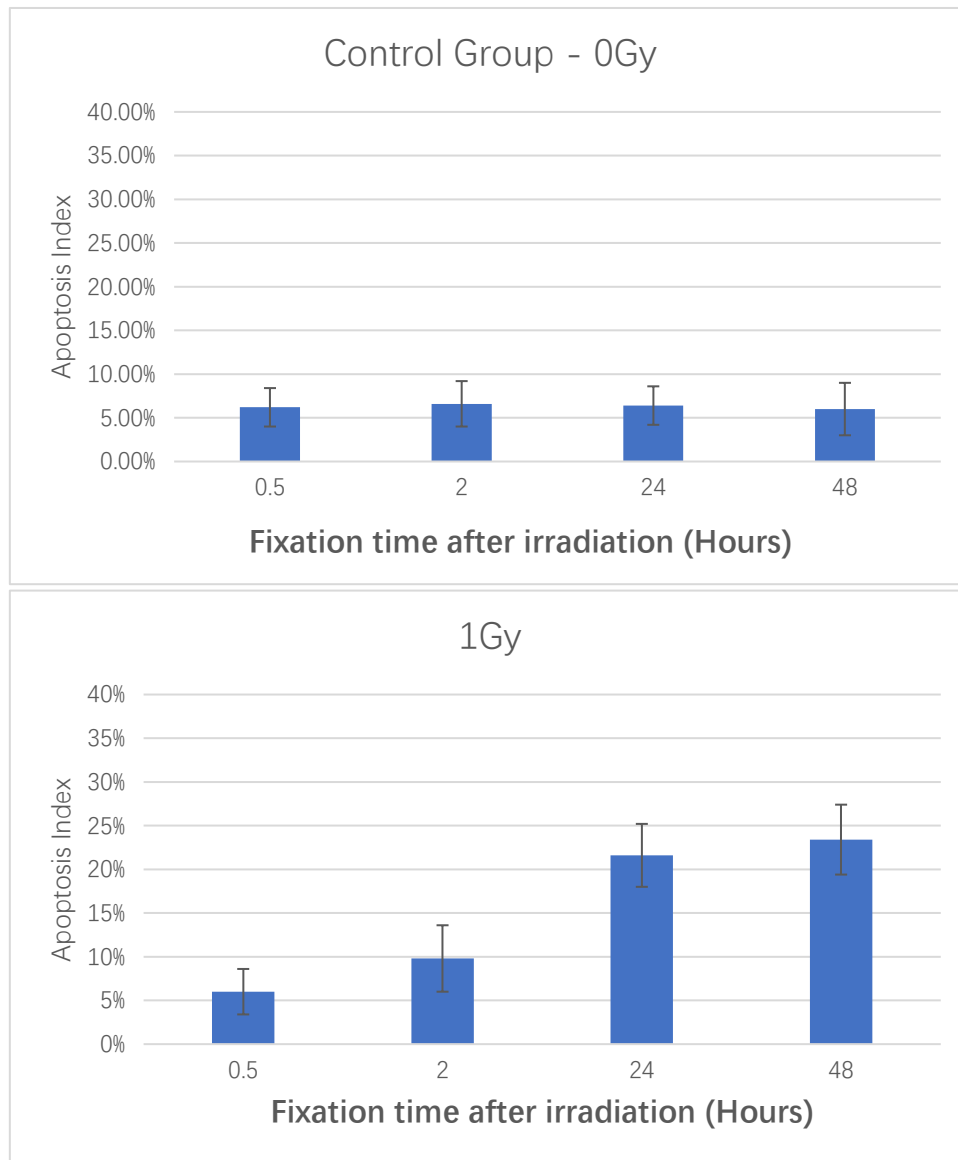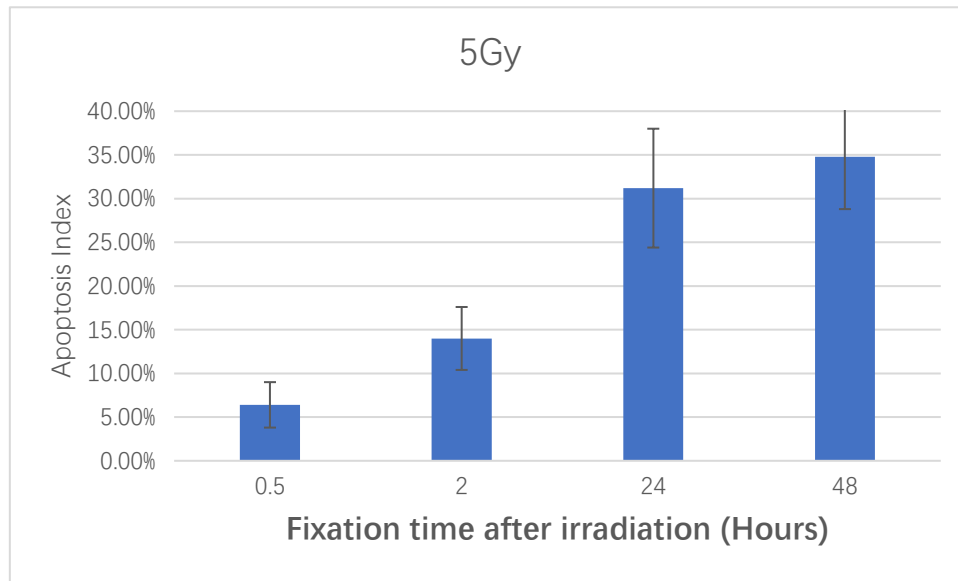
Figure 66: Apoptosis index expression levels of 2D HT29 colorectal cells for 0Gy, 1Gy and 5Gy photon irradiation. Samples were fixed at 0.5h, 4h, 8h and 24h after irradiation of Sample set 2

The apoptosis expression level indicates the fluorescence intensity of apoptosis fluorescent marker in the nuclei area, after being stained by the DAPI solution. Figure 65 shows the apoptosis expression of 2D HT29 colorectal cells in the second sample group. The control group has a fluorescent intensity of 25 to 29 for all samples were fixed at different time points. For 1Gy irradiation dose and 5Gy irradiation dose, the samples fixed at 2h after irradiation had the highest fluorescent intensity, meaning high apoptosis levels. The fluorescent intensity decreased in samples fixed at 24h after irradiation and further decreased to the lowest fluorescent intensity at 48h after irradiation. This indicates that cells will recover after irradiation, and the highest apoptosis occur at 2h among different time points. The fluorescent intensity of the 5Gy-irradiated sample was higher than the 1Gy-irradiated sample. This indicates that dose after higher irradiation will induce more cell apoptosis. Figure 66 shows the apoptosis index of the same sample. The apoptosis index is defined as the percentage of a number of cells undergo apoptosis. Therefore, the total number of cells undergo apoptosis needs to be measured and the number is divided by the measured total number of cells.

4.1.3. Sample set 3: Fluorescent staining of apoptosis marker Caspase-3 on the 2D culture HT29 colorectal cancer cell line after photon irradiation

Dose: 0Gy, 1Gy and 5Gy

Fixation time: 0.5h, 4h, 8h and 24h after irradiation

Repeats: 3
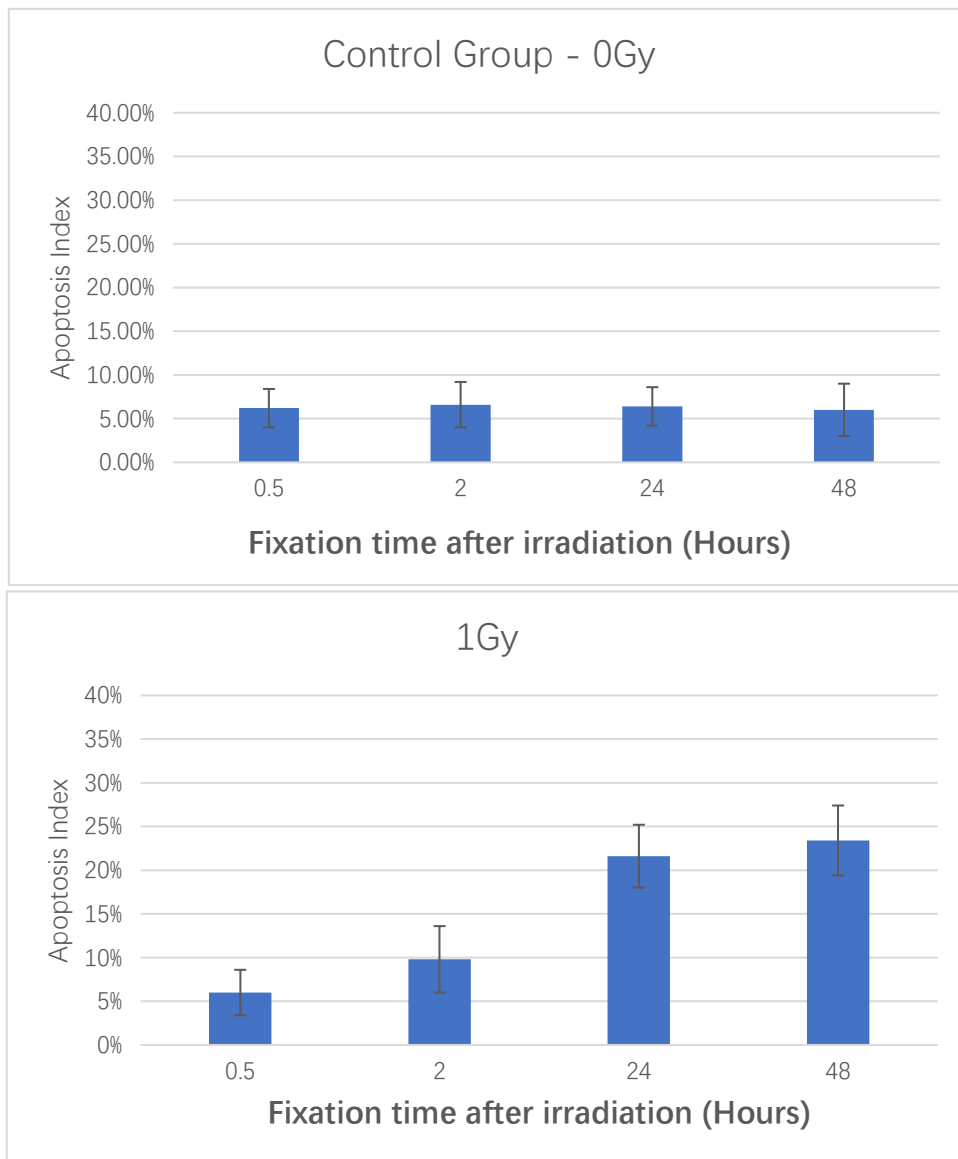
Figure 67: Apoptosis expression level of 2D HT29 colorectal cells for 0Gy, 1Gy and 5Gy photon irradiation. Samples were fixed at 0.5h, 4h, 8h and 24h after irradiation of sample set 3.

Figure 67 shows the apoptosis expression level of 2D HT29 colorectal cells of the third sample group. The measurement method was the apoptosis index instead of the fluorescent intensity. The control group had an apoptosis index from 4% to 6.5% for all sample groups. For 1Gy irradiation, the apoptosis index increased from 6.5% to 19% with fixation time after irradiation. For 5Gy irradiation, the apoptosis index increased from 9% to 30%. From the time point perspective, at 0.5h after irradiation, the control group, 1Gy and 5Gy irradiated samples had similar low apoptosis index, indicating that 0.5h after irradiation, there was less cell death. When the fixation time after irradiation was increased, the apoptosis index increased in both 1Gy and 5Gy sample groups. The 5Gy-irradiated sample group had a higher apoptosis index than that of the 1Gy irradiated sample group. The result shows that the apoptosis level increases after irradiation, and higher irradiation dose induces more cell death. Right after irradiation, the cell death needs around 4 hours to show up.

4.2. Changes in apoptosis levels at different fixation times (result of the 2D culture experiment)

The aim of this experiment was to find the repair kinetics of cancer cells in a 3D model after irradiation.

4.2.1. Sample set 1: Fluorescent staining of apoptosis marker Caspase-3 on the 2D culture HT29 colorectal cancer cell line after photon irradiation

Dose: 0Gy, 1Gy and 5Gy

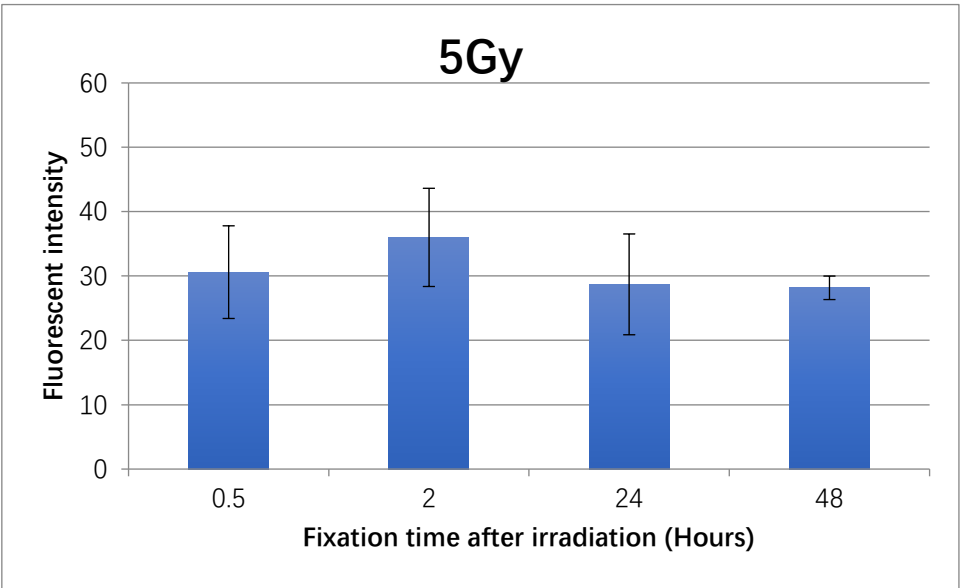Fixation time: 0.5h, 2h, 24h and 48h after irradiation
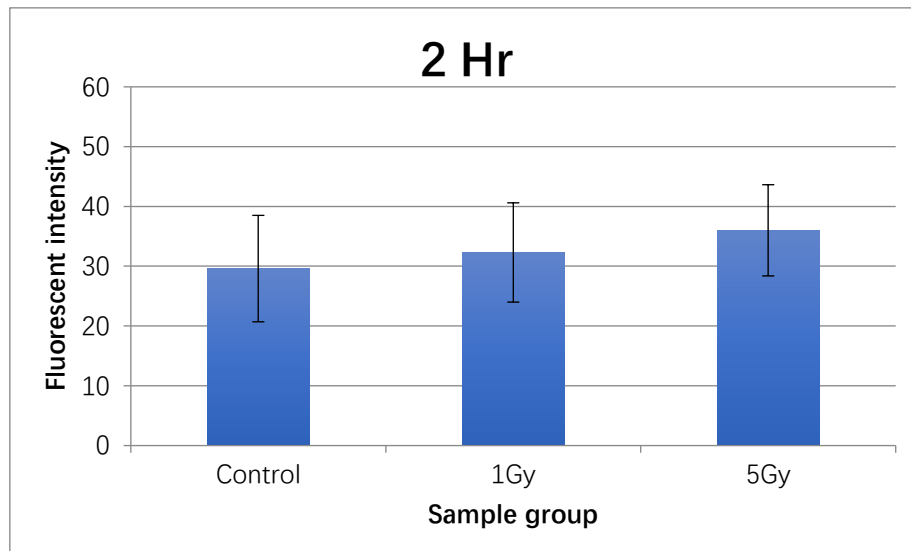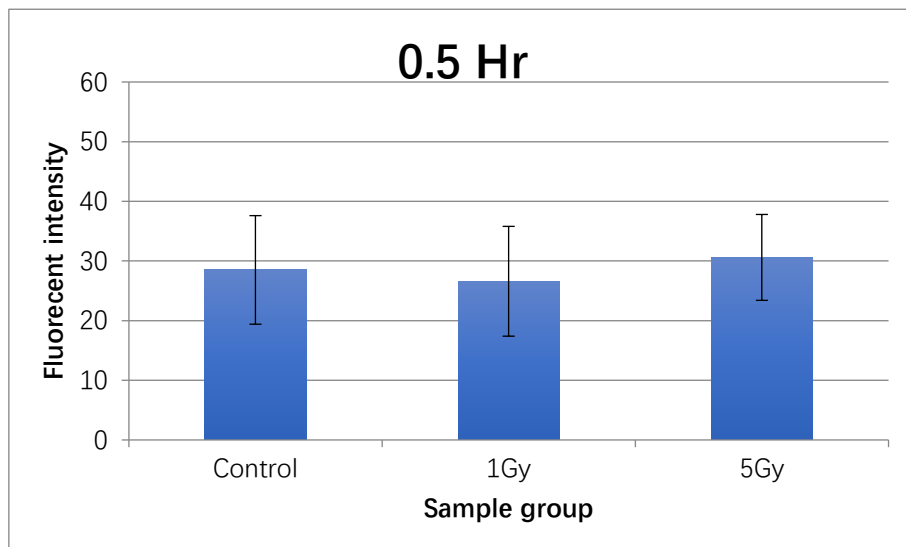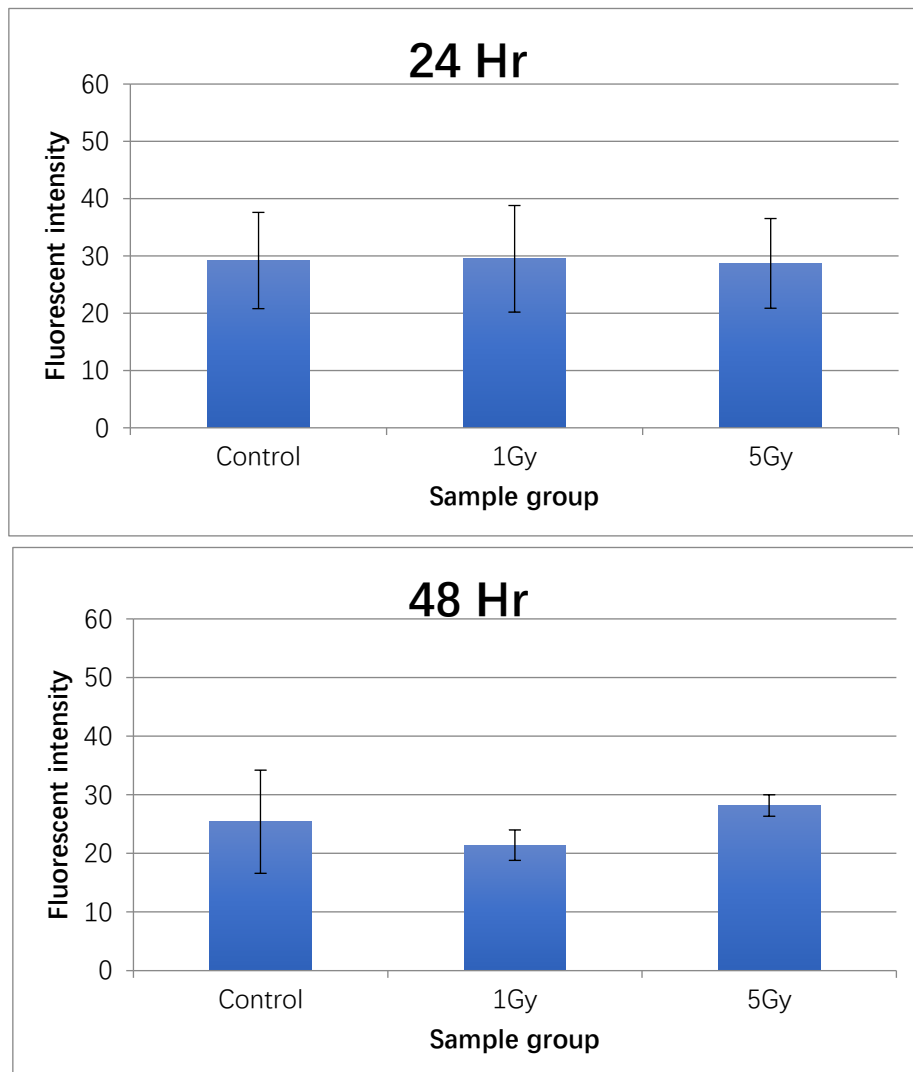
Repeats: 3

Figure 68: Apoptosis fluorescence expression level of 2D HT29 colorectal cells (0Gy, 1Gy and 5Gy photon irradiation) x (3 repeats) x (fixed at 0.5h, 2h, 24h and 48h after irradiation) / Sample set 1

0.5 Hr

2 Hr

24 Hr
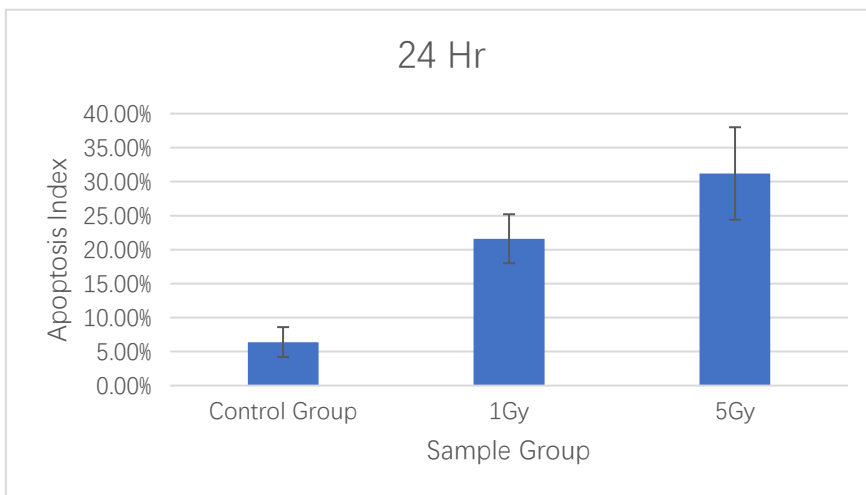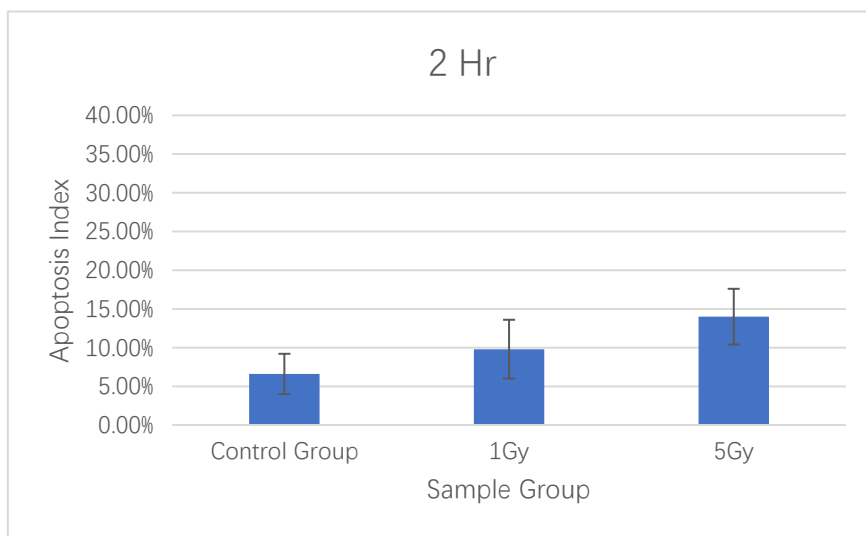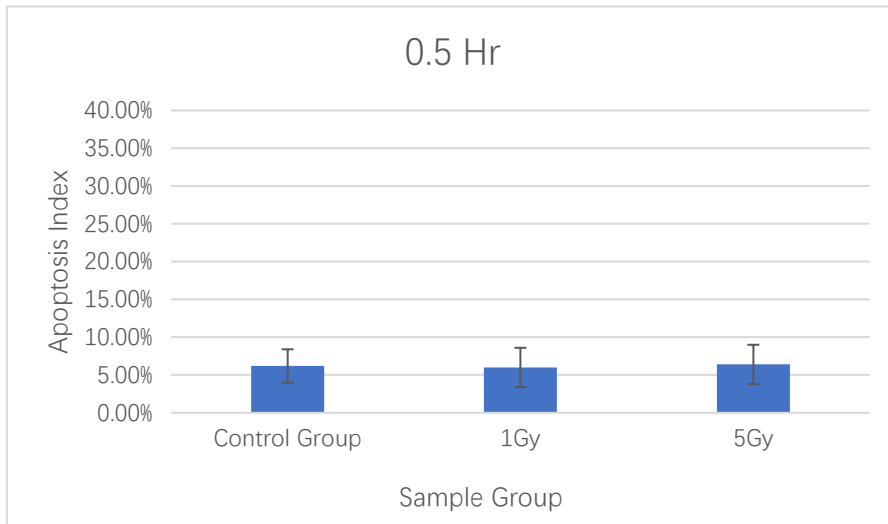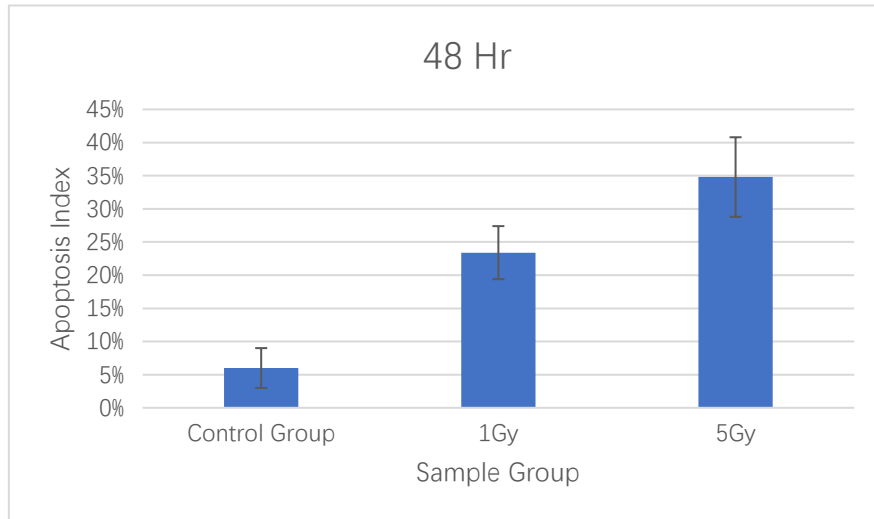
Figure 69: Apoptosis index expression level of 2D HT29 colorectal cells (0Gy, 1Gy and 5Gy photon irradiation) x (3 repeats) x (fixed at 0.5h, 2h, 24h and 48h after irradiation) / Sample set 1

The plots in Figure 69 showed that a high apoptosis index on a high irradiation dose indicated a more cell apoptosis rate. The fixation time mattered if irradiation occurred. The apoptosis expression showed upregulation in 2h after irradiation. The apoptosis index reached the highest level for the 5Gy irradiated sample group.

4.2.2. Sample set 2: Fluorescent staining of apoptosis marker Caspase-3 on the 2D culture HT29 colorectal cancer cell line after photon irradiation

Dose: 0Gy, 1Gy and 5Gy

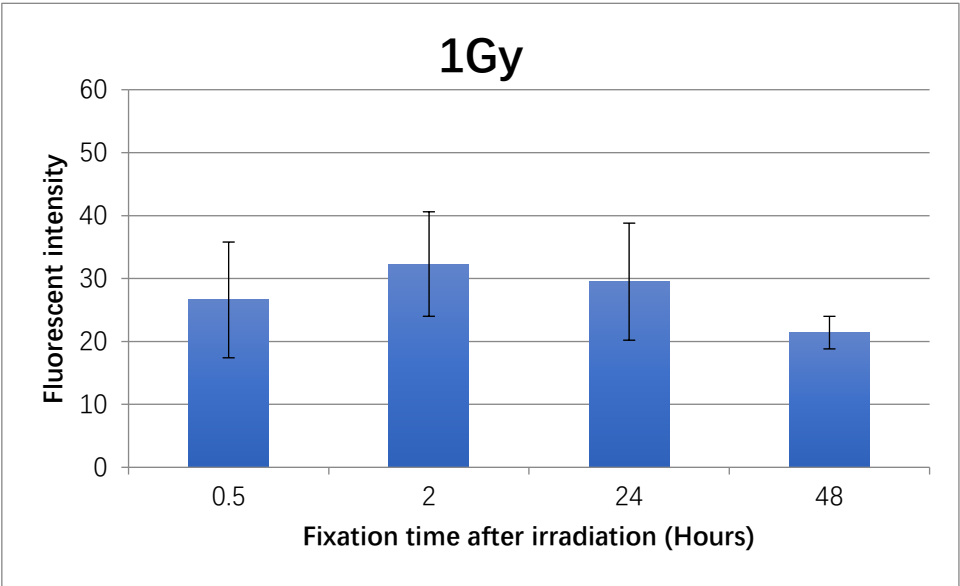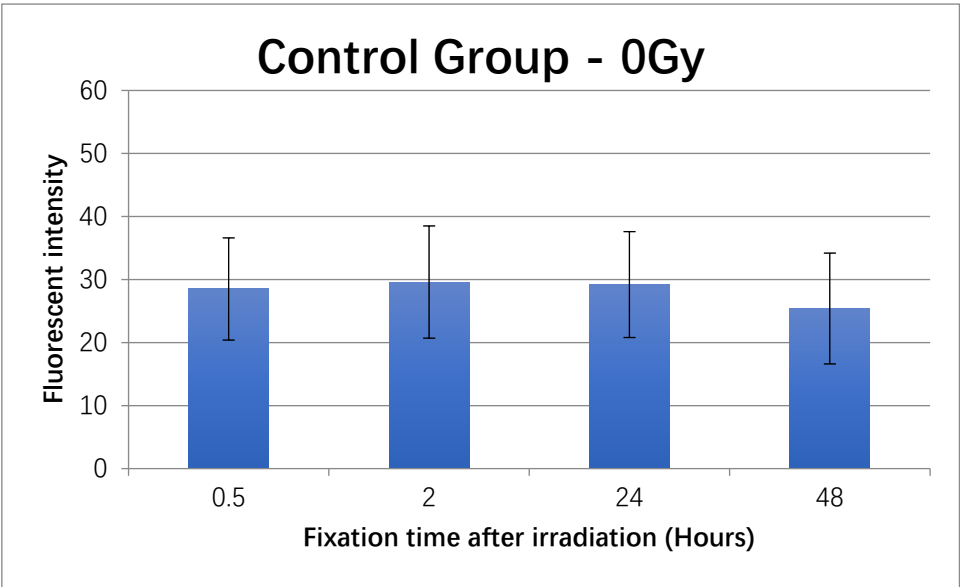Fixation time: 0.5h, 4h, 8h and 24h after irradiation
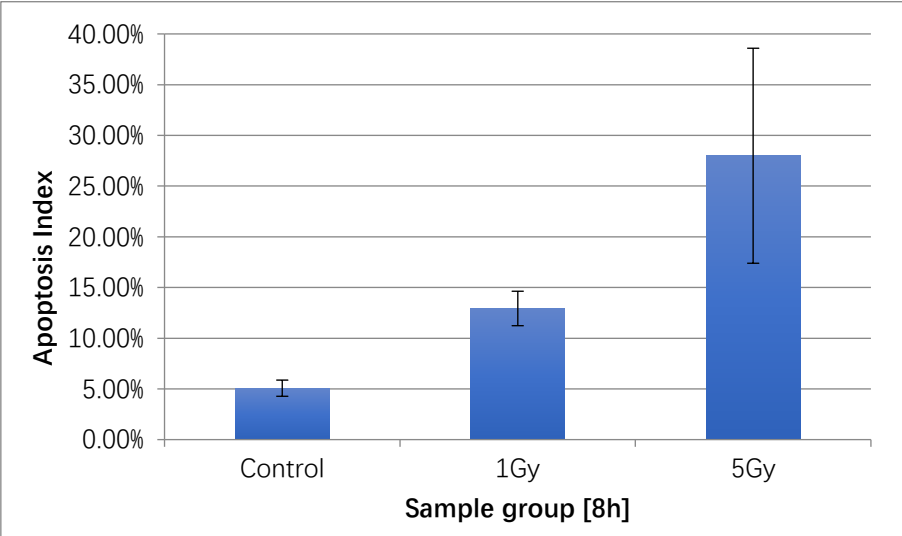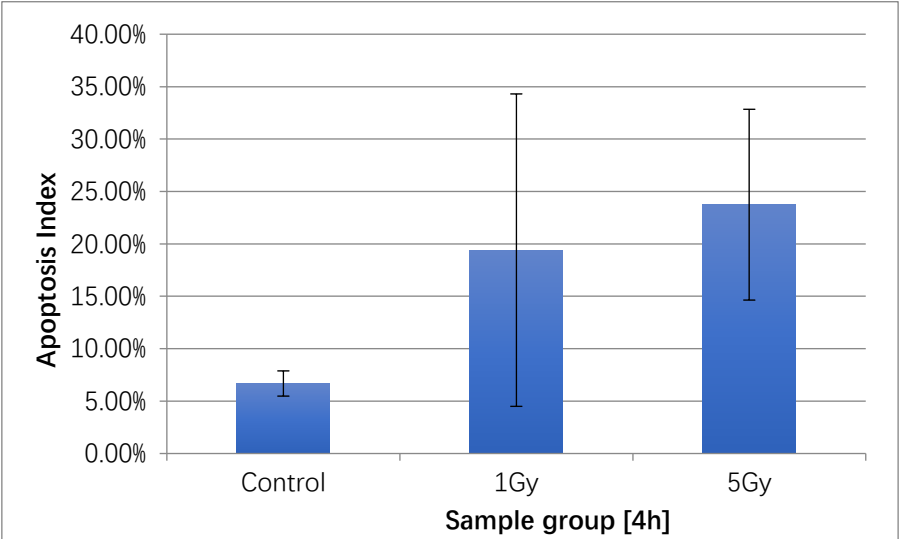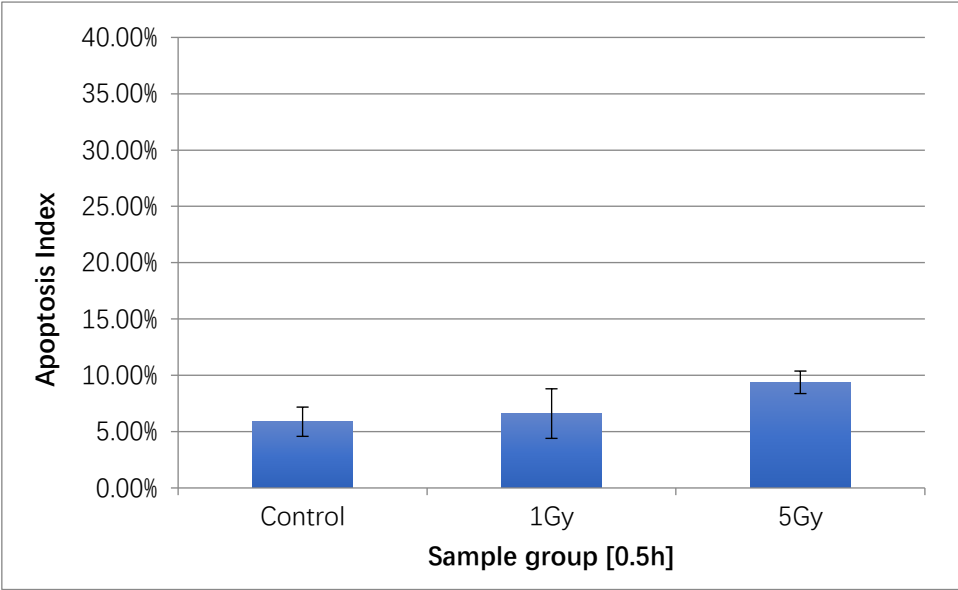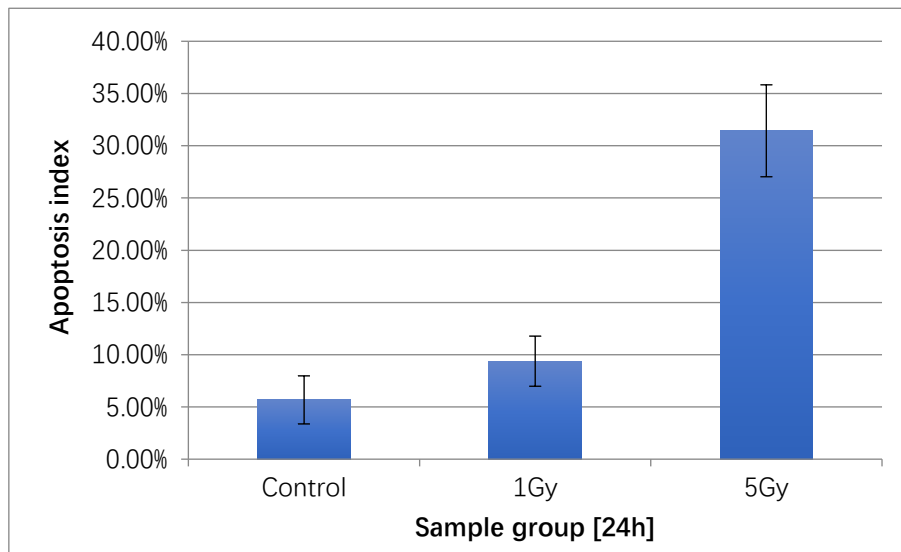
Repeats: 3

Figure 70: Apoptosis expression level of 2D HT29 colorectal cells (0Gy, 1Gy and 5Gy photon irradiation) x (3 repeats) x (fixed at 0.5h, 4h, 8h and 24h after irradiation)

The plots in Figure 70 showed that a high apoptosis index on a high irradiation dose indicated a more cell apoptosis rate. The fixation time mattered as soon as 0.5h after irradiation. The apoptosis index was half of the value of 4h after irradiation. The apoptosis expression showed upregulation in 4h after irradiation.

4.3. Radiation-induced apoptosis levels between 2D and 3D cell models (results from the 3D culture experiment)

4.3.1. Fluorescent staining of apoptosis marker Caspase-3 on the 3D culture HT29 colorectal cancer cell line after photon irradiation

Dose: 0Gy, 1Gy and 5Gy

Fixation time: 0.5h, 2h, 24h and 48h after irradiation

Repeats: 3

	DAPI staining of nuclei	Caspase-3 staining of cell apoptosis
0Gy		
1Gy		
5Gy		
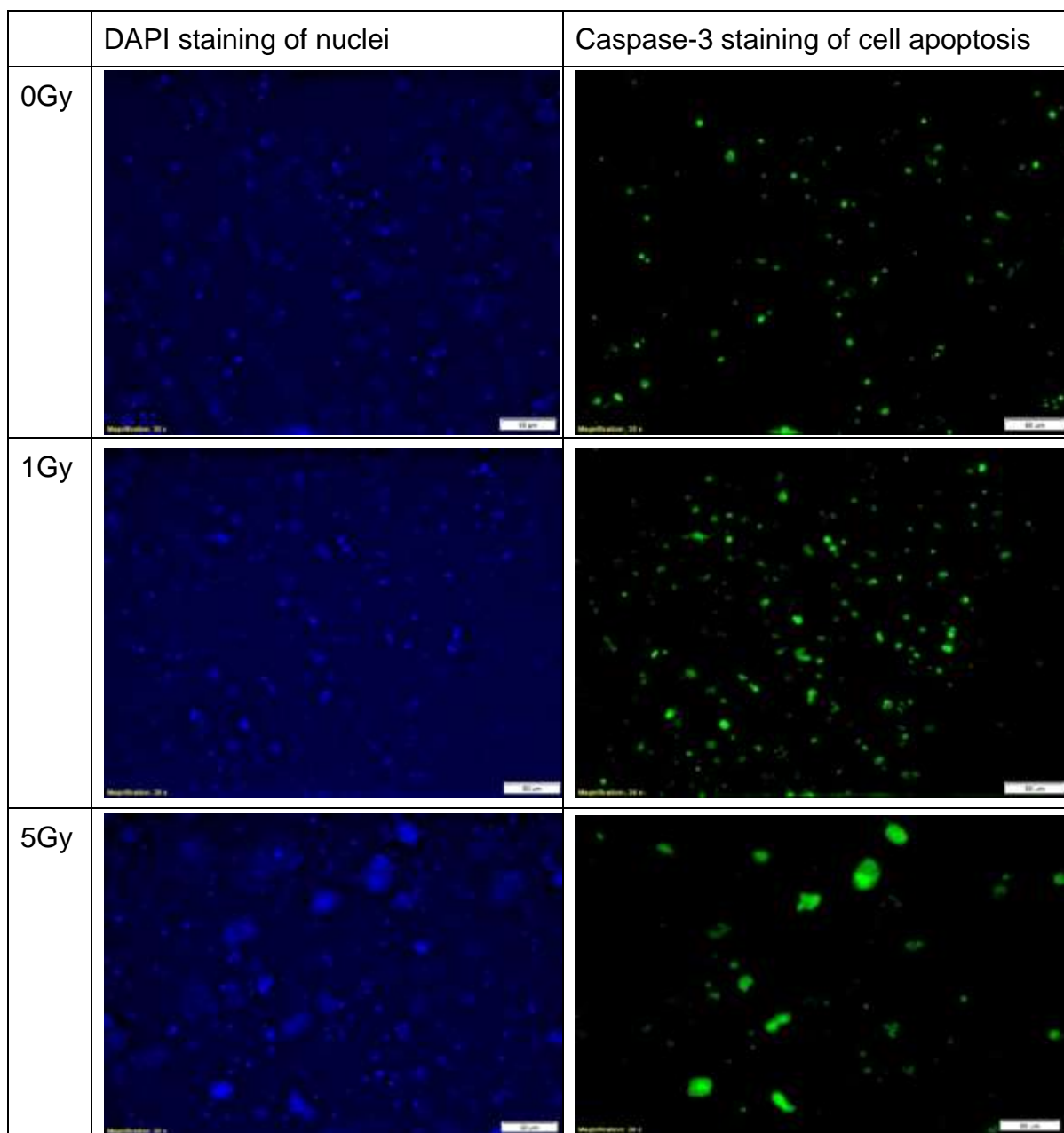
Figure 71: Sample images of photon-irradiated 3D HT29 colorectal cancer cell line culture. The nuclei was stained by the DAPI solution (left) and the apoptosis marker was Caspase-3 (right). The first row shows the 0Gy control group fixed at 0.5h after irradiation. The second row shows the 1Gy-irradiated group fixed at 0.5h after irradiation. The third row shows the 5Gy-irradiated group fixed at 0.5h after irradiation. The magnification power was 20x. The length of the scale bar was 50µm.

The 3D apoptosis of the HT29 colorectal cancer cell line after photon irradiation had one experimental plan. Figure 67 shows the sample images of photon-irradiated 3D

HT29 colorectal cancer cell line culture. The nuclei were stained by the DAPI solution (left) and the apoptosis marker was Caspase-3 (right). The first row shows the 0Gy control group fixed at 0.5h after irradiation. The second row shows the 1Gy-irradiated group fixed at 0.5h after irradiation. The third row shows the 5Gy-irradiated group fixed at 0.5h after irradiation. The magnification power was 20x. The plots in Figure 69 show the local fluorescent expression of the single frame. By stitching the single frame in order of the proton beam irradiation distance, the apoptosis expression of the collagen cancer model throughout the whole irradiation dose profile is shown in Figure 70. For the fluorescent level in the 3D HT29 tumouroid model using FluoroDish, there was no significant difference between control group and 1Gy- and 5Gy-irradiated sample groups. No trend could be concluded based on the fixation time of the control group, 1Gy- and 5Gy-irradiated sample groups.

4.3.2. Fluorescent staining of apoptosis marker Caspase-3 on the 3D culture HT29 colorectal cancer cell line after proton irradiation

Dose: 0Gy, 1Gy and 5Gy
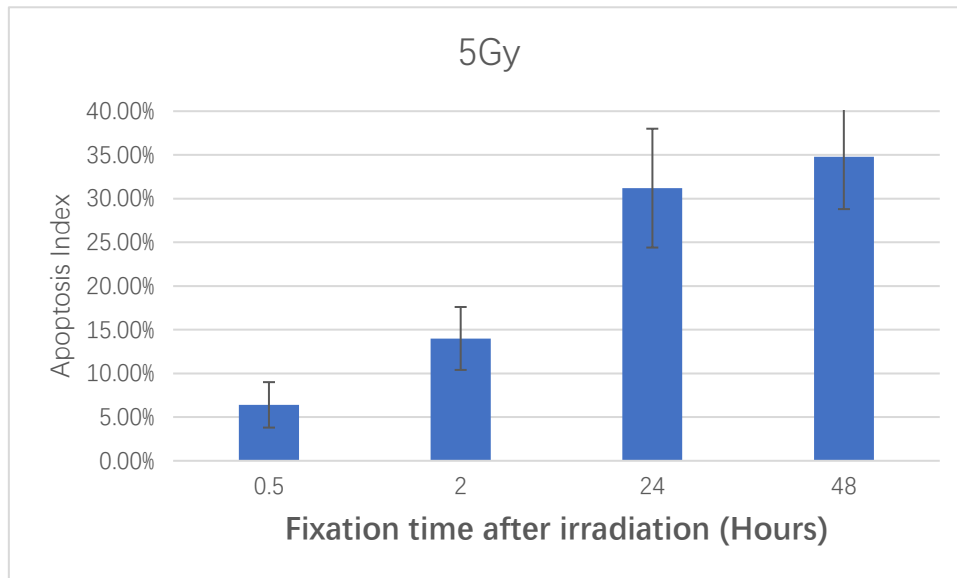
Fixation time: 0.5h and 24h after irradiation

Repeats: 3
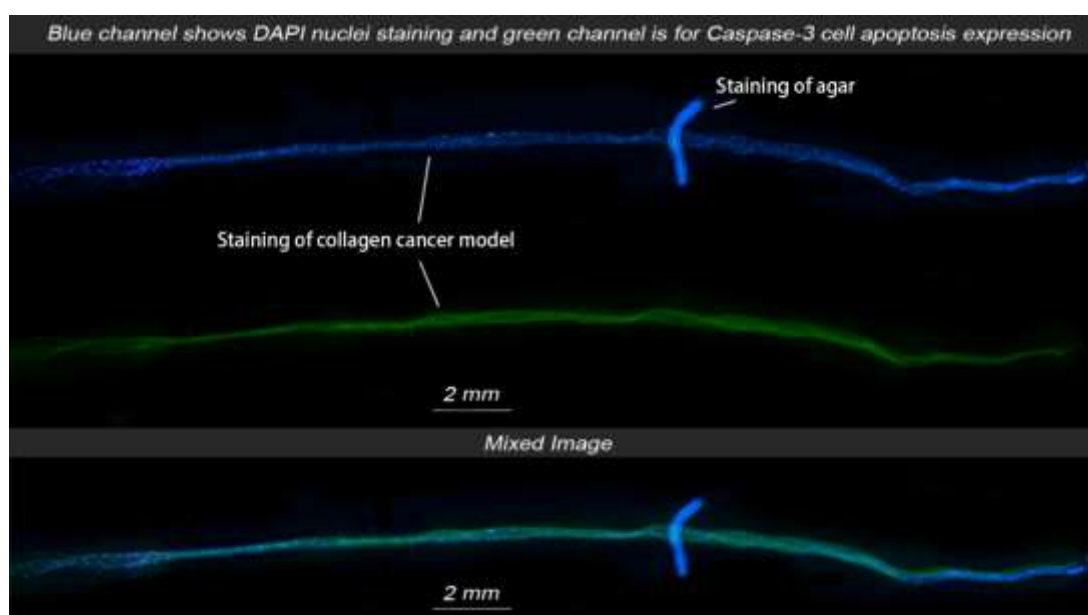
Figure 72: Example of cell apoptosis expression of 3D collagen cancer model after

5Gy proton irradiation and fixed at 24h after irradiation. The nuclei were stained using the DAPI solution in blue and the apoptosis marker Caspase-3 was used to stain the apoptosis area in green (Alexa Fluor 488 was used as the secondary antibody). The magnification power was 4x.
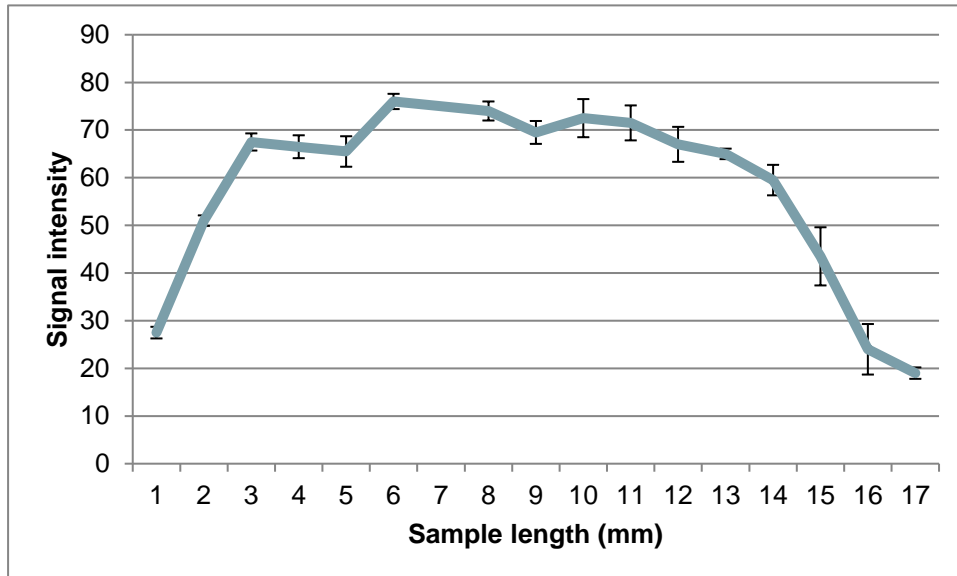
Figure 73: Plot of cell apoptosis expression intensity distribution throughout the sample length of proton irradiation profile. The HT29 3D tumouroid sample was taken 5Gy proton irradiation and was fixed at 24h after irradiation. The sample was fixed and processed in selected direction, so that the sample length was equal to the sample depth in the dose profile.
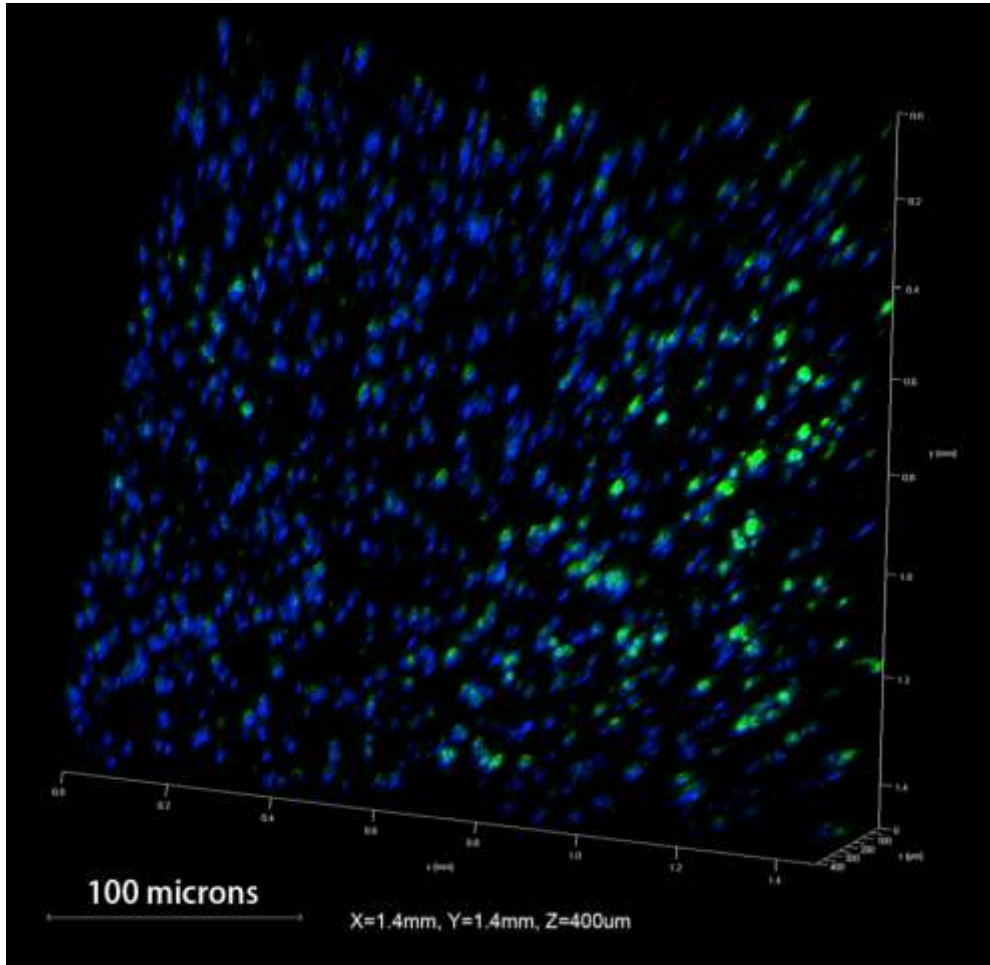
Figure 74: 3D sample confocal fluorescent images of the boundary area of spread-out Bragg peak which has a uniform dose (5Gy proton beam irradiation, fixed at 24h after irradiation). The nuclei were stained using the DAPI solution in blue and the apoptosis marker Caspase-3 was used to stain the apoptosis area in green (Alexa Fluor 488 was used as the secondary antibody). The magnification power was 40x. Differences existed in the relative dose, as shown in Figure 61, which was the dose profile. In the boundary area of the enter dose and SOBP solution at the right hand side of this picture, there were differences in apoptosis expression levels.
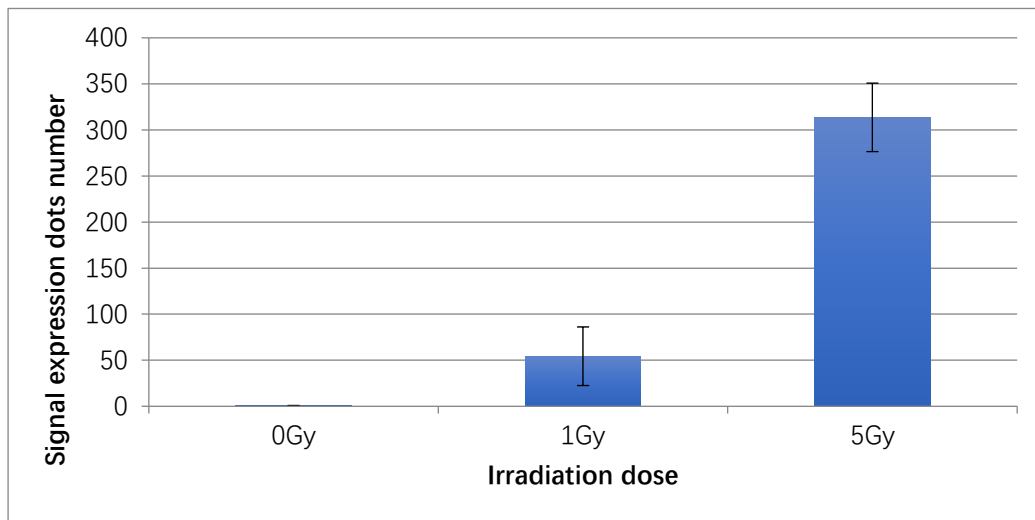
Figure 75: The average number of cell apoptosis signal expression light dots VS proton irradiation dose (0Gy, 1Gy and 5Gy irradiation, fixed at 24h and 0.5h after irradiation) (3 repeats)

The magnification power was low for the confocal microscopy images of the proton-irradiated 3D collagen HT29 cancer model. The apoptosis level for individual cell was difficult to measure, because the image covered the whole tumouroid area and the cell density of those sample groups were similar. The apoptosis marker was used to stain the apoptosis area in bright dots, and then the signal expression dots number of the tumouroid area with the same cell density were measured and compared with other sample groups.

4.3.3. Quantitative comparison of the apoptosis level after photon irradiations between 2D culture and 3D culture.

Figure 67 and Figure 75 were compared to find the signal intensity differences between 2D culture and 3D culture. The fixation time was the same: 0.5h, 2h, 24h and 48h after irradiation and the radiation doses were also the same: 0Gy for control, 1Gy and 5Gy. Because the culture condition was different, data comparison suggested that significant differences existed between 2D culture and 3D culture in apoptosis signal expression.
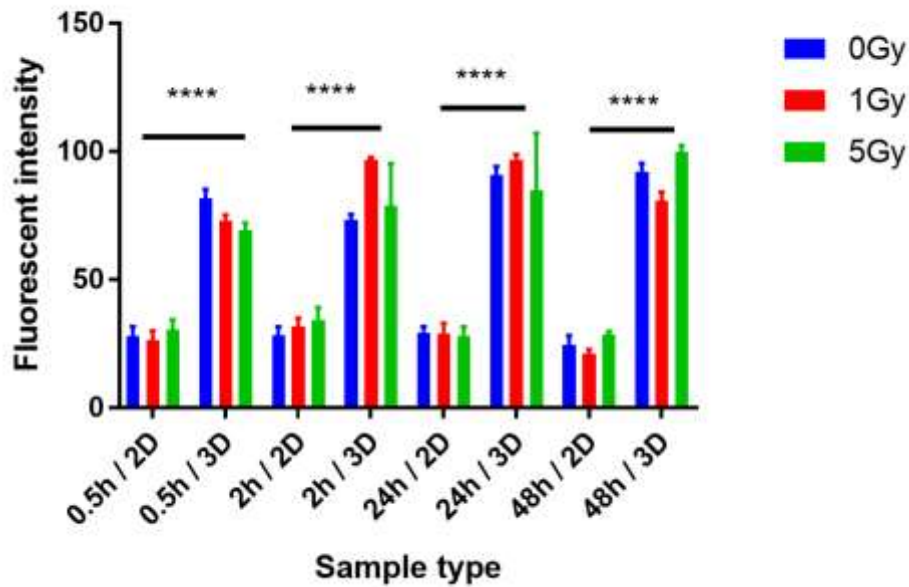
Figure 76: Comparison of apoptosis levels after photon irradiations between 2D culture and 3D culture according to experiment results (3 repeats)

In 3D culture, the focal plane was too narrow to count cell numbers. Therefore, the apoptosis fluorescent intensity was a better measurement than the apoptosis index. In Figure 76, the 2D and 3D culture apoptosis fluorescent intensity were compared. For all the fixation time points (0.5h, 2h, 24h and 48h after irradiation), the 3D culture showed significant higher apoptosis level than 2D culture.

4.4. Measuring DNA damages as a function of increasing radiation doses

4.4.1. Sample set 1: Fluorescent staining of DNA double strand break marker 53BP1 on the 3D culture HT29 colorectal cancer cell line after photon irradiation

Dose: 0Gy, 1Gy and 5Gy

Fixation time: 0.5h and 48h after irradiation

Repeats: 3
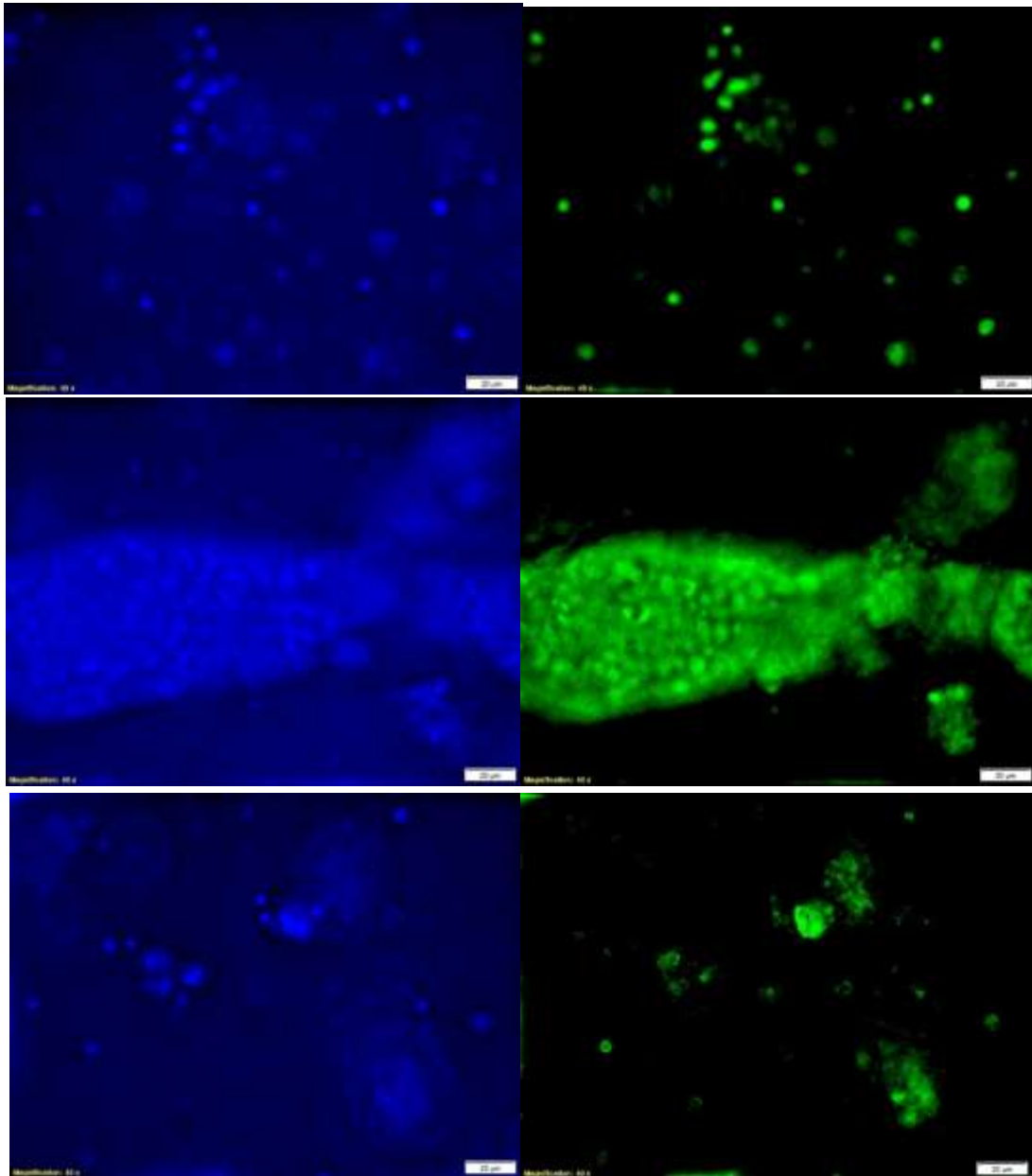
Figure 77: Sample images of the 3D HT29 tumouroid model after photon irradiation and marked using the DAPI solution (left) and DNA double strand marker 53BP1 (right). The first row shows the 0Gy control group fixed at 0.5h after irradiation. The second row shows the 1Gy-irradiated group fixed at 48h after irradiation. The third row shows the 5Gy-irradiated group fixed at 48h after irradiation. The magnification power was 40x. The length of scale bar was 20μm.

4.4.2. Sample set 2: Fluorescent staining of DNA double strand break marker 53BP1 on the 3D tumouroid culture HT29 colorectal cancer cell line after proton

irradiation

Dose: 0Gy and 1.5Gy

Fixation time: 0.5h and 24h after irradiation

Repeats: 3
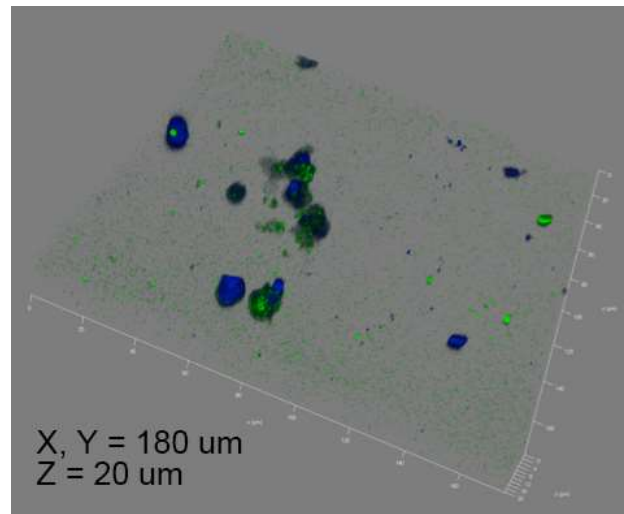
Figure 78: The co-localized sample confocal image of 3D cultured HT29 colorectal cancer cells which were stained with DAPI in blue and stained with DNA double strand break marker 53BP1 in green (Alexa Fluor 488 is used as the secondary antibody). The cells are proton irradiated and fixed 24h after irradiation. The magnification power is 63x.

The 3D HT29 colorectal cancer cell line model is cultured in the slide flask. The cell seeding number is 1 million cells per tumouroid. The cancer cells are uniformly distributed in a 4ml 3D collagen matrix before gelation. The proton irradiated 3D cancer model is fixed and then seeded into an agar mould prior to vibratome sample processing. The final sample slice after vibratome processing has a thickness of 200μm. The sample slice is stained with fluorescent markers and then imaged by confocal microscope in Department of Bioscience at UCL.
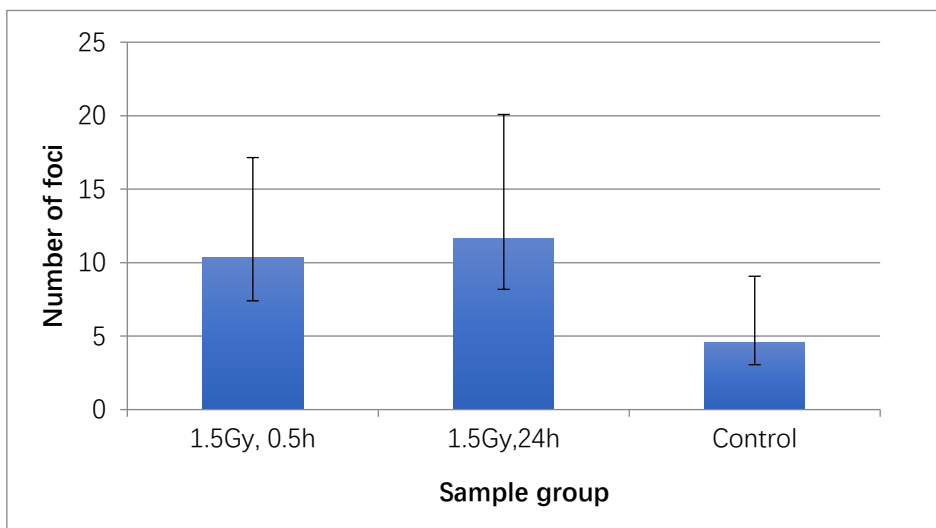
Figure 79: Average DNA damage foci number for sample groups and their standard derivation. The sample groups are 0Gy control group, 1.5Gy proton irradiated 3D HT29 colorectal cancer cell tumouroid fixed 0.5h after irradiation and 1.5Gy proton irradiated 3D HT29 colorectal cancer cell tumouroid fixed 24h after irradiation. Repeat number is 3. (50 nuclei were counted, and control group is fixed 0.5h after other sample group irradiations)
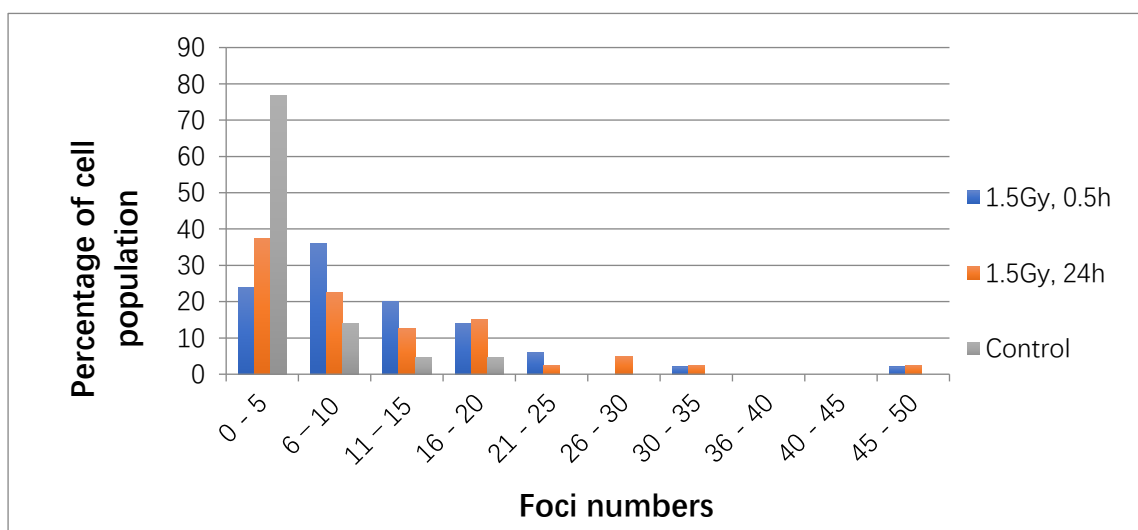
Figure 80: The foci number per cell is categorized in several ranges. The percentage of cell population in each range of foci number is plotted. The sample groups are 0Gy control group, 1.5Gy proton irradiated 3D HT29 colorectal cancer cell tumouroid fixed 0.5h after irradiation and 1.5Gy proton irradiated 3D HT29 colorectal cancer cell tumouroid fixed 24h after irradiation. Repeat number is 3. (50 nuclei were counted)

For 3D HT29 colorectal cancer cell line model after proton irradiation. The experiment has an irradiation dose of 0Gy and 1.5Gy. The samples were fixed 0.5h and 24h after irradiation. Figure 78 shows the co-localized sample confocal image of 3D cultured HT29 colorectal cancer cells which were stained with DAPI in blue and stained with DNA double strand break marker 53BP1 in green (Alexa Fluor 488 is used as the secondary antibody). The cells were proton irradiated and fixed 24h after irradiation. The magnification power is 63x. From the counting and statistics from Figure 79 and Figure 80, for the same 1.5Gy irradiation dose, the samples fixed 24h have higher average number of foci than the sample fixed 0.5 hours after irradiation, but the percentage of cell population shows that the most foci are in 6-10 range for 0.5 hour and 0-5 range for 24 hours. This can be seen in positive standard derivation in Figure 79. This means the cells start to repair after irradiation but not all the cells are affected. When compared with control group, it is obviously that without irradiation there are less average foci number and there is no large foci numbers distribution. This means the irradiation can cause DNA double strand break.

4.6. Measurement of microenvironment factor: Hypoxia

The first aim is to establish a methodology to measure hypoxic changes in 3D collagen cancer model, and the second aim is to correlate hypoxia level with radiation damage such as DNA damage or cell apoptosis. Unfortunately, the samples for proton irradiation is processed faulty, so that the sample set is not able to compare with any other radiobiology behavior.

4.8.1. Sample set 1: The fluorescent staining of hypoxia marker CAIX on 3D culture HT29 colorectal cancer cell line after proton irradiation

Dose: 0Gy, 1Gy and 5Gy

Fixation time: 0.5h and 24h after irradiation

Repeats: 3

Figure 81: Sample confocal fluorescence images of hypoxia expression after proton irradiation (A) 1Gy irradiation fixed at 24h after irradiation (B) 5Gy irradiation fixed at 24h after irradiation. The nuclei were stained with the DAPI solution in blue and the hypoxia marker CAIX was used to stain the hypoxia areas in green (Alexa Fluor 488 was used as the secondary antibody). The magnification power was 40x.

Hypoxia expression signal intensity versus sample depth of control group
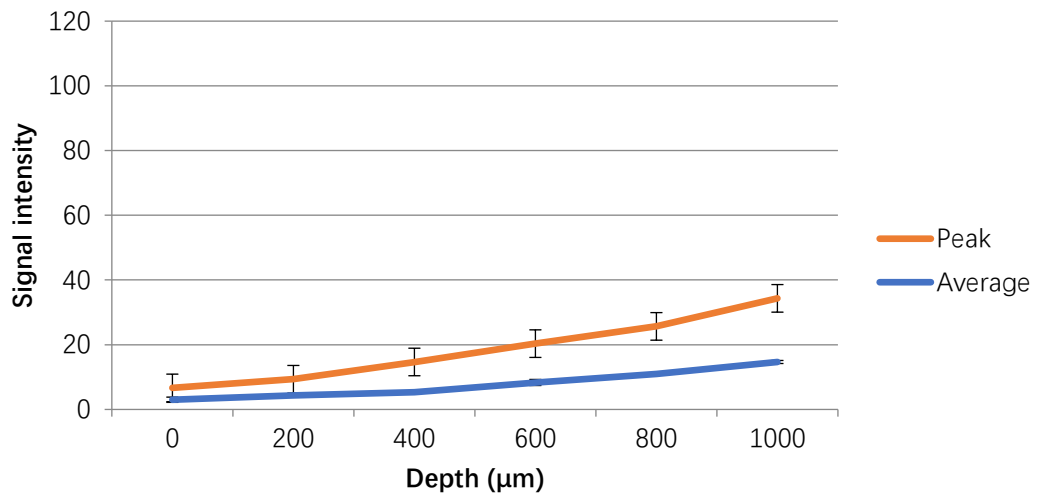
Hypoxia expression signal intensity versus sample depth of 1Gy irradiation sample
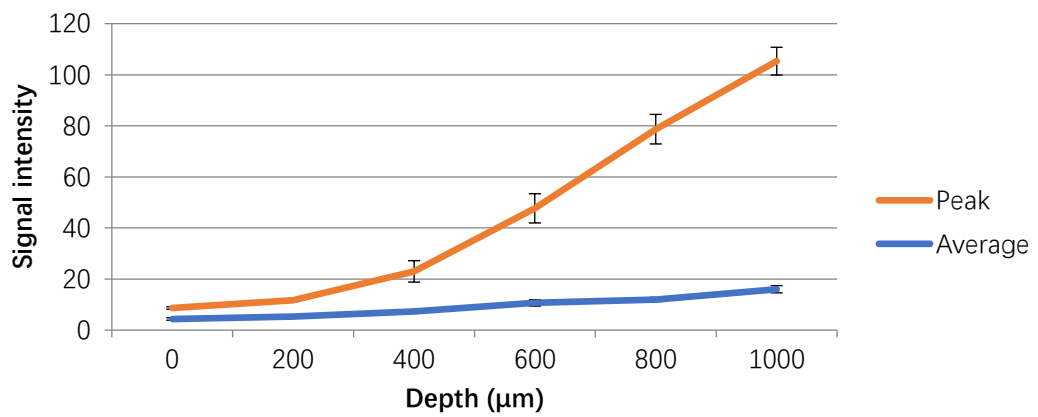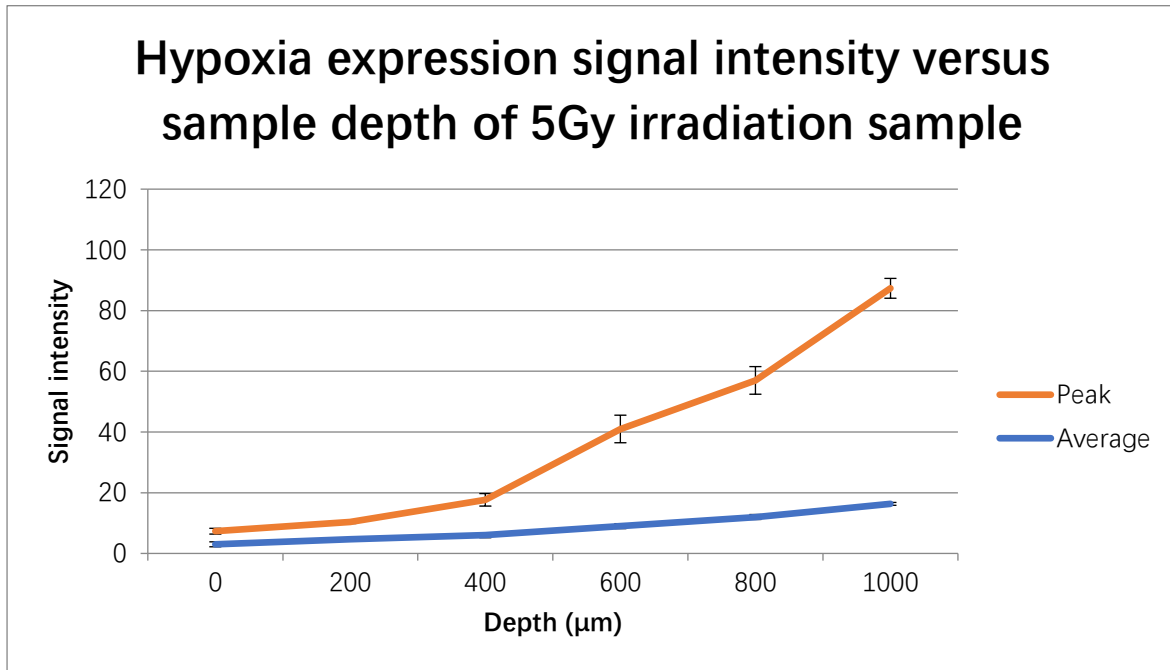
Figure 82: Hypoxia expression signal intensity versus sample depth for proton irradiation sample (0Gy, 1Gy and 5Gy irradiation doses, fixed at 24h and 0.5h after irradiation) (3 repeats)
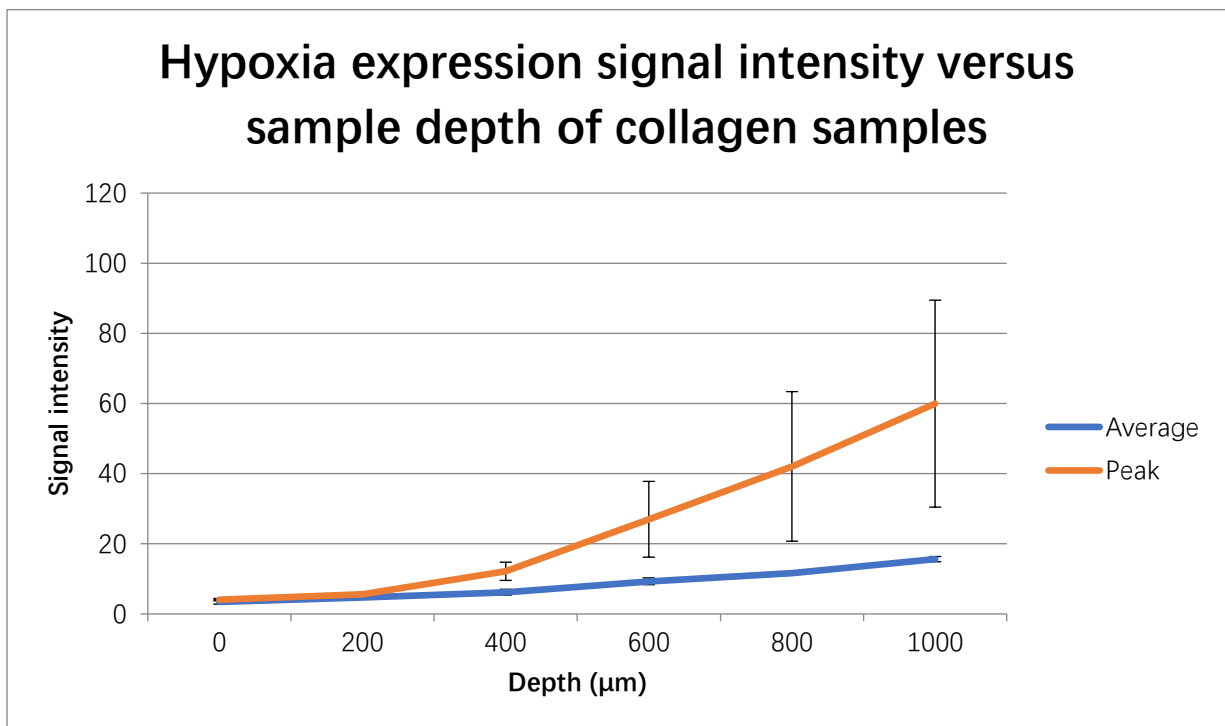
Figure 83: Hypoxia expression signal intensity versus sample depth of all 3D collagen HT29 colorectal cancer cell line models (3 repeats).

Figure 82 plots the hypoxia signal intensity of 0Gy, 1Gy and 5Gy proton-irradiated 3D collagen HT29 cancer model. Due to heavy background fluorescence, the measurements were at both the average fluorescent level and peak fluorescent level. The average fluorescent level represented the mean fluorescent level of the tumouroid area, including the background fluorescence. The peak fluorescent level just represented the fluorescence level of peak bright dots within the tumouroid area because hypoxia level expression was not dependent on the irradiation dose. Figure 83 plots the average fluorescent intensity of 0Gy, 1Gy and 5Gy sample groups and shows that the hypoxia level was dependent on the sample depth but not irradiation dose.

4.7. An alternative 3D cell model of micrometastasis – spheroids (The invasion and growth of HT29 3D spheroid model after photon irradiation.)

The aim of this experiment was to develop a 3D cancer spheroid model for irradiation studies. The micrometastasis such as spheroid invasion and growth were analyzed with increasing irradiation doses.

Dose: 0Gy, 4Gy, 8Gy and 12Gy

Spheroid number: 30 wells per plate and each well contain at least one spheroid. 15 spheroids with regular round shapes were selected for analysis
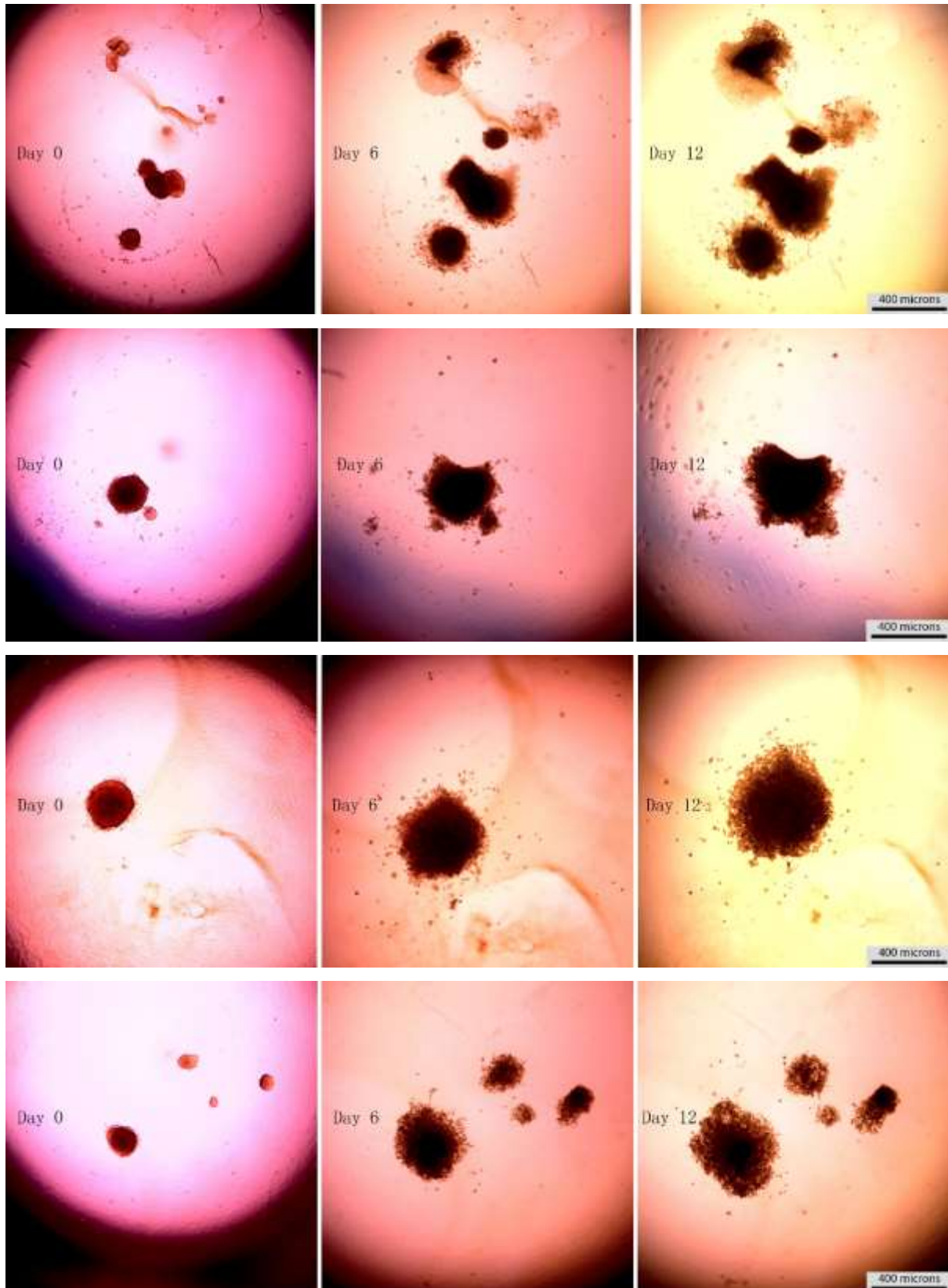
Figure 84: Sample images of HT29 colorectal cancer cell spheroid growth after 0Gy, 4Gy, 8Gy and 12Gy irradiation on day 0, day 6 and day 12. The first row shows the 0Gy sample group, the second row 4Gy sample group, the third row 8Gy sample group

and the fourth row 12Gy sample group of irradiated spheroids. Day 0 indicated the day of irradiation, which is 1 day after spheroid transfer.

Figure 85 shows the typical spheroid morphology in one well of the 96-well tissue culture plate. There was at least one spheroid in each well. On day 0, just the first day after spheroid transfer from ultra-low attachment 96-well plate to 3D collagen matrix on 96-well tissue culture plate, the morphology of spheroid was round, and the center of a spheroid had a higher cell density than the periphery area. On day 6, the spheroid grew and invaded into the collagen matrix. On day 12, the invasion phenomenon was intensified.

4Gy

Volume of spheroid (Cubic micrometer) / Logarithmic scale — Millions
Days after irradiation

Spheroid 1
Spheroid 2
Spheroid 3
Spheroid 4
Spheroid 5
Spheroid 6
Spheroid 7
Spheroid 8
Spheroid 9
Spheroid 10
Spheroid 11
Spheroid 12
Spheroid 13
Spheroid 14
Spheroid 15

8Gy

Volume of spheroid (Cubic micrometer) / Logarithmic scale — Millions
Days after irradiation

Spheroid 1
Spheroid 2
Spheroid 3
Spheroid 4
Spheroid 5
Spheroid 6
Spheroid 7
Spheroid 8
Spheroid 9
Spheroid 10
Spheroid 11
Spheroid 12
Spheroid 13
Spheroid 14
Spheroid 15

Figure 85: Volume of 3D HT29 colorectal cancer cell spheroid after 0Gy, 4Gy, 8Gy and 12Gy irradiation and cultured from Day 0 to Day 12 (imaged every 2 days, 15 individual spheroids on track).
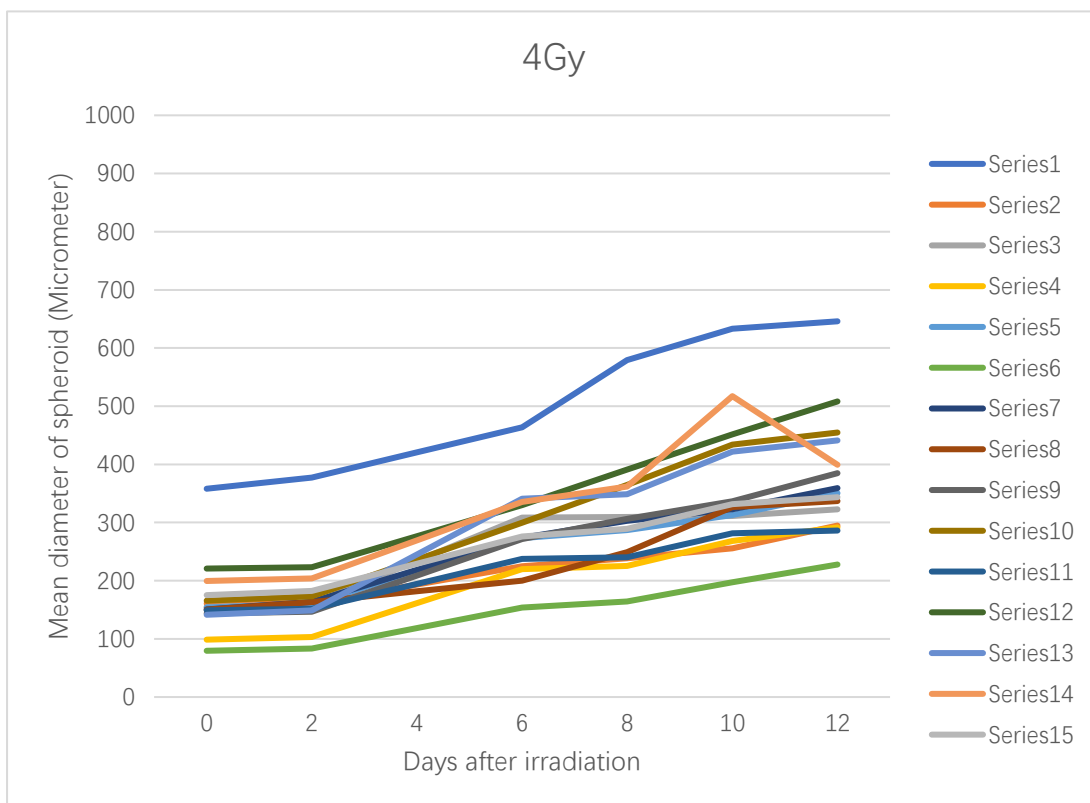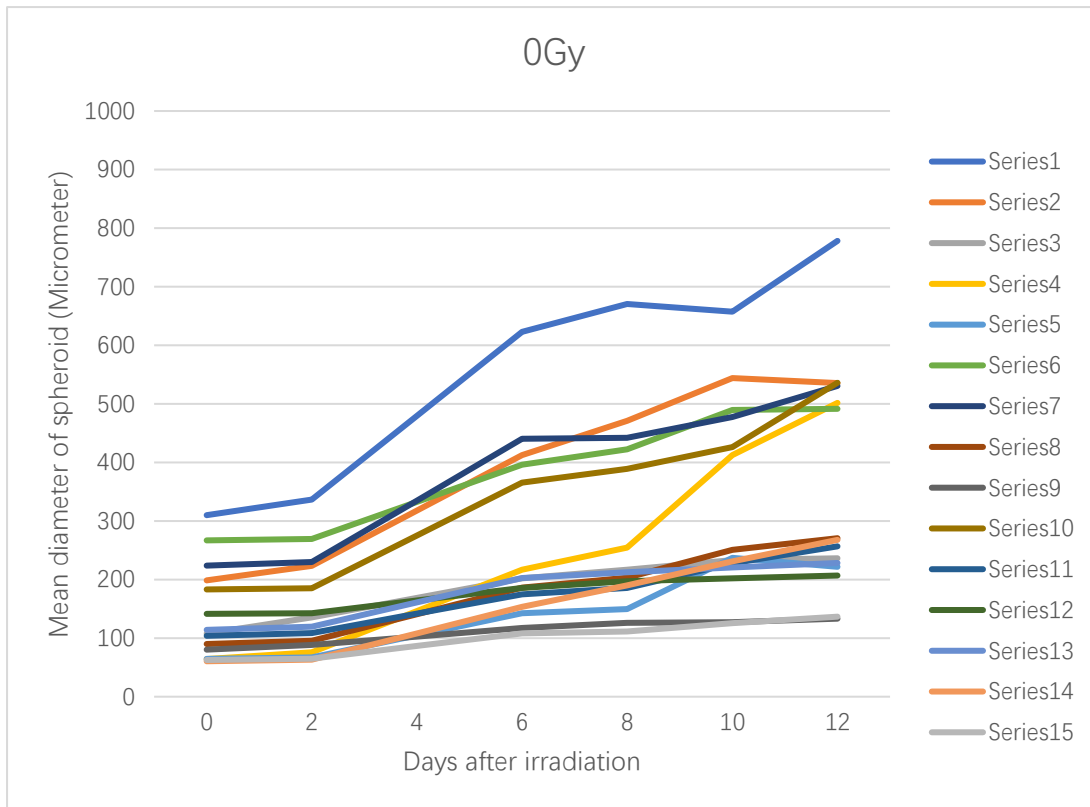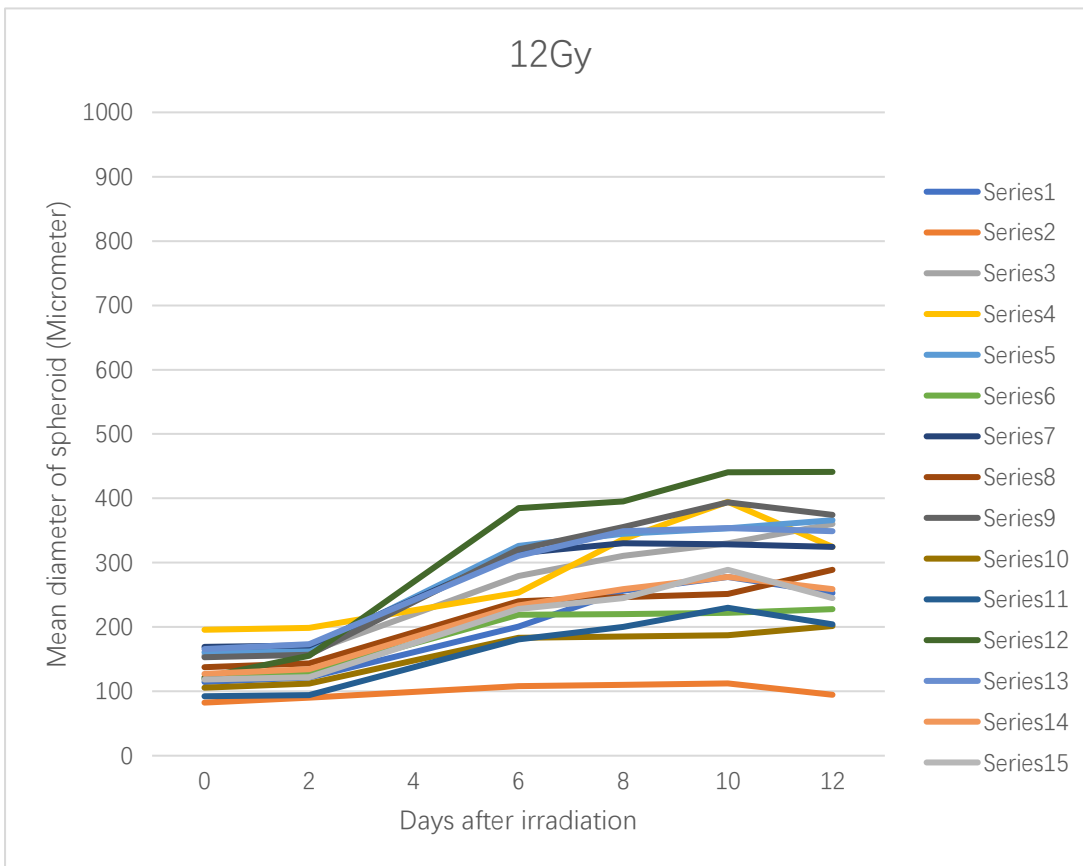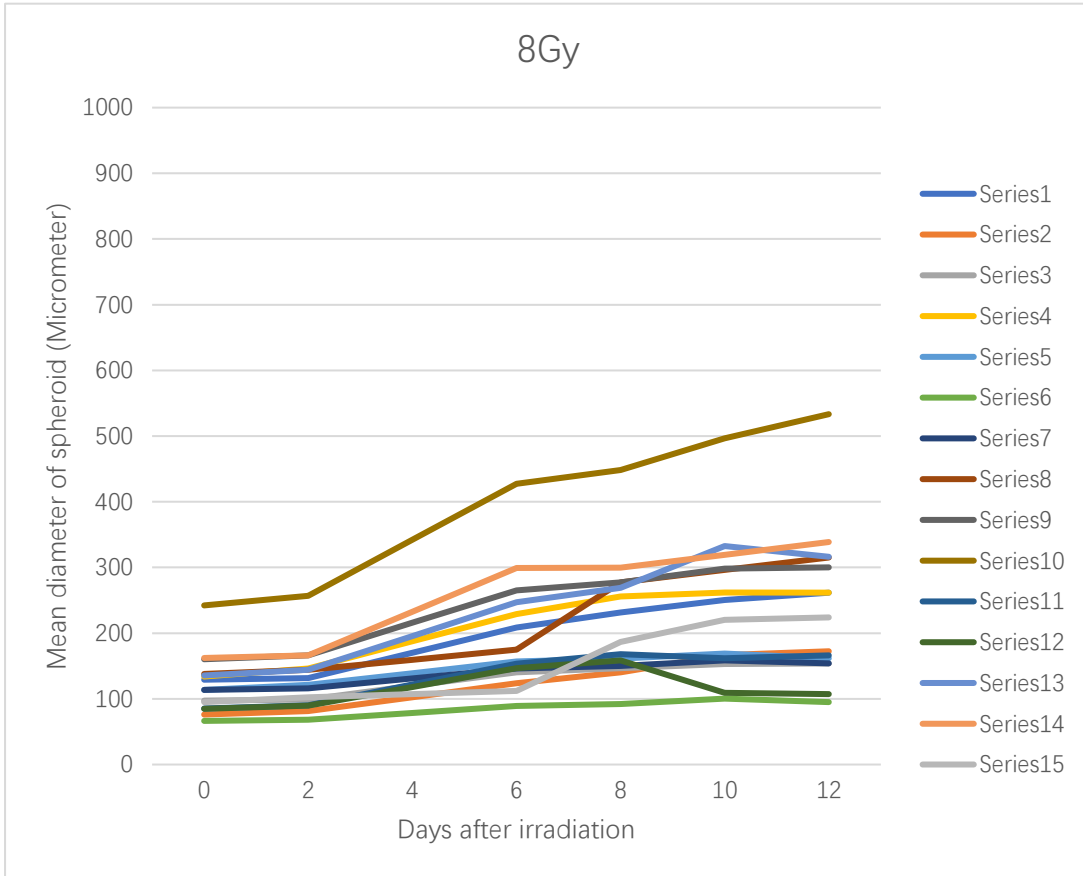
Figure 86: Mean diameter of 3D HT29 colorectal cancer cell spheroid after 0Gy, 4Gy,

8Gy and 12Gy irradiation and cultured from Day 0 to Day 12 (imaged every 2 days, 15 individual spheroids on track)

For 0Gy, 20% of the spheroids decreased in size by day 12 and 80% of the spheroids were still growing. For 4Gy, 6.6% of the spheroids decreased in size by day 12 and 93.3% of the spheroids were still growing. For 8Gy, 33.3% of the spheroids decrease in size by day 12 and 66.6% of the spheroids were still growing. For 12Gy, 66.6% of the spheroids decreased in size by day 12 and 33.3% of the spheroids were still growing. A higher irradiation dose indicated a higher percentage of spheroids that decreased their volume (shrinkage) at day 12. From the morphology of Figure 80, if a higher irradiation dose was adopted, the core of a spheroid broke down and cells were spread out from the spheroid. This indicated the cell death after irradiation.

5. Discussion

5.1. Fluorescent staining problem of the 3D tumouroid model

A typical fluorescent-stained image of cells has a secondary antibody to bind with specific primary antibody and clearly shows the fluorescent color under the interested wavelength. However, 3D fluorescent staining has problems in antibody penetration, non-specific binding and emphasized background fluorescence [163]. One research pointed out that the antibody failed to penetrate a 3D matrix of mouse brain cell culture deeper than a few hundred microns [163]. Figure 75 shows the sample images of the 3D HT29 tumouroid model after photon irradiation and the DAPI solution (left) and DNA double strand marker 53BP1 (right) were used. The first row shows the 0Gy control group fixed at 0.5h after irradiation. The second row shows the 1Gy-irradiated sample group fixed at 48h after irradiation. The third row shows the 5Gy-irradiated sample group fixed at 48h after irradiation. The magnification power was 40x. Compared with 2D DNA double strand break fluorescent expression, 3D DNA double strand break staining showed the bulk fluorescent color inside some nuclei instead of light dots at foci fragments. There were distinguishable nuclei stained with DAPI, but the blue fluorescent overspread into the whole 3D collagen matrix. The 53BP1 DNA

double strand break antibody marked the foci inside the nuclei, but the bulk fluorescence of nuclei was senseless for measuring the degree of DNA double strand breakage. I can't draw any conclusion from Figure 75. There are two examples to show the influence of microscopy instrument on fluorescent signals. The first example is displayed in Figure 73, showing the sample confocal fluorescent images of the boundary area of Bragg peak (5Gy proton beam irradiation, fixed at 24h after irradiation). The nuclei were stained with the DAPI solution in blue and the apoptosis marker Caspase-3 was used to stain the apoptosis area in green (Alexa Fluor 488 was used as the secondary antibody). The magnification power was 40x. The second example is displayed in Figure 79, showing th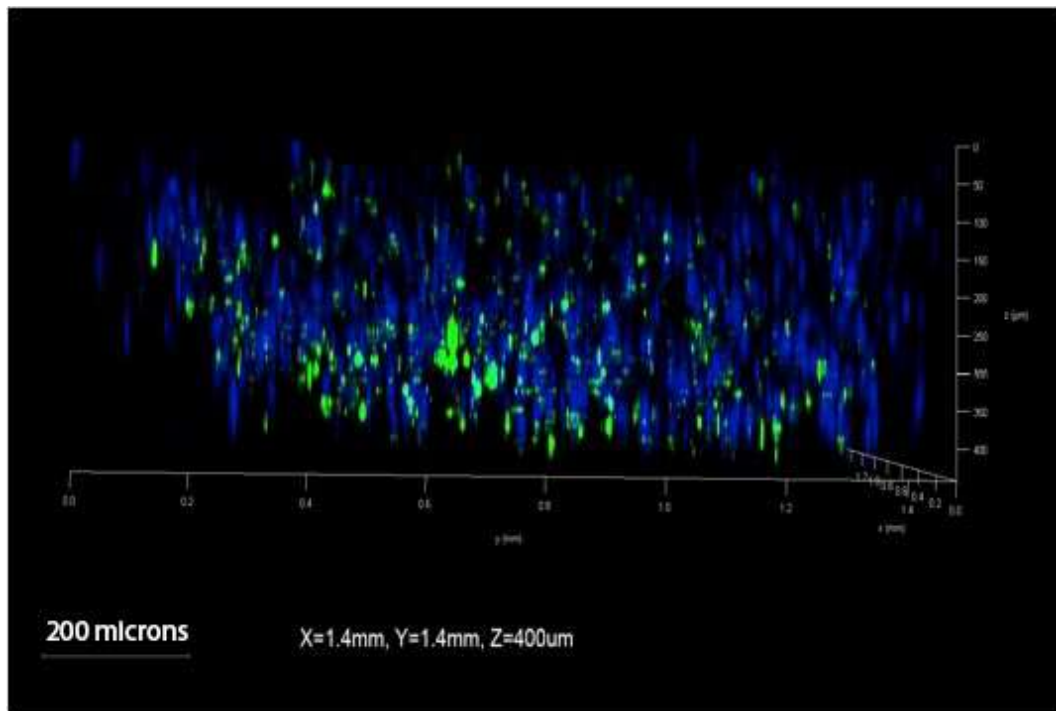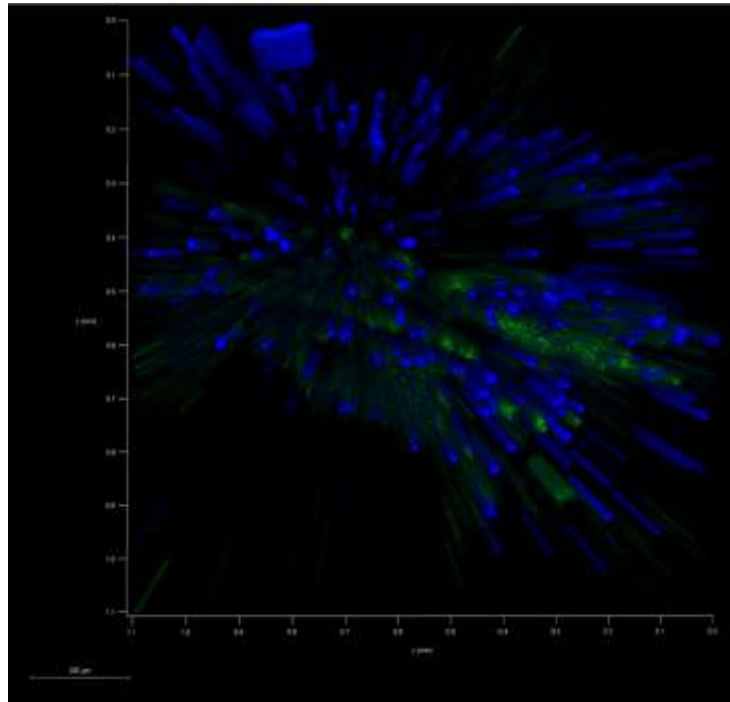e sample confocal fluorescence images of hypoxia expression after being proton irradiation (A) 1Gy irradiation, fixed at 24h after irradiation (B) 5Gy irradiation, fixed at 24h after irradiation. The nuclei were stained using the DAPI solution in blue and hypoxia marker CAIX was used to stain the hypoxia areas in green (Alexa Fluor 488 was used as the secondary antibody). The magnification power was 40x. In both examples of 3D staining, the cells were in similar seeding condition with different cell seeding number. The expression of antibodies and nuclei is clearly visible compared with that in Figure 69. Figure 69 used EVOS fluorescent microscopy and Figure 73, 77 used advanced Leica TCS SPE confocal microscopy system. According to the results shown in Figure 73 and 79, conclusions could be easily drawn according to the images because the staining was clear. It meant that the quality of microscopy instrument affects the image quality of fluorescent staining, and poor microscopy instrument will lead to problems in fluorescent staining.

5.2. Difference in biological expression between 2D and 3D after irradiation

5.2.1. Apoptosis expression

For 2D apoptosis expression of the HT29 colorectal cancer cell line, 3 sample groups were used in the experiment. The irradiation doses were the same for all sample groups, i.e. 0Gy for control, 1Gy for low irradiation dose and 5Gy for high irradiation

dose. The first sample group was fixed at 0.5h and 24h after irradiation for preliminary study. The second sample group had a fixation time of 0.5h, 2h, 24h and 48h after irradiation. The third sample group had a fixation time of 0.5h, 4h, 8h and 48h after irradiation.

The experiment design of the second sample group was similar to that of the third sample group. The same conclusion was drawn, indicating that the high irradiation dose will induce more cell apoptosis. The difference lay in the measurement method. The result indicated that the highest apoptosis occurred at 2h after irradiation rather than at 24h or 48h after irradiation in the third sample group. The fourth sample group had the highest apoptosis level at 48h after irradiation. However, the standard derivation was high for the third sample group and the fourth sample group was improved from previous experiments. The reproducibility was better, and the experiment design was optimized. The standard derivation was also lower.

The problem of 3D fluorescent staining has been discussed in the previous section. The microscopy instrument is the main limitation to get accurate results. As shown in Figure 67, the 0Gy, 1Gy and 5Gy sample groups had similar apoptosis marker expression. The interesting thing was that the control group also exhibited an elevated level of apoptosis.

One experiment plan was conducted for 3D apoptosis of the HT29 colorectal cancer cell line after proton irradiation. Figure 73 shows the difference in apoptosis expression at the boundary of the spread-out Bragg peak area. Figure 71 shows the splice of several images along the proton beam irradiation direction. Figure 72 shows the fluorescent level along the proton beam irradiation direction. The fluorescent level along the proton beam can correlated to the dose profile shown in Figure 72. The spread-out Bragg peak was a flat dose region. Therefore, the average fluorescent expression level at the spread-out Bragg peak area was measured, as shown in Figure

72. Figure 74 shows that the 5Gy proton irradiation beam induced significant cell apoptosis in the spread-out Bragg peak area over 1Gy proton irradiation dose and control group.

5.2.2. Hypoxia expression

2D hypoxia was not measured because the flat culture did not provide an oxygen depth gradient to show the hypoxia phenomenon. For 3D HT29 colorectal cancer cells after proton irradiation, Figure 79 shows the sample confocal fluorescence images of hypoxia expression after proton (A) 1Gy irradiation, fixed at 24h after irradiation (B) 5Gy irradiation, fixed at 24h after irradiation. The nuclei were stained with the DAPI solution in blue and the hypoxia marker CAIX was used to stain the hypoxia areas in green (Alexa Fluor 488 was used as the secondary antibody). The magnification power was 40x. Both images were Z-stack 3D confocal microscope images. The direction of images was converted to fit the proton beam irradiation direction. The bottom of the images had the same position with the bottom of samples. The Y-axis of both images indicated the depth of the cell-collagen matrix. The bottom area had more hypoxia fluorescent marker signal expression. The bottom area had less oxygen content from the surface of the cell-collagen matrix. Figure 80 plots the hypoxia expression signal intensity versus sample depth for proton irradiation samples. The irradiation doses were 0Gy, 1Gy and 5Gy. Samples were fixed either at 24h or at 0.5h after irradiation. Due to the fluorescent staining problem of 3D sample mentioned previously, I measured the peak fluorescent expression and the average fluorescent expression of the whole tumouroid area. The sample images were sectorized into areas. The Image J software was used to measure the fluorescent level of those area and plot the figures. The results showed that as the depth increased, both average fluorescent expression of hypoxia and peak fluorescent expression of hypoxia were enhanced. The hypoxia expression depended on the sample depth but not the irradiation dose. The average fluorescent expression had less standard derivation, and peak fluorescent expression value was not stable. I also plot the hypoxia expression signal intensity versus sample

depth of all 3D collagen HT29 colorectal cancer cell line models in Figure 81. It equaled to the average value of the control group, 1Gy- and 5Gy-irradiated sample groups. The result could reach the same conclusion.

5.2.3. DNA double strand break expression

Figure 85 shows the 2D MB231 breast cancer cells which were stained using the DAPI solution in blue and were stained using the 53BP1 antibody in green (Alexa Fluor 488 as the secondary antibody). The cell was proton irradiated with 1.5Gy dose and fixed at 0.5h. The clear shape of blue area indicated the position of nuclei, and the light dots of green color inside the nuclei indicated the foci fragments after DNA double strand breakage. The magnification power was as high as 63x. Figure 75 shows the 3D HT29 tumouroid model after photon irradiation that was marked with the DAPI solution (left) and the DNA double strand marker 53BP1 (right). The first row shows the 0Gy control group fixed at 0.5h after irradiation. The second row shows the 1Gy-irradiated sample group fixed at 48h after irradiation. The third row shows the 5Gy-irradiated sample group fixed at 48h after irradiation. The magnification power was40x. As mentioned previously, no conclusion has been drawn from Figure 75 due to the fluorescent staining problem. Figure 75 is a good example, and the work was accessed from Keir Ovington and Manish Trivedi. Their project was about the effect of gold nanoparticles on the biological effectiveness of proton therapy. They drew the conclusion that DSBs were not significantly affected in number with higher LET proton beam radiation [164]. However, the cell line was different, i.e. MB231 breast cancer cell line against HT29 colorectal cancer cell line. The accessed conclusion was not helpful for my project.

5.3. Spheroid growth and migration after irradiation

5.3.1. Dose dependence

Figure 83 and Figure 84 plot the volume and diameter of 15 individual spheroid per irradiation dose. Most of the spheroids had an initial diameter between 100μm and 200μm. In the control group, spheroids with initial diameter around 100 μm grew to a

diameter of 200μm on day 12. Spheroids with initial diameter around 200μm grew to a diameter of 500μm on day 12. In the 4Gy- irradiated sample group, spheroids with initial diameter around 100μm grew to a diameter of 250μm on day 12. Spheroids with initial diameter around 200μm grew to have a diameter of 400μm on day 12. In the 8Gy-irradiated sample group, spheroids with initial diameter between 75μm to 100μm grew to a diameter of 100μm to 350μm on day 12. In the 12Gy-irradiated sample group, spheroids with initial diameter between 100μm to 200μm grew to a diameter of 200μm to 350μm on day 12. The results showed that higher irradiation doses caused spheroid size shrinkage compared with lower irradiation doses.

5.3.2. Spheroid growth

Figure 82 shows that HT29 colorectal cancer cell spheroids were still growing after photon irradiation. On day 0, which was the second day after spheroid transfer from the 96-well ultra-low attachment plate to the 96-well tissue culture plate and the first day of photon irradiation, the spheroids kept the original round shapes and show clear boundaries. On day 6, the spheroid body grew, and the boundary became unapparent. The spheroids had already invaded into surrounding collagen matrixes on day 6. On day 12, the spheroids further grew and invaded. Adjacent spheroids were trend to bind together. On day 12 and day 6, the shape of spheroid may not be round.

Figure 84 shows the diameter of the 3D HT29 colorectal cancer cell spheroid after 0Gy, 4Gy, 8Gy and 12Gy irradiation, and the spheroid was cultured from Day 0 to Day 12. Samples were imaged every 2 days, and there were 15 individual spheroids on track per sample group. Because the spheroids varied in size, large spheroids had growth behavior different from that of tiny spheroids.

6. Conclusion

To further implement 3D collagen cancer models to meet the photon and proton irradiation experiment requirements, I adopted the immunofluorescent staining

method to measure biological behavior changes after irradiation through confocal and fluorescent microscopy. Firstly, the 3D collagen HT29 colorectal cancer model was built in FluoroDish dishes for photon irradiation, and in slide flasks for proton irradiation. Caspase-3 marker was used to stain the 2D photon experiment and 3D photon and proton experiments. The comparison between 2D results is significantly different from 3D signal intensity because of the culture type. The measurement of apoptosis index suggested that high apoptosis index with high irradiation dose led to a greater cell apoptosis rate. The fixation time matters. For example, the apoptosis index of the sample fixed at 0.5h after irradiation was half the same as the value of the sample fixed at 4h after irradiation. For proton irradiation, the confocal microscopy image module was used to get high quality results than fluorescent microscopy in our department. The key novelty of my experiment is to build a methodology that can measure cell behavior changed after proton irradiation and such cell behavior can correlate to dose profile. The apoptosis study of the 3D proton-irradiated collagen cancer model was vibratome processed to obtain slices along the direction of the spread-out Bragg peak. By measuring the fluorescent intensity along the Bragg peak, a series of cell behavior can be analyzed to find their relationships. For example, the cell apoptosis or DNA double strand break can correlate to the depth of hypoxia gradient. Currently, the design methodology still needs to be improved. For example, the fluorescent staining of DNA double strand breakages shows no valuable result due to sample processing (i.e. high magnification power is requiring focusing on foci inside of nuclei. However, the sample slice should be ultra-thin. Current vibratome sample slicing does not have a high reproducibility). Hypoxia analysis confirms that hypoxia level expression is not dependent on the irradiation dose. It depended on the sample depth. For the 3D HT29 colorectal cancer cell spheroid model, higher irradiation dose led to higher percentage that the spheroids decrease their volume (shrinkage) at day 12. For example, in the 12Gy photon-irradiated 3D spheroid model, on day 12, 66.6% of the spheroids decreased in size by day 12 and 33.3% of the spheroids are still growing. From the morphology analysis in Figure 80, when the irradiation dose is high,

the core of spheroid breaks down and the cells spread out from spheroids, indicating that the cell was dead after irradiation.

Further works

The 3D cancer model is a flexible platform which can be tailored to different applications such as the drug delivery test and targeting because the cancer cells in 3D geometry is fluorescent imageable. The design geometry of 3D model is flexible as well, it can be spheroid or tumoroid with different cell seeding and collagen density. Further biological property characterization of the 3D cancer model depends on application types. The basic characterization of 3D colorectal tumoroid is done but not for spheroid model. The project mainly investigates the 3D spheroid seeding, transferring and culturing techniques. Further works can be the metabolism study of 3D cancer spheroid model, biomarker expression and the control of spheroid size after seeding.

The resolution improvement of MRI machine is important to obtain data with higher-accuracy analysis. As mentioned in discussion session of Chapter 3, the uniformity and reproducibility of 3D tumouroid is low for conventional 3D collagen fabrication method. RAFT^{TM} 3D tumouroid has higher uniformity and controllable collagen density. A RAFT^{TM} 3D tumouroid model can be used to produce the same tumouroid layout and design of Study I, Study II and Study III described in Chapter 3. These would help find the relationship between MR imaging contrast, collagen, and cell density.

For radiobiology of the 3D cancer model, the method of sample slicing should be improved for better reproducibility and thickness controls by choosing a different biomaterial to strengthen the physical structure of soft collagen models prior to sample slicing. The effect of radiation dose on hypoxia, which is how hypoxic cells are radiation resistant, could be measured by the same method to plot a curve of the apoptosis markers fluorescent expression versus sample length against proton or photon irradiation dose. The 3D collagen spheroid model could be proton or photon irradiated as well.

Summary

The 3D collagen cancer model can be used as an imageable biophantom for biological researches after characterization. The metabolism of cancer cells in this model is dependent on cell lines. Cell viability and the number of culture days are negatively correlated. The decrease rate is graduate for all seeding numbers. The collagen density of the model can be controlled. Traditional metal mould compression can create collagen density ranging from 1.25% to 3.5%. With the aid of a 4mm plastic blocker to stop the compression, the collagen density can increase up to 20%. This increase the application range of the model because it can simulate specific tumour microenvironment. The cutting of 3D tumouroids will affect the invasion of cancer cells. The cancer cells are not uniformly distributed in any artificial cancer mass because the physical compression increases the local collagen density at the boundaries. For a more invasive SW620 cancer cell line, cells start to invade on day 6, and on day 18 the mean invasion distance may be 416µm in uncompressed collagen gels. Invading bodies change the morphology from single cells to cluster of cells, and finally there are formation of spheroids. This phenomenon is obvious on day 18. For a less invasive HT29 cancer cell line, there is less invasion and depending on cell seeding numbers. A 1,000 initial cell seeding number per well is suggested to culture spheroid on 96-well ultra-low attachment plates, and the cells are ready to harvest on day 9. Extra high cell seeding number will cause random elongated morphology of spheroids. The fibers will guide the invasion of spheroids, and adjacent spheroids are binding together after cell culture. The problems of current 3D collagen cancer models occur with low reproducibility due to the pH level control inaccuracy and compression methodology. The uniformity of tumouroids is also low. These problems can be improved by changing the compression method such as the application of RAFT™ 3D collagen system. The aim of the second chapter was to design an MR-imageable 3D *in vitro* tumour model to investigate what properties of the tumour model contributed to image signal, and to set up an MR environment that can image samples. The 3D collagen

tumouroid model is designed biocompatible and can show imaging contrast under MRI sessions. T_1 inversion recovery RARE and T_2 MSME MR imaging sequences are processed to imaging four individual sample groups. Due to the low reproducibility of collagen compression, pH neutralization accuracy and low sample uniformity after collagen compression, the signal intensity inside tumouroids is lower than that of dense collagen boundaries (boundary effect is discussed in Chapter 2). T_2 MSME MR imaging sequences can get more signal contrast from the inside of tumouroids so that more accurate data can be obtained. The T_2 MSME imaging sequences also has a shorter error bar than T_1 inversion recovery RARE imaging sequences. The images of four studies suggest 1000ms TI, 12ms TE and 10000ms TR for T_1 Inversion recovery RARE to get best signal contrast and suggest 400ms TE and 5000-6000ms TR for T_2 MSME MR imaging sequence to get the best signal contrast. The methodology of RAFT^{TM} 3D collagen cancer model system can increase the sample reproducibility and uniformity. Such model was used in Study IV to test the relationship between MR signal contrast and different collagen density. The morphology had confirmed the sample uniformity, and the technique was reproducible. The result suggests that there was no significant relation between collagen density and MR imaging contrast. This conclusion is the same as the analysis of Study II which is the MRI session of two acellular tumouroids. For result of Study I and Study III, the uncompressed collagen, the acellular tumouroid, 5M and 10M cells/ml seeding density tumouroids showed no significant difference in greyscale intensity. For dense collagen boundaries, the acellular, 5M and 10M cells/ml seeding density tumouroids had the highest level of greyscale threshold, but it was not increasing with ascending cell seeding densities. For inside of the tumouroid, the acellular, 5M and 10M cells/ml seeding density tumouroids had higher greyscale threshold than uncompressed collagen area, but this was formed to be significant. There was no evidence that MR imaging contrast was enhanced with increasing cell seeding density from the plot. There was no significant greyscale difference between acellular tumouroid and 7.5×10^6 cells/ml seeding density HT29 tumouroid for uncompressed collagen in Study I. Therefore, currently the plots

suggest that the imaging contrast is not significantly dependent on neither cell seeding density nor collagen density. However, the pixel resolution and imaging quality affect the accuracy of region-of-interest approach. These affecting elements could be improved by changing imaging acquisition settings to the highest level, which requires a longer data acquisition time and optimizing imaging equipment. Further work is to have an MRI session of reproducible and high uniformity RAFT^{TM} 3D collagen models with different cell seeding density to explore the relationship between cell seeding density and MRI contrast. Last chapter is to further implement 3D collagen cancer models to meet the photon and proton irradiation experiment requirements, I used the immunofluorescent staining method to measure biological behavior changes after irradiation by confocal and fluorescent microscope. Firstly, the 3D collagen HT29 colorectal cancer model was building in FluoroDish dishes for photon irradiation and in slide flasks for proton irradiation. The Caspase-3 marker was used for staining in the 2D photon experiment and 3D photon and proton experiments. The comparison between 2D results was significantly different from 3D signal intensity because of the cell culture type. The measurement of apoptosis index suggests that high apoptosis index on high irradiation dose leads to a more cell apoptosis rate. The fixation time matters. The apoptosis index halved at 0.5h after irradiation compared with that at 4h after irradiation. For proton irradiations, the confocal microscopy image module was used to get higher quality result than fluorescent microscope in our department. The key novelty of my experiment is to build a methodology that can measure cell behavior changed after proton irradiation, and such cell behavior can correlate to dose profile. The apoptosis study on the 3D proton irradiated collagen cancer model is vibratome processed to get slices along the direction of spread-out Bragg peak. By measuring the fluorescent intensity along the Bragg peak, a series of cell behavior can be analyzed and find their relationships. For example, the cell apoptosis or DNA double strand breakage can correlate to the depth of hypoxia gradient. Currently, the design of methodology still needs to be improved. For example, the fluorescent staining of DNA double strand break doesn't show any valuable results due to sample processing

(i.e. High magnification power requires focus on foci inside nuclei. However, the sample slice should be ultra-thin. Current vibratome sample slicing does not have a high reproducibility). According to hypoxia analysis, hypoxia level expression does not depend on the irradiation dose, but on the sample depth. For the 3D HT29 colorectal cancer cell spheroid model, if a high irradiation dose is used, the volume (shrinkage) of spheroids is more likely to decrease on day 12. For example, 12Gy photon-irradiated 3D spheroid model on showed that 66.6% of the spheroids decreased in size on day 12, and only 33.3% of the spheroids were still growing. According to the analysis of morphology shown in Figure 80, when a higher dose of irradiation was used, the core of spheroids broke down, and the cells spread out from the spheroids, which meant that the cells were dead after irradiation. In summary, the 3D collagen cancer model is flexible and imageable biophantom for MRI and radiation studies. Therefore, this model is applicable to lots of analysis methods to show satisfactory results.

References:

1. GBD 2015 Mortality and Causes of Death Collaborators "Global, regional, and national life expectancy, all-cause mortality … Study 2015", Lancet, 8th October 2016. 388 (10053): 1459-1544, Doi: 10.1016/S0140-6736(16)31012-

2. Cancer data and statistics in numbers, Cancer Research UK [Online source] Accessed from [July, 2018]: http://www.cancerresearchuk.org/health-professional/cancer-statistics-for-the-uk.

3. "National Cancer Registration and Analysis Service Cancer statistics: availability and location". Public Health England, PHE publications, published in April 2017.

4. Jasveer Kaur, John Broggio. "Cancer registration statistics, England: first release, 2016", Office for National Statistics, 25th January 2018.

5. Cancer data dashboard, Public Health England [Online source] Accessed from [July 2018]: https://www.cancerdata.nhs.uk/dashboard#?tab=Overview.

6. Colorectal cancer 5-year survival rate [Online source] Accessed from [July, 2018]: https://seer.cancer.gov/report_to_nation/statistics.html.

7. Douglas H., Robert A. W. "The hallmarks of cancer", Cell, Vol. 100, Page 57–70, 7th January 2000.

8. Douglas H., Robert A. W. "The hallmarks of cancer: The next generation", Cell, Vol. 144, Page 646-675, 4th March 2011.

9. Cheng N., Chytil A, etc. "Transforming growth factor signaling in mammary carcinoma cells to promote scattering and invasion", Molecule Cancer Research, Vol. 6, Page 1521-1533, 2008.

10. Bonnet D., Dick J. E., "Human acute myeloid leukemia is organized as a hierarchy that originates from a primitive hematopoietic cell", Nat. Med, Vol. 3, Page 730-737, 2004.

11. Wertz I. E., Dixit V. M., "Regulation of death receptor signaling by the ubiquitin system", Cell Death Differ. Vol. 17. Page 14-24, 2010.

12. Burkhart D. L., Sage J., "Cellular mechanisms of tumour suppression by the

retinoblastoma gene", Nat. Rev. Cancer, Vol. 8, Page 671-682, 2008.

13. Adams J. M., Cory S., "The Bcl-2 apoptotic switch in cancer development and therapy". Oncogene, Vol. 26, Page 1324-1337, 2007.

14. Willis S. N., Adams J. M., "Life in the balance: how BH3-only proteins induce apoptosis", Curr. Opin. Cell Biol. Vol. 17, Page 617-625, 2005.

15. Blasco M. A., "Telomeres and human disease: ageing, cancer and beyond", Nat. Rev. Genet. Vol. 6, Page 611-622, 2005.

16. Shay J. W., Wright W. E., "Hayflick, his limit, and cellular ageing", Nat. Rev. Mol. Cell Biol. Vol. 1, Page 72-76, 2000.

17. Hanahan D., Folkman J., "Patterns and emerging mechanisms of the angiogenic switch during tumorigenesis", Cell, Vol. 86, Page 353-364, 1996.

18. Baeriswyl V., Christofori G., "The angiogenic switch in carcinogenesis", Semin. Cancer Biol. Vol. 19, Page 329-337, 2009.

19. Nagy J. A., Chang S. H., etc. "Heterogeneity of the tumor vasculature", Semin. Thromb. Hemost. Vol. 36, Page 321-331, 2010.

20 Raza A., Franklin M. J., Dudek A. Z., "Pericytes and vessel maturation during tumor angiogenesis and metastasis", Am. J. Hematol. Vol. 85, Page 593-598, 2010.

21. Bergers G., Song S. "The role of pericytes in blood-vessel formation and maintenance". Neuro-oncol. Vol. 7. Page 452-464, 2005.

22. Berx G., Van Roy F., "Involvement of members of the cadherin superfamily in cancer". Cold Spring Harb. Perspect. Biol. Vol. 1, a003129, 2009.

23. Talmadge J. E., Fidler I. J. "AACR centennial series: the biology of cancer metastasis: historical perspective", Cancer Res. Vol. 70, Page 5649-5669, 2010.

24. John Mendelsohn, Peter M. Howley, etc. "The molecular basis of cancer", Third Edition, Elsevier (2011), ISBN: 9787030316073.

25. The tumor-suppressor gene [Online Document] are accessed from: http://science.education.nih.gov/supplements/nih1/cancer/guide/under standing2.htm

26. The differences between cancer and normal cell [Online Image] are accessed from : http://en.wikipedia.org/wiki/File:Normal_cancer_cell_differences_from_NIH.png.

(Originally resource comes from National Cancer Institute).

27. Xu Zhang, "Teaching material – canceration of cells", Bulletin of Biology, Vol. 12, Issue No. 5, 2012.

27+: Shahzina Kanwal, "Effect of O-GlcNAcylation on tamoxifen sensitivity in breast cancer derived MCF-7 cells", Research Gate Unpublished Thesis.

28. Colon cancer characteristics [Online Resource] Accessed from [July, 2018]: https://www.botanical-online.com/english/colon-cancercharacteristics. htm.

29. Nicki R. Colledge, Brian R. Walker and Stuart Haralson. Davidson's Principles and Practice of Medicine, 21st ed. United Kingdom: Churchill Livingstone Elsevier, P. 909-12, 2010.

30. T. A. M. Alkarboly, "Characteristics of colorectal cancer patients in Kurdistan center for gastroenterology and hepatology", Int. J. Dev. Res., Vol. 5, Issue 12 (2015), pp. 6327-6333.

31. T. Colangelo, G. Polcaro, etc. "Friend or foe? The tumour microenvironment dilemma in colorectal cancer", Biochimica et Biophysica Acta (BBA) – Reviews on cancers, Vol. 1867, Issue 1, Jan. 2017, Page: 1-18.

32. J. Guinney, R. Dienstmann, X. Wang, etc, "The consensus molecular subtypes of colorectal cancer", Nat. Med., 21 (2015), pp. 1350-1356.

33. G. Cui, A. Yuan, R. Goll, B. Vonen, J. Florholmen, "Dynamic changes of interleukin-8 network along the colorectal adenoma-carcinoma sequence", Cancer Immunol. Immunother., CII, 58 (2009), pp. 1897-1905.

34. R.N. Dubois, "Role of inflammation and inflammatory mediators in colorectal cancer", Trans. Am. Clin. Climatol. Assoc., 125 (2014), pp. 358-372, discussion 372-353.

35.R.N. Apte, S. Dotan, M. Elkabets, M.R. White, E. Reich, Y. Carmi, X. Song, T. Dv ozkin, Y. Krelin, E. Voronov. "The involvement of IL-1 in tumorigenesis tumor invasiveness, metastasis and tumor-host interactions", Cancer Metastasis Rev., 25 (2006), pp. 387-408.

36. R. Apte, Y. Krelin, X. Song, S. Dotan, E. Recih, M. Elkabets, Y. Carmi, T. Dvorkin, R. M. White, L. Gayvoronsky, S. Segal, E. Voronov, "Effects of micro-environment-and malignant cell-derived interleukin-1 in carcinogenesis, tumour invasiveness and tumour-host interactions", Eur. J. Cancer, 42 (2006), pp. 751-759.

37. M. Krzystek,Korpacka, D. Diakowska, B. Kapturkiewicz, M. Bebenek, A. Gamian, "Profiles of circulating inflammatory cytokines in colorectal cancer (CRC) high cancer risk conditions, and health are distinct. Possible implications for CRC screening and surveillance", Cancer Lett., 337 (2013), pp. 107-114.

38. C. Maihofner, M.P. Charalambous, U. Bhambra, T. Lightfoot, G. Geisslinger, N.J. Gooderham, "Expression of cyclooxygenase-2 parallels expression of interleukin-1beta: interleukin-6 and NF-kappaB in human colorectal cancer", Carcinogenesis, 24 (2003), pp. 665-671.

39. C. Maihofner, M.P. Charalambous, U. Bhambra, T. Lightfoot, G. Geisslinger, N.J. Gooderham, "Expression of cyclooxygenase-2 parallels expression of interleukin-1beta: interleukin-6 and NF-kappaB in human colorectal cancer", Carcinogenesis, 24 (2003), pp. 665-671.

40. SM Powell, N Zilz, Y Beazer-Barclay, TM Bryan, SR Hamilton, SN Thibodeau, et al. "APC mutations occur early during colorectal tumorigenesis", Nature, 359 (6392) (1992), p. 235.

41. LN Kwong, WF. Dove, "APC and its modifiers in colon cancer", APC Proteins, Springer (2009), pp. 85-106.

42. I Spier, S Holzapfel, J Altmüller, B Zhao, S Horpaopan, S Vogt, et al. "Frequency and phenotypic spectrum of germline mutations in POLE and seven other polymerase genes in 266 patients with colorectal adenomas and carcinomas", International Journal of Cancer, 137 (2) (2015), pp. 320-331.

43. E Lucci‑Cordisco, M Risio, T Venesio, M. Genuardi, "The growing complexity of the intestinal polyposis syndromes", American Journal of Medical Genetics Part A, 161 (11) (2013), pp. 2777-2787.

44. DB Lombard, KF Chua, R Mostoslavsky, S Franco, M Gostissa, FW. Alt, "DNA repair, genome stability, and aging", Cell, 120 (4) (2005), pp. 497-512.

45. E Sanz-Garcia, G Argiles, E Elez, J. Tabernero, "BRAF mutant colorectal cancer: prognosis, treatment, and new perspectives", Annals of Oncology, 28 (11) (2017), pp. 2648-2657.

46. A Calon, E Espinet, S Palomo-Ponce, DV Tauriello, M Iglesias, MV Céspedes, et al. "Dependency of colorectal cancer on a TGF-β-driven program in stromal cells for metastasis initiation", Cancer Cell, 22 (5) (2012), pp. 571-584.

47. M Toyota, N Ahuja, M Ohe-Toyota, JG Herman, SB Baylin, J-P Issa, "CpG island methylator phenotype in colorectal cancer", Proceedings of the National Academy of Sciences, 96 (15) (1999), pp. 8681-8686.

48. De Craene B, Berx G (2013). "Regulatory networks defining EMT during cancer initiation and progression". Nature Reviews Cancer. 13: 97–110.

49. Chakrabarti R, Hwang J, etc (2012). "Elf5 inhibits the epithelial-mesenchymal transition in mammary gland development and breast cancer metastasis by transcriptionally repressing Snail2", Nat Cell Biol. 14 (11): 1212–1222.

50. Kalluri, Raghu; Weinberg, Robert A. (2009). "The basics of epithelial-mesenchymal transition". The Journal of Clinical Investigation. 119 (6): 1420–1428.

51. Lindsay J, McDade SS, Pickard A, McCloskey KD, McCance DJ (2011). "Role of DeltaNp63gamma in epithelial to mesenchymal transition". J Biol Chem. 286 (5): 3915–24.

52. Trung Vu, Pran K. Datta, "Regulation of EMT in Colorectal Cancer: A Culprit in Metastasis", Cancers (Basel). 2017 Dec; 9(12): 171.

53. Francí C., Gallén M., Alameda F., Baró T., Iglesias M., Virtanen I., de Herreros A.G. "Snail1 protein in the stroma as a new putative prognosis marker for colon tumour". PLoS ONE. 2009; 4: e5595.

54. Shioiri M., Shida T., Koda K., Oda K., Seike K., Nishimura M., Takano S., Miyazaki M. "Slug expression is an independent prognostic parameter for poor survival in colorectal carcinoma patients". Br. J. Cancer. 2006; 94:1816–1822.

55. Zhang G.J., Zhou T., Tian H.P., Liu Z.L., Xia S.S. "High expression of ZEB1 correlates with liver metastasis and poor prognosis in colorectal cancer". Oncol. Lett. 2013; 5:564–568.

56. Gomez I., Peña C., Herrera M., Muñoz C., Larriba M.J., Garcia V., Dominguez G., Silva J., Rodriguez R., de Herreros A., et al. "TWIST1 is expressed in colorectal carcinomas and predicts patient survival". PLoS ONE. 2011;6: e18023.

57. Yu H., Jin G.Z., Liu K., Dong H., Yu H., Duan J.C., Li Z., Dong W., Cong W.M., Yang J.H. "Twist2 is a valuable prognostic biomarker for colorectal cancer". World J. Gastroenterol. 2013; 19:2404–2411.

58. General Info. about colon cancer [Online resource] accessed from [19th July 2018] https://www.cancer.gov/types/colorectal/patient/colon-treatment-pdq.

59. AJCC (American Joint Committee on Cancer) Cancer Staging Manual, 7th edition, Edge, SB, Byrd, DR, Compton, CC, et al (Eds) (Eds), Springer, New York 2010. p.143.

60. Carolyn C. Compton, "Pathology and prognostic determinants of colorectal cancer", Uptodate, Jun 2018, Online Journal.

61. The tumor microenvironment [Online Image] are accessed from [July 2018]: http://www.journalofextracellularvesicles.net/index.php/jev/article/view/20304/26321

62. Amsden B and Turner N, "Diffusion characteristics of calcium alginate gels", Biotechnol. Bioeng. 1999, 65, 605–10.

63. Kate P. M. Pepper. "Nanoparticles for tumour diagnostics", Degree of Doctor of Philosophy report from UCL, 2011, Page: 1-231.

64. K. Stock, M. F. Estrada, etc., "Capturing tumor complexity in vitro: comparative analysis of 2D and 3D tumor models for drug discovery", Sci. Rep., 6 (2016), p. 28951.

65. J. Friedrich, C. Seidel, etc., "Spheroid-based drug screen: considerations and practical approach", Nat. Protoc., 4 (2009), pp. 309-324.

66. Mehmetoğlu Ü, Ateş S and Berber R, "Oxygen diffusivity in calcium alginate gel beads containing Gluconobacter suboxydans", Artif. Cells Blood Substit. Immobil. Biotechnol., 2010, 24, 91–106.

67. Cheema U, Rong Z, Kirresh O, MacRobert A J, Vadgama P and Brown R A,

"Oxygen diffusion through collagen scaffolds at defined densities: implications for cell survival in tissue models". J. Tissue Eng. Regen Med., 2012, 6, 77–84.

68. Navarro, M.; Michiardi, A.; Castaño, O.; Planell, J.A. "Biomaterials in orthopaedics". J. R. Soc. Interface 2008, 5, 1137–1158.

69. Nair, L.S.; Laurencin, C.T. Polymers as biomaterials for tissue engineering and controlled drug delivery. Adv. Biochem. Eng. Biotechnol. 2006, 102, 47–90.

70. J. Udayabhanu, T. Karthik, "Recent Advances in Biomaterials for 3D Printing and Tissue Engineering", J. Funct. Biomater. 2018, 9, 22.

71. Di Lullo, Gloria A.; Sweeney, Shawn M.; Körkkö, Jarmo; Ala-Kokko, Leena & San Antonio, James D. "Mapping the Ligand-binding Sites and Disease-associated Mutations on the Most Abundant Protein in the Human, Type I Collagen". J. Biol. Chem. 2002, 277 (6): 4223–4231.

72. "Leather grown using biotechnology is about to hit the catwalk". The Economist. Archived from the original on 2017-09-01.

73. Sabiston textbook of surgery board review, 7th edition. Chapter 5: wound healing, question 14.

74. Harpreet K Dhimana, Alok R Raya, Amulya K Pandac, "Three-dimensional chitosan scaffold-based MCF-7 cell culture for the determination of the cytotoxicity of tamoxifen", Biomaterials 26 (2005) 979-986.

75. Hughes, C.S., Postovit, L.M., Lajoie, G.A. "Matrigel: a complex protein mixture required for optimal growth of cell culture". Proteomics. 2010, 10 (9): 1886–90.

76. Benton, G., George, J., Kleinman, H.K., Arnaoutova, I. "Advancing science and technology via 3D culture on basement membrane matrix". Journal of Cellular Physiology. 2009, 221 (1): 18–25.

77. H.K. Kleinman, G.R. Martin, "Matrigel: Basement membrane matrix with biological activity", Semin. Cancer Biol., 15 (2005), pp. 378-386.

78. Tyler K. Merceron, Sean V. Murphy, "Hydrogels for 3D bioprinting applications", Essentials of 3D Biofabrication and Translation, 2015, Pages 249-270.

79. M. Rimann, U. Graf-Hausner, "Synthetic 3D multicellular systems for drug development", Curr. Opin. Biotechnol., 23 (2012), pp. 803-809.

80. Satyavrata Samavedi, Nikhita Joy, "3D printing for the development of in vitro cancer models", Current Opinion in Biomedical Engineering, Vol. 2, June 2017, Pages 35-42.

81. N. Picollet-D'hahan, M.E. Dolega, et al, "A 3D toolbox to enhance physiological relevance of human tissue models", Trends Biotechnol. 34 (2016) 757–769.

82. J. M. Rios, J. Wubetu, et al, "Colorectal tumor 3D in vitro models: advantages of biofabrication for the recapitulation of early stages of tumour development", Biomed. Phys. Eng. Express, Vol. 4, 2018, 045010.

83. M. Zanoni, F. Piccinini, et al. "3D tumor spheroid models for in vitro therapeutic screening: a systematic approach to enhance the biological relevance of data obtained", Sci. Rep., 6 (2016), p. 19103.

84. Chun Liu, Daniela L. Mejia, etc., "Hybrid collagen alginate hydrogel as a platform for 3D tumor spheroid invasion", Acta Biomaterialia, Volume 75, 15 July 2018, Pages 213-225.

85. A. Khurana, C. Godugu, "Alginate-based three-dimensional in vitro tumor models: a better alternative to current two-dimensional cell culture models" (2018), pp. 157-183.

86. M. Alonso-Nocelo, C. Abuín, R. López-López, M. De La Fuente, "Development and characterization of a three-dimensional co-culture model of tumor T cell infiltration", Biofabrication, 8 (2016), pp. 1-13.

87. C. Yamanishi, K. Jen, S. Takayama, "Techniques to Produce and Culture Lung Tumor Organoids, in: Humana Press", Cham, 2018: pp. 1–15.

88. Sato T, Stange DE, et al. "Long-term expansion of epithelial organoids from human colon, adenoma, adenocarcinoma, and Barrett's epithelium". Gastroenterology. 2011;141(5):1762–72.

89. Katherine Castle, Mark Chen, etc., "Genetically engineered mouse models for studying radiation biology", Trans. Cancer Research, 2017, Vol 6, Supplement 5.

90. F. A. Cucinotta, Hooshang Nikjoo, Dudley T. Goodhead," Applications of amorphous track models in radiation biology", Radiation and Environmental Biophysics, July 1999, Volume 38, Issue 2, pp 81–92.

91. David S. Hill, Neil D. P. Robinson, etc., "A novel fully-humanised 3D skin equivalent to model early melanoma invasion", Mol Cancer Ther. 2015, Nov; 14(11): 2665–2673

92. R. Wood, K. Bassett, V. Foerster, et al. "1.5 tesla magnetic resonance imaging scanners compared with 3.0 tesla magnetic resonance imaging scanners: systematic review of clinical effectiveness", CADTH Technol Overv, 2 (2) (2012), p. e2201.

93. Yosef Nasseri, Sean J. Langenfeld, "Imaging for colorectal cancer", Surgical Clinics of North America, Volume 97, Issue 3, June 2017, Pages 503-513

94. M.Barral, C. Eveno, C. Hoeffel, etc, "Diffusion-weighted magnetic resonance imaging in colorectal cancer", Journal of Visceral Surgery, Volume 153, Issue 5, November 2016, Pages 361-369

95. Introduction to radiation biology [Online PowerPoint] is accessed from [July 2018]: https://www.utoledo.edu/med/depts/radther/pdf/Lecture%202%20-%20Survey%20R adiobiology%20handouts.pdf

96. Mohammad Mirza-Aghazadeh-Attari, Saber G. Darband, etc., "DNA damage response and repair in colorectal cancer: Defects, regulation and therapeutic implications", DNA Repair, Available online from 17th July 2018

97. Pooja M. Tiwari, Komal Vig, etc. "Functionalized gold nanoparticles and their biomedical applications". Nanomaterials. Vol. 1 (2011), Page 31-63

97+. Franck Bonnier, Tomasz P. Wrobel, etc. "Cell viability assessment using the Alamar blue assay: A comparison of 2D and 3D cell culture models", Toxicology in Vitro,29, pp. 124-131. doi:10.1016/j.tiv.2014.09.014

98. The working theory of AlamarBlueTM assay from official product manual [Online source] is accessed from: https://tools.thermofisher.com/content/sfs/manuals/PI DAL10251100_TI%20alamarBlue%20Rev%201.1.pdf

99. Dimension of Corning multi-well plate [Online source] is accessed form: http://csmedia2.corning.com/LifeSciences/Media/pdf/cc_surface_areas.pdf

100. Abedin, Monika and Nicole King (December 2010). "Diverse evolutionary paths to cell adhesion". Trends in Cell Biology. 20 (12): 734-742. doi:10. 1016/j.tcb. 2010.08.002.

101, Kumar; Abbas; Fausto. Robbins and Cotran: "Pathologic Basis of Disease" (7th ed.). Philadelphia: Elsevier. ISBN 0-7216-0187-1.

102. Resolution and contrast in confocal microscopy [Online source] is accessed from: https://www.olympus-lifescience.com/en/microscoperesource/primer/techniques/con focal/resolutionintro/

103. Introduction to Fluorescence Microscopy [Online source] is accessed from: https://www.microscopyu.com/techniques/fluorescence/introduction-to-fluorescence-microscopy

104. Dubessy C., Merlin J.M., Marchal C., Guillemin F. Spheroids in radiobiology and photodynamic therapy. Crit Rev Oncol Hematol. 2000; 36:179–192

105. Durand R.E., Sutherland R.M. Effects of intercellular contact on repair of radiation damage. Exp Cell Res. 1972; 71:75–80

106. Chapman J.D., Dugle D.L., Reuvers A.P., Meeker B.E., Borsa J. Letter: studies on the radiosensitizing effect of oxygen in Chinese hamster cells. Int J Radiat Biol Relat Stud Phys Chem Med. 1974; 26:383–389.

107. Ferrante A., Rainaldi G., Indovina P., Indovina P.L., Santini M.T. Increased cell compaction can augment the resistance of HT-29 human colon adenocarcinoma spheroids to ionizing radiation. Int J Oncol. 2006; 28:111–118

108. Olive P.L., Durand R.E. Drug and radiation resistance in spheroids: cell contact and kinetics. Cancer Metastasis Rev. 1994; 13:121–138

109. Quintiliani M. Int J Radiat Biol. 1986; 50:573–594

110. Rockwell S. Manual de Radiotherapia Oncologia. Yale University; New Haven CT: 1989. Principios de radiobiologia.

111. Y.-L. Chiu, S.-C. Chen, C.-J. Su et al., "pH-triggered injectable hydrogels prepared from aqueous N-palmitoyl chitosan: in vitro characteristics and in vivo

biocompatibility," Biomaterials, vol. 30, no. 28, pp. 4877–4888, 2009.

112. Alberts, B.; A. Johnson; J. Lewis (2002). "Fibroblasts and Their Transformations: The Connective-Tissue Cell Family". Microbiology of the Cell (4th ed.). New York: Garland Science.

113. Agata Nyga, Marilena Loizidou, Mark Emberton, Umber Cheema, "A novel tissue engineered three-dimensional in vitro colorectal cancer model", Acta Biomaterialia, Volume 9, Issue 8, August 2013, Pages 7917-7926

114. D. Ahmed, P. W. Eide, I. A. Eilertsen, etc. "Epigenetic and genetic features of 24 colon cancer cell lines", Oncogenesis, 2013 Sep; 2(9): e71, doi: 10.1038/oncsis. 2013.35, PMCID: PMC3816225

115. Ktubg E. Fung, Xiaojing Su, etc. "Understanding the impact of 2D and 3D fibroblast cultures on in vitro breast cancer models". PLoS One Vol. 8, Issue no. 10 (2013) October 4th

116. A. Nyga, U. Cheema, and M. Loizidou, Tissue Engineering for Cancer Therapy: In vitro modelling of tumour invasion. PhD thesis, University College London, Division of Surgery and Interventional Sciences, Aug. 2011.

117. Parenteau-Bareil R, Gauvin R, Berthod F. Collagen-based biomaterials for tissue engineering applications. Materials (Basel)2010; 3(3): 1863–1887

118. Coulson-Thomas VJ, Coulson-Thomas YM, Gesteira TF, de Paula CA, Mader AM, Waisberg J, Pinhal MA, Friedl A, Toma L, Nader HB Cell Tissue Res. 2011 Nov; 346(2):223-36.

119. Yip D, Cho CH. "A multicellular 3D heterospheroid model of liver tumour and stromal cells in collagen gel for anti-cancer drug testing", Biochem. Biophys Res Commun. 2013 Apr 12;433(3):327-32. doi: 10.1016/j.bbrc.2013. 03.008

120. Smith and Hashemi, "Foundations of materials science and engineering". 5th Edition, ISBN-10: 0073529249

121. Macmillan McGraw-Hill Company. "Chapter 17: Biomaterials" PowerPoint [Online Resource] Accessed from: http://slideplayer.com/slide/6324211/

122. R. K. Willits and S. L. Skornia, "Effect of collagen gel stiffness on neurite extension," Journal of Biomaterials Science, vol. 15, no. 12, pp. 1521–1531, 2004.

123. Walsh AJ., Cooke RS., etc. "Collagen density and alignment in responsive and resistant trastuzumab-treated breast cancer xenografts", J Biomed Opt. 2015 Feb;20(2):26004. Doi: 10.1117/1.JBO.20.2.026004.

124. Weijing Han, Shaohua Chen, etc. "Oriented collagen fibers direct tumour cell intravasation", PNAS, 11208–11213, Doi 10.1073/pnas.1610347113

125. Rasheena Edmondson, Jessica J. Broglie, etc. "Three-Dimensional Cell Culture Systems and Their Applications in Drug Discovery and Cell-Based Biosensors", Assay Drug Dev Technol. 2014 May 1; 12(4): 207–218. Doi: 10.1089/adt.2014.573

126. Xiao Wan, Zhaohui Li, etc. "Three-dimensional perfused tumour spheroid model for anti-cancer drug screening", Biotechnol Lett. 2016; 38: 1389-1395. Doi: 10.1007/s10529-016-2035-1

127. Patrice Penfornis, Joseph D. Fernandes, etc. "Three-dimensional spheroid model using cancer and stromal cells for in vitro drug screening assays", J Stem Cell Res Med, Volume 2(1): 1-5; 2017 Doi: 10.15761/JSCRM.1000117

128. D. Schmaljohann, "Thermo- and pH-responsive polymers in drug delivery," Advanced Drug Delivery Reviews, vol. 58, no. 15, pp. 1655–1670, 2006.

129. H. Tan, C. M. Ramirez, N. Miljkovic, H. Li, J. P. Rubin, and K. G. Marra, "Thermosensitive injectable hyaluronic acid hydrogel for adipose tissue engineering," Biomaterials, vol. 30, no. 36, pp. 6844–6853, 2009.

130. Y.-L. Chiu, S.-C. Chen, C.-J. Su et al., "pH-triggered injectable hydrogels prepared from aqueous N-palmitoyl chitosan: in vitro characteristics and in vivo biocompatibility," Biomaterials, vol. 30, no. 28, pp. 4877–4888, 2009.

131. J. Yan, L. Yang, G. Wang, Y. Xiao, B. Zhang, and N. Qi, "Biocompatibility evaluation of chitosan-based injectable hydrogels for the culturing mice mesenchymal stem cells in vitro," Journal of Biomaterials Applications, vol. 24, no. 7, pp. 625–637, 2010.

132. B. R. Williams, R. A. Gelman, D. C. Poppke, and K. Piez, "Collagen fibril formation.

Optimal in vitro conditions and preliminary kinetic results," Journal of Biological Chemistry, vol. 253, no. 18, pp. 6578–6585, 1978.

133. D. L. Helseth Jr. and A. Veis, "Collagen self-assembly in vitro. Differentiating specific telopeptide-dependent interactions using selective enzyme modification and the addition of free amino telopeptide," Journal of Biological Chemistry, vol. 256, no. 14, pp. 7118–7128, 1981.

134. C. H. Lee, A. Singla, and Y. Lee, "Biomedical applications of collagen" International Journal of Pharmaceutics, vol. 221, no. 1-2, pp. 1–22, 2001.

135. Ktubg E. Fung, Xiaojing Su, etc. "Understanding the impact of 2D and 3D fibroblast cultures on in vitro breast cancer models". PLoS One Vol. 8, Issue no. 10 (2013) October 4th

136. Oren J. Becher and Eric C. Holland, "Genetically Engineered Models Have Advantages over Xenografts for Preclinical Studies", Cancer Res 2006; 66: (7). April 1st, 2006

137. Tarig Magdeldin, Víctor López-Dávila, etc. "The efficacy of cetuximab in a tissue-engineered three-dimensional in vitro model of colorectal cancer", J Tissue Eng. 2014 Jan-Dec; 5: 2041731414544183.

138. Michele Zanoni, Filippo Piccinini, Chiara Arienti, etc. "3D tumour spheroid models for in vitro therapeutic screening: a systematic approach to enhance the biological relevance of data obtained", Scientific Reports, 6:19103, DOI: 10.1038/srep19103

139. Leica microscope system, "Confocal Optical Section Thickness" [Online Source] Accessed from: https://www.leica-microsystems.com/science-lab/confocal-optical-section-thickness/

140. Karen Nygard, Nicole Bechard, "Confocal Sample Preparation Guide" [Online Source] Accessed from: https://www.uwo.ca/sci/research/biotron/pdf/microscopy/ LSM_SampleGuide.pdf

141. Reihani SN, Oddersheda LB, "Confocal microscopy of thick specimens", J Biomed Opt. 2009 May-Jun;14(3):030513. doi: 10.1117/1.3156813

142. H. Jaganathan, D. L. Hugar, and A. Ivanisevic, "Examining MRI contrast in three-

dimensional cell culture phantoms with DNA-templated nanoparticle chains," ACS Appl Mater Interfaces, vol. 3, pp. 1282–1288, Apr. 2011.

143. Michael Brady, "Basics of MRI" Lecture PowerPoint [Online Source, 2004] Accessed from: http://www.robots.ox.ac.uk/~jmb/lectures/medimanallectu re1.pdf

144. Annelies V. D. Plas, "MRI technique" [Online Source, 2015] Accessed from: http://www.startradiology.com/the-basics/mri-technique/

145. UCL, "NMR Spectroscopy Lecture Notes" [Online Source] Accessed from: https://www.ucl.ac.uk/nmr/NMR_lecture_notes/L5_3SH_web_shortened.pdf

146. K. V. R. Chary and G. Govil, NMR in Biological Systems: From Molecules to Human. Springer, Science & Business Media, Apr. 2008.

147. Catarina Veiga, "Development of a novel 3D artificial cancer mass for imaging applications" PhD Thesis, Department of Medical Physics and Bioengineering, UCL, 2015

148. Bing Q. Huang and Edward C. Yeung, "Chemical and Physical Fixation of Cells and Tissues: An Overview", Plant Microtechniques and Protocols, DOI 10.1007/978-3-319-19944-3_2

149. A. Purea and A. G. Webb, "Reversible and irreversible effects of chemical fixation on the NMR properties of single cells," Magn Reson Med, vol. 56, pp. 927–931, Oct. 2006.

150. R. J. Dawe, D. A. Bennett, J. A. Schneider, S. K. Vasireddi, "Postmortem MRI of human brain hemispheres: T2 relaxation times during formaldehyde fixation," Magn Reson Med, vol. 61, pp. 810–818, Apr. 2009

151. Radiation Effects Research Foundation, "How irradiation affect cells" [Online Source] Accessed from: http://www.rerf.jp/radefx/basickno_e/ radcell.htm

152. Macluskey M, Chandrachud LM, Pazouki S, Green M, Chisholm DM, Ogden GR, et al. Apoptosis, proliferation, and angiogenesis in oral tissues. Possible relevance to tumour progression. J Pathol. 2000;191(4):368–75.

153. Soini Y, Pääkkö P, Lehto VP. Histopathological evaluation of apoptosis in cancer. Am J Pathol. 1998;153(4):1041–53.

154. Kerr JF, Winterford CM, Harmon BV. Apoptosis. Its significance in cancer and cancer therapy. Cancer. 1994;73(8):2013–26.

155. G Kroemer, L Galluzzi, P Vandenabeele, etc. "Classification of cell death", Cell Death Differ. 2009 Jan; 16(1): 3–11.

156. Eric J. Hall, "Radiobiology for the radiologist", 2nd Edition, Harper and row publisher, ISBN: 0-06-141074-8

157. Rockwell S. Dobrucki IT, and etc. "Hypoxia and radiation therapy: past history, ongoing research, and future promise", Curr Mol Med. 2009 May; 9(4):442-58.

158. Rogakou, E. P, Boon, C., etc. "Megabase chromatin domains involved in DNA double-strand breaks in vivo", J. Cell Biol. 146. 905–916. doi:10.1083/jcb.146.5.905

159. Van Gent, D. C., Hoeijmakers, J. H. J. and Kanaar, R. (2001). "Chromosomal stability and the DNA double-stranded break connection." Nat. Rev. Genet. 2, 196–206. doi:10.1038/35056049

160. Mailand, N., Bekker–Jensen, S., Faustrup, H., Melander, F., Bartek, J., Lukas, C. and Lukas, J. (2007). "RNF8 ubiquitylates histones at DNA double-strand breaks and promotes assembly of repair proteins." Cell 131, 887–900. doi: 10.1016/j.cell.2007.09.040

161. Asao Noda, Yuko Hirai, Kanya Hamasaki, etc. "Unrepairable DNA double-strand breaks that are generated by ionizing radiation determine the fate of normal human cells", J cell Sci, 2012, 125: 52805287

162. Abigail T. Berman, etc. "Proton Beam Therapy for Non-Small Cell Lung Cancer: Current Clinical Evidence and Future Directions", Cancers 7(3), July 2015:1178-1190

163. Jacqueline A. Gleave, Jason P. Lerch, etc. "A Method for 3D Immunostaining and Optical Imaging of the Mouse Brain Demonstrated in Neural Progenitor Cells", PLOS ONE, August 6th, 2013

164. Manish Trivedi, "The effect of gold nanoparticles on the biological effectiveness of proton therapy", MSc thesis, UCL Department of Surgery and Interventional Science, 2015